FRICTION STIR WELDING OF SPHERES, CYLINDERS, AND T-JOINTS: DESIGN, EXPERIMENT, MODELLING, AND ANALYSIS

By

David H. Lammlein

Dissertation

Submitted to the Faculty of the

Graduate School of Vanderbilt University

in partial fulfillment of the requirements

for the degree of

DOCTOR OF PHILOSOPHY

in

Mechanical Engineering

December, 2010

Nashville, Tennessee

Approved:

Professor Alvin M. Strauss

Professor George E. Cook

Professor D. Greg Walker

Professor Jon F. Edd

Professor D. Mitch Wilkes

ACKNOWLEDGEMENTS

Financial support for this work was provided by the NASA Tennessee Space Grant Consortium, Vanderbilt University, and Los Alamos National Laboratory. I would like to thank Prof. Alvin Strauss and Prof. George Cook for conceiving and directing this research. Prof. Greg Walker, Prof. Mitch Wilkes, and Prof. Jon Edd, I would like to thank for serving on my committee. I would like to acknowledge the machining and design expertise of Bob Patchin and John Fellenstein. I thank Kate Lansford for assistance in cross-sectioning weld samples and UTSI Tullahoma for use of their facility. I recognize the assistance of Robin Midgett in mechanical testing of weld samples. I would like to thank Dr. Paul Fleming, Dr. Dave DeLapp, Dr. Russ Longhurst, Jeff Bernath, Chase Cox, Brian Gibson, Dr. Dan Hartman, Thomas Bloodworth, Dr. Reginald Crawford, Dr. Thomas Lienert, Tracie Prater, and Matt Bement for research input. Completion of this work was made possible by research licenses from The Welding Institute of England (TWI) for use of the friction stir welding process and Edison Welding Institute (EWI) for use of a variable penetration tool.

Lastly, I would like to thank Dr. David R. Lammlein for inspiration, and Presley and Fonda Carpenter for their boundless love and support. I dedicate this work to my mother, father, and brother; whose consistent guidance and support have made this possible.

TABLE OF CONTENTS

TABLE OF FIGURES

LIST OF ABBREVIATIONS AND SYMBOLS

$\dot{\gamma}$ - shear strain-rate

δ - contact state variable

λ - time constant

μ_∞ - infinite shear viscosity

$\tau_{contact}$ – contact shear

σ_e - equivalent steady state flow stress (Mpa)

μ_o - zero shear viscosity

τ_{yield} – yield shear stress or shear strength (Pa)

“ – inches (e.g. 4” = 4 inches)

μ - friction coefficient

A – visco-plastic model material constant

A_{horz} – horizontal tool area

AMP – Advanced Metal Products Inc.

CFD – computational fluid dynamics

C_p – specific heat

CT - computed tomography imaging

EWI – Edison Welding Institute (Ohio)

FE – finite element

FEA - finite element analysis

FSW - friction stir welding

h – tool probe height

HAZ – heat affected zone

ipm – inches per minute

K – kelvin (absolute temperature unit)

m – meters (length unit)

m - power law non-Newtonian fluid index

mm – millimeters (length unit)

mol - mole (SI base unit of amount of substance)

MPa – megapascal

N – newton (force unit)

n - visco-plastic model material constant

Ø – diameter

ORNL – Oak Ridge National Lab

P – weld power (Watts)

Pa – pascal (pressure unit)

Q - heat generation (Watts)

Q_n – heat generated by a narrow (3/16" or 4.8mm diameter) probe tool

Q_{ps} - probe side surface heat input

Q_s - total tool surface heat input

Q_{ss} - shoulder surface heat input

Q_v – volume heat contribution

Q_w - heat generated by a wide (0.246" or 6.0mm diameter) probe tool

Q_{weld} – weld heat input

Q_{wp} – heat dissipated to the weld plate

r - radius

R – the gas constant

rad – radians (angular unit)

r_p ($_{or}$ R_p) – tool probe (pin) radius

rpm – revolutions per second

RPT – retractable probe tool

r_s ($_{or}$ R_s) – tool shoulder radius

s – second (time unit)

TIG - tungsten inert gas type fusion welding

TMAZ – thermo-mechanically affected zone

T_o - reference temperature for Carreau equation

TWI – The Welding institute of England (Cambridge)

UAV – unmanned aerial vehicle

UTS – ultimate tensile strength

V_{matrix} - velocity of the material adjacent to the tool surface

VPT – variable penetration tool

W – watt (power unit)

Z – the Zener-Hollomon parameter

α - visco-plastic model material constant

β (Beta) – power efficiency factor

η (eta) – power efficiency factor

ω (omega) - tool rotational speed (rad/s)

Ω (Omega) - torque (N·m)

INTRODUCTION

Friction Stir Welding, FSW, is a materials joining process with great potential as joint quality is exceptionally high and the process is very repeatable. Additionally, the process does not use fillers and, like fusion welding, eliminates the need for fasteners, which add weight to a structure. These attributes combined with its particular effectiveness on low-melting point alloys (which happen to be low-density) like aluminum and magnesium make FSW very applicable to vehicular applications where costs can easily be justified by increases in strength versus weight and high joint quality. One current limitation of the process is its range of application with respect to joint geometry.

In this work, the FSW process is applied to butted hemispherical joints and butted pipe joints of small diameter (approximately 4 inches). These joints are nonstandard and the application of FSW to these geometries, with such small diameters, has not been presented in the literature. These cases present complications to the standard FSW process and equipment. These complications arise from the surface curvature of these geometries and from the circular nature of the weld path required to join them. The circular nature of the weld path means that either the tool (and the bulk of a spindle motor and control instrumentation) must orbit the work or that the work itself must be rotated on its axis. Either approach presents difficulties. An orbital tool requires a complicated and bulky orbital apparatus. The apparatus must be bulky enough to provide the large down-force required for weld consolidation and material containment in friction stir welding. In addition, this apparatus must be made to orbit smoothly around the pipe or sphere.

Rotating the work presents its own difficulties. The primary difficulty is that the entirety of the work must be rotated about an axis. In the case of a pipe, the length of the sections to be joined is indefinite. In addition, the bulk of the work must be rotated smoothly about its axis, with the eccentricity of this rotation limited within the ability of a force feedback control system to compensate for changes in the height of the work surface with respect to the tool. In the case of an experimental testbed, the choice of a

rotating work, or rotary, type apparatus over an orbiting tool, or orbital, type apparatus is an easy one because the length of pipe sections can be limited to something easily managed. In an experimental setting it makes sense to rotate the work because the work sections are small specimens. In an industrial setting, the orbital option should be considered.

The circular nature of the weld path presents a secondary complication. The weld initiation and weld termination sites must either be coincident or the weld tool must pass through the weld initiation site before weld termination. Regardless, the weld initiation site will be subjected to a secondary heating period. This secondary thermal input at near the weld initiation site will cause a rise in weld temperature as a warm weld initiation zone will be exposed to the thermal effects of the weld process for a second time. Because the thermal and mechanical aspects of the FSW process are highly coupled, this may adversely affect the qualities of the welded material unless compensated for with reduced weld thermal input in the latter stages of the circumferential weld.

The most obvious complication associated with FSW of hemispheres and pipes is the curved nature of the work surface. In traditional FSW, a flat shoulder contacts a flat workpiece and provides frictional heating, downward pressure, and material containment. In the case of a pipe with surface curvature and a sphere with dual surface curvature; a flat, circular tool shoulder does not mate in an ideal fashion with the work surface. In the case of a sphere, it is logical to cup the tool shoulder in such a fashion to mate with the exterior of the spherical work. The effectiveness of this approach is demonstrated in this work. In the case of a pipe, a tool geometry in combination with an appropriate orientation relative to the work must be found, which produces acceptable welds joining two butted pipes. In this work an effective method of joining butted pipe sections by FSW is demonstrated.

The problems presented in sphere and pipe welding by secondary heating, work rotational eccentricity, and surface curvature are exacerbated in the case of small diameter work. Work specimens with a small radius of curvature present a shorter circumferential weld path resulting in a smaller time period between primary heating at the weld initiation site and the secondary heating described earlier. Additionally, for small diameter work heat is more readily conducted throughout the workpiece because of

reduced conduction lengths. In small diameter, as compared to large diameter work, the radial velocity of the tool around the circular weld path is higher because the circumference of the work is smaller. This relationship results in more rapid changes in the work surface height relative to the tool for the same rotational eccentricity. Small diameter work also presents the most highly curved surface for FSW and creates the greatest difficulty in the problem of tool shoulder mating described earlier.

The conical tool study presented attempts to address an additional issue associated with FSW of butted hemispheres and butted pipes. In traditional FSW, the weld tool leaves a defect at the weld termination site. This defect is either a tearing at the boundary of the work where the thermal and mechanical influences of the weld zone rip the tool out of the end of the material or, more commonly, a hole left by the tool probe when the tool traverse is stopped and the tool is vertically retracted from the work. Pipes and spheres present closed contours which do not provide a convenient location for weld termination. Unlike a linear weld, there is no abrupt boundary to the work material. The entirety of the pipe or sphere is critical and there is no location where a weld termination defect is acceptable. A method of weld termination must therefore be used that extracts the tool from the material with minimal defect. Complicated solutions to this problem exist, such as a retractable probe tool (RPT) and a runoff tab method. These solutions have significant drawbacks. The RPT adds significant cost and complication to the machine, and the runoff tab method requires that a tab be welded over the welded path during welding and before weld termination. A conical tool, or variable penetration tool (VPT), is potentially a simple and elegant solution to this problem.

In addition to expanding the range of application of FSW to nonstandard joint configurations, this work seeks to join pieces at a high traverse rate for application to manufacturing and automation. Welding at a high traverse rate can increase the output of the FSW machine and justify the significant cost associated with the technology. In this work hemispheres and pipes are joined successfully at traverse rates of 10.4 and 17 inches per minute respectively. At this speed, the full circumference of the pipe sections is joined in under 50 seconds.

The studies presented here are accompanied by computational fluid dynamic (CFD) models which reliably predict the temperature fields present during welding, the

flow of material during the process, and process forces. Significant expense is necessary for the design and implementation of a FSW experiment. The FSW machine is an expensive piece of equipment and the design of a FSW experiment is a significant undertaking. The weld tool, work geometry, and work fixturing must be designed and machine time must be used to perform the experiment. The difficulty of obtaining empirical data in FSW creates a need for a useful numerical tool for assessing a FSW environment prior to welding. The models presented use relatively simple process model equations and reliably predict the critical aspects of the FSW process for a wide variety of FSW process environments.

CHAPTER I

LITERATURE REVIEW: COMPUTATIONAL MODELING OF FRICTION STIR WELDING

Introduction

Friction Stir Welding

Friction stir welding (FSW) is a relatively new, solid-state, metal joining process invented by Wayne Thomas et al. at the Welding Institute of England (now TWI) in 1991 [1]. A FSW butt weld is made by following the joint-line of two butted pieces of material with a rotating tool while applying a significant down-force through the tool. Heating is provided at or near the tool-work interface by the rotating tool, traditionally a single piece comprised of a shoulder, which contacts the material surface, and a submerged probe. In addition to providing heat, the shoulder also serves to contain the deforming metal beneath it. The process is simple in that it involves only the movement of a non-consumable tool through a joint. This apparent simplicity is however only superficial as the actual mechanisms of weld formation are complex and highly coupled.

Most generally, a weld is formed via the mechanical deformation of a thin layer of plasticized work material surrounding the tool. Projected along the joint-line, this becomes a channel of welded material. During a weld, tool motion and pressure combine to create material strain along with viscous and frictional heating at or near the weld interface. The result is plasticity and large scale deformation. The work material in this region is deformed to such a degree that its deformation is frequently referred to as flow, despite minimal fluid-state material at welding parameters that are reasonable for a given material and tooling.

Computational Modeling

FSW is not unlike other industrial process in that its primary development has been made via empirical observation. Much can be learned about a process, particularly in its nascent stages, through the sometimes arbitrary adjustments to parameters and tooling. However, past advancements in our understanding of various other processes have been made with the aid of computational models and there is no doubt that this will more and more frequently be the case with computing power continually increasing. Computational modeling will likely guide task specific tool geometry selection and weld parameter optimization. Additionally, FSW computational modeling has potential for the determination of weld microstructure, residual stress, and defect formation [3].

Computational, or numerical models as they are sometimes called, require process specific input data for the assignment of initial conditions, boundary conditions, and material properties. Input data is obtained from experiment and mathematical models of the various process mechanisms. These process models can be analytically based, empirically based, or based on some combination of the two. A common and acceptable approach is the use of an analytically developed equation containing parameters dependent on experimental results. This construct is often preferable to a purely empirical approach (e.g. curve fitting) as the researcher is left with more intuitively useful results. An example of one frequent application of this technique in FSW modeling is the representation of tool contact condition (particularly shoulder contact condition) for the calculation of heat input. Computational modeling is applied to a system of analytical equations whose complexity renders its solution by traditional means exceedingly tedious.

Computational modeling of the FSW process involves an intense treatment of the thin region in the vicinity of the tool-work interface. FSW model complexity lies not in the geometry or kinematics of the tool, but in the mechanisms by which a weld is created in the work material. The material flow is limited to the region enveloping the tool and process variables in this region are coupled in a manner which excludes an independent treatment. Viscosity, for example, is strongly dependent on temperature and strain rate; which are themselves dependent on the frictional condition at the interface. The

frictional condition at the interface is however highly dependent on material viscosity, creating a closed loop relationship. Viscous heating (or plastic dissipation) and frictional heating at or near the tool surface produce steep temperature gradients in both the work material and the tool itself near their interface. The steep process variable gradients in this region are contrasted with the lack of such gradients throughout the remainder of an FSW model.

As discussed above, computational (or numerical) modeling is an evolved form of process modeling. The topic of process modeling in FSW can be subdivided into four somewhat distinct areas: heat generation, thermal boundary conditions, material thermo-physical properties, and material flow. Heat generation or power input is arguably the starting point in any such modeling. Thermal boundary conditions are then necessary to establish a control volume. Material thermal properties in turn govern heat conduction within that volume and establish a temperature gradient. Material flow is obtained as a consequence of these forces and the tool motion. Tool motion drives the evolution of each of these concepts but is itself trivial.

Process Models

Experimental and Analytical Bases for Assignment of Heat Input Boundary Conditions

The heat generated during the weld process is equivalent to the power input into the weld by the tool, minus some losses due to micro-structural effects [10] and potentially due to other effects. This total heat input or heat generation includes heat conducted up the tool and not simply into the weld material. Longitudinal travel of the tool can be neglected [2]. St-Georges et al. [63] report the tool travel contribution to be typically less than 5% for 6mm thick AA6061 plate. The power dissipated by the tool (power input) can be obtained experimentally from the weld moment and spindle speed [8-11, 19, 17, 29, 44, 63]:

$$\textbf{\textit{Power = P =}}\omega\cdot\Omega + F\cdot v \quad \textbf{\textit{(1.1)}}$$

where P is the weld power (Watts), ω is the tool rotational speed (rad/s), Ω is the measured torque (N·m), F is the traverse force (N) and ν (m/s) is the traverse velocity. The heat generation (Watts) input near the interface is therefore:

$$Q = P\eta$$

where η (sometimes β) is the fraction of power dissipated by the tool into the weld material and the tool that is directly converted into heat. This value is understood to be high. Santiago et al., [10], estimate this value to be 0.9 and De Vuyst et al. [65] quote a range of 0.9-1.0. Nandan et al. [7] refer to this as the power efficiency factor, C_f. Most assume this value to be 1.0 and define the weld efficiency simply as weld power minus the portion of the heat dissipated via conduction through the tool [8,9, 23-26]. Regardless, the percentage of mechanical work dissipated by the tool, which is converted to heat, is very high. The fraction of total heat dissipated through conduction up the tool shank is discussed extensively in the proceeding section on thermal boundary conditions.

Analytical models of heat input estimate power input in the absence of weld moment data or predict heat input based on material properties and weld parameters. These models also address the contact conditions at the tool interface. The so-called friction model states that an incremental heat input contribution, dq, for a given area, dA, can be expressed in terms of the contact shear, $\tau_{contact}$, at a given centroid radius, r:

$$\textbf{\textit{dq = }}\omega\cdot\tau_{contact}\cdot r\cdot dA \quad \textbf{\textit{(1.2)}}$$

The above form was developed by [13] for friction welding and has since been frequently used as the basis for obtaining values of heat input at tool surfaces for FSW [10,12,14,18,19,21, 28].

One can see that an analytical prediction of the total heat input is dependent on the tool contact condition. Of consideration are the total area of contact and the nature of

contact. The contact area can include all or part of the surface and the nature of this contact can be stick, slip, or stick/slip.

In the case of a stick condition (μ=1), the power is equivalent to that necessary for interfacial shearing of the material in the vicinity of the tool. For a finite area dA at the tool surface at a centroid radius, r, from the tool rotational axis; the corresponding, heat input is:

$$dq = \omega \cdot \tau_{yield} \cdot r \cdot dA \qquad (1.3)$$

where ω is the radial velocity of the tool and τ_{yield} is the shear strength of the weld material. The shear strength of the material is obtained from the yield strength of the material by applying the von Mises yield criterion in uniaxial tension and pure shear (as is the case for the weld material at the tool surface):

$$\tau_{yield} = \frac{\sigma_{yield}}{\sqrt{3}}$$

The yield strength is strongly dependent on temperature and to a lesser extent, strain rate. This relationship will be discussed to a great extent in the material thermal properties section.

For a slip or frictional (μ<1) interface condition, the torque required to overcome friction is used to define heat input. Here the incremental heat input is defined as:

$$dq = \omega \cdot \tau_{friction} \cdot r \cdot dA = \omega \cdot \mu \cdot p \cdot r \cdot dA \qquad (1.4)$$

where p is the average tool surface pressure over the incremental area. In the case where $\mu p > \tau_{yield}$, one must differ to the first case as interfacial shearing will occur.

Schmidt et al. define an additional variable, the contact state variable (δ), for the slip/stick contact condition:

$$\delta = V_{matrix} / V_{tool}$$

where V_{matrix} represents the velocity of the material adjacent to the tool surface. These three cases from the following contact condition table [23]:

Condition	Matrix velocity	Tool velocity	Shear stress	State variable
Sticking	$v_{matrix} = v_{tool}$	$v_{tool} = \omega r$	$\tau_{friction} > \tau_{yield}$	$\delta = 1$
Sticking/sliding	$v_{matrix} < v_{tool}$	$v_{tool} = \omega r$	$\tau_{friction} \geqslant \tau_{yield}$	$0 < \delta < 1$
Sliding	$v_{matrix} = 0$	$v_{tool} = \omega r$	$\tau_{friction} < \tau_{yield}$	$\delta = 0$

Figure 1: Possible contact conditions, figure from [23].

The matrix velocity and coefficient of friction, and therefore the contact state variable and frictional shear respectively, must be adjusted to obtain an agreement with experiment. An intense debate exists over the predominant nature of the contact condition.

The sum of the heat contributions of all incremental interface surfaces is equal to the total heat input from the tool and is some large fraction of the experimentally determined weld power:

$$Q = dq_1 + dq_2 + \ldots \qquad (1.5)$$

The surface of a tool with radial symmetry can be divided into horizontal sections (e.g. shoulder, cylindrical probe bottom), vertical sections (e.g. cylindrical probe wall), and inclined sections.

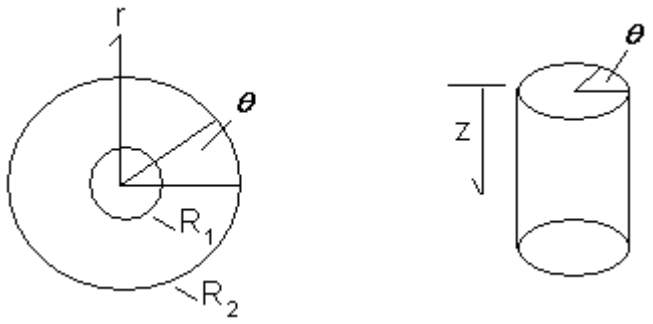

Figure 2: Schematic of tool surface variables.

For horizontal sections, a heat input value can be obtained via ***(1.2)***:

$$Q_{horizontal} = \int_0^{2\pi} \int_{R_1}^{R_2} \boldsymbol{\omega} \cdot \boldsymbol{T}_{contact} \cdot r^2 \partial r \partial \theta$$

$$= \frac{2}{3} \pi \boldsymbol{T}_{contact} \boldsymbol{\omega} (R_2{}^3 - R_1{}^3) \textbf{ (1.6)}$$

And for vertically oriented tool faces:

$$Q_{vertical} = \int_0^{2\pi} \int_0^{H_{wall}} \boldsymbol{\omega} \boldsymbol{T}_{contact} R_{wall}{}^2 \partial z \partial \theta$$

$$= 2\pi \boldsymbol{T}_{contact} \boldsymbol{\omega} R^2{}_{wall} H_{wall} \textbf{ (1.7)}$$

In the case of faces inclined with respect to the horizontal axis by an angle less than 45 degrees, Schmidt et al. introduce an inclination factor. The inclination factor treats the heat contribution as a summation of the vertical and horizontal contributions of the surface. The factor is applied to shallow angle (<45° off horizontal), concave surfaces (i.e. a concave shoulder), but is presumably meant to apply to shallow angle, convex (or conical) surfaces as well.

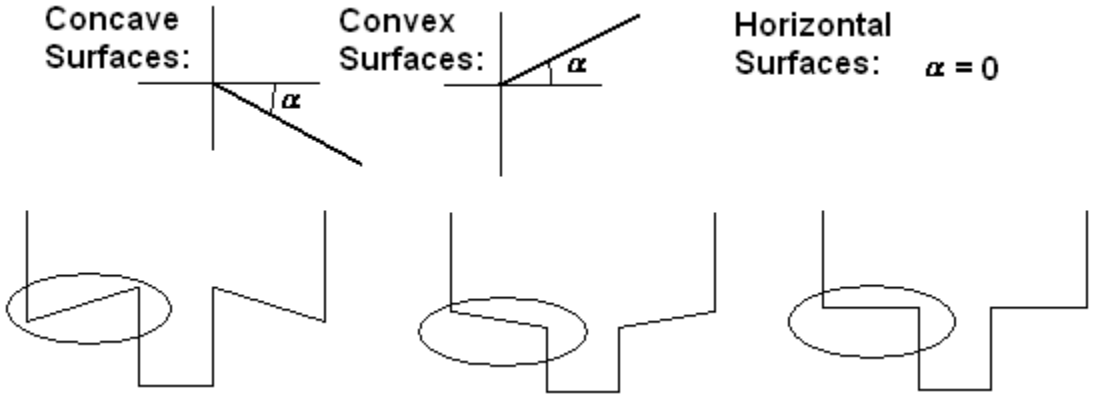

Figure 3: Tool surface inclination factors.

The inclination factor is applied as follows to equation ***(1.6)***:

$$Q_{\propto} = \frac{2}{3}\pi \boldsymbol{T}_{contact}\boldsymbol{\omega}(R_2^{\,3} - R_1^{\,3})\tan(1+\propto) \quad for\ \boldsymbol{\alpha} \le 45^\circ off\ \underline{horizontal}\ plane \textbf{(1.8)}$$

This form of approximation can presumably be extended to faces inclined by an angle greater than 45° with respect to the horizontal axis by applying the same inclination factor formulation with respect to off-vertical inclinations of less than 45°. An inclination with respect to the vertical axis could be applied to the heat generation equation for vertical surfaces, equation ***(1.7)***:

$$Q_{\propto} = 2\pi \boldsymbol{T}_{contact}\boldsymbol{\omega}R^{2}_{\ wall}H_{wall}\tan(1+\propto) \quad for\ \boldsymbol{\alpha} \le 45^\circ off\ \underline{vertical}\ plane \textbf{(1.9)}$$

These approximations are clearly overestimations of the effective surface area of the inclined face. In addition, the author points out the limitation of the face heat contribution approach only to surfaces with rotational symmetry. This excludes the direct treatment of threads or flutes with this approach. Simplifications must be made to the calculations for these surfaces and things such as effective surface area, radial distance, and facial orientation may need to be approximated.

Tool tilt angle, θ, is accounted for with the introduction of an additional factor expressed in terms of the tilt angle [18]. This factor is applied to equation ***(1.6)***.

$$Q_{tilt\_surf} = \frac{2}{3}\pi \boldsymbol{T}_{contact}\boldsymbol{\omega}(R_2^{\,3} - R_1^{\,3})(1/\cos\boldsymbol{\theta})^3 \quad \textbf{(1.10)}$$

With this factor, heat generation is increased at increasing tool tilt angles. The factor assumes that the shoulder plunge depth is adjusted to maintain shoulder contact on the leading edge of the weld as tool tilt angle increases.

Colegrove et al. [17] estimate the ratio of heat generated by a cylindrically threaded probe to be 20% of the heat generated by the shoulder and probe using the following formulation of equation ***(1.7)***:

$$Q_{\text{pin}} = 2\pi r_p h \bar{Y} \frac{V_m}{\sqrt{3}} + \frac{2\mu \bar{Y} \pi r_p h V_{rp}}{\sqrt{3(1+\mu^2)}} + \frac{4F\mu V_m \cos\theta}{\pi} \quad \textbf{(1.11)}$$

where r_p is the probe (pin) radius, h is the probe height, $\bar{Y}$ is the average shear stress over the probe surface, μ is the coefficient of friction, F is the translational force during welding, and λ is the thread helix angle. The remaining terms are defined as follows:

$$\theta = 90 - \lambda - \tan^{-1}(\mu)$$

$$V_m = \frac{\sin\lambda}{\sin(180 - \theta - \lambda)} V_p$$

$$V_{rp} = \frac{\sin\theta}{\sin(180 - \theta - \lambda)} V_p$$

$$V_p = \omega r_p$$

Russell et al. [12] estimate the contribution of the probe to the total heat generation near the interface to be approximately 2% using equation ***(1.7)*** and assuming the contact shear stress to be 5% of its room temperature value (taking into account material softening with temperature and strain). Simar et al. [8] estimate 12% for this same value. These analytically calculated probe contributions are tool geometry, material, and parameter dependent, as are the empirical values.

Debate exists over the predominant nature of the tool interface contact condition, particularly for the shoulder, and how best to model it. Schmidt et al. [24] assume full shoulder contact with a constant frictional coefficient over the shoulder surface. Under these conditions, slip occurs where the frictional shearing does not exceed the shear yield strength of the material, and stick occurs elsewhere. Colgrove et al. [22] use a stick condition with an artificially small contact radius and achieve good agreement with experiment. The authors however concede this approach to be physically unrealistic. Its use is justified as a simplification. The authors state that a slip condition

likely predominates near the shoulder edge but the corresponding interfacial shear stress is too difficult to estimate.

In addition to the torque based method of empirical heat input estimation, the heat input into weld material has been estimated via inspection of the width of the weld heat affected zone (HAZ) [20]. Others have used a combination of imbedded thermocouples readings and HAZ size measurements [14, 15, 16, 19]. Although individually these studies cover a narrow range of parameters, together they show a strong correlation between heat input to the weld and the size of the HAZ. Heurtier et al. successfully correlate microhardness readings with weld temperature [21].

These experimental measurements are required in the implementation of a realistic computational model. Heat generation and heat dissipation must be tuned and balanced to obtain agreement with experimental temperature data. This process will be discussed in more detail in the proceeding section on thermal boundary conditions.

Model Dependent Heat Generation

In each of the methods above, either the heat input or the temperature of the shoulder and pin surfaces are obtained via analytical and empirical means outside of the model and applied as a boundary condition to the model. Schmidt et al. [25], De Vuyst et al. [65] and Santiago et al. [10] apply model dependent plastic dissipation heat generation. The region of volumetric type heating is experimentally confirmed and agreed upon in literature to occur in the so-called thermomechanically heat affected zone (TMAZ) where plastic dissipation occurs. The minimum extent of the TMAZ is the width of the shoulder at the material surface and the width of the pin at the weld root [4, 36-38]. Plastic dissipation heating is applied to each element of the model as the product of the deviatoric stress tensor, s_{ij}, the plastic strain tensor (also called deformation rate), $\dot{\varepsilon}_{ij}^{pl}$, [43] and a plastic energy dissipation efficiency term, η_{pd}:

$$q_{vol} = \eta_{pd} s_{ij} \dot{\varepsilon}_{ij}^{pl} \quad \textbf{(1.12)}$$

This efficiency term, η_{pd}, is know in some fields as the Taylor-Quinney coefficient, β. Its value is typically between 0.9 and 1.0 [65]. Here the efficiency term is adjusted within the model to conform with the experimentally observed thermal gradient. He et al. [27] apply an identical formulation but do not mention the use of an efficiency term. Frictional heating on the surface of the material cannot be applied in a model dependent fashion as the pressure and frictional coefficient terms (and thus contact shear stress) in equation ***(1.4)*** are difficult to reliably reproduce in model.

Heat Dissipation and Thermal Boundary Conditions

The discussion of heat generation above applies to the thermal boundary conditions at the weld interface. For the establishment of a control volume, thermal boundary conditions must be established on all the model external surfaces in addition to heat input at and near the interface. Heat loss occurs via conduction to the tool, the backing plate, and any unmodeled portion of the weld material. Convective heat loss to the surrounding atmosphere also occurs. The heat lost through convection is considered negligible and has been shown in numerous studies to have no effect on temperatures within the weld plate [3].

Of the total heat generated near the welding interface, a majority is dissipated by way of the plate as opposed to via the tool shank. Knowing the temperature at two points along the length of the tool, the heat flux in Watts dissipated through its shank can be calculated:

$$Q_{tool} = \frac{\lambda_{tool}(T_1 - T_2)}{d} \quad \textbf{(1.13)}$$

where λ_{tool} is the thermal conductivity (e.g. W/m·K) of the tool shank, T_1 is the temperature at a position near the shoulder, T_2 is the temperature at a position further up

the shank, and d is the distance along the height of the shank from thermocouple position one to two. Again, convective losses associated with the rotating tool in air are believed to be negligible, but may be modeled using a surface convective coefficient. The heat dissipated through the tool can be compared with some calculated value of total heat input to produce a ratio some call the weld efficiency [8, 9, 25, 29] ($\eta_{weld\_thermal}$ is used here for clarity):

$$\eta_{weld\_thermal} = \frac{Q_{shoulder} + Q_{probe}}{Q_{shoulder} + Q_{probe} + Q_{tool\_shank}} = \frac{Q_{weld}}{Q_{total}} = \frac{Q_{weld}}{\eta_{power\_to\_heat} P_{dissipated\_mechanical}}$$

This ratio will vary with variations in the experimental setup and parameters. Schmidt et al. [25] estimate the fraction of total heat input transferred to the work piece to be approximately 75% in a particular set of experimental welds. Simar et al. [8] arrive at a value of 95% and Dickerson et al. [29] at a value of 92% by placing thermocouples on the tool shank and throughout the weld plate.

The weld heat input, Q_{weld}, can be divided into surface and volume heat contributions due to frictional or viscous (plastic dissipation) heating respectively. Simar et al. [9] introduce a term, γ, for this purpose:

$$Q_v = \gamma Q_{weld}$$

$$Q_s = (1-\gamma) Q_{weld}$$

where Q_v is the volume heat contribution and Q_s is the total tool surface heat contribution. In [9], it is concluded that a value of $\gamma = 0$, corresponding to pure slip, produces best agreement with experimental thermal data for thermal computational models which take into account fluid flow. This is presumed to be due to both the thin nature of the deforming layer around the tool and the decreasing rates of strain and deformation occurring as one moves away from the tool.

The heat input on the tool surface is typically treated by defining a constant heat flux (e.g. W/m^2) over the interface surface or one which varies with some spatial parameter, typically radius. While frictional heating does occur essentially at the interface, the assignment of the viscous dissipation heating contribution to the interface is an approximation based on the assumption that the layer of dissipation surrounding the tool is reasonably thin. Again, this assumption can generally be made without loss of model accuracy for thermal-fluid models. The heat generation in both the pin and shoulder is typically treated as axis-symmetric since tool rotation and circumferential material flow around the tool largely render this to be the case. The following formulation for shoulder surface heat flux input, Q_{ss}, distribution over the tool shoulder is commonly used [8,9,26].

$$q_{ss}(r) = \left(\frac{3}{2\pi}\right)\left(\frac{Q_{ss} \cdot r}{R_s^3 - R_p^3}\right) \text{ with } R_p \le r \le R_s \quad \textbf{(1.14)}$$

Shoulder heat input per unit area increases with radial distance from the probe surface as the tangential velocity increases. The probe side surface heat flux input, Q_{ps}, is distributed as an even heat flux over its height:

$$q_{p\_side}(r) = \left(\frac{1}{2\pi}\right)\left(\frac{Q_{ps}}{R_p \cdot h_p}\right) \quad \textbf{(1.15)}$$

Simar et al. [9] neglect the probe tip surface heat flux input distributing the full probe heat contribution over its side surface. A probe tip surface distribution could be formulated in the manner of equation **(1.14)** (with R_p=0, R_s= R_p , and Q_{probe_tip} in place of Q_{ss}) if desired. Q_{ss}, Q_{ps} , and Q_{probe_tip} can be found analytically via equations ***(1.6)***, ***(1.7)***, and again ***(1.6)*** respectively. Heat generation in the pin can be modeled as a uniform, volume heat source (i.e. W/m^3) without loss of model accuracy.

The majority of heat of heat is dissipated ultimately through the backing plate (through the clamps, un-modeled plate portions of the plate, and directly through the backing plate) as opposed to the tool shank and surface convection of the plate in air

[3]. The primary method [22] of achieving good agreement with experimental thermal gradients is the method of adjustment of model heat input and backing plate heat dissipation used by [30-35, 16, 17]. Heat transfer between the backing plate and work material is often modeled using a uniform heat transfer coefficient over the interface. Colegrove et al. [22, 3] note however that the contact condition under the tool is more intimate than elsewhere at the backing plate and weld plate interface due to the pressure and heat present. In addition, during a full penetration weld the thermomechanically heat affected zone (TMAZ) extends to the backing plate resulting in a more intimate contact in the region passed over by this zone. Weld material fills microscale scratches and notches in the backing plate and as a result there exists a higher conductance over the interface in this area. Based on these observations two improvements over the uniform interfacial conductance have been suggested. The first method is to assign a temperature dependant conductance at the backing plate top surface. In some numerical models it may be a simple matter to increase thermal coupling with temperature at the interface. The second method is to assign one coefficient of conductance to the general interface and a larger coefficient to the area under the tool and the tool path behind the tool:

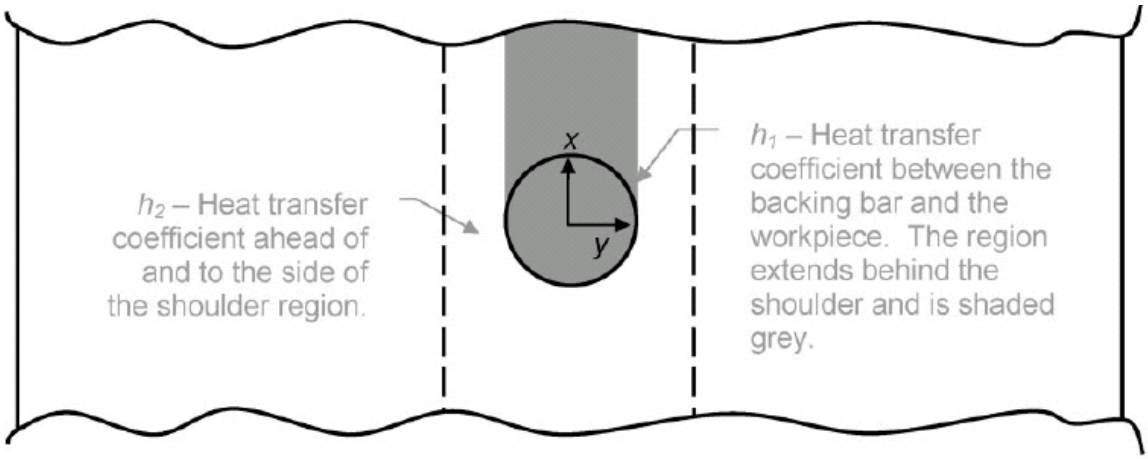

Figure 4: The heat transfer coefficient between the work and anvil is greater under the traveled path of the tool where heat and pressure have forced a more intimate bond. Figure from [22].

The heat transfer coefficient between the work and anvil is greater under the traveled path of the tool where heat and pressure have forced a more intimate bond [22].

The added complication of these methods is warranted due to the importance of the heat removal of the backing plate.

Conduction losses to the weld plate are accounted for within the model by assigning a uniform heat transfer coefficient over the modeled/unmodeled weld plate boundary. This boundary is generally greater than one shoulder diameter from the tool axis of rotation and where the approximation of a uniform conductance is acceptable due to small temperature gradients. The heat loss over a cylindrical boundary surrounding the weld tool can be approximated in a radial fashion with temperature, T, at some radial distance, r, is defined by:

$$T(r) = T_o + \frac{Q_{wp}}{2\pi kh} \ln \frac{R_o}{r}$$

where Q_{wp} is the heat dissipated to the weld plate, T_0 is the temperature at a distance R_o from the axis of rotation of the tool (average temperature on an interior cylindrical face, e.g. interface temperature at probe radius), k is the thermal conductivity of the weld metal, and h is the height of the cylindrical conduction zone (usually height of the pin or the thickness of the weld plate). Knowing the temperature at the interior and exterior surface boundaries, the total heat loss over the exterior surface and to the unmodeled weld plate can be calculated:

$$Q_{wp} \cong \frac{2\pi kh(T - T_o)}{\ln \frac{R_o}{R}}$$

where R is the radius of the exterior cylindrical surface (i.e. modeled/unmodeled plate boundary).

Heat loss from the weld plate top surface to the surroundings is governed by radiation and convection. The heat loss per unit area on the top of the plate can be approximated using the following equation:

$$q_{top} = \sigma\varepsilon(T^4 - T_a^4) + h_t(T - T_a)$$

where σ is the Stefan-Boltzmann constant, ε is the emissivity of the plate, T is the temperature of the plate top surface, T_a is the ambient temperature, h_t is the convective heat transfer coefficient of the plate in air. As discussed earlier in this section, the heat lost in this way is low and is often ignored.

Material Thermo-Physical Properties

Heat flow within the modeled volume is dependent on material flow around the tool and on material thermal properties. It is governed by Fourier's Law:

$$\dot{Q} = -k(\nabla \mathrm{T})$$

where k is thermal conductivity, ∇T is the temperature gradient, and $\dot{Q}$ is the heat flux. The temperature gradient is nearly symmetric (radial) about the tool axis of rotation as a consequence of material flow. Heurtier et al. [21] note a slight asymmetry about the weld line with the higher temperatures found on the advancing side. The traverse direction opposes tool motion on the advancing side resulting in a vortex velocity field. It is noted that a material element spends more time on the advancing side due to the complicated nature of the flow on this side as compared to the retreating side where material flow is largely in the direction of tool motion. Crawford et al. [52] note a similar asymmetry in Fluent CFD models of threaded pins. Higher rotational speeds are also seen to shift the HAZ further towards the advancing side.

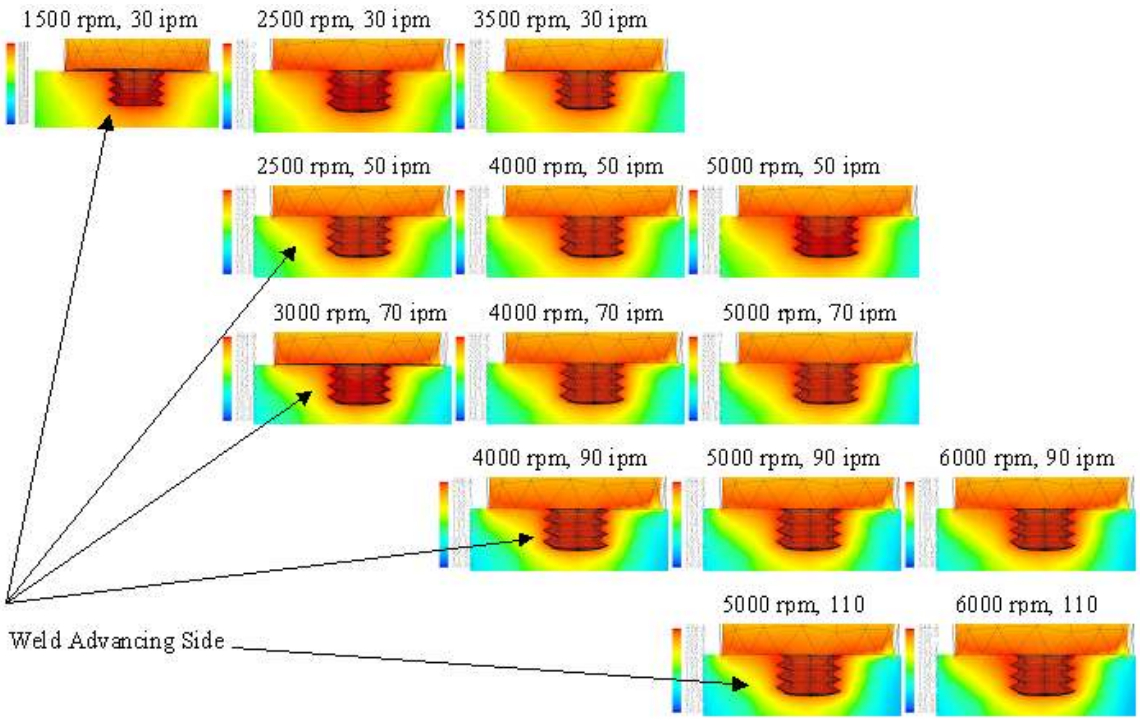

Figure 5: Lateral cross sections of temperature contours at various rotational and travel speeds, figure from [52].

Conductive heat flow is governed by thermal conductivity (k or λ), specific heat (c_p), and density (ρ). These properties are each dependent on temperature and, for alloys, microstructure evolution [3]. The dependence on temperature for aluminum alloys is known in the absence of other effects. (Table from [5])

Recommended values for the thermophysical properties of Al alloy - 6061-T6

T °C	Density kg m^{-3}	C_p J K^{-1} g^{-1}	H_T-H_{25} Jg^{-1}	10^6a m^2s^{-1}	λ Wm^{-1} K^{-1}	η mPas
25	2705	0.87	0	-	-	
100	2695	0.95	69	76	195	
200	2675	0.98	166	77.5	203	
300	2655	1.02	266	78	211	
400	2635	1.06	370	76	212	
500	2610	1.15	480	75	225	
600[a]	2590	1.16	596	66.5	200	
642[a]	2580	[1.16][b]	[645][b]			
642[a]	2415	1.17[c]	981	32	90	[1.15][c]
700	2400	1.17[c]	1049	32.5	91	[1.05][c]
800	2372	1.17[c]	1166	33[b]	92	[1.0][c]

[a] = melting range [b] = extrapolated value [c] = estimated value

Figure 6: Thermophysical properties of Al-6061-T6, figure from [5].

The complex and chaotic evolution of weld microstructure including the dissolution of precipitates and local melting has a significant effect on the thermal properties of the metal. A number of studies [40–42, 45–48] show that precipitates are significantly coarsened in the HAZ in comparison to those in the unaffected base plate and weld nugget. Su et al. [50] report on precipitate evolutions occurring in AA7050 FSW. Their findings showed a coarsening of precipitates from the base plate into the TMAZ, with increasing dissolution and re-precipitation occurring from the TMAZ to the interior weld nugget. Sato et al. [49] looked at a number of locations in the HAZ and the weld nugget of AA6063 FSW and observed that the precipitates experienced increasing dissolution toward the weld center.

The computational cost of modeling the effect of microstructure evolution is however too high and its effects are therefore not modeled. This unmodeled contribution is masked by comparable uncertainties elsewhere in the model [3]. Temperature dependent values like in the table above are often used. Colegrove et al. [22] report better agreement with thermocouple temperature gradients using a constant thermal conductivity value, noting that data book values represent an equilibrium state rather than the rapid thermal cycles present in FSW.

Flow stress in aluminum alloys is dependent on temperature and strain-rate. Sellars and Tegart [6] proposed an initial formulation which represented the TMAZ region as a rigid, visco-plastic fluid. Sheppard and Wright [39] modified their formulation into the following commonly used form:

$$Z = \dot{\varepsilon} \exp(\frac{Q}{RT}) = A(\sin \alpha\sigma_e)^n$$

or equivalently [43]

$$\sigma_e = \frac{1}{\alpha} \sinh^{-1}\left[\left(\frac{Z}{A}\right)^{\frac{1}{n}}\right] \qquad Z = \dot{\varepsilon} \exp\left(\frac{Q}{RT}\right)$$

where α, *A*, *n* are material constants (α = 0.045 $(Mpa)^{-1}$, Q = 145 kJ mol^{-1}, A = 8.8632E6 s^{-1}, n = 3.55), σ_e is the equivalent steady state flow stress (Mpa), *R* the gas constant (R = 8.314 $mol^{-1}K^{-1}$), *T* the absolute temperature (K), Q is the activation energy (J mol^{-1}) and Z is the Zener-Hollomon parameter. The material constants used are determined using a standard compression test. The material viscosity is defined in the following manner:

$$\mu = \frac{\sigma_e}{3\dot{\varepsilon}}$$

The visco-plastic model holds at temperatures reasonably below the metals solidus temperature. As the material approaches the solidus temperature significant softening occurs. Seidel and Reynolds [51] proposed reducing the flow strength in a linear fashion from its value at some arbitrary temperature, T_m, to zero at the solidus temperature, T_s. [51] and [22] define the so-called empirical softening regime by setting T_m at 50°C below the solidus temperature.

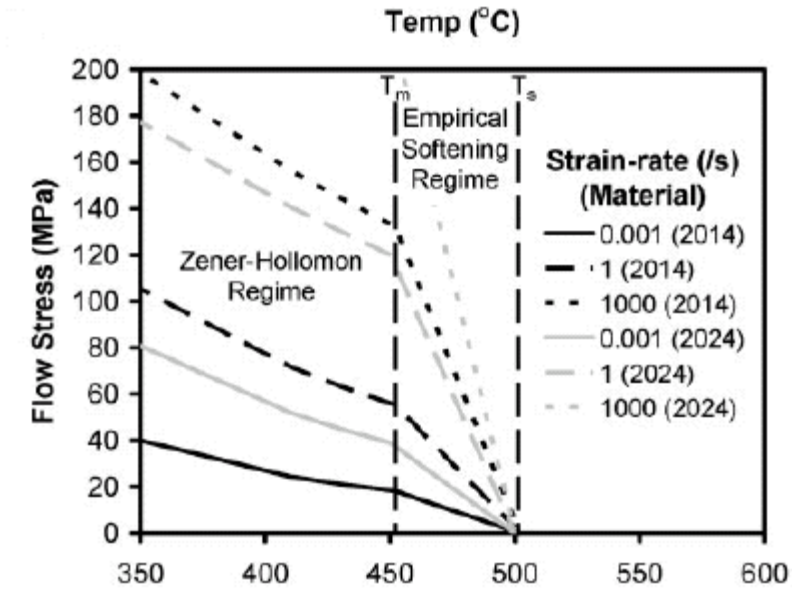

Figure 7: Constitutive behavior of Al-7449 (T_s -T_m=50℃ and T_s=500℃), figure from [22].

Increasing the range of the empirical softening regime is found to have the effect of increasing the size of the TMAZ in thermo-mechanical models. A Carreau viscosity model is employed by Atharifar et al. [67] and is discussed later with computational modeling studies.

Analytical Models of Material Flow

Schnieder and Nunes [57] attempt to dissect the FSW metal flow into three separate incompressible flow fields:

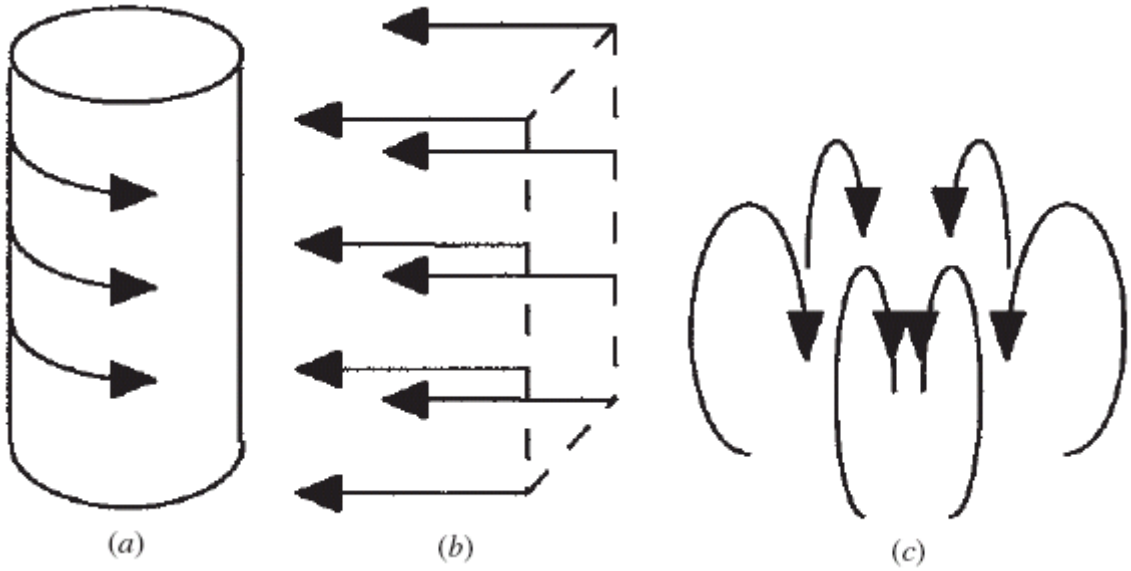

Figure 8: Three flow fields a) rotation b) translation c) ring vortex; figure from [57]

It is postulated that the summation of these three fields results in a thru-current on the retreating side and a maelstrom current surrounding the probe:

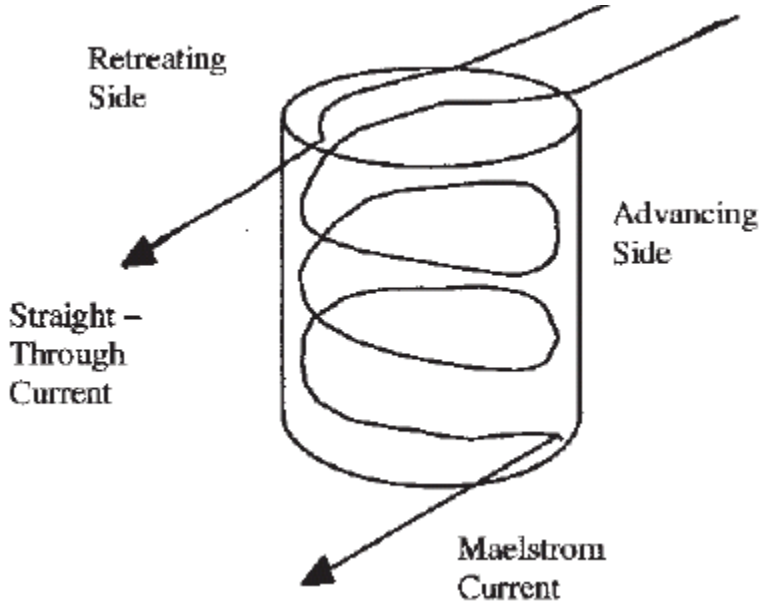

Figure 9: Summation of three flow fields yields two flow currents, figure from [57].

The downward spiral exhibited in the maelstrom current is said to be a result of the ring-vortex which is in turn a consequence of the downward effects of probe threading (left-hand threaded probe spun clockwise or right-hand threaded probe spun

counterclockwise). This downward forcing is claimed to be reversible with opposite threading. One consequence of this deconvolution model is that material in the advancing side flow current resides in the flow region longer than that on the retreating side. The model further attempts to explain the onion ring surface microtextures and the entrained oxide film defect found.

An inverted x-ray tomography study [58] provides some confirmation of the two flow theory. Figure 10 shows the post-weld distribution of two streams of lead marker material placed in two positions parallel to the weld line. The marker material along the center of the weld line is deposited in a chaotic fashion behind the tool whereas the marker material placed further to the retreating side is deposited in a linear fashion consistent with the thru-current flow path.

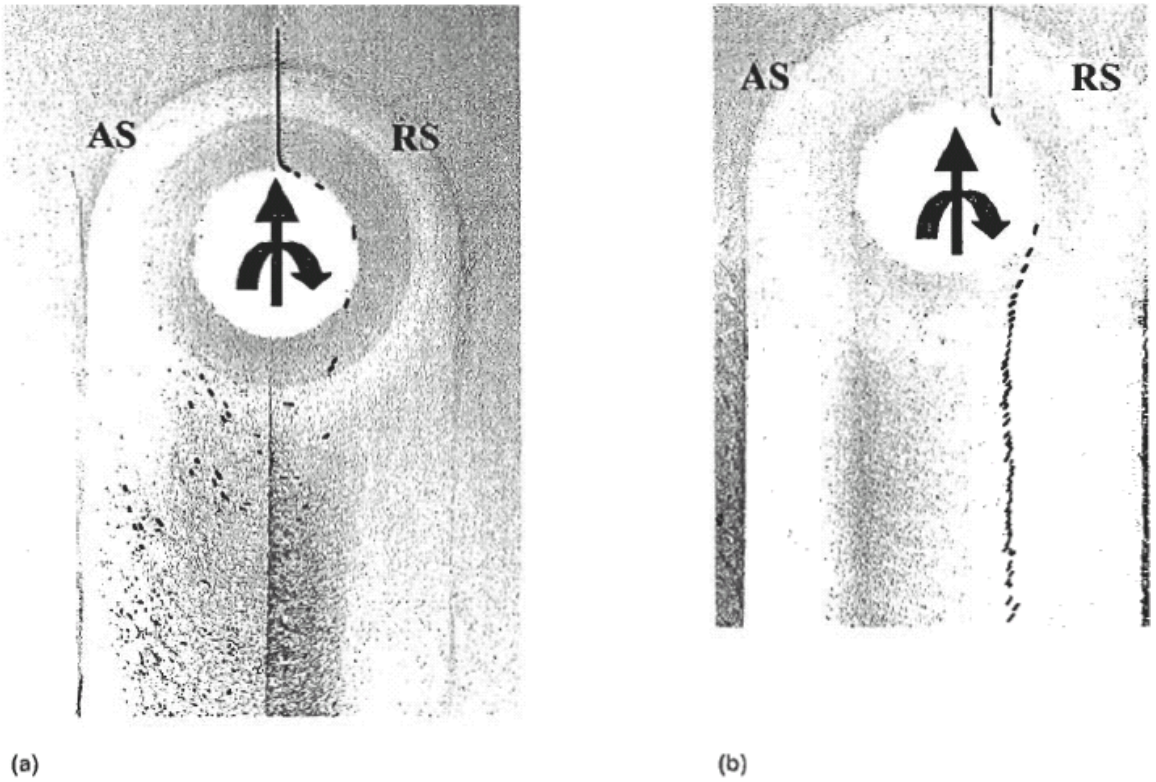

Figure 10: Inverted x-ray radiography a) centerline marker dispersal (consistent with maelstrom flow path) b) retreating side marker dispersal (consistent with thru-current flow path), figure from [58].

Abregast [59] presents a metalworking model of FSW flow dividing the process into five sequential processes: preheat, initial deformation, extrusion, forging,

and post-weld cool-down. This model has the probe forcing material downward during the initial deformation zone except near the shoulder where it is initially forced upward. The material is then rotated around the pin and deposited in the cavity behind the moving tool during the extrusion period. The forging period encompasses consolidation of the extruded material by the downward pressure of the shoulder heel.

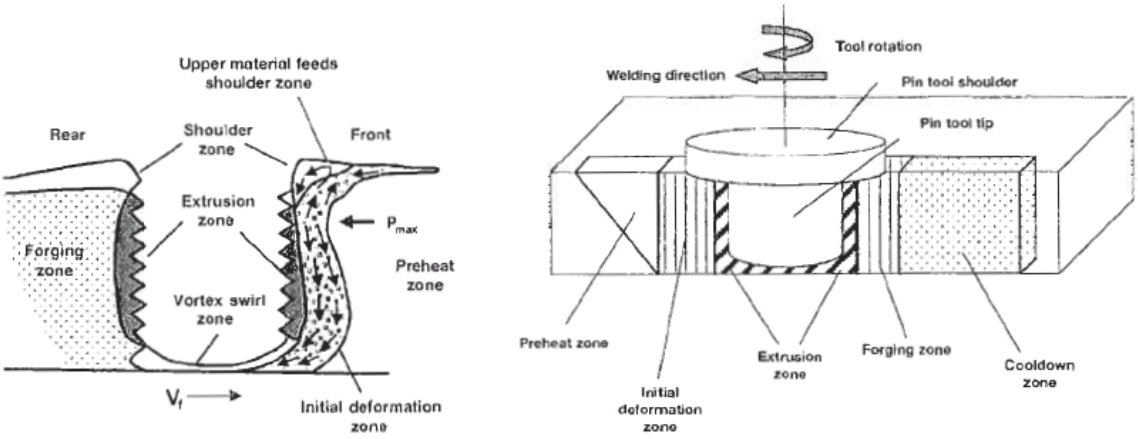

Figure 11: Graphic depictions of Abregast metalworking FSW model, figure from [59].

Chen et al. [66] use a probe breaking technique to observe in-process weld dynamics. The author notes that this technique results in the probe slowing to a stop over some unknown number of revolutions after breaking from the shoulder.

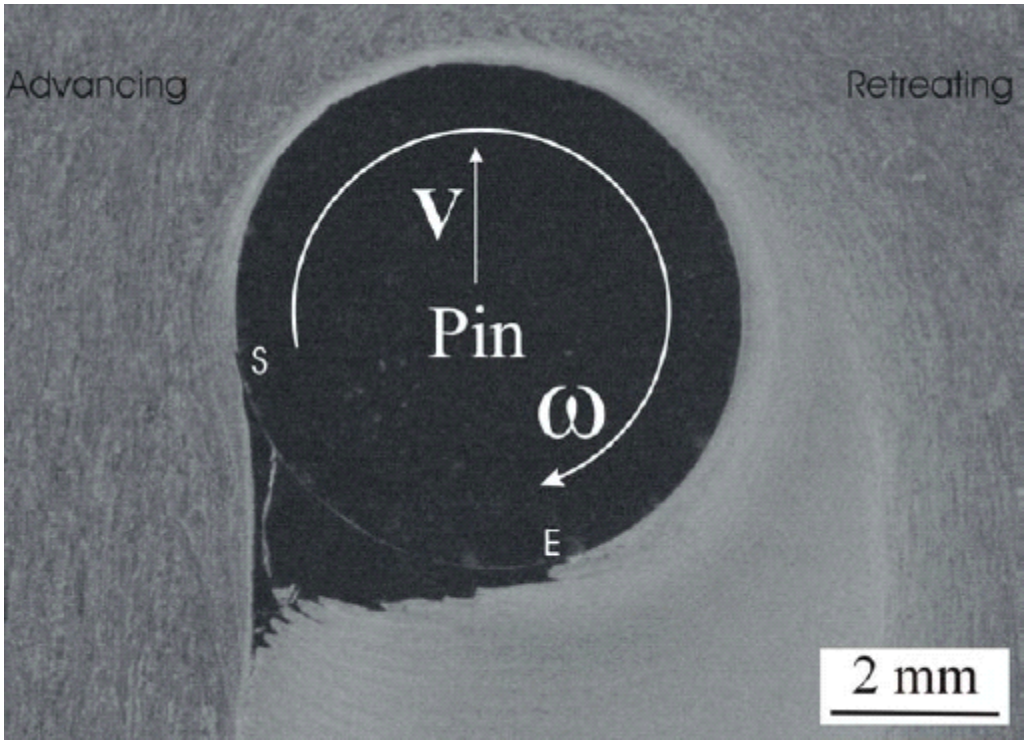

Figure 12: Horizontal cross-section taken at mid-plane of AA5083 plate with embedded pin after break test(v=2mm/s, ω =750, head tilt =3 °), figure from [66].

It can be seen that shear layers are deposited sequentially along the trailing edge of the weld from the retreating side to the advancing side. The author uses the rotational speed of the tool, the travel speed, and the distance traveled by each successive shear layer to calculate the shear velocity. The shear velocity is calculated to be ~16mm/s while the periphery of the pin is traveling at ~235mm/s. This results in a shear/pin periphery velocity of 0.07 (where 0.0 is pure slip and 1.0 is pure stick). The authors, therefore, conclude a slip condition to be dominant in this situation. It is mentioned that this ratio compares well with results obtained by Schmidt et al. [24] who arrive at a values in the range of 0.1-0.3. The authors of [66] further contend that a liquid film exists at the shear interface which facilitates the slip condition.

Computational Modeling Studies

Williams et al. [60] use a 2D-axisymmetric flow model coupled with a 3D translating thermal model and COSMOL multi-physics software to simulate the FSW process. The figure below depicts their methodology.

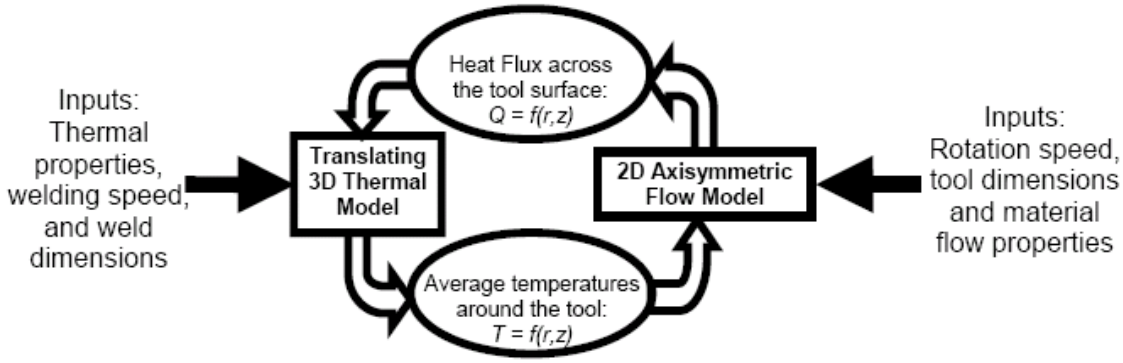

Figure 13: Input/output flow diagram for the 2D and 3D models, figure from [60].

Using a slip condition at the shoulder interface, a good agreement was made with experimental macrosections on the extent of the TMAZ.

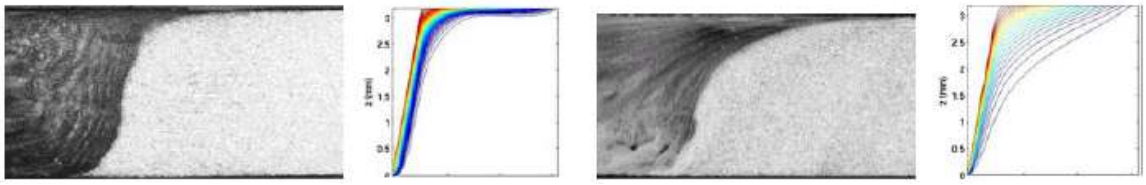

Figure 14: Rotational flow diagrams from 2D model and corresponding weld macrosections. Welds made in AA2014 at 200mm/min (Left:1600rpm, Right:400rpm), figure from [60].

The paper further attempts to integrate a residual stress, microstructure development, and hardness prediction submodels within the same software package. It is concluded by the authors that this technique has the potential for streamlining FSW modeling by obtaining many outputs related to weld performance from a single input/output process.

Schmidt and Hattel [61] use computational tomography (CT) to observe the flow of marker material around the tool and varying depths and compare this with a CFD model of flow paths. The weld is stopped mid-process and the weld sample is sliced horizontally. The deflection of marker material towards advancing side behind the probe

in is note in slices near the shoulder (first slice is just below the shoulder an slice depth increases successively). The slices show a reduced shoulder influence with depth.

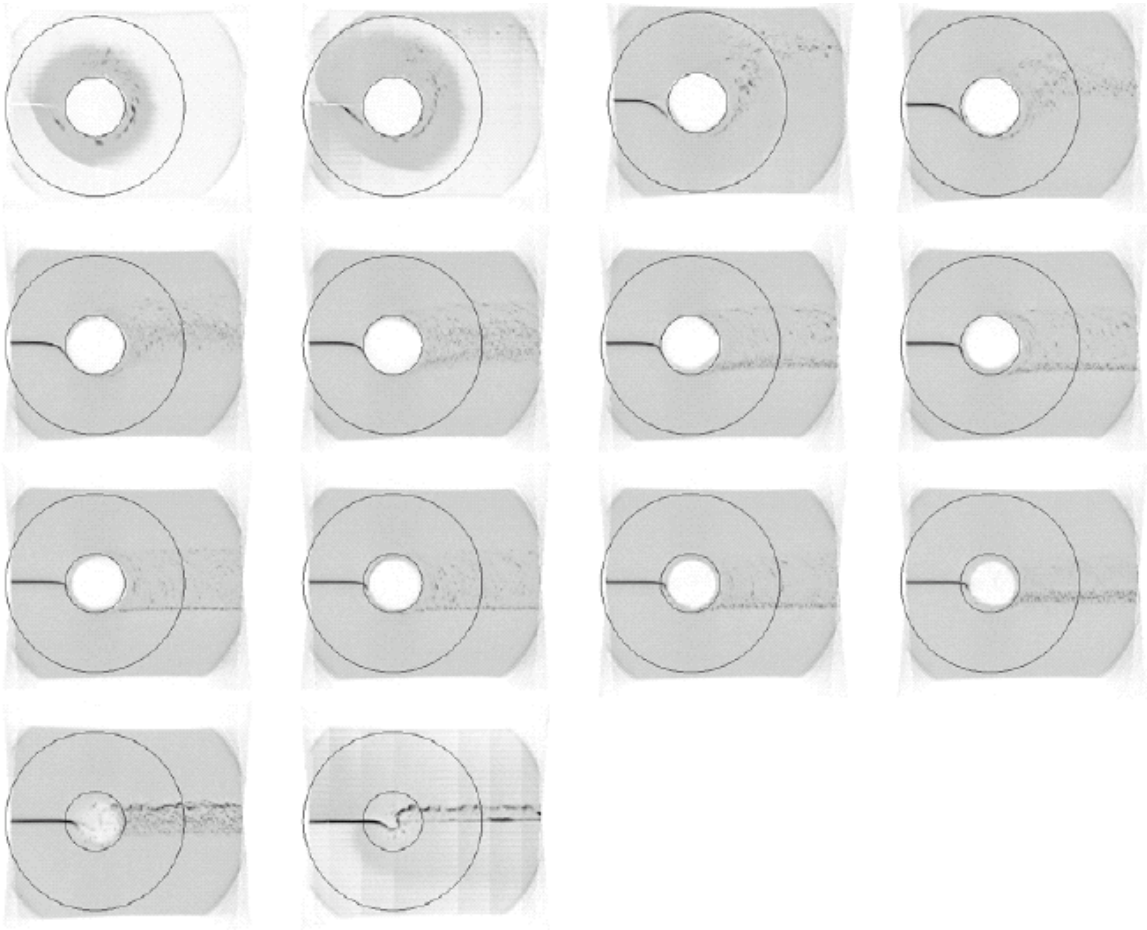

Figure 15: 2D overhead CT scans of horizontal slices showing the dispersal of marker material by a FSW tool. The inner and outer rings represent the outline of the pin and shoulder respectively. Slices are in order of increasing depth from shoulder and are in 0.25mm increments, figure from [61].

Experimental results are compared with an analytical streamline model and a COSMOL 3.2 FE model streamline. A good agreement is found between the three data sets:

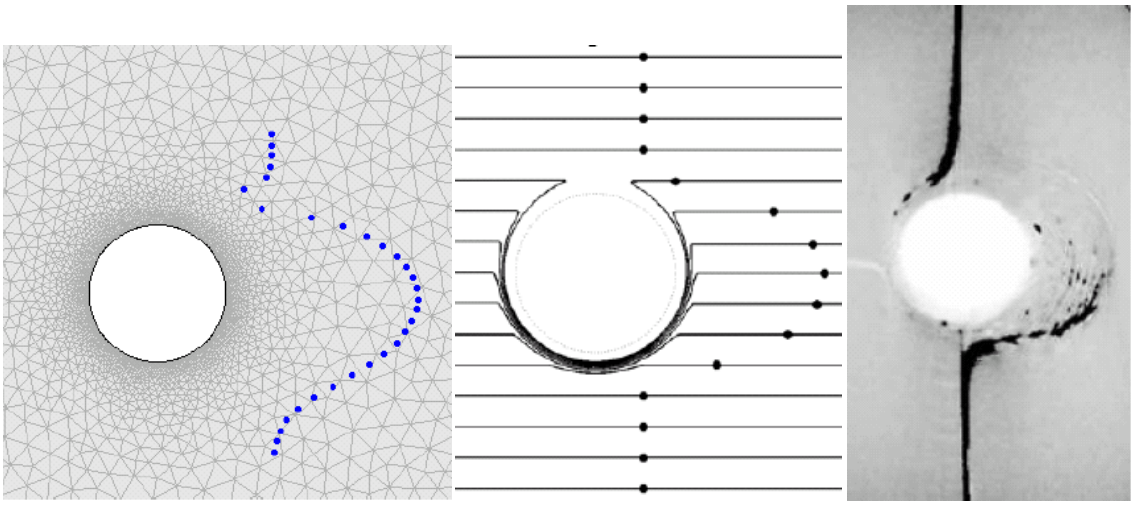

Figure 16: Left(FE streamline), Middle(analytical streamline),Right(CT). Figure from [61].

Sato et al. [62] use Acusolve™ CFD software based on the Galerkin/Least-Squares FE method to obtain temperature and velocity field data at various parameters for a self reacting FSW tool. An Eulerian (or ALE) framework is used. A visco-plastic model is used along with a slip-stick boundary condition at the shoulder. A schematic of the model mesh is shown below with increasing refinement with tool proximity.

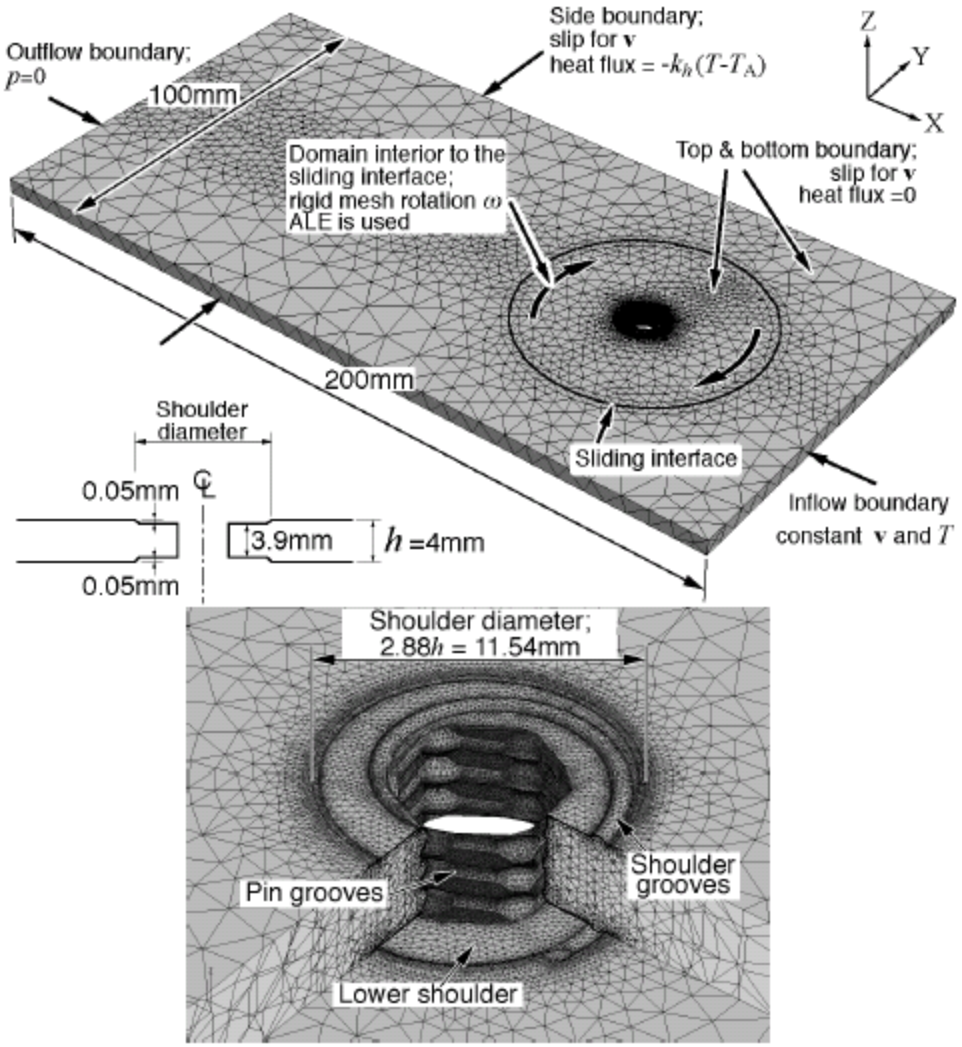

Figure 17: Finite element mesh and boundary conditions, figure from [62].

A rotating mesh is used around the tool with a sliding interface at the mesh exterior surface. Temperature contours are presented over a horizontal cross-section in the vicinity of the tool and over the modeled portion of the A6NO1 alloy aluminum plate.

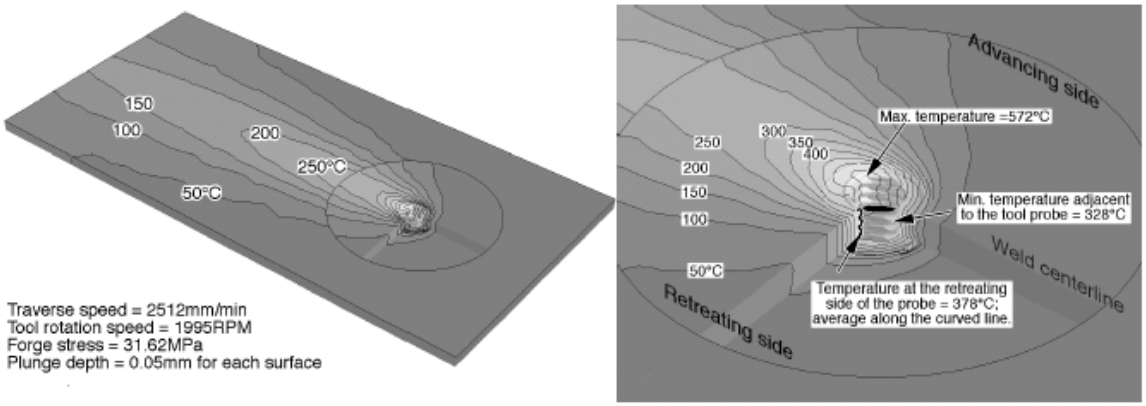

Figure 18: Temperature contour over the plate(left), and in the vicinity of the tool(right), figure from [62].

St.Georges et al. [63] use CosmosFlow CFD code to develop a thermal-fluid model of FSW in 6mm thick Al-6061 plates. A liquid with temperature dependent viscosity is used with adjustment based on experimental material behavior. Other material properties (ρ, c_p, k) are assigned constant values. Model temperature distributions are presented for the weld conditions below. Tool rotation is initially not considered.

Material	AA6061-T6
Thickness	12,7 mm
Shoulder radius	25 mm
Pin radius	6 mm
Pin length	11 mm
Rotational speed	637 rpm
Traverse speed	1,59 mm/s
Vertical force	25 kN
Friction coefficient	0,4
Shear stress	5,40 MPa
Shoulder Torque	174,41 Nm
Pin Torque	0,09 Nm
Total torque	176,94 Nm

Figure 19: CFD and empirical weld parameters and average process force data, figure from [63].

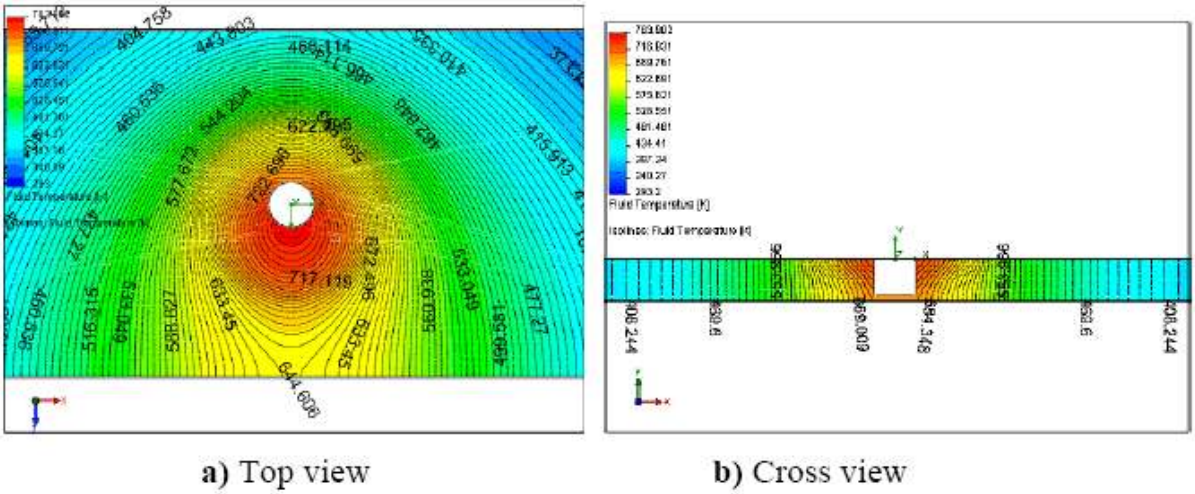

Figure 20: Modeled temperature distributions without considering tool rotation, figure from [63].

Temperature contours produced by Song and Kovacevic [64] using identical parameters and similar process forces using a different CFD model are presented for comparison:

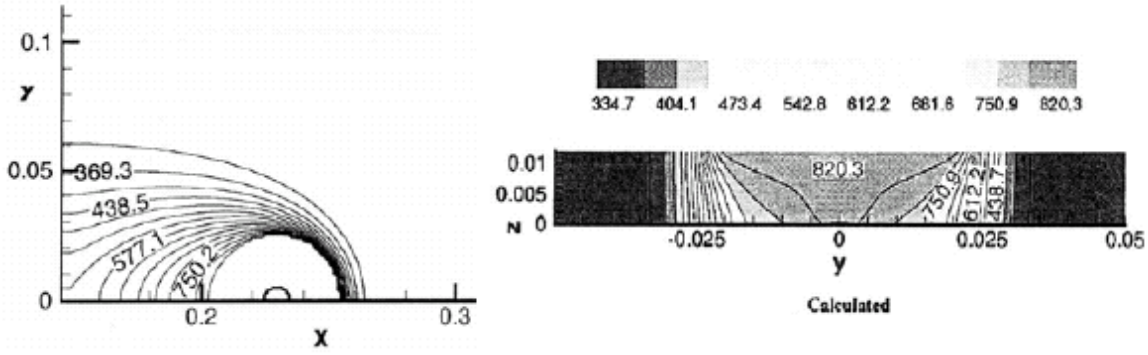

Figure 21: Modeled temperature distributions without considering tool rotation, figure from [64].

It is noted in [63] that CFD models presented in [63] and [64] achieve similar results. St.Georges et al. [64] goes on to present temperature contours with consideration for tool rotation:

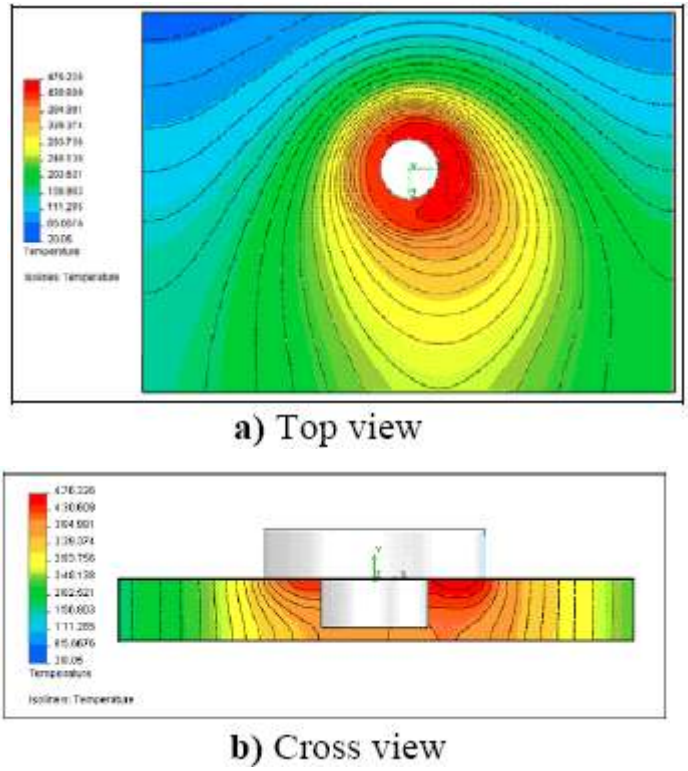

Figure 22: Temperature distribution with consideration of tool rotation, figure from [64].

De Vuyst et al. [65] use MORFEO finite element software and an Eulerian formulation with mixed velocity-pressure discretization for the fluid flow. A the work material is modeled with a visco-plastic fluid law. Empirical studies of embedded copper foil and wire marker material are used for model validation. A simplification of the Norton-Hoff material law is used:

$$s = 2K(\sqrt{3}\dot{\varepsilon})^{m-1}\dot{\varepsilon} \qquad \textit{Norton-Hoff Material Law}$$

where m=1 results in a Newtonian fluid of viscosity K, s is viscosity, and $\dot{\varepsilon}$ is the strain rate. For this model, K and m are chosen as constant values averaged over the full temperature range. This results in a weak coupling between the flow and temperature fields. The temperature field is dependent only on viscous dissipation and thus on the flow field. The flow field is however independent of temperature in this model.

The authors have a supercomputer available to them (28 Intel Itanium 2 processors with 2GB per processor RAM memory and 1.4TB available disk space) and

their mesh is composed of nearly 1.5 million linear tetrahedral mesh elements and 250,000 nodes. Nonetheless a simplified approach is used with respect to the tool features (shoulder scroll and probe threading). It was determined that explicit modeling of tool features would be to computationally costly. Unique boundary conditions are therefore established within predefined feature zones. A boundary zone is therefore created around the tool as shown:

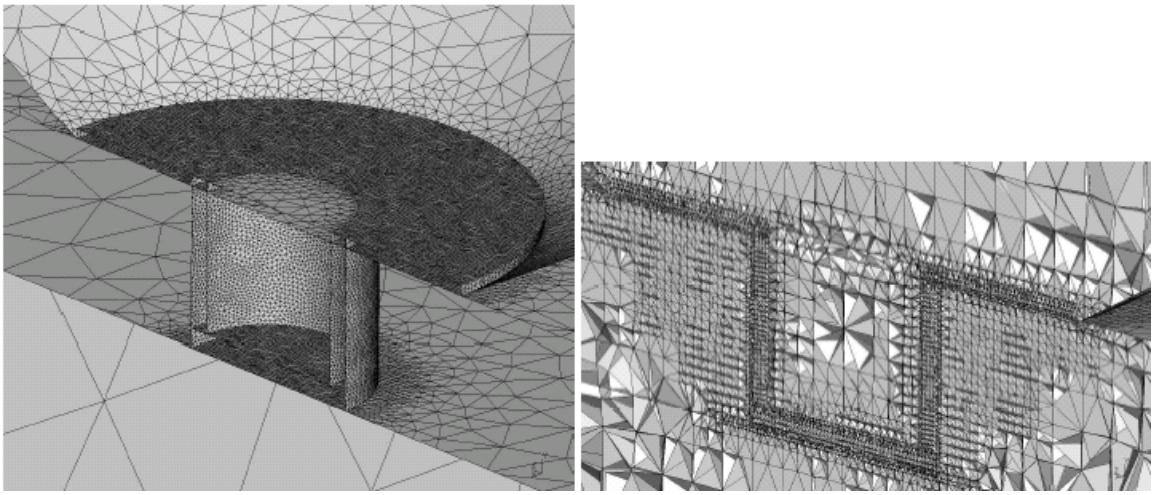

Figure 23: Finite element mesh with boundary zone around tool surface, figure from [65].

An approach used by Ulysse et al. [43] is applied to the tool boundary zone to account for the effect of tool the tool features. In this technique the velocity field component of the feature effects is added to the velocity field in these zones to account for the downward forcing of the tool threads and the inward radial forcing of the shoulder scrolling. The velocity profile around the tool mesh is presented:

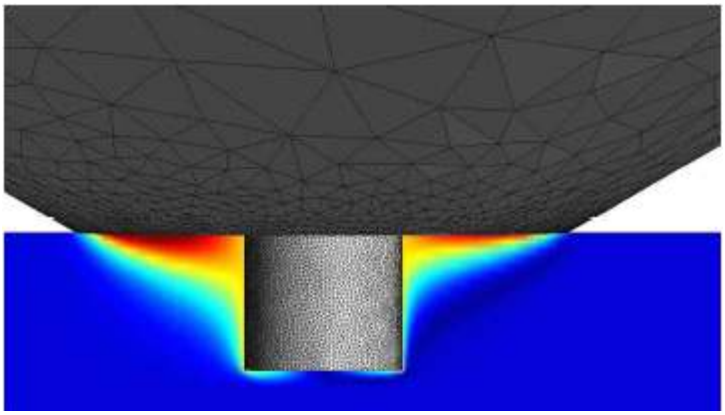

Figure 24: Lateral velocity contour (RS on left), figure from [65].

The authors note a larger velocity magnitudes on the retreating side of the weld (parameters are not given).

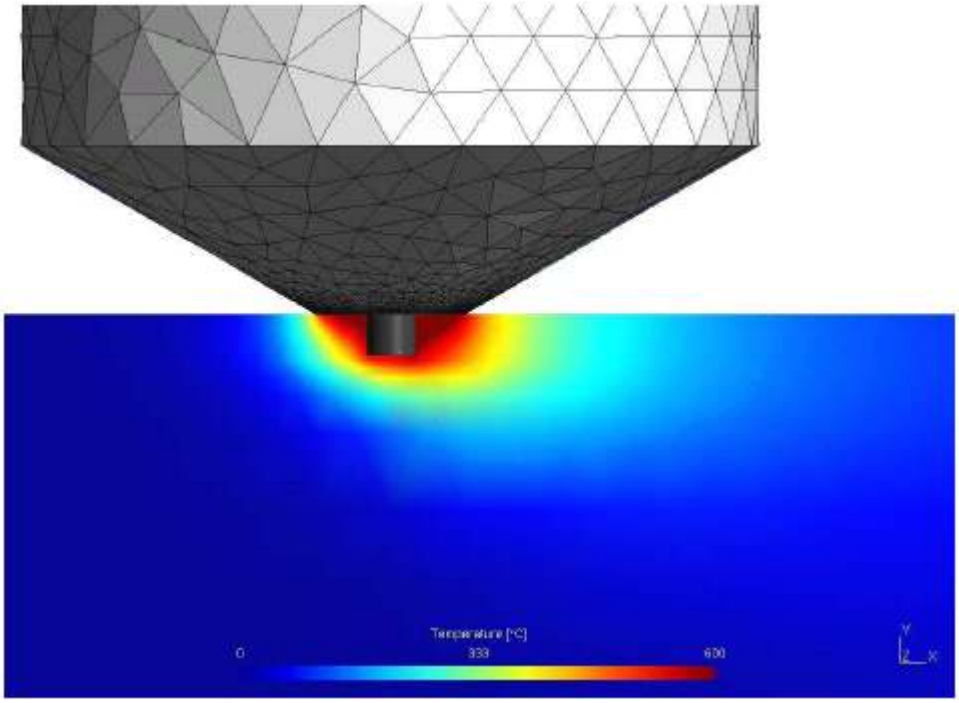

Figure 25: Temperature contour at the weldline (longitudinal cross-section with weld travel direction to the left), figure from [65].

The models are compared with a series of marker material imbedded horizontal weld slices. This is similar to the experiments run in [61] with the difference here being the lateral orientation of the marker material plane. Here the method of analysis is specified as metallographic (i.e. macrosections) as opposed to CT scans. The horizontal slices are presented in order of increasing depth (distance below shoulder plane) and the model predicted marker dispersal is superimposed (gold) over the experimental marker material (white).

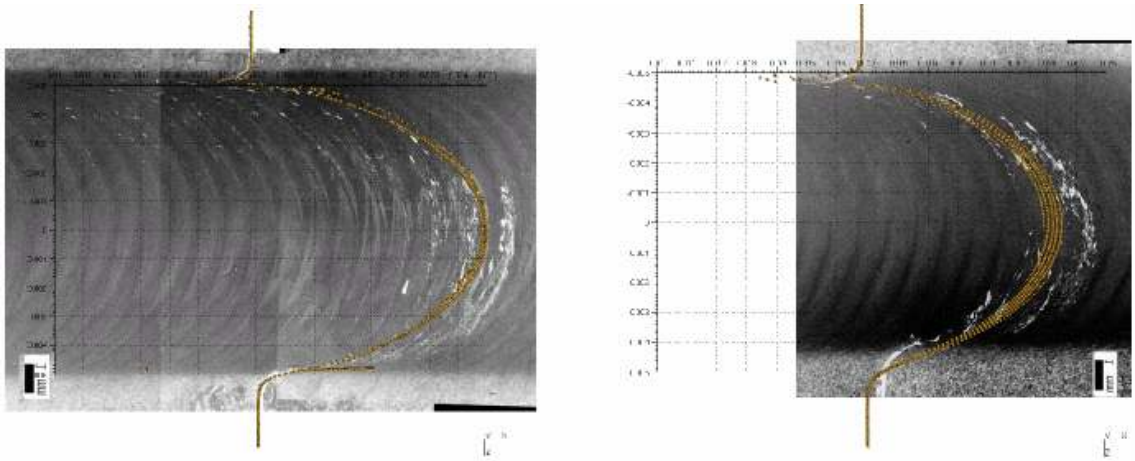

a) b)

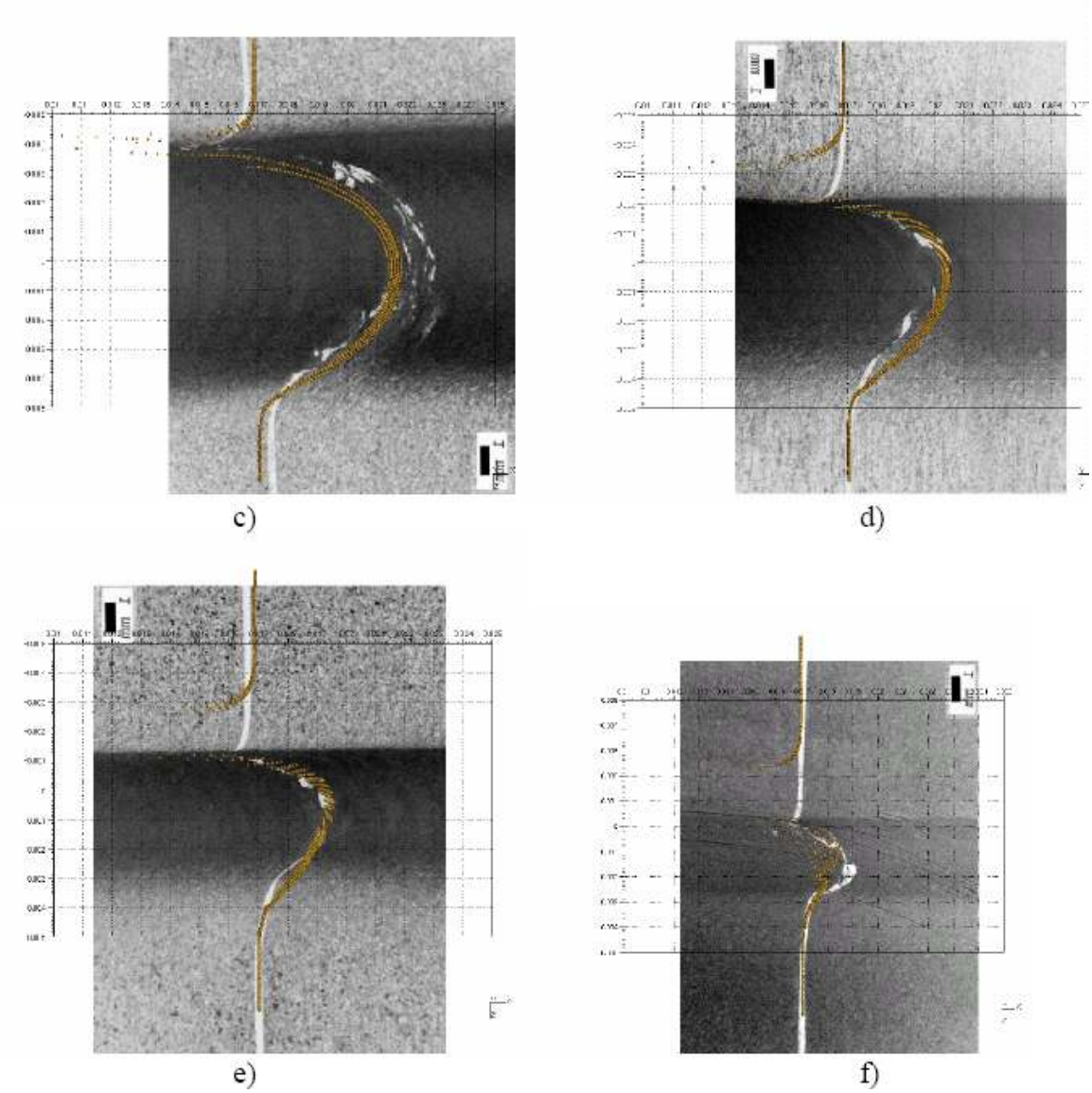

Figure 26: Experimental(white) versus model predicted(gold) marker material dispersal. Depth in mm: a)0.0 b)0.6 c) 1.1 d)1.6 e)2.1 f)2.6; figure from[65].

As in [61] one sees the decreased shoulder influence with depth in a reduced deflection of marker material. The authors note a good agreement with experiment.

The following lateral macrosections show the dispersal of marker material imbedded parallel to the weld-line (longitudinally) compared with three model based predictions:

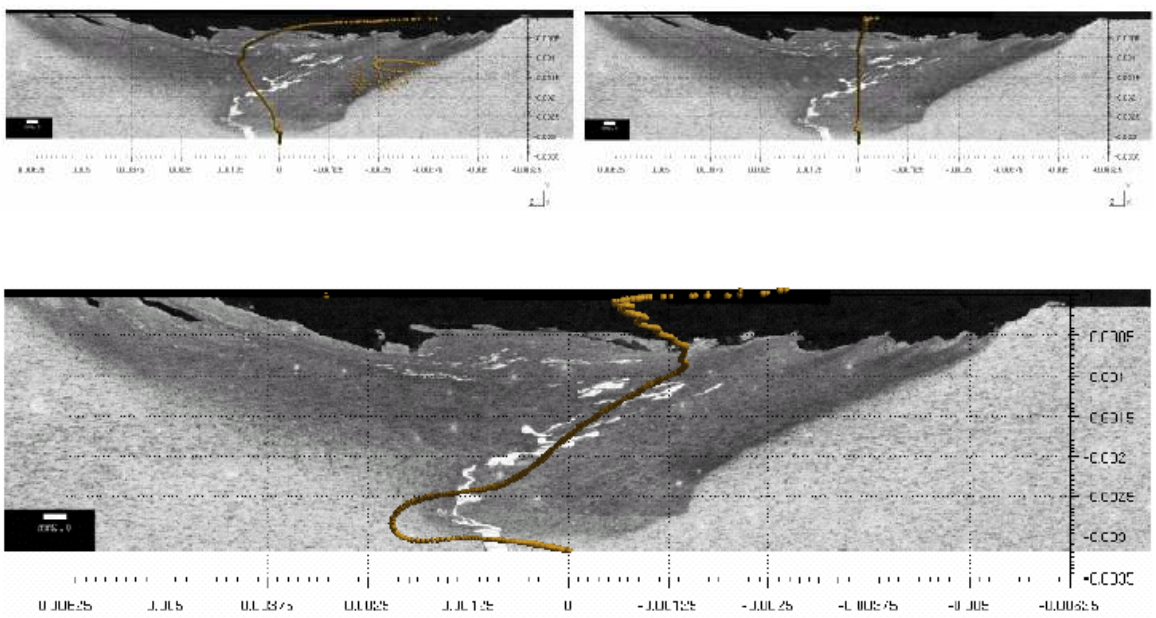

Figure 27: Model prediction (top left) without the threading vertical velocity effect, (top right) without the vertical or the radial scrolling velocity effect, (bottom) with both vertical and radial velocity effects imposed, figure from [65].

The authors present these macrographs as evidence for the necessity of a 3D thermo-fluid model (as opposed to 2D) which includes some accounting for feature effects. It is noted that the model that does not include imposed velocity fields to account for feature effects results in the simulated longitudinal marker material being deposited in a simple linear fashion, similar to its pre-welded position.

Atharifar, Lin and Kovacevic [67] use Fluent CFD software to identify the occurrence of a downstream stagnation point. The downstream stagnation point has been indicated by Shinoda [68] as the likely point of initiation of the tunnel-like defect in FSW.

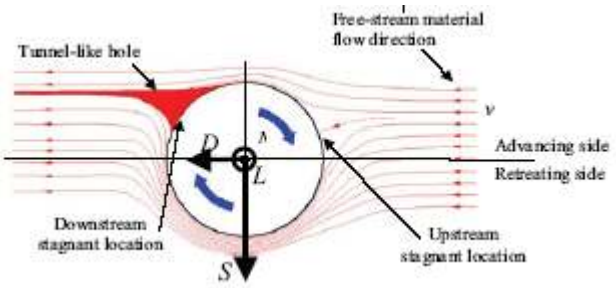

Figure 28: Top view schematic of tunnel defect initiation, figure from [67].

The authors use the Carreau model for pseudo-plastics to assign material viscosity:

$$\mu = \mu_\infty + (\mu_0 - \mu_\infty)\left[1 + (\dot{\gamma}\lambda \exp(\frac{T_0}{T}))^2\right]^{\frac{(m-1)}{2}}$$

where λ is the time constant, m is the power law non-Newtonian fluid index, μ_∞ and μ_o are the infinite and zero shear viscosities, $\dot{\gamma}$ is the shear strain-rate, and T_o is a reference temperature. The Carreau viscosity model is found as an embedded function in Fluent. The required constants have been obtained through experiment by Sheppard and Jackson [69]. A stick condition is used at the tool interface and a uniform heat flux is assigned to the interface surface. The heat input is calculated using equation **(2.4)**.

The downstream dynamic pressure along the traversing direction of the tool is examined at various heights relative to the shoulder for welds at various parameters. Experimental welds are performed to verify the occurrence of tunnel-like defects and to record the depth at which the defects occur (on the surface or submerged at some depth, y). The dynamic pressure trend lines below represent welds and weld heights which do and do not contain defects.

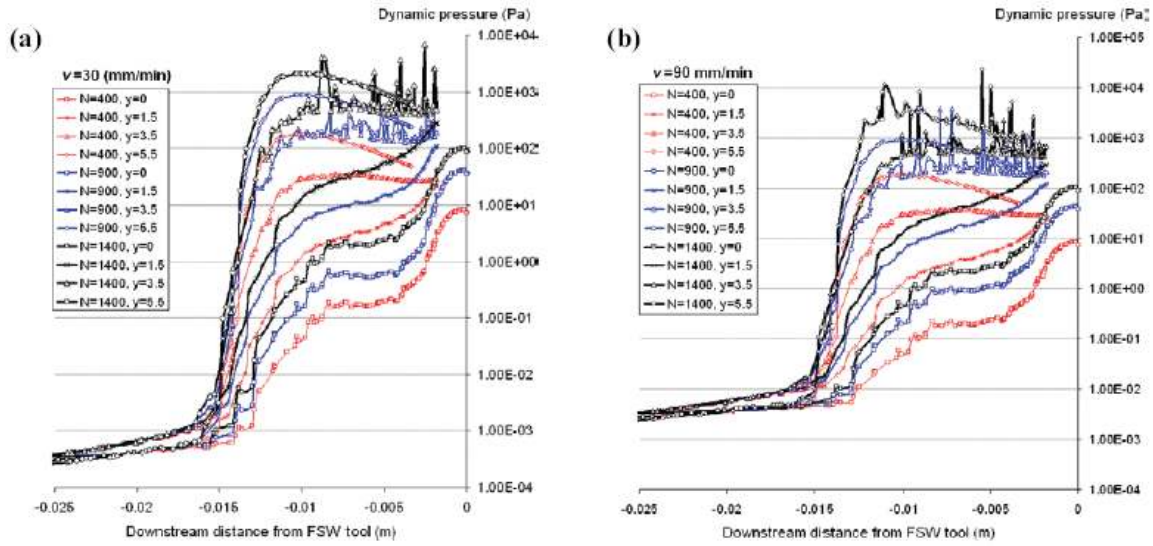

Figure 29: Dynamic pressure trend lines for spindle speed N and depth y at weld speed a) v=30mm/min b)90 mm/min. Figure from [67].

Defects can be identified in the trend lines above by spikes, which correspond to perturbations. In chart a) defects occur in experimental welds of N=900 and N=1400 at a depth of y=3.5. In chart a) defects occur in experimental welds of N=900 at y=3.5 and N=1400 from y=3.5 to the surface. By correlating defects in experimental welds with dynamic pressure trend lines from Fluent CFD models the authors are able to accurately predict the parameters at which a tunnel-defect occurs for a given tooling and material along with the depth at which the defect occurs.

References:

[1] Thomas W.M., et al. 1991, Friction Stir Butt Welding. International Patent Application # PCT/GB92/02203, GB Patent Application #9125978.8, and GB Patent # 2,306,366.

[2] Shercliff HR, Colegorve PA; "Modelling of friction stir welding", In *Mathematical Modelling of Weld Phenomena, 6th Edition*. H. Cerjak and H. Bhadeshia, Maney Publishing, London, UK, pp. 927-974.

[3] Shercliff HR, Colegrove PA; Chapter 10: Process Modeling. In *Friction Stir Welding and Processing*, Rajiv SM, Mahoney MW (Editors), ASM International, 2007.

[4] Threadgill PL; Terminology in friction stir welding; *Sci. Technol. Weld. Join.*, 2007, 12, (4), 357-360.

[5] Taylor RE, Groot H, Goerz T, Ferrier J, Taylor DL: Measurement of the electric resistivity of metals up to and above the melting temperature; *High Temp-High Pressures,* 30 (1998) 269-275.
[6] Sellars CM, Tegart WJM; Hot workability; *Int.* Metall. *Rev.*, 1972, 17, 1-24
[7] R. Nandan, G. G. Roy, and T. Debroy, "Numerical Simulation of Three-Dimensional Heat Transfer and Plastic Flow During Friction Stir Welding," *Metallurgical and Materials Transactions,* vol. 37A, pp. 1247-1259, April 2006.
[8] Simar A, Pardoen T, de Meester B; Influence of friction stir welding parameters on the power input and temperature distribution on friction stir welding; *Proc. of the 5th International Symposium on Friction Stir Welding*, 2004.
[9] Simar A, Pardoen T, de Meester B; Effect of rotational material flow on temperature distribution in friction stir welds; *Science and Technology of Welding and Joining*, Vol.12, No.4, p324, 2007.
[10] Santiago DH, Lombera G, Santiago U; Numerical modeling of welded joints by the friction stir welding process; *Materials Research*, Vol.7, Num.4, p569, 2004.
[11] Pew JW, Nelson TW, Sorensen CD; Torque based weld power model for friction stir welding; *Science and Technology of Welding and Joining*,Vol.12, Num.4, p341, 2007.
[12] Russell MJ, Shercliff HR; Analytical modeling of microstructure development in friction stir welding; *Proc. of the 1st International Symposium on Friction Stir Welding*, Session 08, 1999.
[13] Milding OT, Grong O; A process model for friction welding of Al-Mg-Si alloys and Al-SiC metal matrix composites; *Acta Metall. Mater*, 42 (5), 1994, p1595.
[14] Frigaard O, Grong O, Bjorneklett B, Midling OT; Modelling of thermal and microstructure fields during friction stir welding of aluminium alloys; *Proc. of the 1st International Symposium on Friction Stir Welding*, Session 08, 1999.
[15] Gould JE, Feng Z; Heat flow model for friction stir welding of aluminum alloys; *Journal of Materials Processing and Manufacturing Science*, 7, p185, 1998.
[16] Song M, Kovacevic R, Ouyang J, Valant M; A detailed three-dimensional transient heat transfer model for friction stir welding; *6th International Trends in Welding Research Conference Proc.*, p212, 2002.
[17] Colegrove P, Painter M, Graham D, Miller T; 3 Dimensional flow and thermal modelling of the friction stir welding process; *Proc. of the 2nd International Symposium on Friction Stir Welding*, 2001.
[18] Chen H-B, Yan K, Lin T, Chen S-B, Jiang C-Y, Zhao Y; The investigation of a typical welding defects for 5456 aluminum alloy friction stir welds; *Materials Science and Engineering* A, 433, p64, 2006.
[19] Linder K, Khandahar Z, Khan J, Tang W, Reynolds AP; Rationalization of hardness distribution in alloy 7050 friction stir welds based on weld energy, weld power, and time/temperature history; *Proc. of the 6th International Symposium on Friction Stir Welding*, 2007.
[20] Midling OT, Rorvik G; Effect of tool shoulder material on heat input during friction stir welding; *Proc. of the 1st International Symposium on Friction Stir Welding*, 1999.
[21] Heurtier P, Jones MJ, Desrayaud C, Driver JH, Montheillet F, Allehaux D; Mechanical and thermal modeling of friction stir welding; *Journal of Materials Proccessing Technology*, 171, p348, 2006.

[22] Colegrove PA, Shercliff HR, Zettler R; Model for predicting heat generation and temperature in friction stir welding form the material properties; *Science and Technology of Welding and Joining*, Vol.12, No.4, p284, 2007.
[23] Schmidt H, Hattel J, Wert J; An analytical model for the heat generation in friction stir welding; *Modelling Simul. Mater. Sc. Eng*. 12 (2004) 143-157.
[24] Schmidt H, Dickerson T, Hattel JH; Material flow in butt friction stir welds in AA2024-T3; *Acta Materialia* (2005).
[25] Schmidt H, Hattel J; A local model for the thermomechanical conditions in friction stir welding; *Modelling and Simulation in Materials Science and Engineering*, 13 (2005) 77-93.
[26] Shi Q-Y, Dickerson T, Shercliff HR; Thermomechanical FE modeling of friction stir welding of al-2024 including tool loads; *Proc. of the 4th International Symposium on Friction Stir Welding*, 2003.
[27] Y. He, D. E. Boyce, and P. R. Dawson, "Three-Dimensional Modeling of Void Growth in Friction Stir Welding of Stainless Steel," in *NUMIFORM '07*, 2007.
[28] Chao YJ, Qi X; Heat transfer and thermo-mechanical analysis of friction stir joining of AA6061-T6 plates; *Proc. of the 1st International Symposium on Friction Stir Welding*, 1999.
[29] Dickerson TL, Shi Q-Y, Shercliff HR; Heat flow into friction stir welding tools; *Proc. of the 4th International Symposium on Friction Stir Welding*, 2003.
[30] Song M, Kovacevic R: A new heat transfer model for friction stir welding; *Trans. NAMRI/SME*, XXX, 562-572, 2002.
[31] Song M, Kovacevic R: Numerical and experimental study of the heat transfer process in friction stir welding; *Proc. Inst. Mech Eng. B, J. Eng. Manuf.*; 217B, 73-85, 2003.
[32] Song M, Kovacevic R: Numerical simulation and experimental analysis of heat transfer process in friction stir welding; *Proc. Inst. Mech Eng. B, J. Eng. Manuf*., 218B, 17-33, 2003.
[33] Chao YJ, Qi X; Thermal and thermo-mechanical modeling of friction stir welding of aluminum alloy 6061-T6; *J. Mater. Process Maunf. Sci.*, 1998, 7, (2), 163-172.
[34] G. Buffa, J. Hua, R. Shivpuri, and L. Fratini, "A continuum based fem model for friction stir welding--model development," *Materials Science and Engineering A,* vol. 419, pp. 389-396, 2006.
[35] Vilaca P, Quintino L, dos Santos JF: iSTIR- Analytical thermal model for fricitno stir welding; *J. Mater. Process. Technol*., 169, (3), 452-465, 2005.
[36] Askari A, Silling ST, London B, Mahoney M: Proc. Semin. On 'FSW flow visualisation and modelling', Geesthacht, Germany, Feb. 2003, GKSS.
[37] Dong P, Lu F, Hong JK, Cao Z: Coupled thermomechanical analysis of friction stir welding process using simplified models; *Sci. Technol Weld. Join*., 6, (5), 281-287, 2001.
[38] Lambrakos SG, Fonda RW, Milewski JO, Mitchell JE: Analysis of friction stir welds using thermocouple measurements; *Sci. Technol. Weld. Join*., 8, (5), 385-390, 2003.
[39] Sheppard T and Wright D: Determination of flow stress: Part 1 constitutive equation for aluminum alloys at elevated temperatures; *Met. Technol*., 6, 215-223, June 1979.
[40] Mahoney M.W., Rhodes C.G., Flintoff J.G., Spurling R.A., Bingel, W.H.: Properties of friction-stir-welded 7075 T651 aluminum; *Metall. Mater. Trans. A*., 29A, 1955-64, July 1998.

[41] Heinz B., Skrotzki B., Eggler G.: Microstructural and mechanical characterization of friction stir welded Al-alloy; *Mater. Sci. Forum*., 331–337, 1757-62, 2000.
[42] Svensson, L.E., Karlsson, L., Larsson, H., Karlsson, B., Fazzini, M. and Karlsson, J.: Microstructural and mechanical properties of friction stir welded aluminum alloys with special reference to AA 5083 and AA 6082; *Sci. Technol. Welding Joining*, 5, 285-296, 2000.
[43] Ulysse P.: Three-dimensional modeling of the friction stir-welding process; *International Journal of Machine Tools & Manufacture*., 42, 1549–1557, 2002.
[44] Nunes A.C., Bernstien E.L., McClure J.C.: A rotating plug model for friction stir welding; *Proc. of the 81st American Welding Society Annual Convention*, Chicago, IL, 2000.
[45] Murr L.E., Liu G., McClure, J.C.: A TEM study of precipitation and related microstructures in friction-stir welded 6061 aluminum; *Mater. Sci.,* 33, 1243-1251, 1998.
[46] Rhodes C.G., Mahoney M.W, Bingel W.H., Spurling R.A., Bampton C.C.: Effects of friction stir welding on microstructure of 7075 aluminum; *Scripta Mater.,* 36, 69-75, 1997.
[47] Jata K.V., Sankaran K.K., Ruschau J.J: Frictio-stir welding effects on microstructure and fatigue of aluminum alloy 7075-T7451; *Metall. Mater. Trans*.A*,* 31A, 2181-2192, Sept. 2000.
[48] Liu, G., Murr, L.E., Niou, C.S., McClure, J.C. and Vega, F.R.; Microstructural aspects of the friction-stir welding of 6061-T6 Aluminum; *Scripta Metall.,* 37, 355-361, 1997.
[49] Sato Y.S., Kokawa H., Enomoto M., Jogan, S.: Microstructural evolution of 6063 aluminum during friction-stir welding; *Metall. Mater. Trans. A,* 30A, 2429-2437, 1999.
[50] Su J.-Q., Nelson T.W., Mishra R., Mahoney, M.: Microstructural investigation of friction-stir welded 7075-T651 aluminum; *Acta Mater.,* 51, 713-729, 2003.
[51] Seidel TU, Reynolds AP: A 2-D friction stir process model based on fluid mechanics; *Sci. Technol. Weld. Join.*, 8, (3), 175-183, 2003.
[52] R. Crawford, G. E. Cook, A. M. Strauss, D. A. Hartman, and M. A. Stremler, "Experimental defect analysis and force prediction simulation of high weld pitch friction stir welding " *Science and Technology of Welding & Joining,* vol. 11, pp. 657-665, 2006.
[53] Reynolds A. P., Deng X., Seidel T. and Xu S.: Recent advancements in FSW process physics; *Proc. Joining of Advanced and Specialty Materials* (St Louis, MO, ASM International) pp 172–177, 2000.
[54] Guerra M., Schmidt C., McClure J.C., Murr L.E., Nunes A.C.; Flow patterns during friction stir welding; *Materials Characterization*., 49, 95-101, 2003.
[55] Colligan K.: Material flow behavior during friction stir welding of aluminum; *Weld. Res. Suppl.*, **6**, 229 –237, July 1999.

[56] Zhao Y.-H., Lin S.-B., Qu F.-X., Wu L.: Influence of pin geometry on material flow in FSW processing; *Materials Science and Technology*, 22 (1), 45-50, 2006.
[57] Schnieder JA, Nunes AC: Characterization of plastic flow and resulting microtextures in a friction stir weld; *Metallurgical and Materials Transactions* B, Volume 35B (2004), 777-783.

[58] Schnieder JA, Beshears R, Nunes AC; Interfacial sticking and slipping in the friction stir welding process, *Mater. Sci. Eng*. A, Vol 435-436 (2006) 297-304.
[59] Arbegast WJ; Modeling friction stir joining as a metal working process: *Hot Deformation of Aluminum Alloys*, (editor Z. Jin), TMS (2003).
[60] Williams SW, Colegrove PA, Shercliff H, Prangell P; Intergrated modeling of the friction stir welding process: *Proc. of the 6th International Symposium on Friction Stir Welding*, 2007.
[61] Schmidt H, Hattel J; Analysis of the velocity field in the shear layer: *Proc. of the 6th International Symposium on Friction Stir Welding*, 2007.
[62] Sato T, Otsuka D, Watanabe Y; Designing of friction stir weld parameters with finite element flow simulation: *Proc. of the 6th International Symposium on Friction Stir Welding*, 2007.
[63] St-Georges L, Dasylva-Raymond V, Kiss LI, Perron AL; Prediction of optimal parameters of friction stir welding: *Proc. of the 6th International Symposium on Friction Stir Welding*, 2007.
[64] Song M, Kovacevic R; Thermal modeling of friction stir welding in a moving coordinate system and its validation: *Materials Science Forum* 2002, (346-402) 1537-1542.
[65] De Vuyst T, Magotte O, Robineau A, Goussian J-C, Alvise LD; Multi-physics simulation of the material flow and temperature field around FSW tool: *Proc. of the 6th International Symposium on Friction Stir Welding*, 2007.
[66] Chen ZW, Pasang T, Qi R, Perris R; Tool-workpiece interface and shear layer formed during friction stir welding: *Proc. of the 6th International Symposium on Friction Stir Welding*, 2007.
[67] Atharifar H, Lin DC, Kovacevic R; Studying tunnel-like defect in friction stir welding process using computational fluid dynamics: *Mat. Sci. Tech.* 2007, Detroit MI.
[68] Shinoda T, Kondo Y; Friction stir welding of aluminum plate: *Welding Int.*, 11(3) (1997), p179-184.
[69] Sheppard T, Jackson A; Constitutive equations for use in prediction of flow stress during extrusion of aluminum alloys: *Mat. Sci. Tech.* 13(3) (1997), p203-209.

CHAPTER II

COMPUTATIONAL ANALYSIS OF FRICTION STIR WELDED T-JOINTS

Computational Analysis of Friction Stir Welded T-Joints; D. H. Lammlein, P. A. Fleming, D. M. Wilkes, George E. Cook, A. M. Strauss, D. R. DeLapp, and D. A. Hartman; Inter-Institutional Report, Vanderbilt University and Los Alamos National Lab, 2008

Misalignment Detection and Enabling of Seam Tracking for Friction Stir Welding; P. A. Fleming, D. H. Lammlein, D. M. Wilkes, G. E. Cook, A. M. Strauss, D. R. DeLapp, and D. A. Hartman; *Science and Technology of Welding and Joining*, Vol. 14, #1, 2008.

Note: This chapter presents the entirety of the former document. Additionally, the portions of the latter relevant to the chapter title are presented.

FEA assessment of FSW Process Geometry for Seam Misalignment Detection

In friction stir welding (FSW), it is commonly know that the process forces transmitted through the tool are dependent on process parameters and process geometries. A threshold level of variation in one or more of these process factors during a given weld will produce a discernible change in the weld process forces. Fleming et al. [1,2] have demonstrated that, for certain process geometries, weld process force feedback can be utilized for online weld seam misalignment detection. Seam misalignment detection in FSW is the estimation, based on some feedback signal, of the lateral tool position with respect to the weld jointline. It is the belief of the authors that weld process forces differ based on lateral tool position wherever the conditions beneath the tool vary with lateral tool position. In the case of the blind type T-joint setup depicted in Figure 30, the geometry of the welded material and fixturing beneath the tool change drastically with lateral tool position and these changes are readily detectable in process force data. This work presents finite element analysis (FEA) as a tool for determining the viability of a given weld process geometry for seam misalignment detection. Using a simple finite

element model of the process geometry, an evaluation for lateral tool position estimation can be made prior to fabrication, setup, and welding.

Welds were performed at 1000 rpm and 4 in/min using 6061 aluminum in the two fixturing configurations depicted in Figure 30 and Figure 31. The configuration in Figure 30 produced the laterally dependent process force variations necessary for seam misalignment detection while the configuration in Figure 31 did not. These configurations will be referred to as the tracked and the untracked configurations respectively.

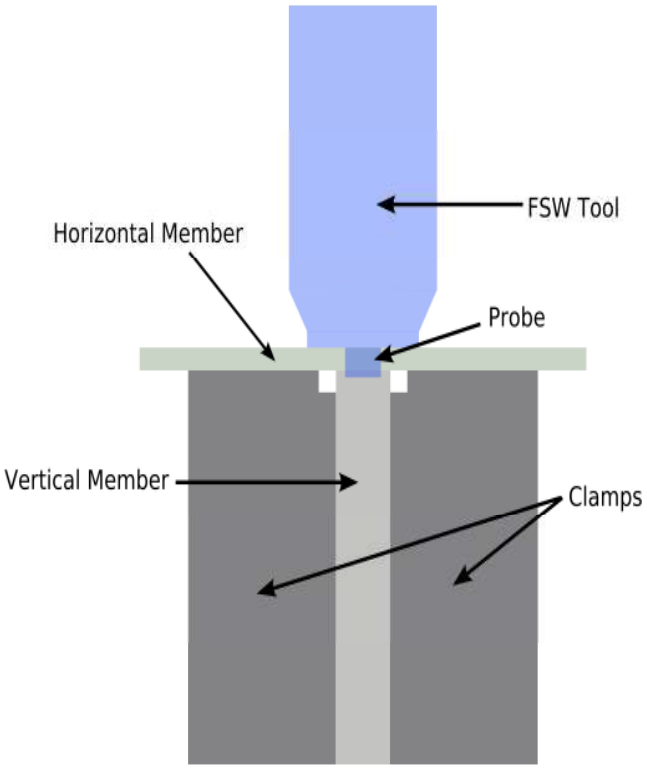

Figure 30: Blind t-joint setup with squared gap (1/8"x1/8") in clamps (tracked configuration).

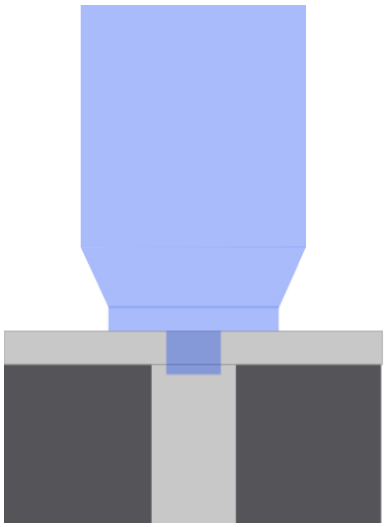

Figure 31: Blind type t-joint setup with no gap in clamps (untracked configuration).

For the untracked configuration, two test welds were performed during which the tool lateral position was adjusted in step movements. In the first weld the tool begins offset to the advancing side and ends on the retreating side. A second weld was performed with an initial retreating side offset and final advancing side offset. This

procedure ensures that process force variations are not somehow related to transient heating effects or some unforeseen longitudinally varying factor. Figure 32 shows solid block data from these trails. No observable trend can be seen in the process forces.

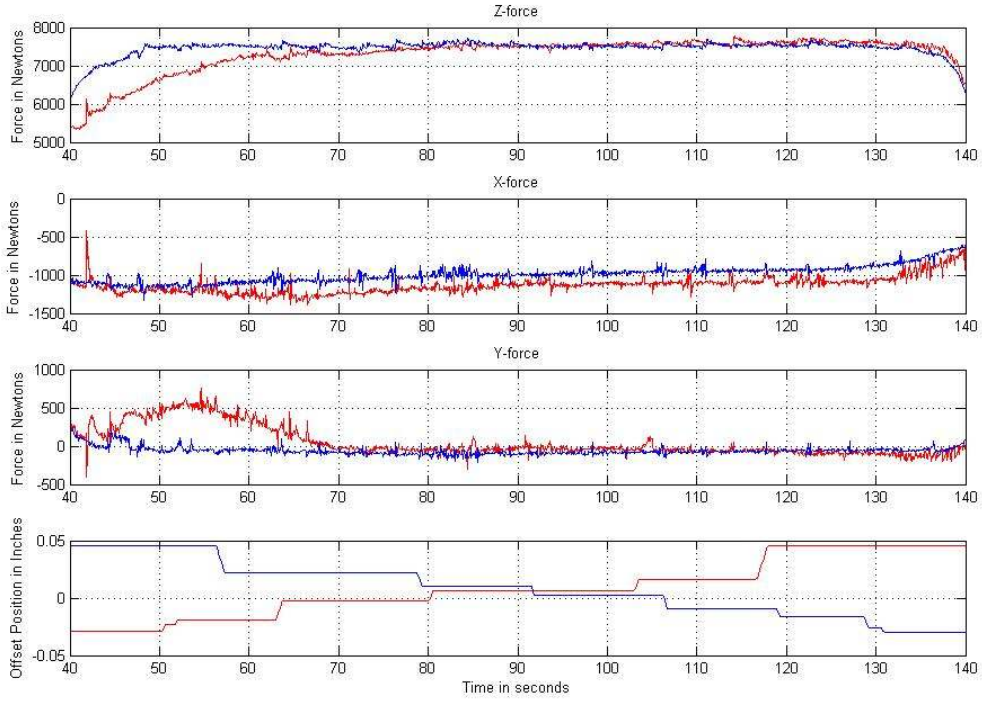

Figure 32: Process forces and lateral offset for two separate welds using the untracked clamp geometry.

In Figure 32, the period between 40 and 70 seconds immediately follows the dwell period of the weld and transient effects are seen. The final 5 to 10 seconds of each weld are affected by the ending of the weld plate. Figure 33 represents the most useful portion of the solid block data, and again shows no useful trend in the untracked case. Figure 34 shows data from a weld made using the tracked geometry. The data seen for the tracked data shows useful force changes with corresponding changes in lateral position.

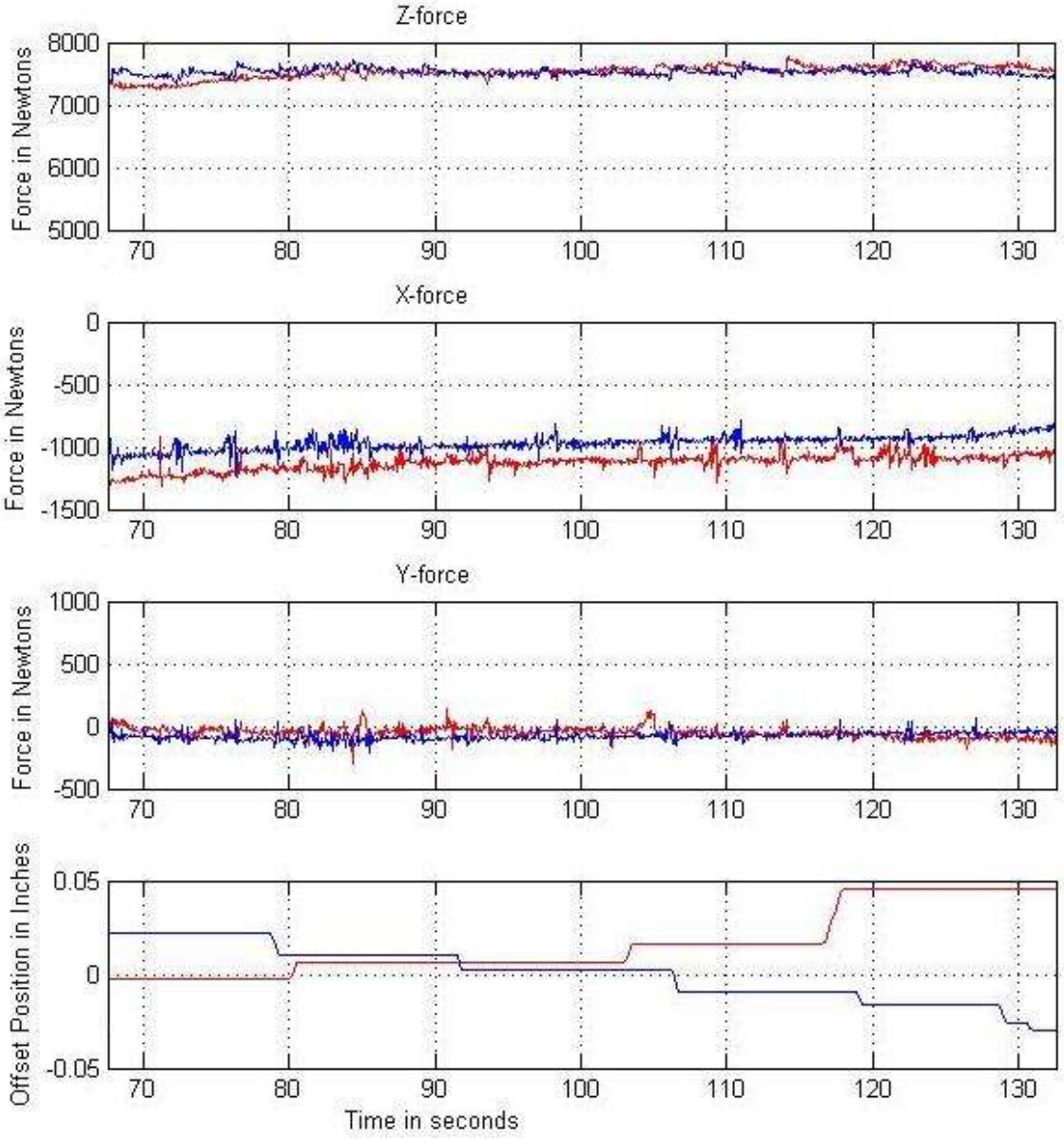

Figure 33: Process forces and lateral offset for two separate welds using the untracked clamp geometry (t=70s to t=130s).

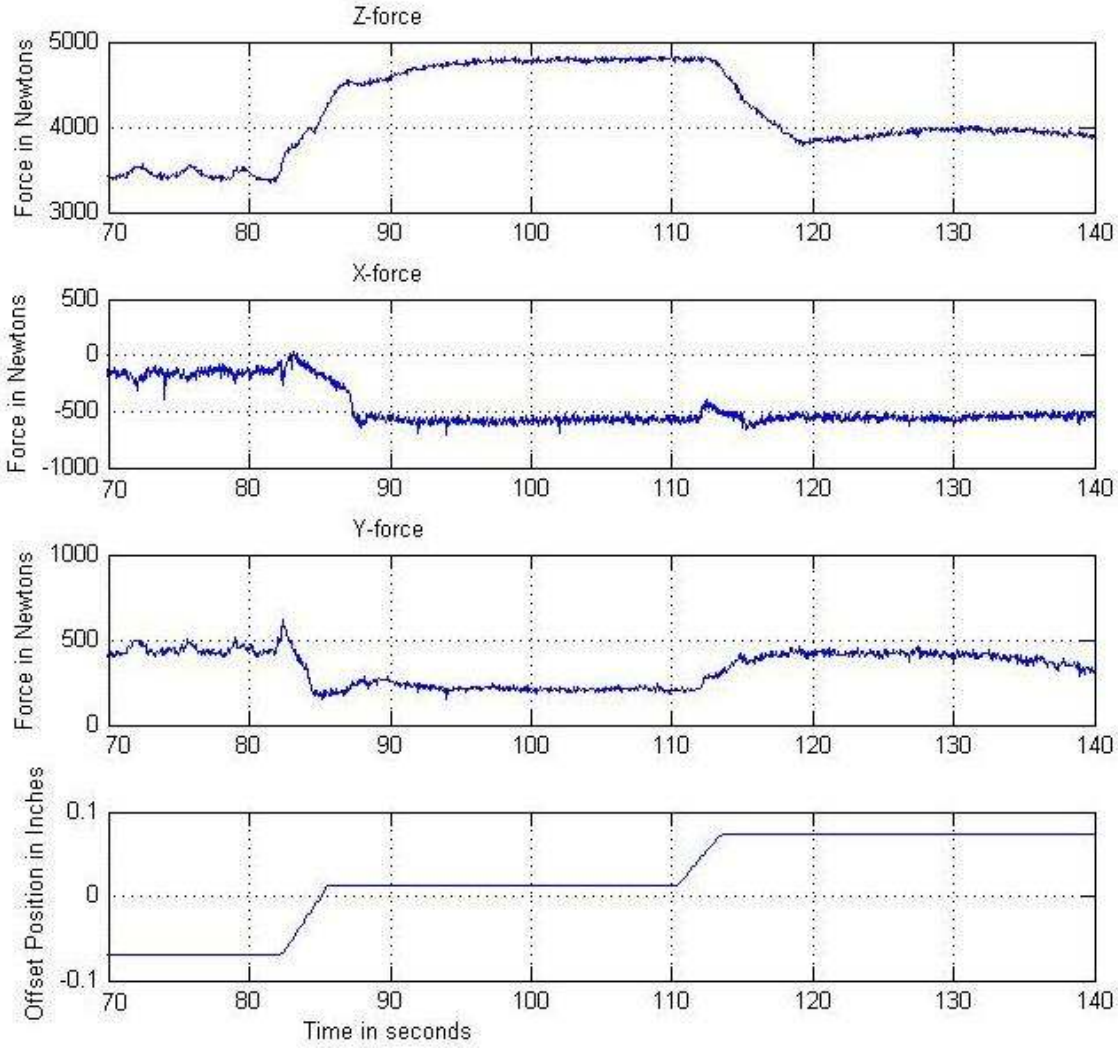

Figure 34: A similar test using the tracked geometry (t=70s to t=130s).

Substantial data was collected for the tracked configuration as this geometry proved useful for seam misalignment detection. For the tracked configuration welds, the axial force was shown to have the greatest change in magnitude with lateral offset, in addition to being several fold the largest process force in magnitude. The remaining process forces showed more complicated and less pronounced variations with lateral position and are thus neglected in this analysis. Fig. 5 shows data collected from 10 separate welds using the tracked geometry. Each point is represents a single weld and is the average axial force value over the steady state weld period where transient effects are minimal.

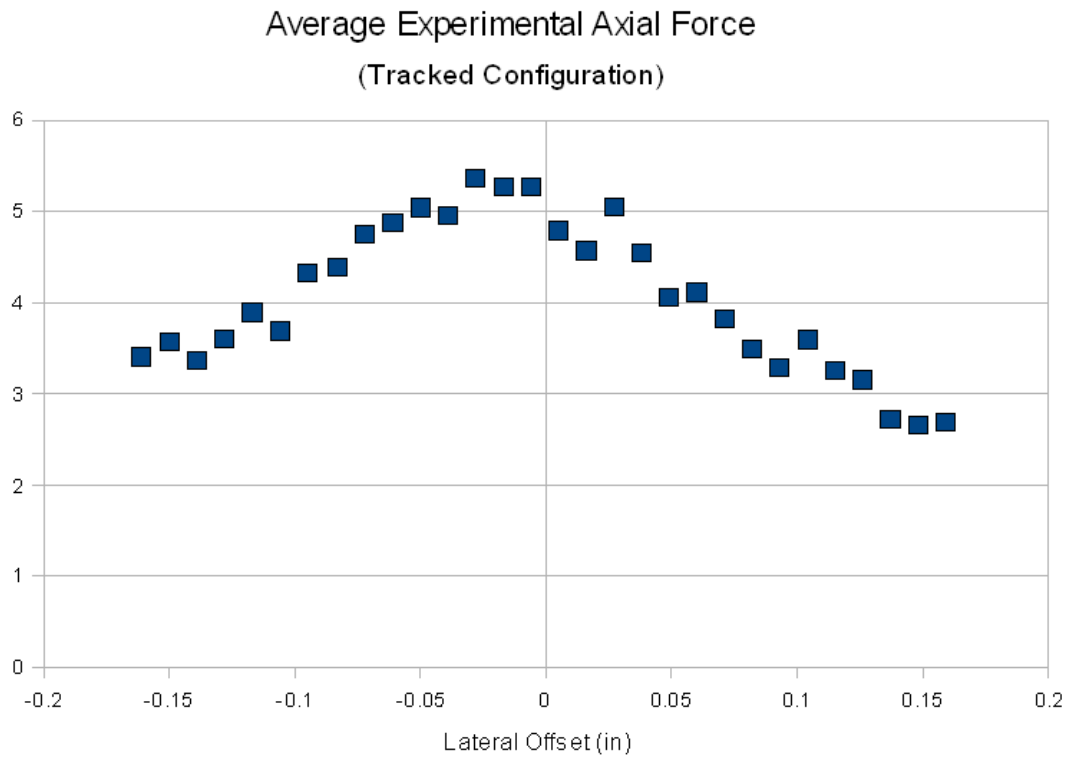

Figure 35: Experimental Welds, Axial force (1000xN) vs. lateral offset(in) for tracked configuration.

The tracked configuration shows generally higher axial forces near the jointline. For effective seam misalignment detection, a substantive axial force trend must hold within a narrow range of offsets near the jointline. Relationships between lateral offset and the X, Y, and moment forces are believed to be secondary effects of the axial force variation combined with tool rotation and travel. Changes in the axial force with lateral offset can be attributed to changes in material geometry and composition below and in the vicinity of the shoulder.

Imposed Axial Load FEA Analysis

The following FEA analysis uses the same axial force applied to the tool for all cases and examines the subsequent material deflection beneath the shoulder with geometry and offset changes. By considering only axial force, the total number of elements in the offset models can be halved with a symmetry plane. A preliminary

analysis which dedicated elements to the steel spacers is presented in appendix A. This analysis shows that the regions of significant deflection are confined to the 6061 aluminum near the tool and not present in the steel spacers of roughly thrice the modulus. The boundaries of the weld material that contact the steel spacers are therefore treated as rigid walls. The model geometry and boundary conditions are shown in Figures 6, 7 and 8. The tracked and untracked boundary conditions differ in the corner region where the gap is present in the spacer of the tracked geometry. For the tracked geometry this region is treated as a free boundary, and for the untracked geometry it is treated as a rigid wall.

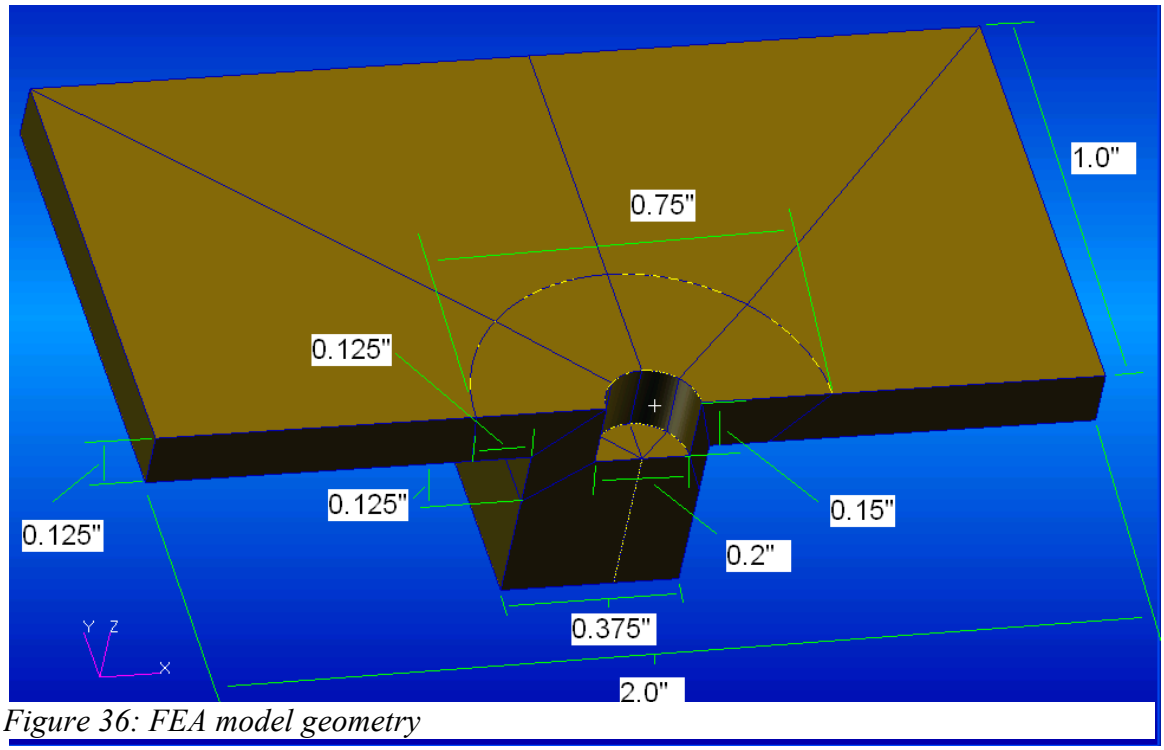

Figure 36: FEA model geometry

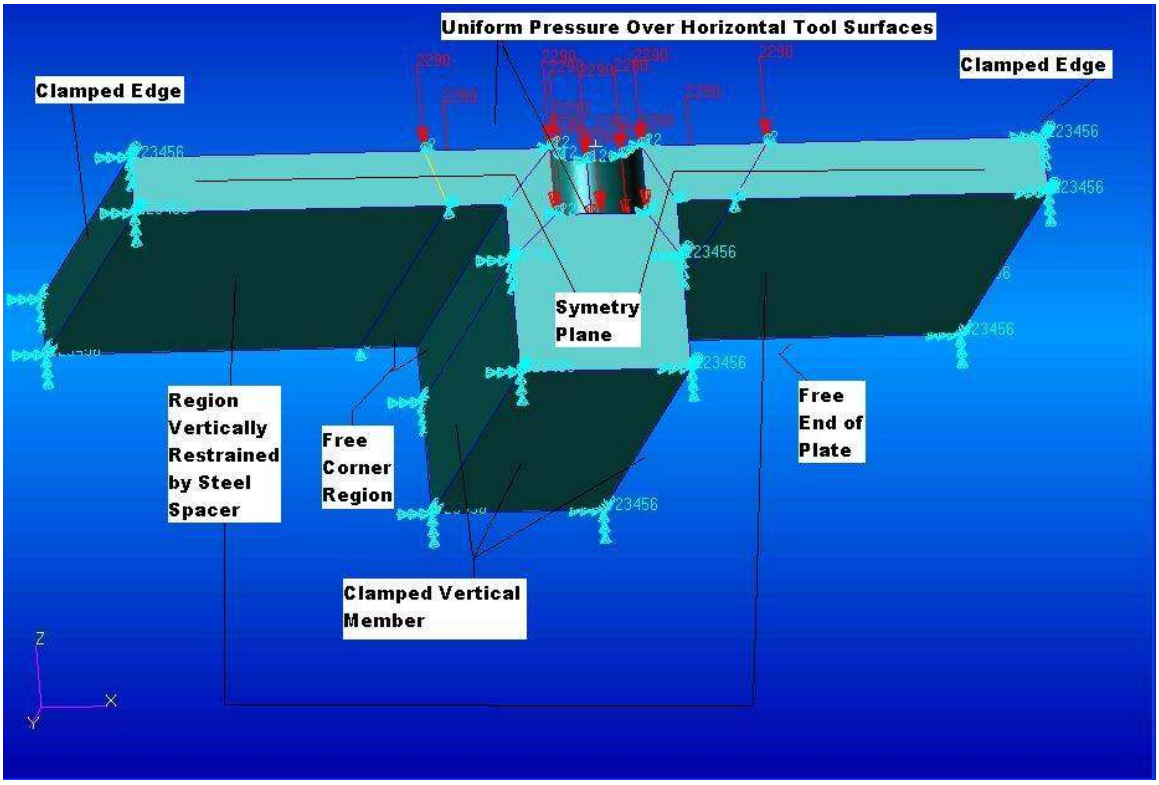

Figure 37: FEA boundary conditions (annotated).

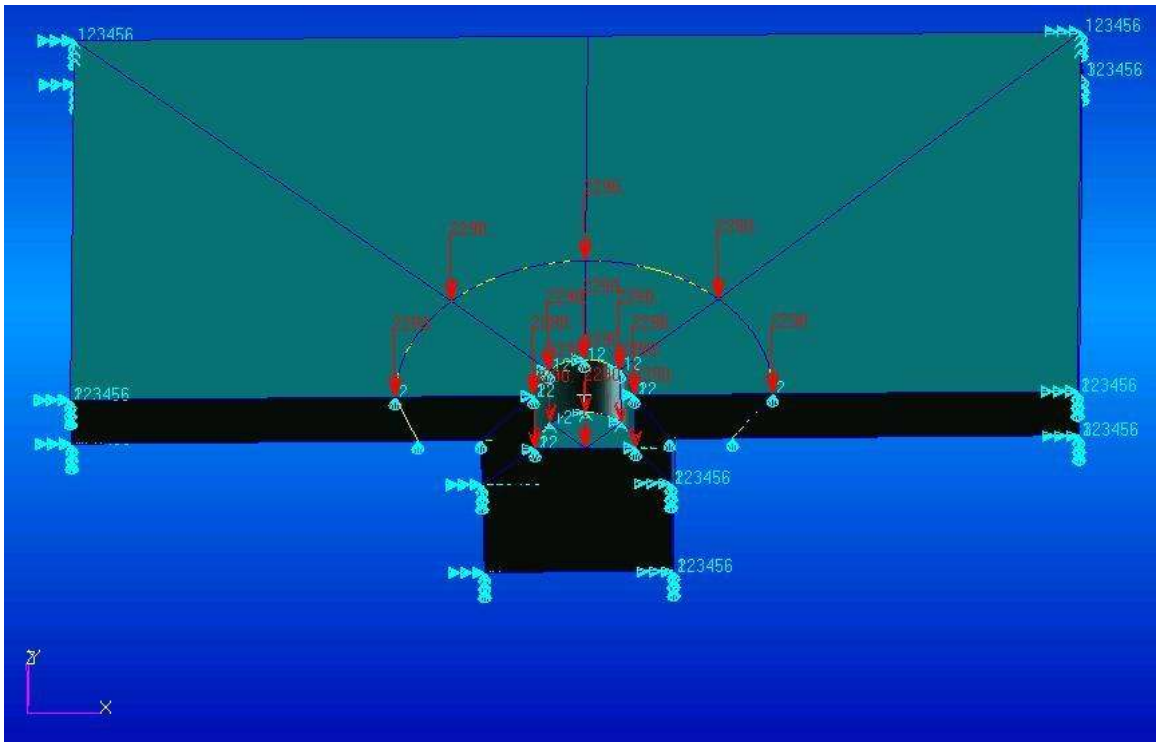

Figure 39: FEA boundary conditions (vectors).

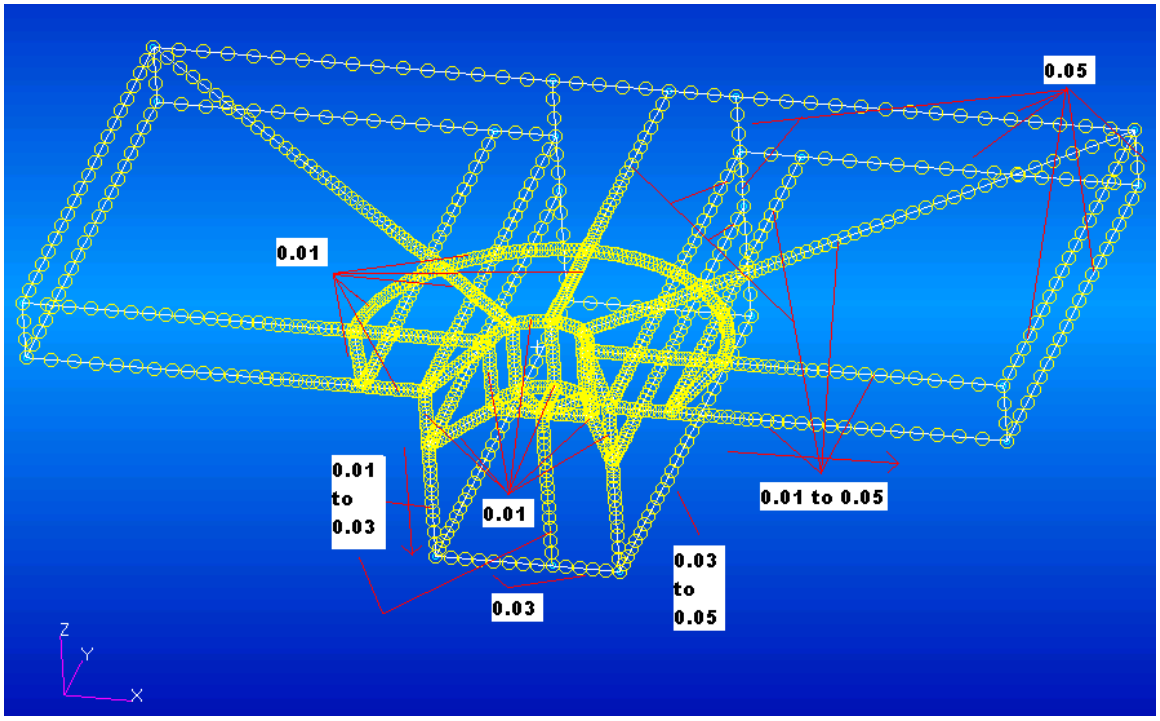

Figure 38: Global edge lengths for data FEA models.

A 4500 N axial force is applied evenly over the horizontal surfaces of the tool for all models and weld process geometry stiffnesses are analyzed. Six offset conditions are created for each geometry configuration starting from a centered case and moving in increments of one hundredth of an inch out to 0.05 inches of offset. The centered case is symmetric about the longitudinal (traverse) weld axis as well as the lateral axis. A preliminary model was therefore created using one quarter of the tool and two planes of symmetry for mesh validation and is presented in appendix B. For consistency an identical mesh seed, shown in Figure 38, was used for all twelve offset and geometry cases including the laterally centered cases of the two geometries. The geometry cases differ in the treatment of the boundary condition in the corner region. The standard model contains approximately 75,000 nodes and 430,000 4-node tetrahedral elements.

For each case, the maximum advancing side and retreating side deflection magnitudes were found in the simulated aluminum weld material. Plots of maximum deflection versus lateral offset are presented in Figure and Figure for the tracked case and the untracked case respectively. An equivalent range is used for the y-axis of each graph to allow for comparison of the tracked and untracked geometry cases.

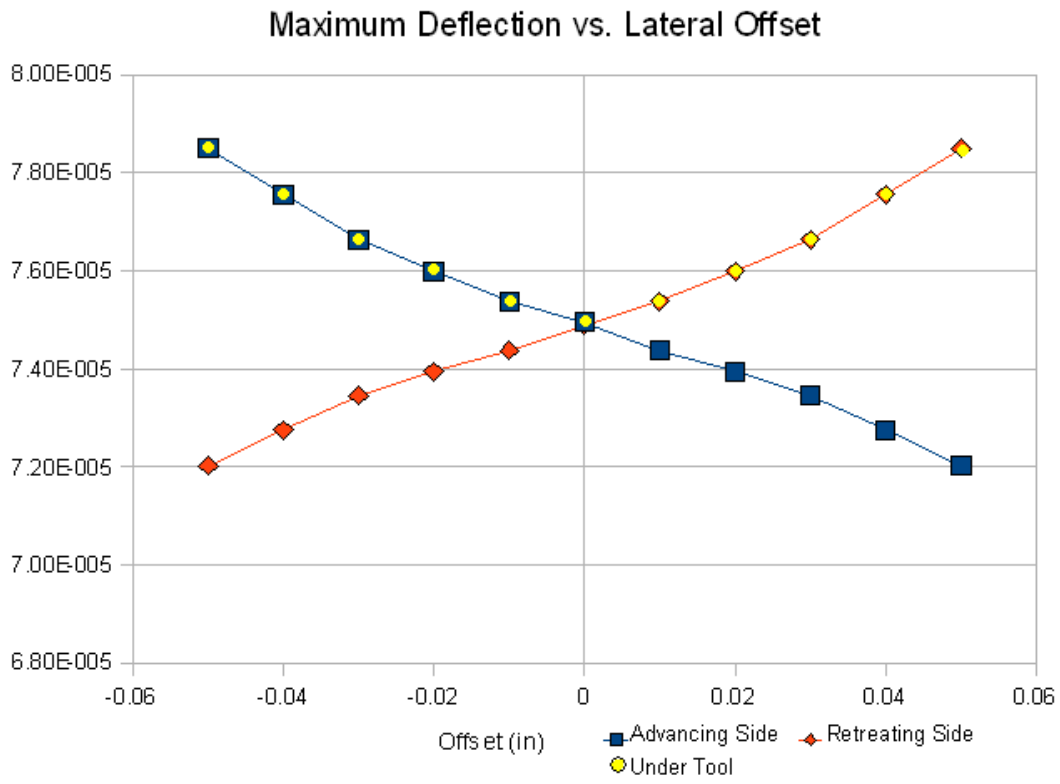

Figure 40: FEA results for tracked (squared gap) geometry.

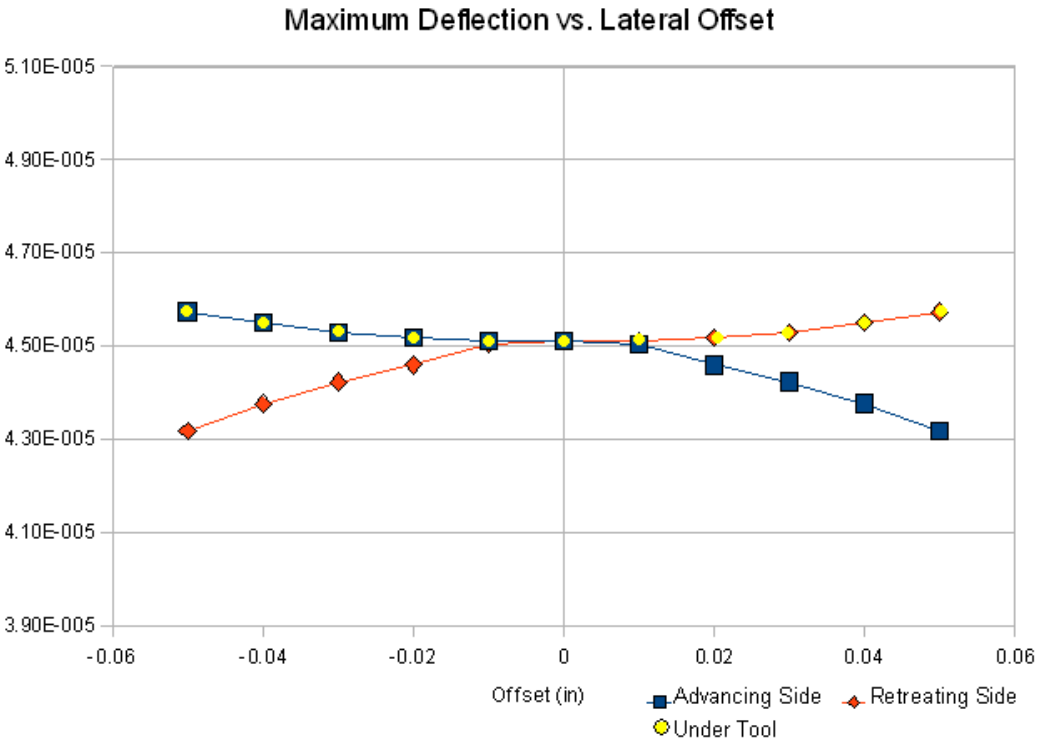

Figure 41: FEA results for untracked (gapless) geometry.

The tracked geometry shows a larger range of maximum deflections, 3.6E-6 in as opposed to 0.6E-6in. This result corresponds to the tool experiencing larger changes in

axial force with lateral offset during welding because the stiffness conditions beneath the tool are changing more drastically with lateral offset. Laterally dependent, changes in x, y, and moment process forces are believed to be dependent on variations in the magnitude of the axial force and its center of application. The difference in the maximum deflection on the advancing side versus that on the retreating side indicates a shift in the center of application of the axial tool pressure. The tracked configuration shows a range of 6.5E-6in as opposed to 2.5E-6in. In addition, the untracked configuration shows little differentiation in deflection results near the center of the jointline. Contour results are presented for the two hundredth offset, tracked geometry case:

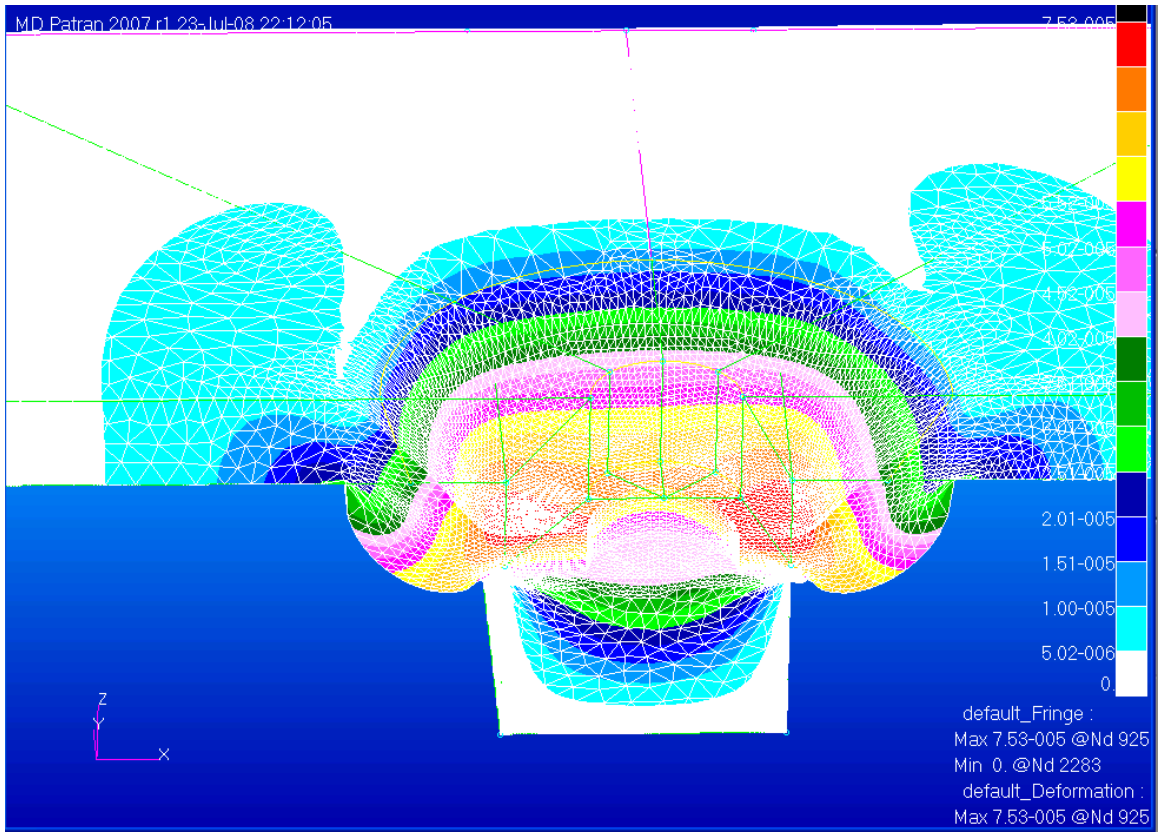

Figure 40: Contour plot of deflection magnitude for 0.02 offset tracked geometry case.

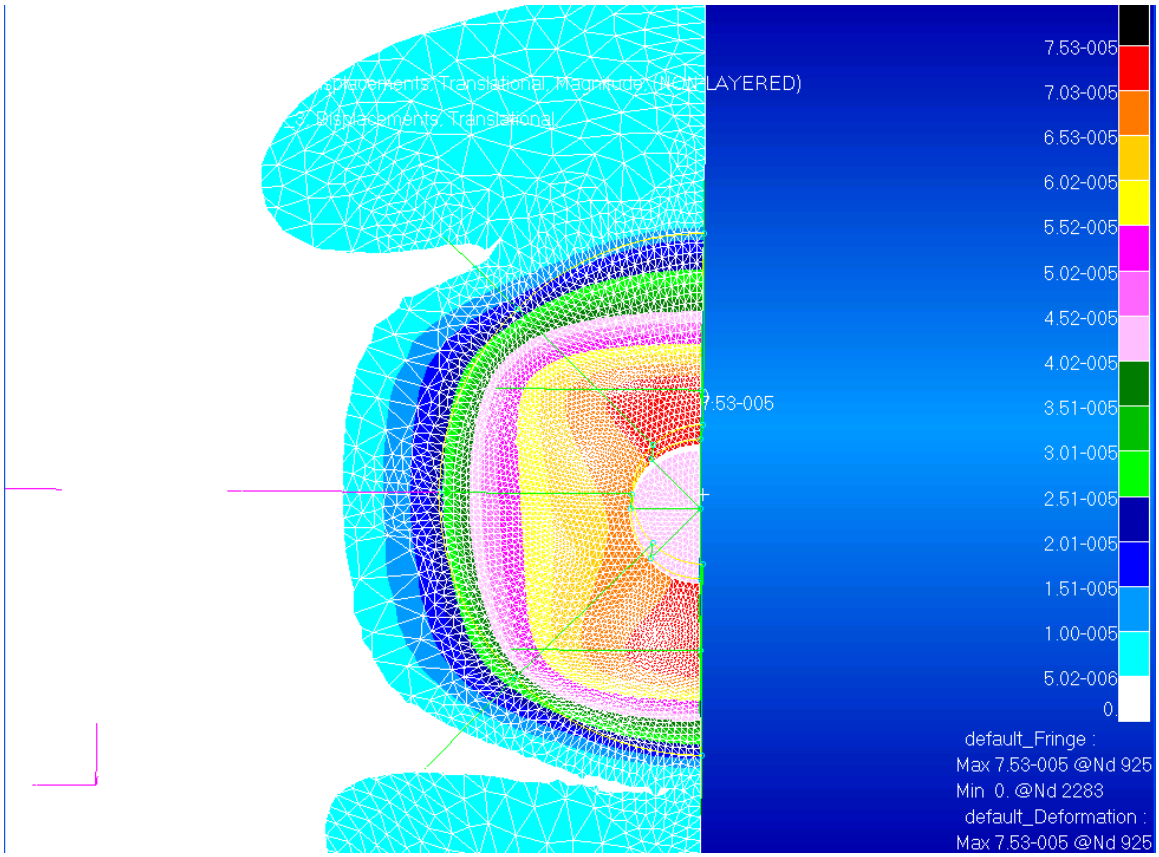

Figure 41: Contour plot of deflection magnitude for 0.02 offset tracked geometry case.

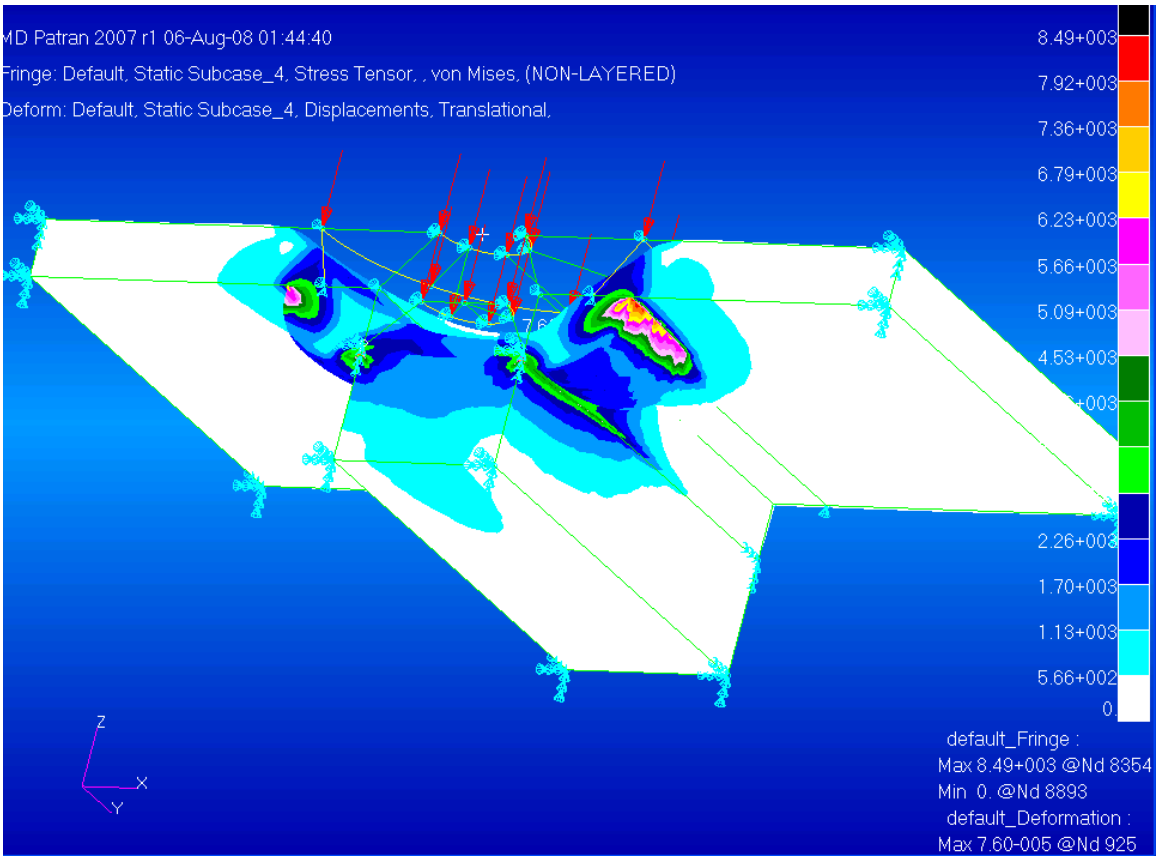

Figure 42: Contour plot of von Mises stress (plotted over the displaced model) for 0.02 offset tracked geometry case.

FEA Appendix A:

Contours taken from the tracked (square gap) geometry with elements dedicated to steel spacer are presented. Note that major displacements and stresses are confined to the vertical and horizontal aluminum members (top and left) and minimal in the steel spacer (lower right).

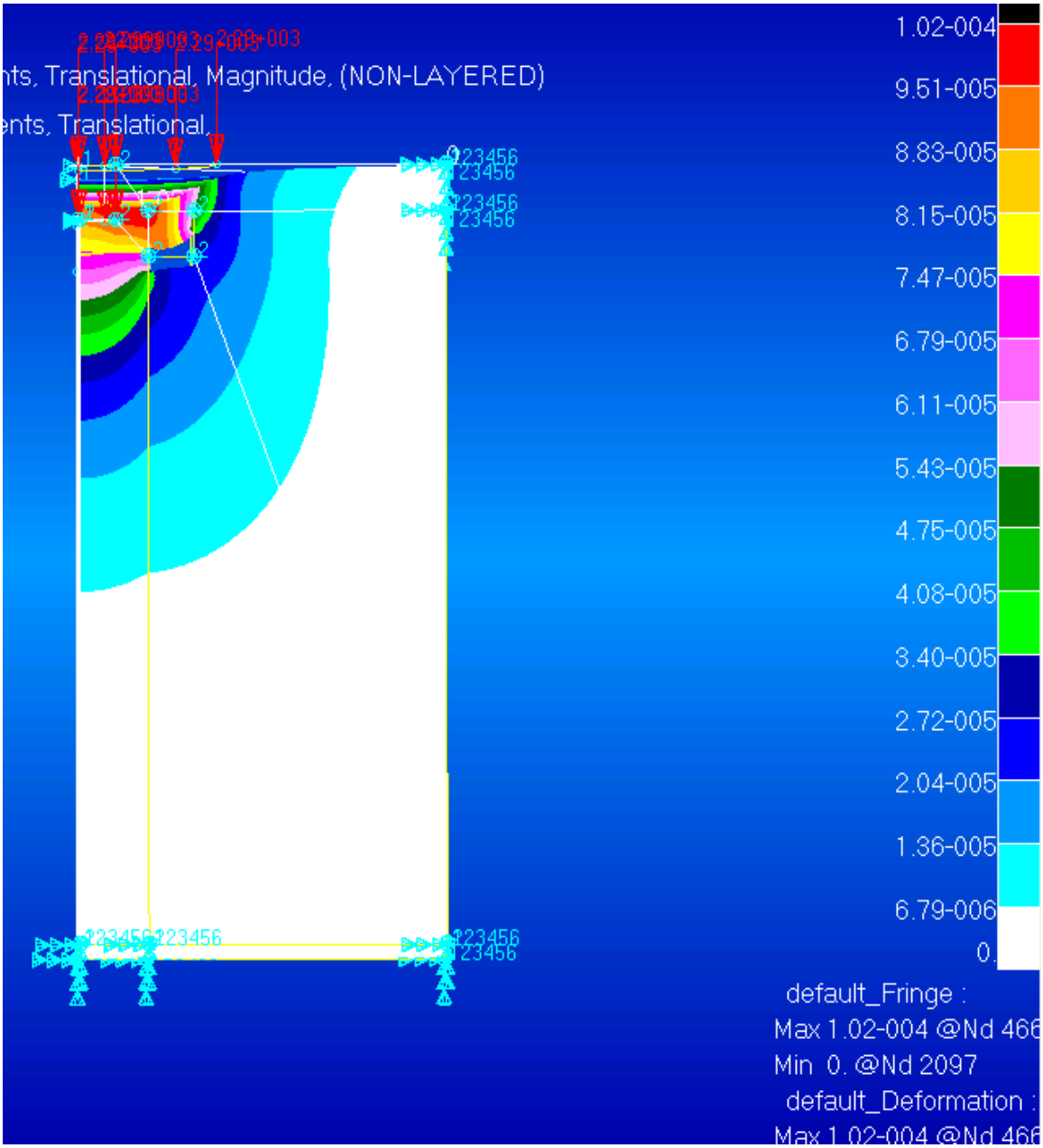

Figure 43: Deformation contour for tracked (square gap) geometry with elements dedicated to steel spacer (front).

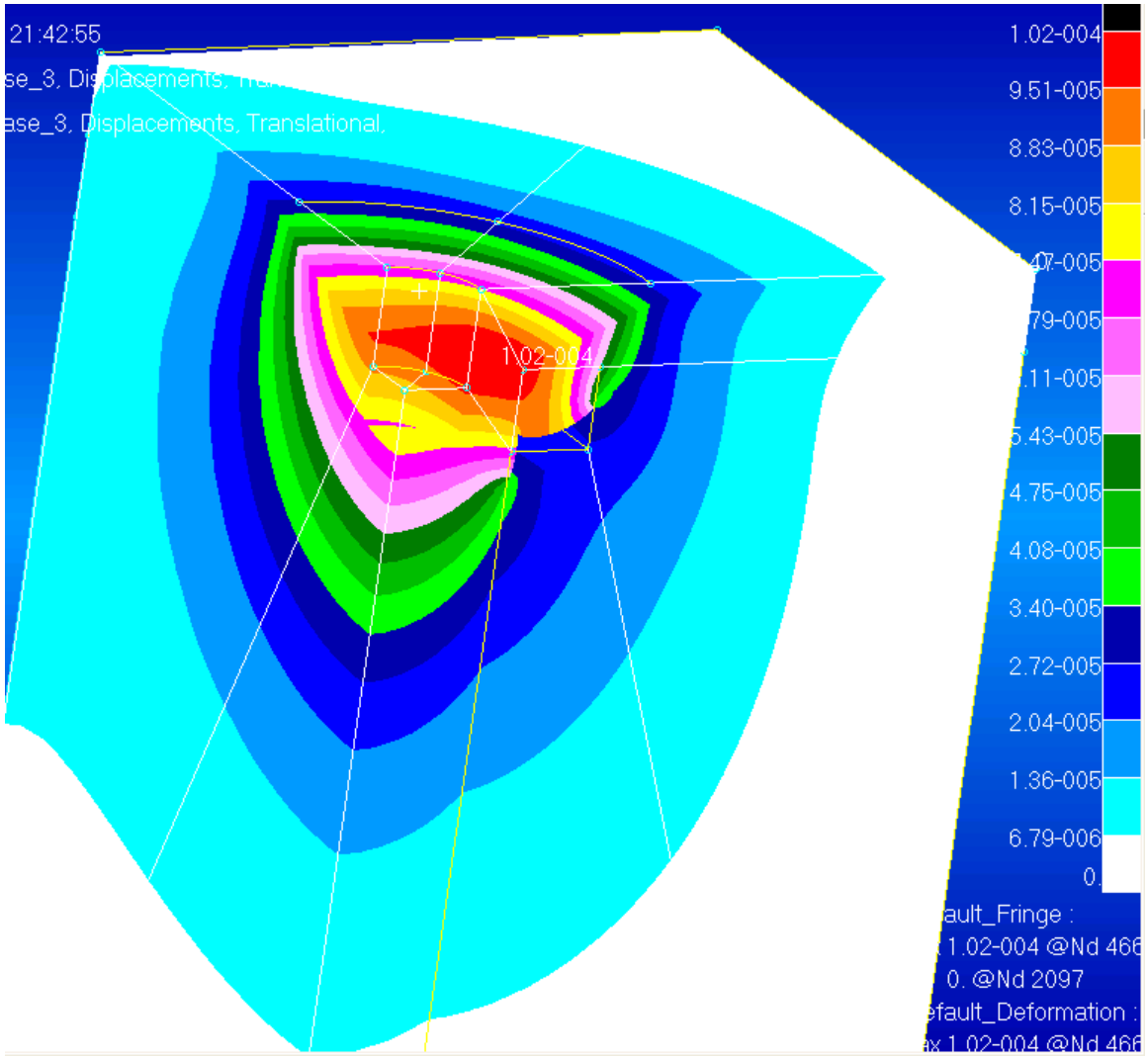

Figure 44: Deformation contour for tracked (square gap) geometry with elements dedicated to steel spacer (iso).

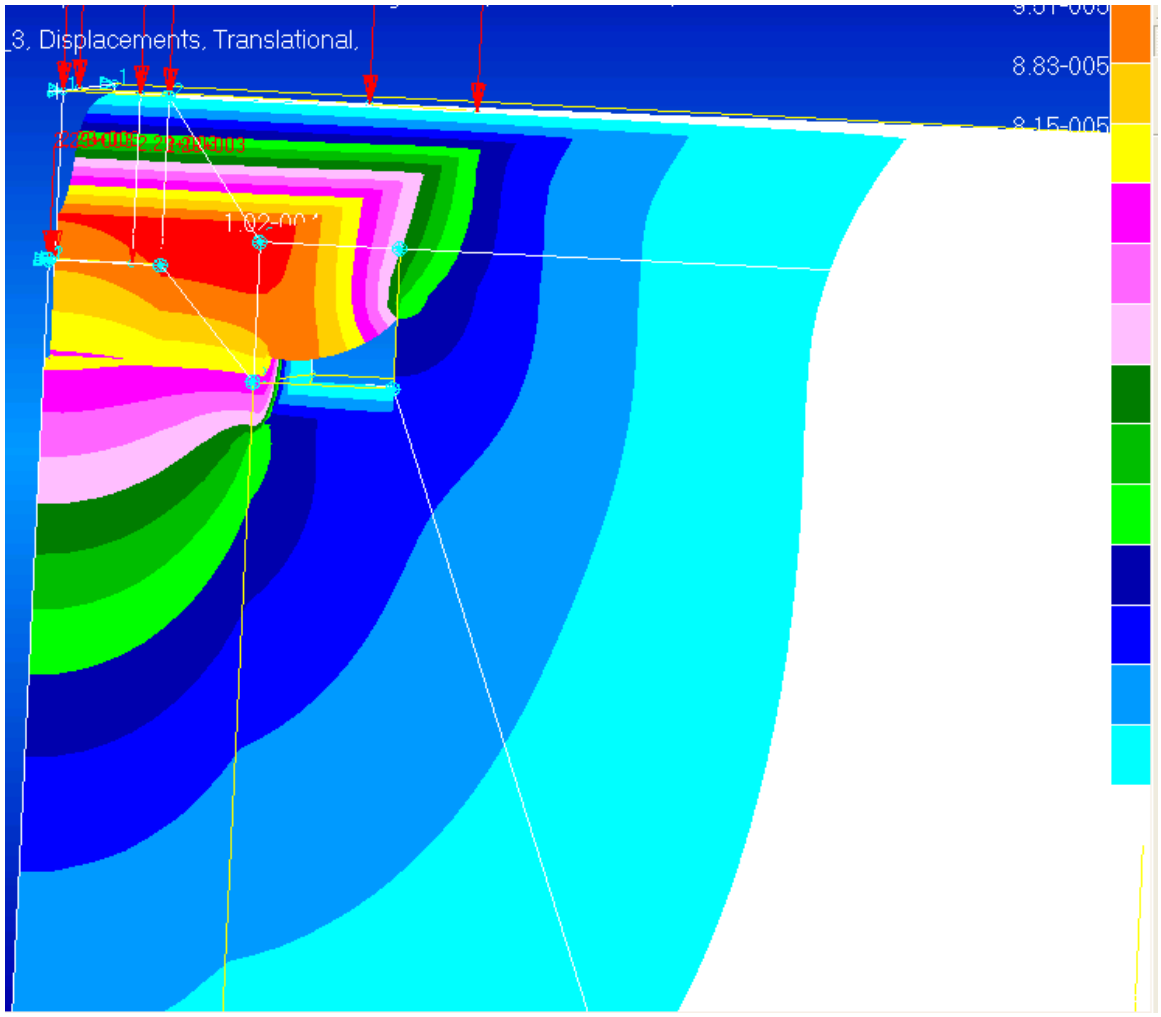

Figure 45: Deformation contour for tracked (square gap) geometry with elements dedicated to steel spacer (zoom).

FEA Appendix B:

Contours taken from the quarter-plate model for laterally centered case with tracked geometry boundary conditions are presented. Results were similar to the standard half-plate model presented.

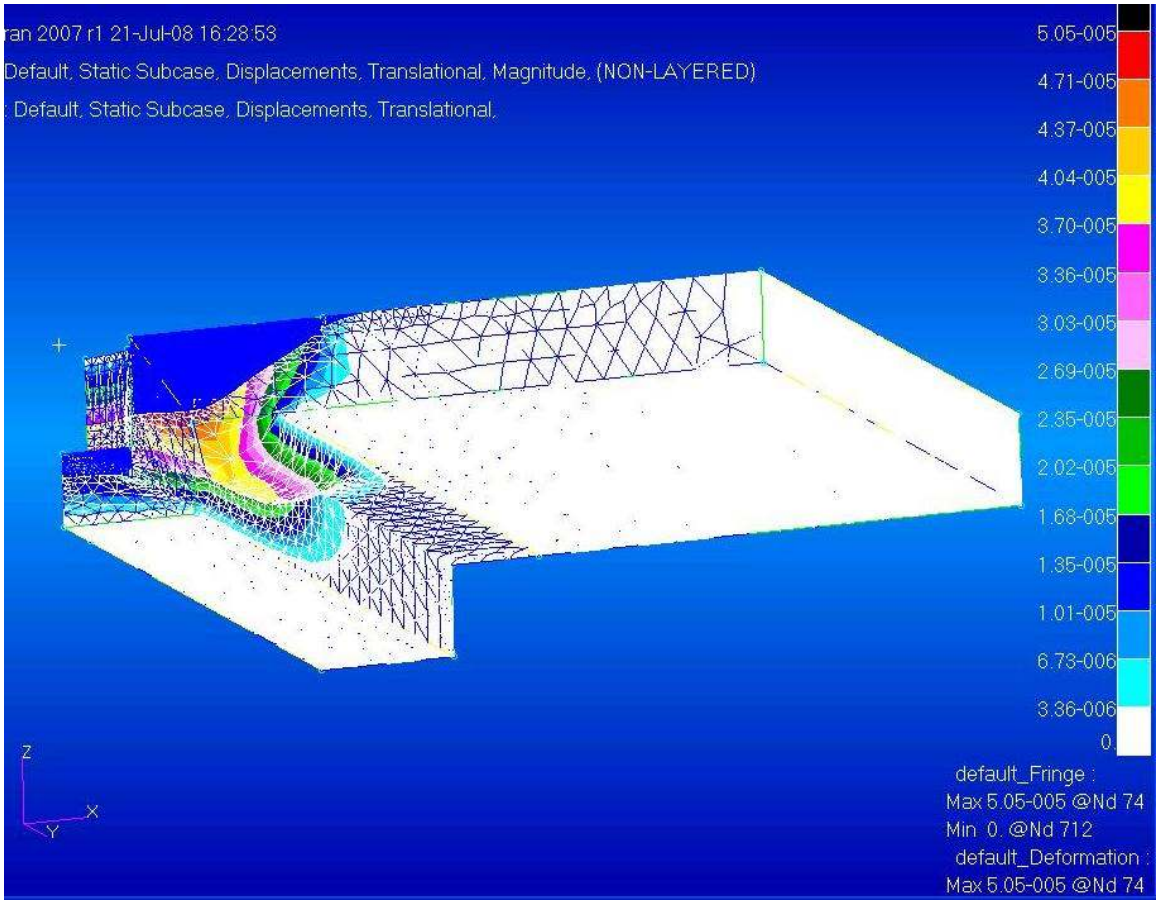

Figure 46: Quarter-plate model for laterally centered case with tracked geometry boundary conditions (iso).

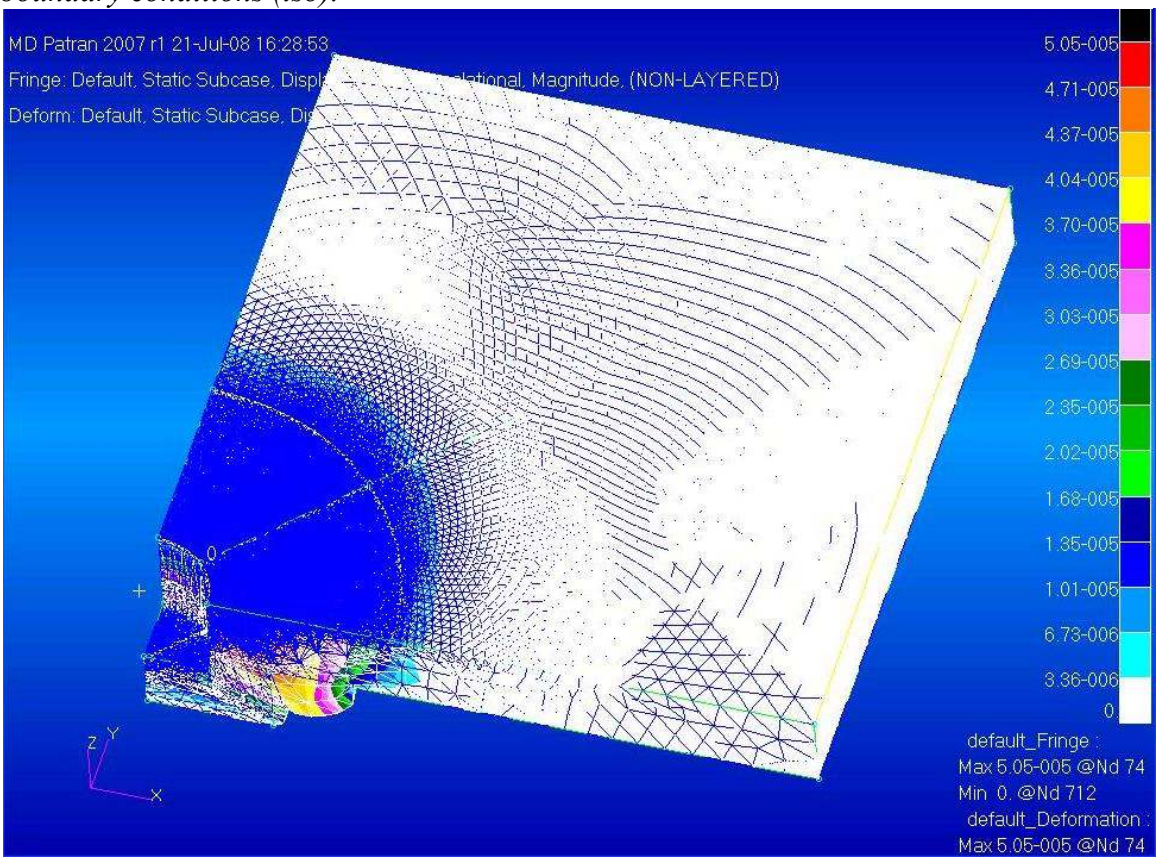

Figure 47: Quarter-plate model for laterally centered case with tracked geometry boundary conditions (top).

Imposed Axial Displacement FEA Analysis

The following FEA analysis uses a constant vertical tool displacement (plunge depth) applied to the FEA plate geometry for all cases and examines the subsequent axial force on the tool with geometry and offset changes. The axial deflection applied to the material interface for both configurations and all offset cases is 0.0001 in. This deflection value obtained axial force values close to those found experimentally. For simplicity, the local plasticization near the tool is ignored and a constant Young's modulus for 6061 alloy Aluminum is used. Geometry and boundary conditions are otherwise identical to the imposed force FEA analysis presented earlier. Results for this analysis are presented below along with experimentally determined values.

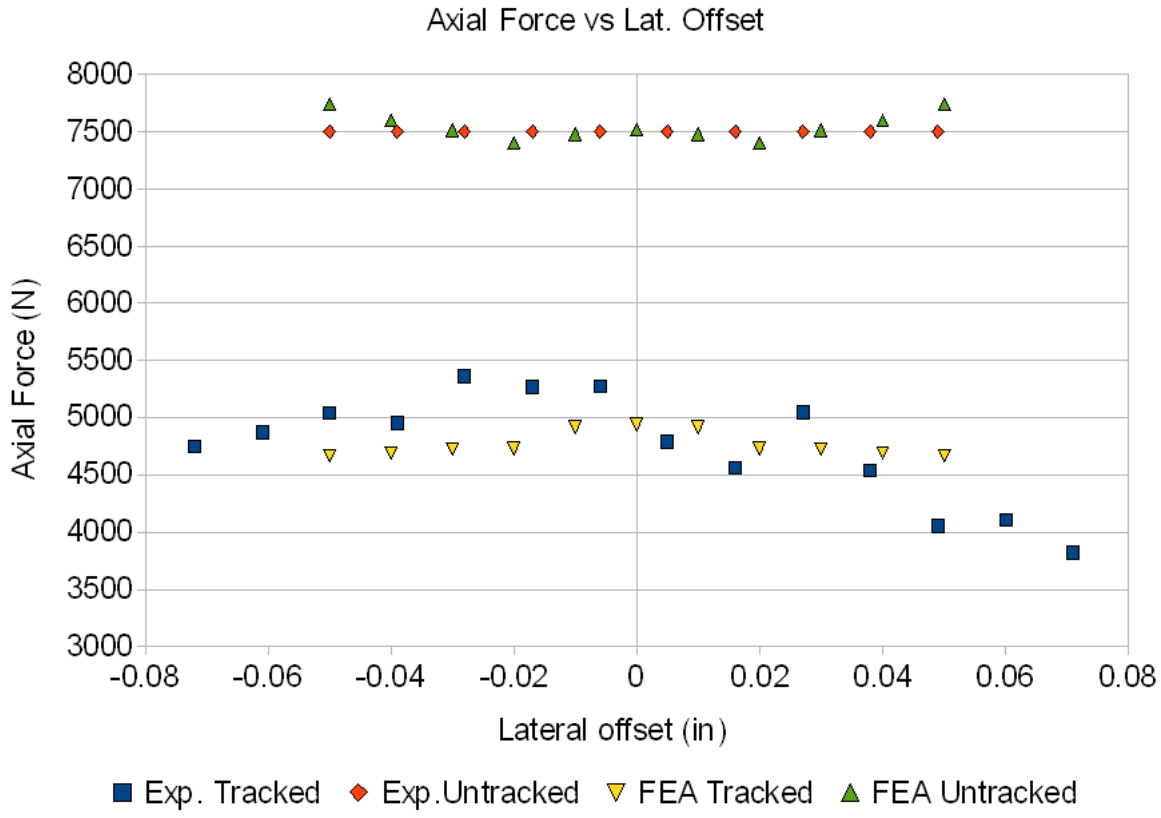

Figure 48: Axial force vs Lat. Offset plot with experimental and FEA data.

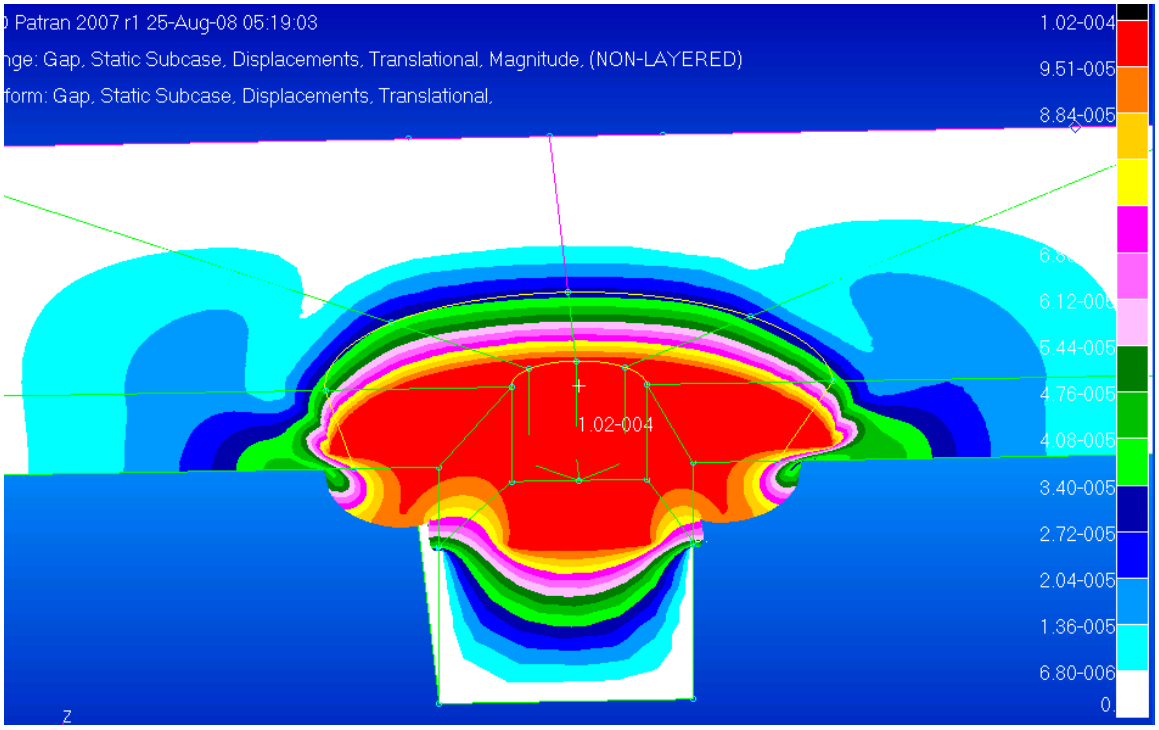

Figure 49: Contour plot of deflection magnitude for 0.02" offset tracked geometry case.

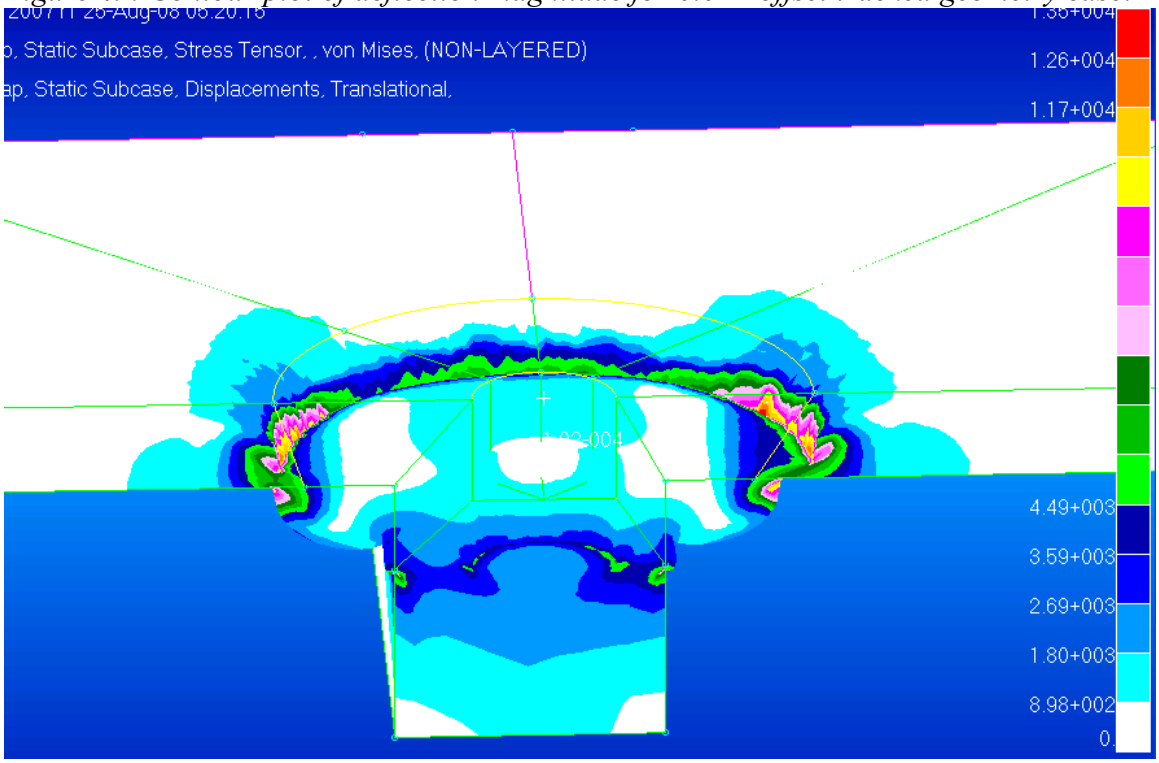

Figure 50: Contour plot of von Mises stress for 0.02" offset tracked geometry case.

CFD Thermo-Plastic analysis of Friction Stir Welded T-joints under Lateral Offset

The Eulerian, finite volume, CFD solver, Fluent was used with the implicit formulation. The weld material viscosity function was set by user-defined function and defined according to the visco-plastic model of Sheppard and Wright [3,] modified from the initial formulation proposed by Sellars and Tegart[4]. Flow stress is defined as an inverse hyperbolic sine function of the local strain rate magnitude and absolute temperature in this following commonly used form:

$$Z = \dot{\varepsilon} \exp(\frac{Q}{RT}) = A(\sin \alpha\sigma_e)^n$$

or equivalently,

$$\sigma_e = \frac{1}{\alpha} \sinh^{-1}\left[\left(\frac{Z}{A}\right)^{\frac{1}{n}}\right] \qquad Z = \dot{\varepsilon} \exp\left(\frac{Q}{RT}\right)$$

where α, *A*, *n* are material constants (α = 0.045 $(Mpa)^{-1}$, Q = 145 kJ mol^{-1}, A = 8.8632E6 s^{-1}, n = 3.55), σ_e is the equivalent steady state flow stress (Mpa), *R* the gas constant (R = 8.314 $mol^{-1}K^{-1}$), *T* the absolute temperature (K), Q is the activation energy (J mol^{-1}) and Z is the Zener-Hollomon parameter. The material constants used are determined using a hot compression test. The material viscosity is defined in the following manner:

$$\mu = \frac{\sigma_e}{3\dot{\varepsilon}}$$

The visco-plastic model holds at temperatures reasonably below the metal's solidus temperature. As the material approaches the solidus temperature significant softening occurs. A variable slip shear condition was set at the weld interface [14]. The tool rotational velocity was set to %70 of the experimental parameter and a pure stick condition was used. This simple boundary condition was used because the actual relationship is unknown.

The total heat input was calculated via the weld power method [5-13]:

$$P = \omega \cdot \Omega$$

$$Q = P \cdot \beta$$

where P is the weld power (W), Q is the heat input to the tool and weld material (W), ω is the tool rotational speed (rad/s), Ω is the measured torque (N·m), and β is the fraction of mechanical work dissipated as heat into the tool shank and the weld. Chao et al.[15] arrive at a β value of approximately 0.8 under similar conditions using a boundary value approach and determine that approximately 5% of this dissipated heat is dissipated via the tool shank. For the models presented here a heat input of 1591.6 Watts is obtained using an experimentally determined weld moment of 19.0 N·m. {Q = (104.72 rad/s)*(19 N·m)*(0.8) }

Weld moment was found experimentally via a rotating cutting force dynamometer and the spindle speed setting was verified by optical interrupters. This calculated total heat input was then applied in the model at the tool-material interface via a user-defined function which varies heat input over the tool surface according to the local tangential velocity magnitude. Heat input is therefore highest near the tool shoulder edge and zero at the center of the probe tip with the total heat input equal to the weld power. Heat input to the tool shank is determined by imposing the local weld material temperature at the interface onto the corresponding local tool surface element via a user-defined function. A heat transfer coefficient of 10 $W/m^2 \cdot K$ is used for the exposed surface of the toolshank. This is appropriate for a the rotating tool steel on air interface [15,16]. A value of 30 $W/m^2 \cdot K$ [15, 16] is used for the exposed aluminum surface and a value of 2000 $W/m^2 \cdot K$ is used for the remaining boundaries which involve intimate metal-metal contact due to material clamping or at continuous metal boundaries[17].

The model temperature field was verified by a Flir SC500 Thermacam model thermal camera. The thermal camera was calibrated to the emissivity of the tool shank surface. The experimental temperature on the tool near the material surface was determined to be 396˚C (669) K and was calculated by taking the average temperature from a rectangular area on the tool shank surface for each image. Ten images at one second intervals were used and those were then averaged to produce an approximation of the temperature on the cone surface during the steady-state portion of the weld. It should be noted that the temperature continued to creep upward even during the steady state period. In addition, welds made later in the day (when the machine, fixturing, and backing plate were warm) were noticeably warmer (as much as 20°C).

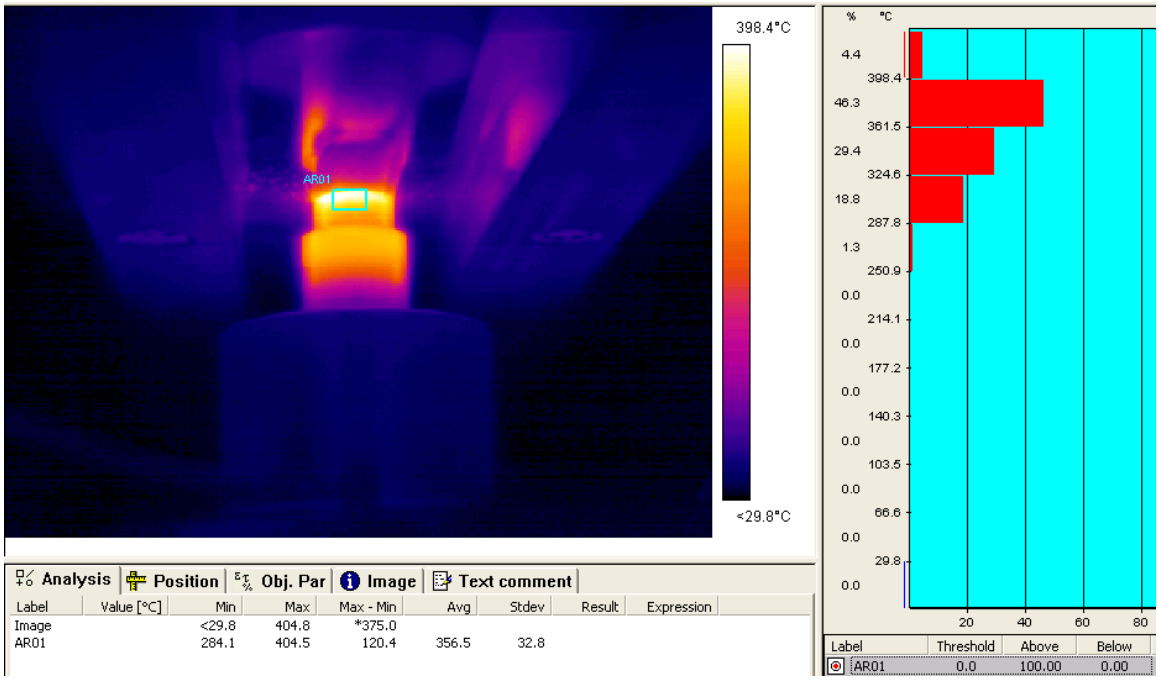

Figure 51: A thermal camera image taken during the steady state weld period of a 1000rpm, 4 ipm, blind-T weld

Model Geometry

Two model geometries were creating representing a centered tool case and an offset case of 0.05 inches to the advancing and retreating side. The tool rotation is varied in the latter to simulate offsets to the retreating and to the advancing side of the weld. The mesh was created in a mesh generation and preprocessing program called Gambit. The model was divided into several continuum zones to account for material type. The models contain approximately 960,000 tetrahedral elements. The work material has been divided into a refined zone of plastic aluminum behavior around the tool and zones of solid aluminum and steel behavior away from the tool where only heat conduction equations are solved. The zone immediately in front and the zone immediately behind the central refined zone are also modeled using a plastic aluminum formulation to create a stabilized flow into and out of the zone of interest around the tool. A velocity inlet set to the traverse rate and an outflow boundary condition are used to establish a relative velocity between the tool and workpiece.

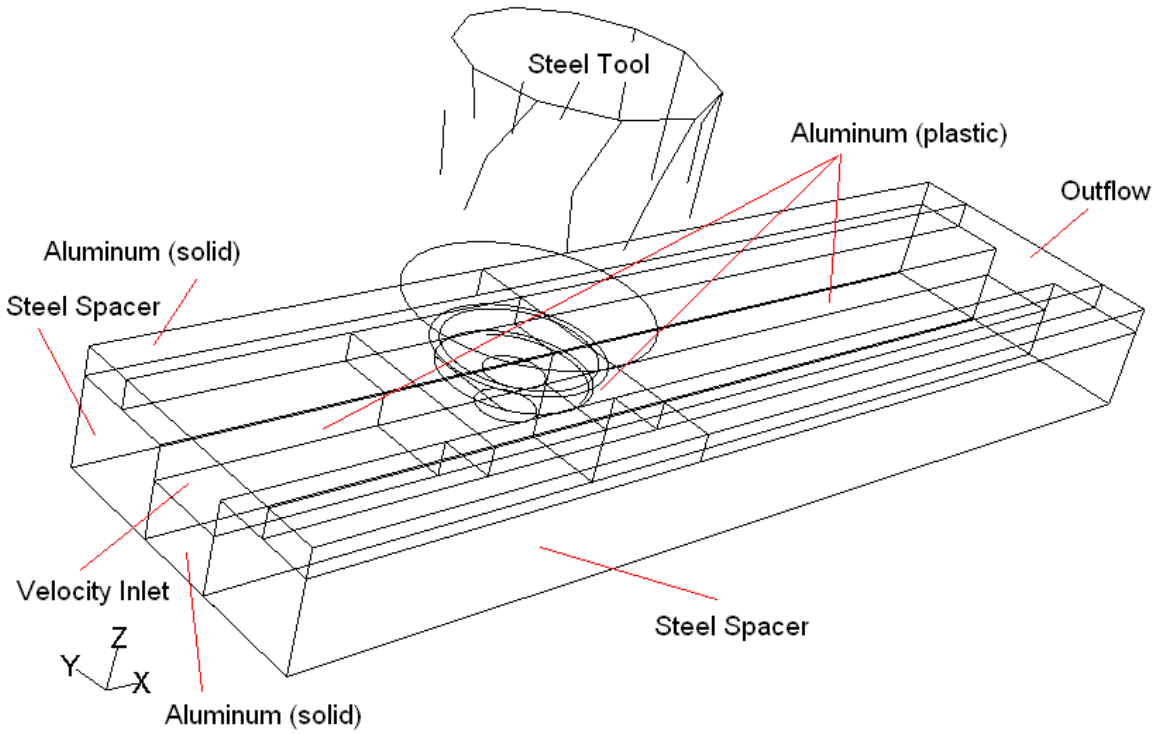

Figure 52: Fluent CFD model zones.

Results:

Surface Heat Fluxes (Watts):

Surface:\Offset:	0.05" to Adv.	Centered	0.05" to Ret.
Pin Bottom	71.24	73.83	73.72
Pin Bottom-Tool	13.62	16.03	14
Pin Side	256.51	265.86	265.46
Pin Side-Tool	26.38	19.72	27.45
Shoulder	937.76	971.94	970.48
Shoulder-Tool	286.1	244.22	240.49
Total:	1591.6	1591.6	1591.6

Figure 53: Surface heat fluxes for CFD model faces.

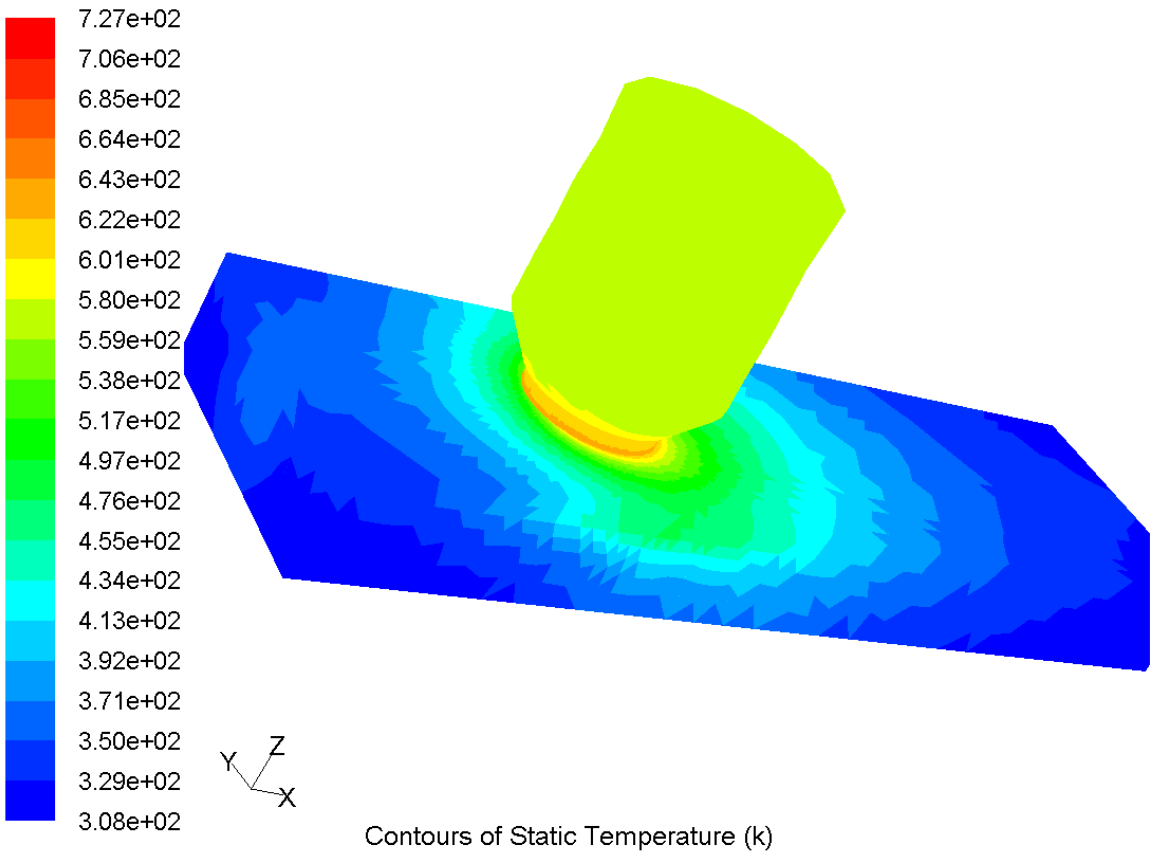

Figure 54: Thermal contour for laterally centered case.

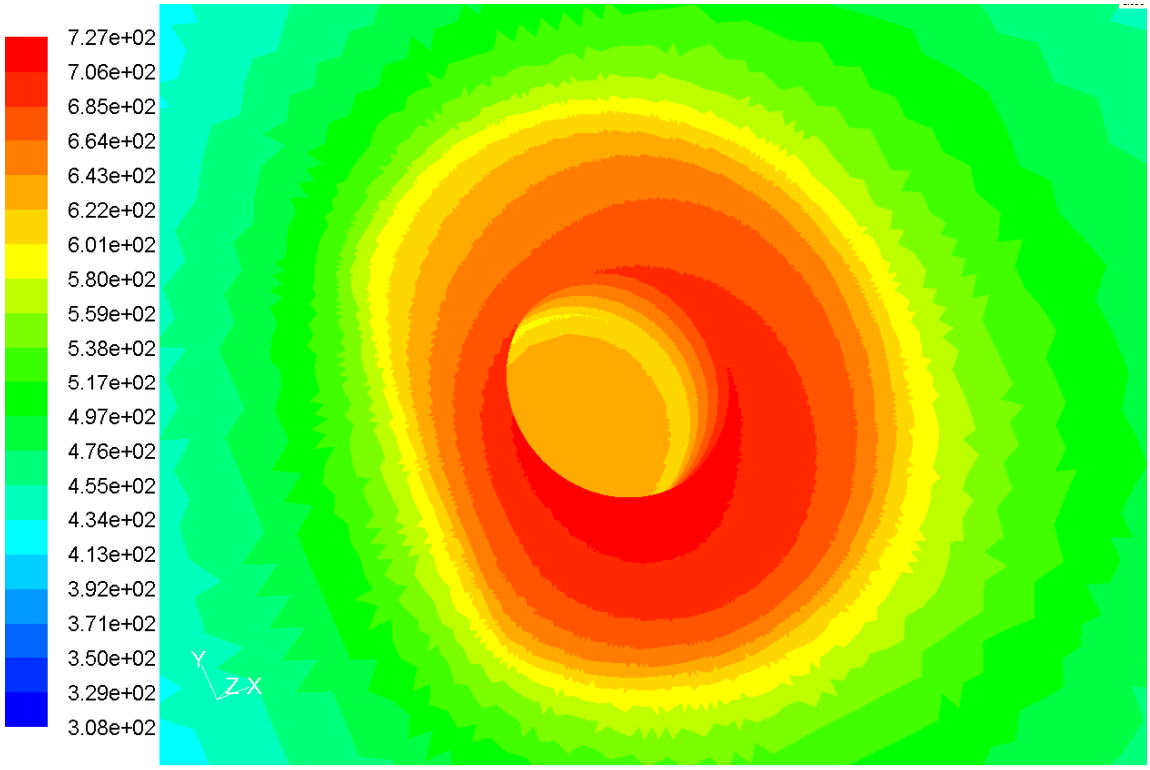

Figure 55: Thermal contour of weld material at the interface for laterally centered case.

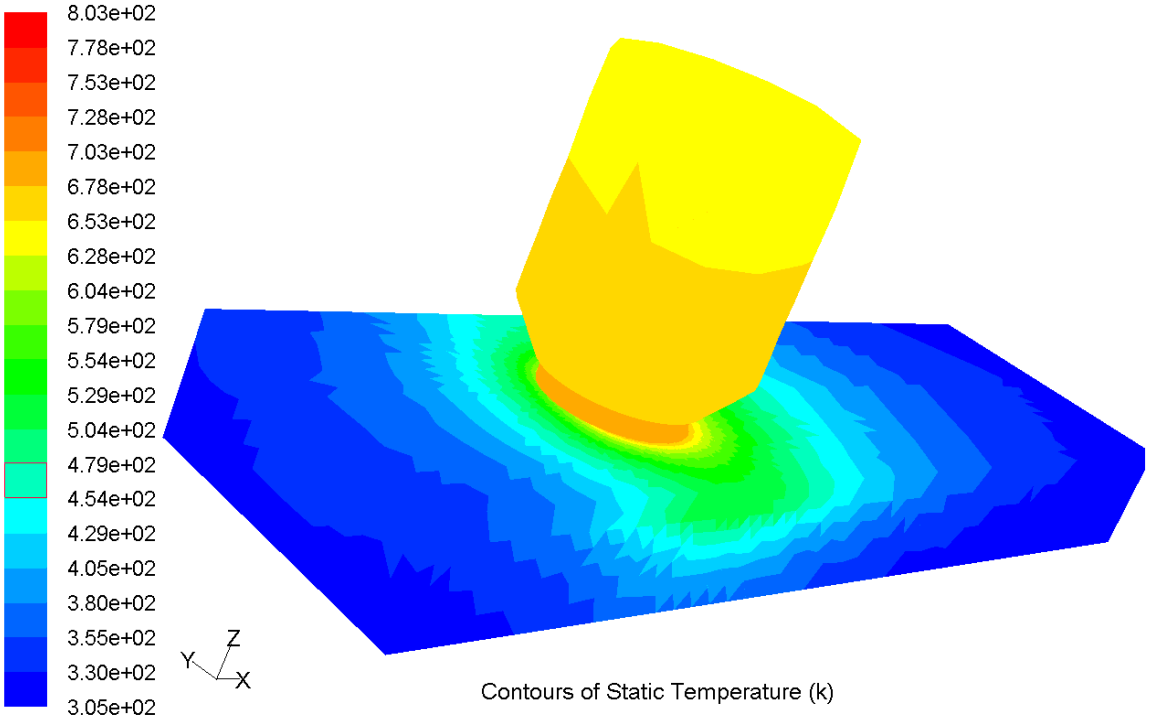

Figure 56: Thermal contour for 0.05in advancing side lateral offset case.

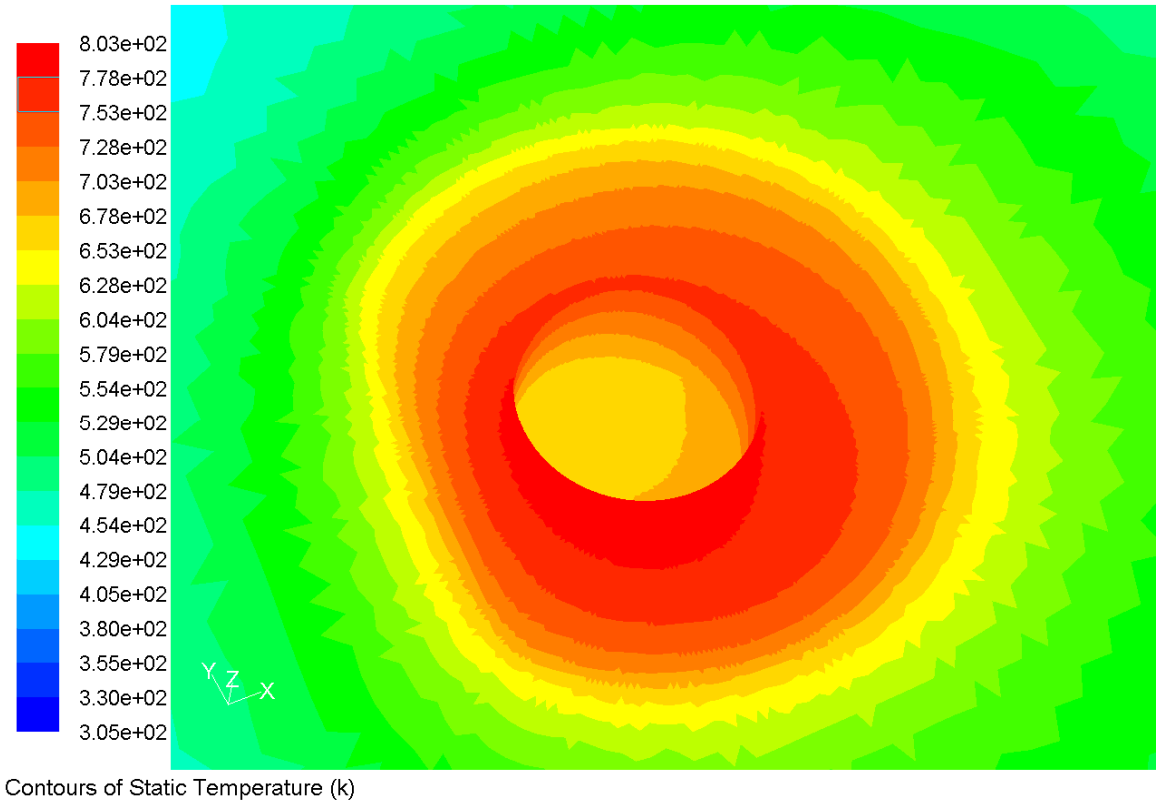

Figure 57: Thermal contour of weld material at the interface for 0.05in advancing side lateral offset case.

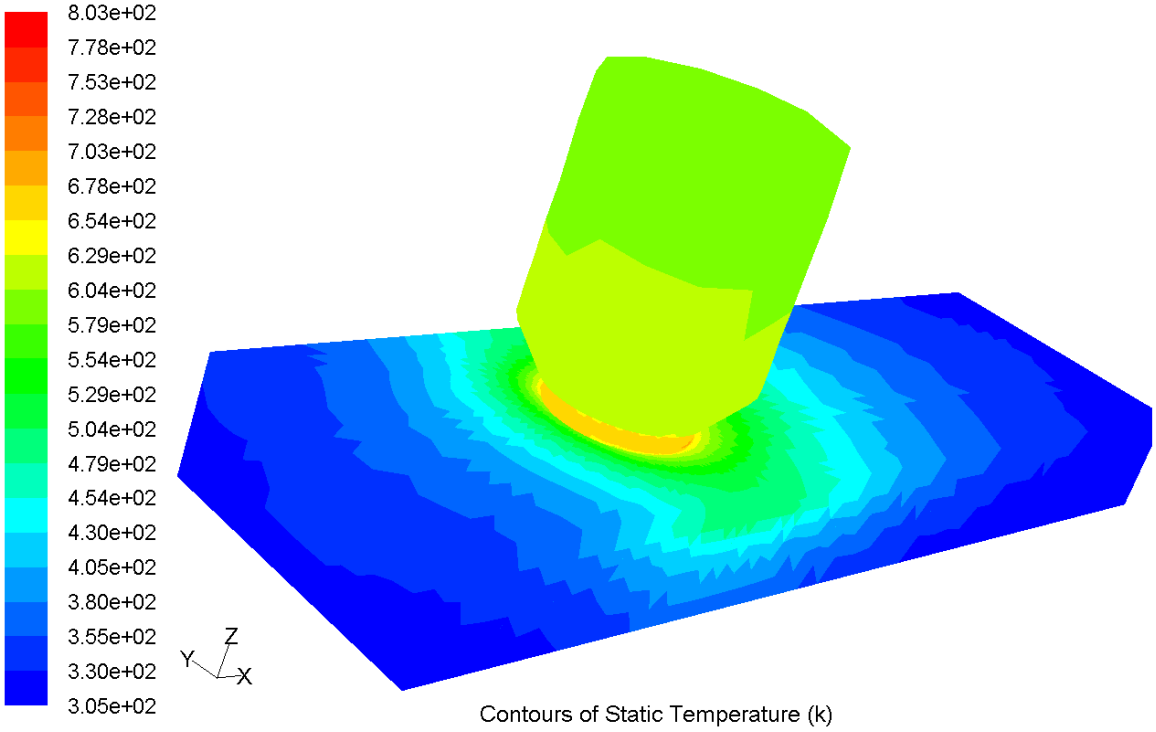

Figure 58: Thermal contour for 0.05in retreating side lateral offset case.

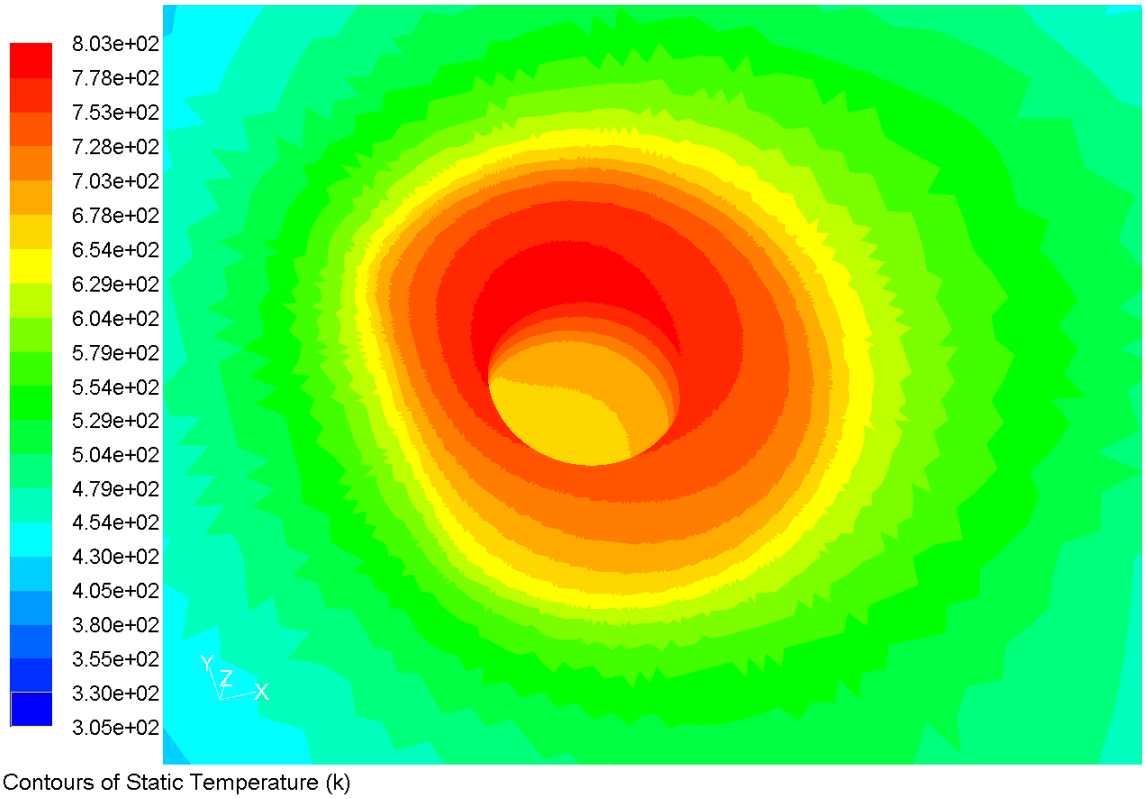

Figure 59: Thermal contour of weld material at the interface for 0.05in retreating side lateral offset case.

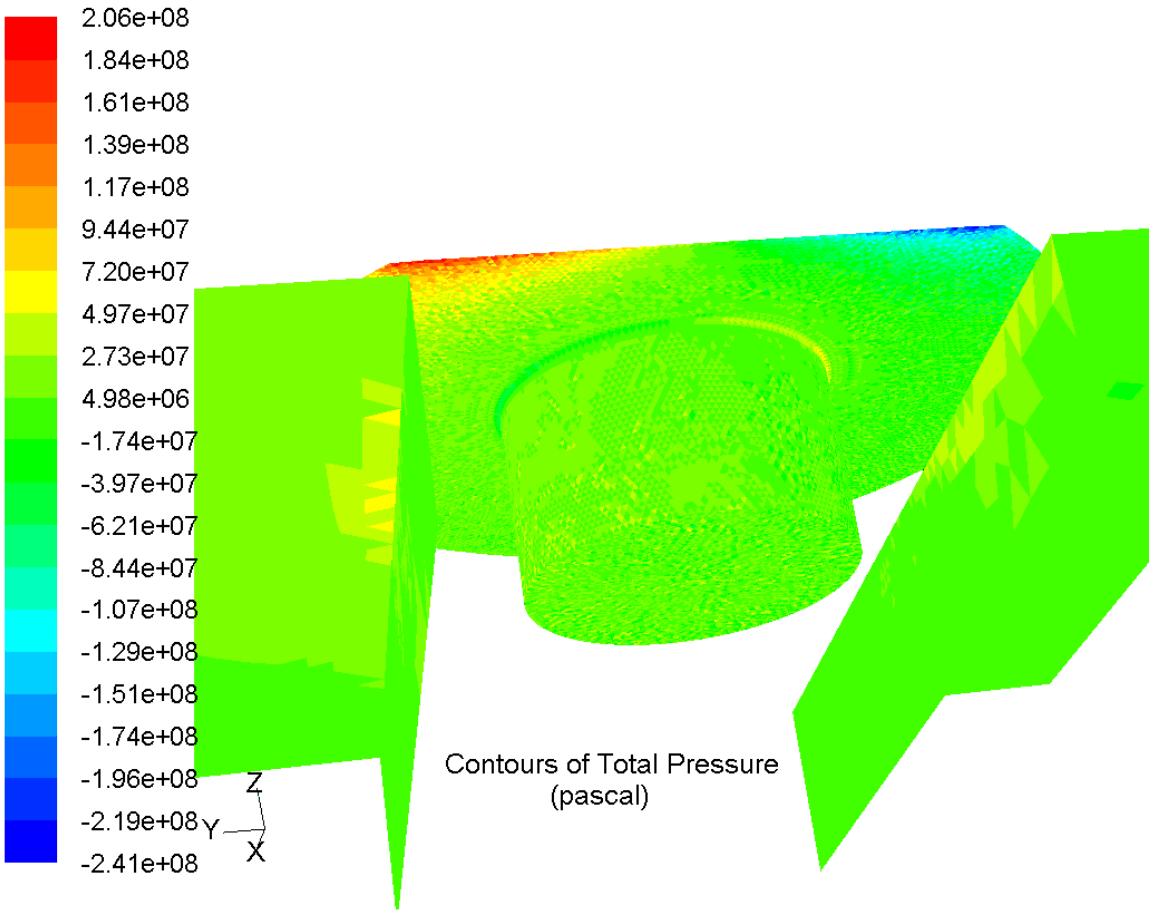

Figure 60: Contour of total pressure for 0.05" advancing side offset case.

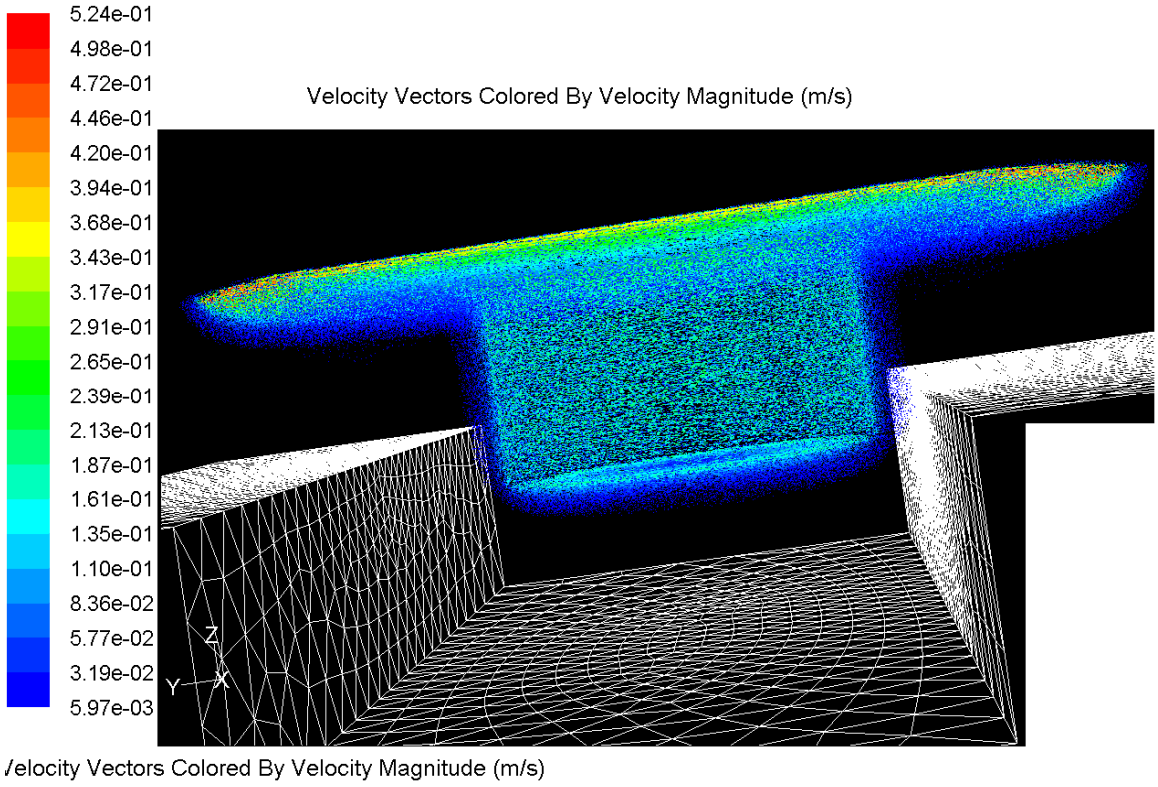

Figure 61: Velocity vectors for 0.05" advancing side offset case.

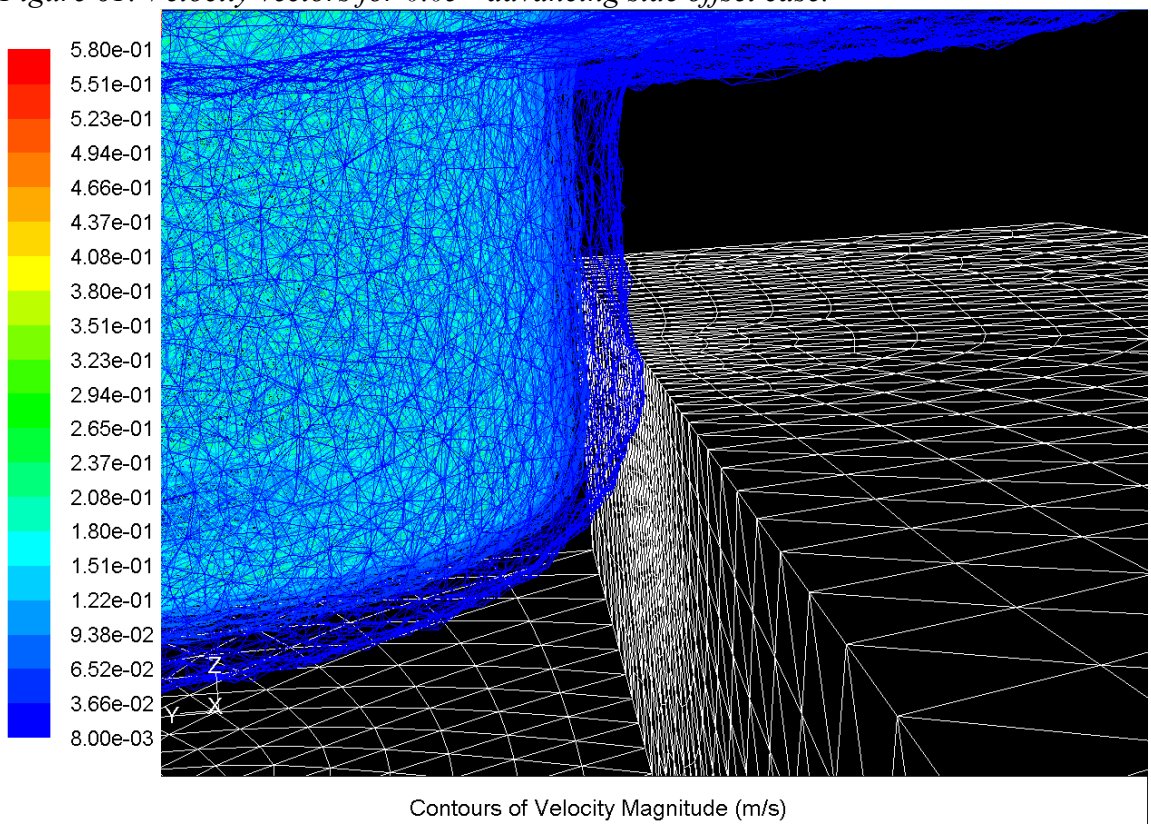

Figure 62: Contour of velocity magnitude for 0.05" advancing side offset case.

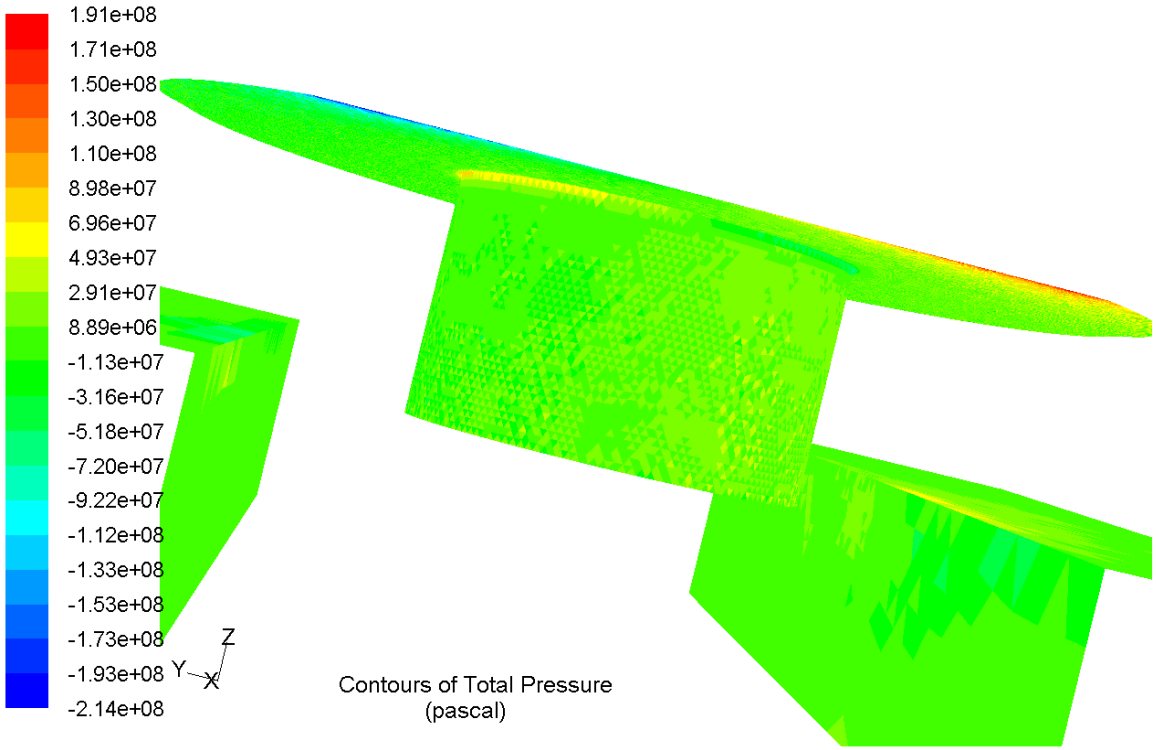

Figure 63: Contour of total pressure for 0.05" retreating side offset case.

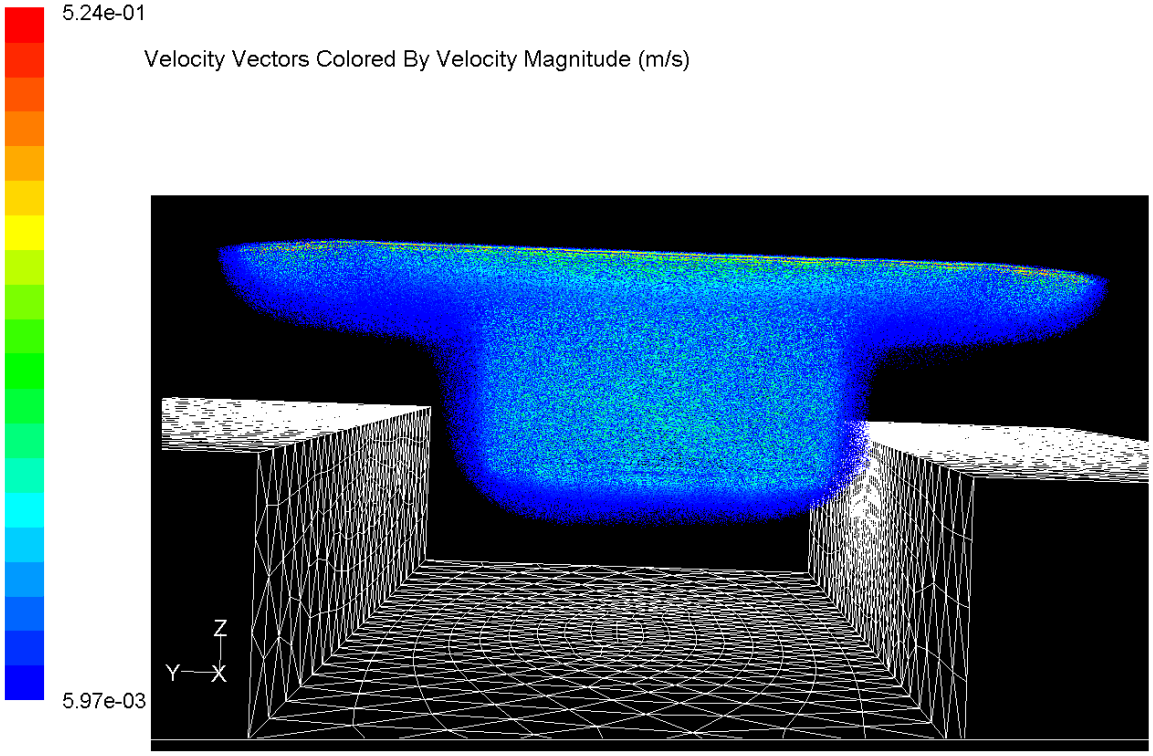

Figure 64: Velocity vectors for 0.05" retreating side offset case.

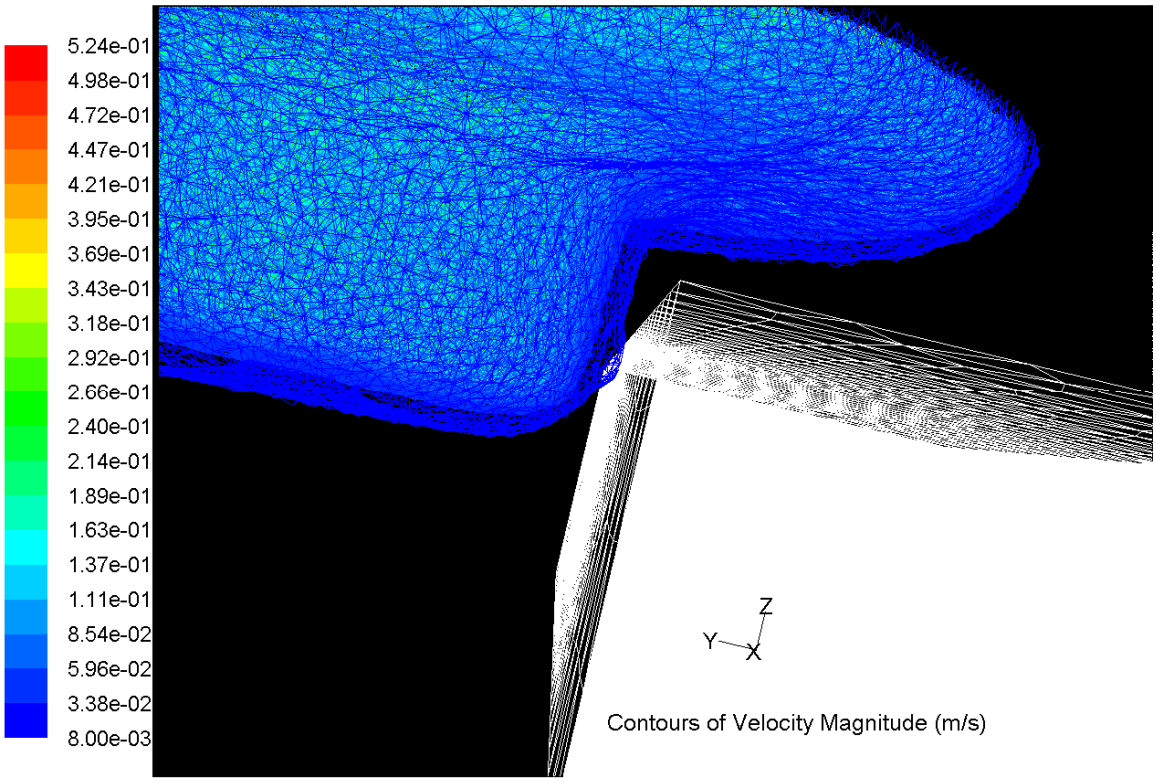

Figure 65: Contour of velocity magnitude for 0.05" retreating side offset case.

References:

[1] P. A. Fleming, D. H. Lammlein, G. E. Cook, D. M. Wilkes, A. M. Strauss, D. DeLapp and D. A. Hartman: Through the tool tracking for friction stir welding. US Patent May 30, 2008. Serial No. 12/130,622.

[2] Paul A. Fleming, David H. Lammlein, D. M. Wilkes, George E. Cook, Alvin M. Strauss, David R. DeLapp, Daniel A. Hartman. "Misalignment detection and enabling of seam tracking for friction stir welding." *Science and Technology of Welding and Joining*. Ref# 0209522-US0, submitted July 2008.

[3] Sheppard T and Wright D: Determination of flow stress: Part 1 constitutive equation for aluminum alloys at elevated temperatures; *Met. Technol*., **6**, 215-223, June 1979.

[4] Sellars CM, Tegart WJM; Hot workability; *Int.* Metall. *Rev*., 1972, **17**, 1-24

[5] Simar A, Pardoen T, de Meester B; Influence of friction stir welding parameters on the power input and temperature distribution on friction stir welding; *Proc. of the 5th International Symposium on Friction Stir Welding*, 2004.

[6] Simar A, Pardoen T, de Meester B; Effect of rotational material flow on temperature distribution in friction stir welds; *Science and Technology of Welding and Joining*, Vol.12, No.4, p324, 2007.

[7] Santiago DH, Lombera G, Santiago U; Numerical modeling of welded joints by the friction stir welding process; *Materials Research*, Vol.7, Num.4, p569, 2004.

[8] Pew JW, Nelson TW, Sorensen CD; Torque based weld power model for friction stir welding; *Science and Technology of Welding and Joining*,Vol.12, Num.4, p341, 2007.
[9] Colegrove P, Painter M, Graham D, Miller T; 3 Dimensional flow and thermal modelling of the friction stir welding process; *Proc. of the 2nd International Symposium on Friction Stir Welding,* 2001.
[10] Linder K, Khandahar Z, Khan J, Tang W, Reynolds AP; Rationalization of hardness distribution in alloy 7050 friction stir welds based on weld energy, weld power, and time/temperature history; *Proc. of the 6th International Symposium on Friction Stir Welding*, 2007.
[11] Dickerson TL, Shi Q-Y, Shercliff HR; Heat flow into friction stir welding tools; *Proc. of the 4th International Symposium on Friction Stir Welding*, 2003.
[12] Nunes A.C., Bernstien E.L., McClure J.C.: A rotating plug model for friction stir welding; *Proc. of the 81st American Welding Society Annual Convention*, Chicago, IL, 2000.
[13] St-Georges L, Dasylva-Raymond V, Kiss LI, Perron AL; Prediction of optimal parameters of friction stir welding: *Proc. of the 6th International Symposium on Friction Stir Welding*, 2007.
[14] Liechty B.C., Webb B.W., Modeling the frictional boundary conditions in friction stir welding: *International Journal of Machine Tools & Manufacture*, 2008, doi:10.1016/j.ijmachtools.2008.04.005
[15] Chao Y., Qi X., Heat Transfer in FSW: Experimental and Numerical Studies; *Journal of Manufacturing Science and Engineering*, February 2003, Vol. 125, 145
[16] R. Nandan, G. G. Roy and T. DebRoy, Numerical Simulation of Three Dimensional Heat Transfer and Plastic Flow during Friction Stir Welding of Aluminum Alloys, *Metallurgical and Materials Transactions* A, 2006, vol. 37A, pp. 1247-1259
[17] Fourment L., Guerdoux S., Numerical Simulation of the Friction Stir Welding Process using Lagrangian, Eulerian and ALE Approaches. *Proceedings of the 5th International Friction Stir Welding Symposium*, TWI, Metz, France (2004)

CHAPTER III

THE APPLICATION OF SHOULDERLESS CONICAL TOOLS IN FRICTION STIR WELDING: AN EXPERIMENTAL AND THEORETICAL STUDY

Lammlein, D. H., DeLapp, D.R., Fleming, P.A., Strauss, A.M., and Cook, G.E., "The application of shoulderless conical tools in friction stir welding: An experimental and theoretical study," Materials and Design, 30 (2009), 4012-4022.

Abstract

A friction stir welding (FSW) tool geometry, consisting of a shoulderless conical probe, is investigated for application to closed contour welding, variable thickness welding, and open loop control welding. By use of a tapered retraction procedure and a ramped rotational velocity, a conical tool may facilitate material disengagement with minimal surface defects in applications that do not permit weld termination defects (e.g. pipes, pressure vessels, fuselages, nosecones). In addition, because the vertical position of the tool relative to the material surface is less critical with a conical tool than with other tool designs, it can be used in an open-loop fashion (i.e. without process force feedback control) and on materials whose thicknesses are highly variable. The use of a conical probe without a shoulder is not documented in the literature, and the aim of this work is to establish the conditions for mechanically sound welds. Effective tool geometries and process variables are found via experimental analysis. Thermal, tensile, macrosection, and process force data are presented along with a computational fluid dynamics (CFD) process model. It is concluded that this type of tooling is capable of producing acceptable welds when applied to butted aluminum plates and that similar methods would likely be effective in the applications described previously.

Introduction

The conical tool design is potentially a simple solution to the problem of closure in friction stir welding (FSW). In FSW, a defect is left at the removal site of the tool and this defect is unacceptable in applications where the entire workpiece is critical. According to Trapp, Fischer, and Bernath of the Edison Welding Institute(EWI) in U.S. Patent #7234626, the appropriate conical inclusive angle can contain weld material regardless of cone penetration depth and during tapered retraction [1,2]. The conical tool (Figure 66) in conjunction with the tapered retraction procedure and spindle velocity ramping could therefore be used to weld closed contours such as cylinders and spheres (e.g. pipes, pressure vessels, fuselages, nosecones) without leaving a defect or hole where the tool exits the material. The conical tool design is especially attractive because it is an easily manufacturable and durable design. The conical tool is potentially a simple and elegant solution to the seemingly complex closure welding problem in FSW. A current solution to the retraction problem that NASA and a number of manufacturers have adopted is an exceedingly complex, hydraulically actuated retractable pin tool apparatus [3]. The conical tool can be used for in-process adjustment of penetration depth for application to variable thickness welds. Additionally, the use of a conical tool does not require force control as with a conventional friction stir weld tool where appropriate shoulder contact with the material is critical. These welds can be performed in an open-loop manner without process force feedback based adjustment of the tool's vertical position. The conical tool can passively accommodate variation in the height of the material surface relative to the tool, due to material thickness variations in linear welds or system eccentricities in rotary welds.

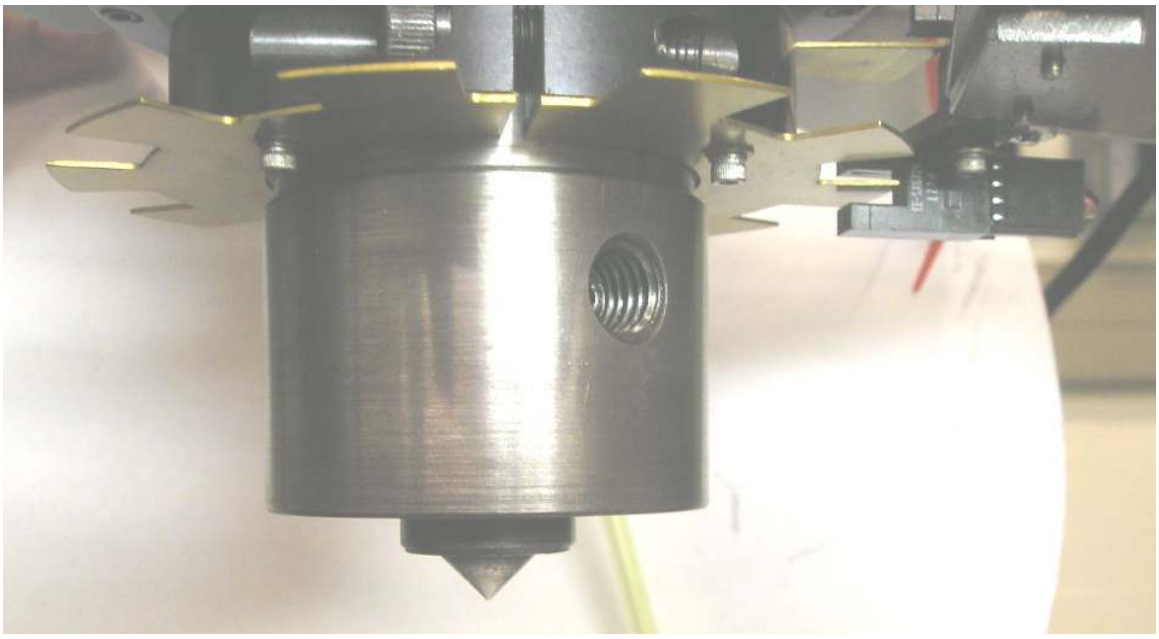

Figure 66: A shoulder-less, conical tool (90º inclusive angle) used in the experiment

As no published literature exists on the design and application of shoulderless conical tools, the primary aim of this work is to find a tool geometry and weld parameter set that produces mechanically acceptable welds. An experimental weld matrix has been performed on 1/8”(0.32cm) thick, butted 6061 alloy aluminum plates. A suitable inclusive angle for FSW was found by testing a range of tool angles (60º, 80º, 90º, and 120º). Suitable weld parameters were established and a 36 weld matrix was performed with the 80º and 90º tools. For these welds, characteristic weld forces were determined via a dynamometer, achievable weld strengths via tensile testing, weld structure and appearance via etching of macrosections, and approximate shoulder edge temperature via thermal camera images. To avoid both collision of the tool with the backing anvil and weld root defect formation, a penetration ligament of 0.01”(0.25mm) was selected for the experiment.

Welds made at a low spindle head angle (0º-2º) resulted in unacceptable force oscillations in the XY plane. Figure 67 shows the XY plane oscillations in the dynamometer force data for a particular weld at 0° spindle head angle. The experiment was therefore conducted at a head angle off 4º where the problem did not arise. The oscillations at low spindle head angles can be attributed to physical tool deflection and a lack of stiffness in the experimental setup. This problem is not perceptible with

conventional tooling and it must therefore be concluded that the conical tool geometry exacerbates XY plane tool deflection and induces force oscillations. The lack of the stabilizing influence of a horizontal shoulder on the material surface is believed to contribute to this deflection. In addition, as compared to conventional tooling, the dynamometer data showed axial (Z) forces (Figure 68) that were lower in magnitude relative to the XY plane forces (Figure 69). The result of this periodic tool deflection was a coarse surface banding as opposed to a fine surface finish. The problem is alleviated at a 4° spindle head angle.

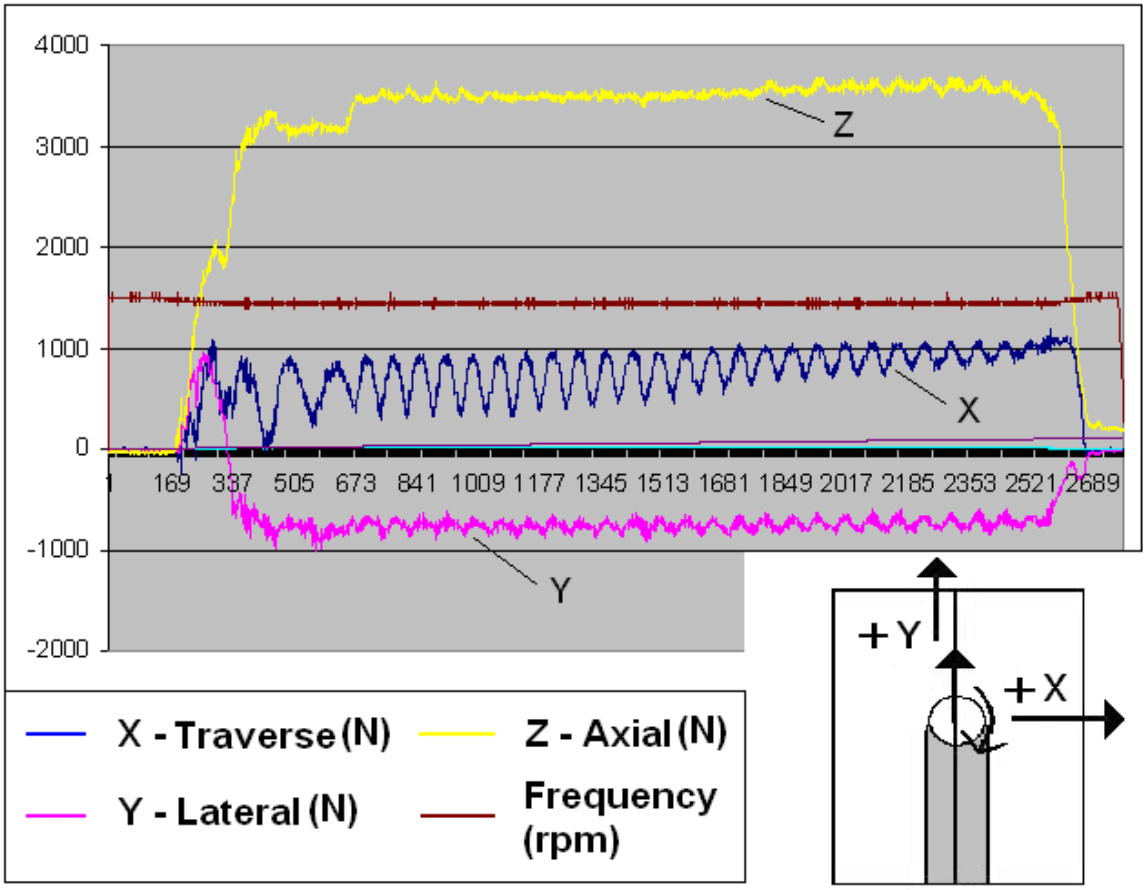

Figure 67: XY plane force oscillations were typically present at low spindle head angles with conical welds, presumably due to the lack a horizontal, stabilizing shoulder. The experiment was therefore performed at a 4° angle where this problem did not exist.

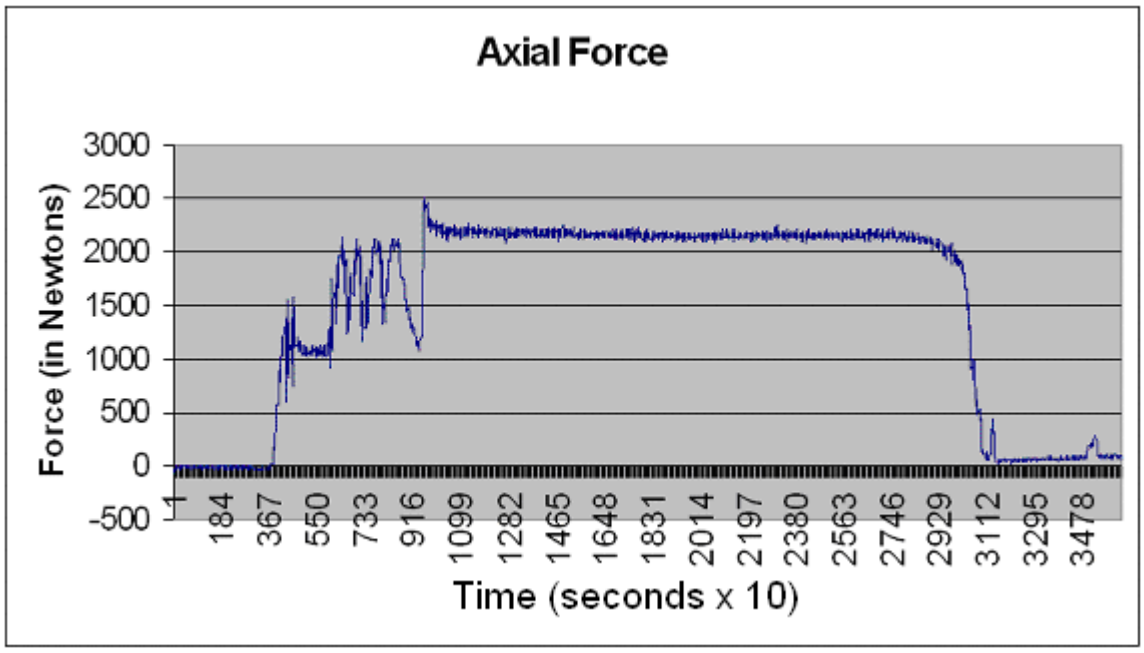

Figure 68: Typical axial(Z-axis) force data.

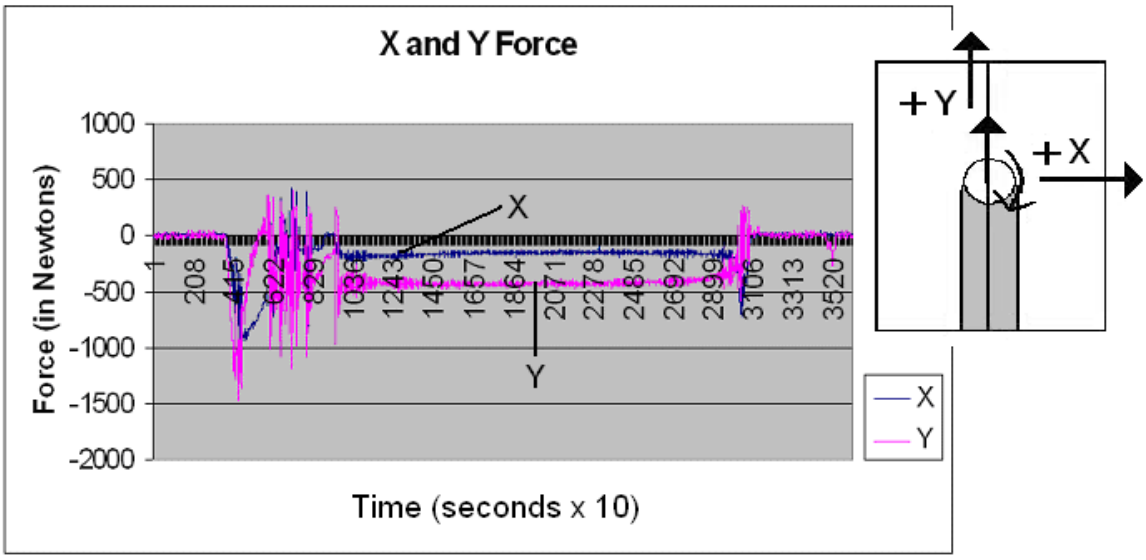

Figure 69: Typical in plane force data.

Conical Inclusive Angle Tests

The 80º and 90º conical tools were selected for the experimental weld matrix because they produced the highest quality welds based on surface appearance. Conical welds typically produced advancing side flash and a trough-like surface defect on the

retreating side (Figure 70). These defects were reduced to acceptable levels using the 80º and 90º conical inclusive angle tools. Macrosections were made for each weld using Boss's reagent for etching. A complete table of macrosections is included in Figure 71 thru Figure 78. Despite a similar superficial appearance and similar weld macrosections, welds made with the 80º tool were vastly inferior in strength (Figure 79 & Figure 80) to those made with the 90º tool at all parameter values and for all runs. Welds made with the 80º tool do however show a pronounced, crack-like defect extending from the root of the weld to the weld nugget center. This defect is less pronounced or absent in the 90º weld macrosections. Typical process forces for this tool type are lower in magnitude to those of a similar conventional weld (Figures 8a-h). The ratio of in-plane force to axial force (i.e. $\sqrt{(x^2 + y^2)} / z$) is however higher for this process which is believed to increase vibration and process instability.

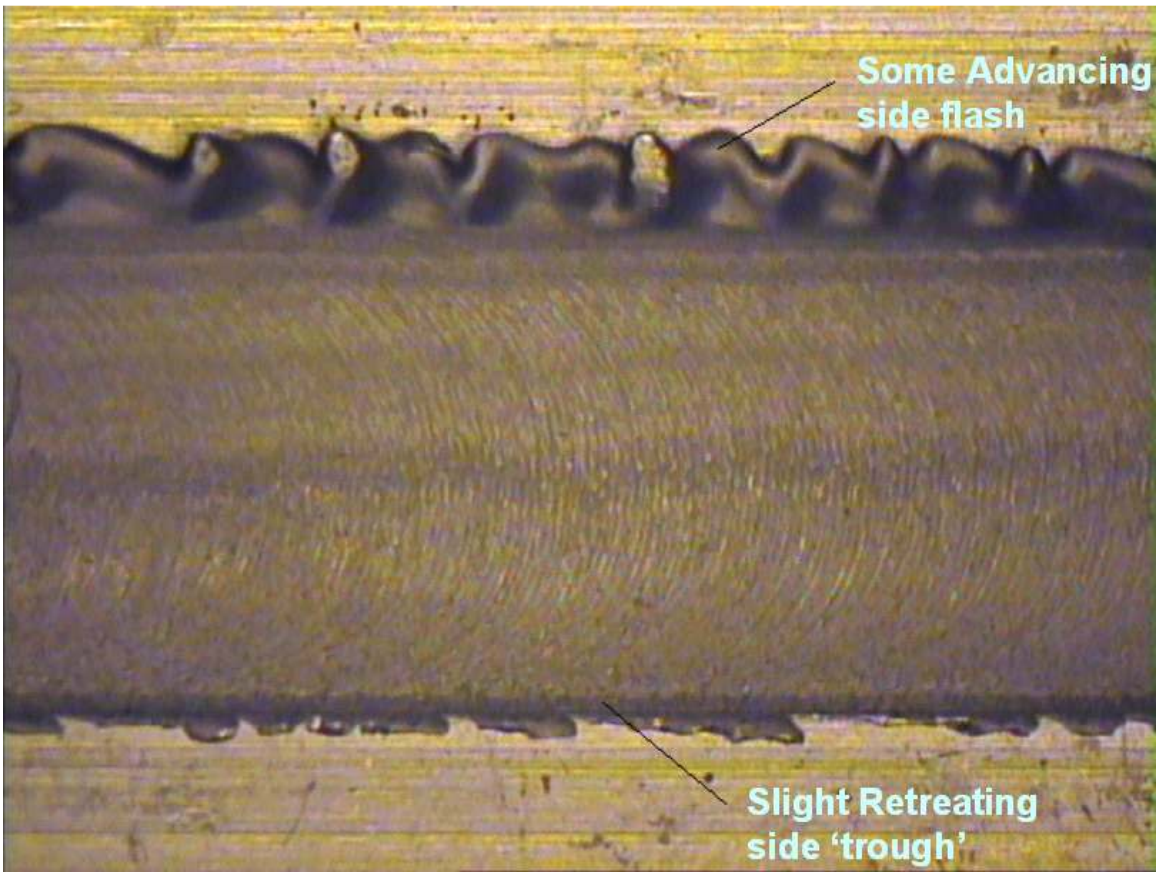

Figure 70: Typical surface appearance for 90° conical tool welds on 1/8" thick butted 6061 alloy aluminum plates. Typical conical surface defects are pointed out.

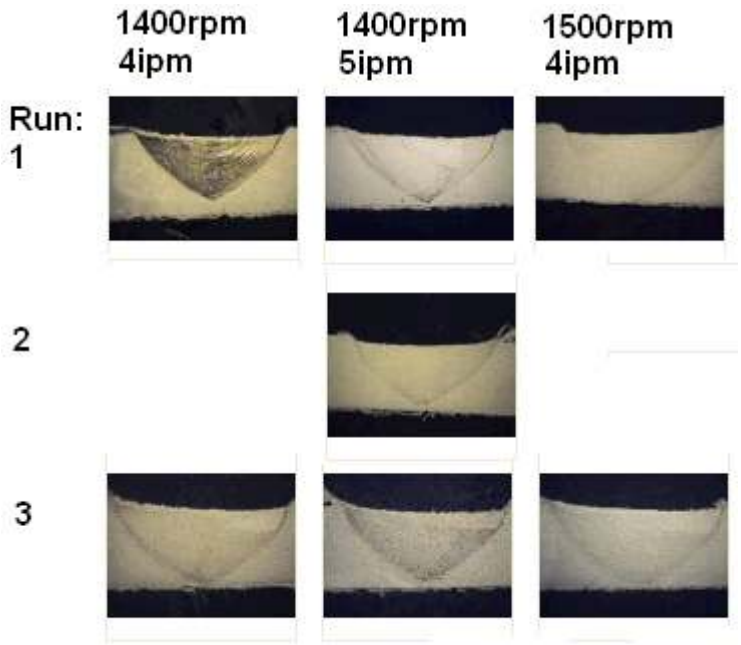

Figure 71: 90° conical tool macrosections. Some 90°,Run2 welds were not macrosectioned.

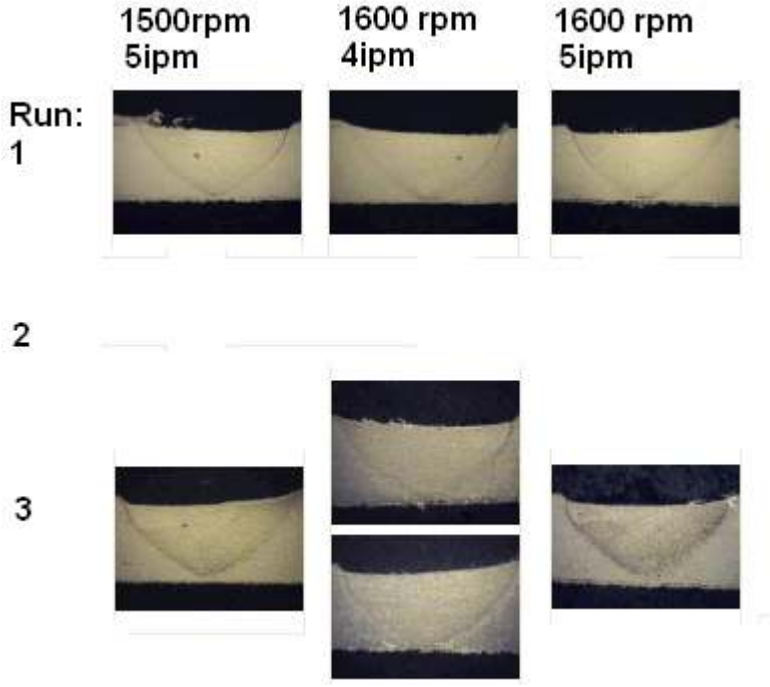

Figure 72: 90° conical tool macrosections. Note: Run 3, 1600rpm, 4ipm, 90° was macrosectioned twice.

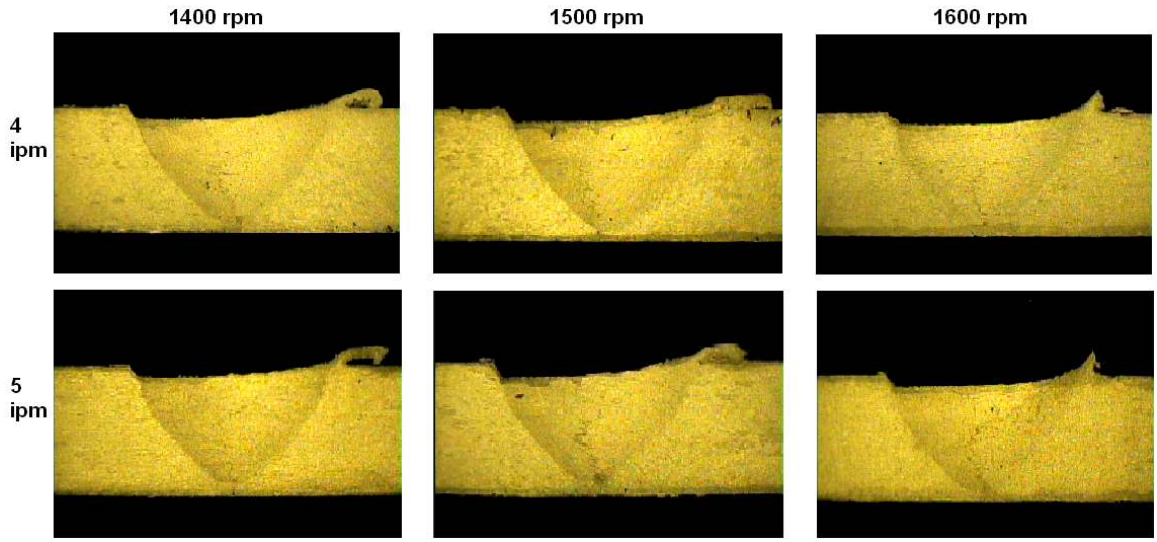

Figure 73: Run 1, 80° conical tool macrosections

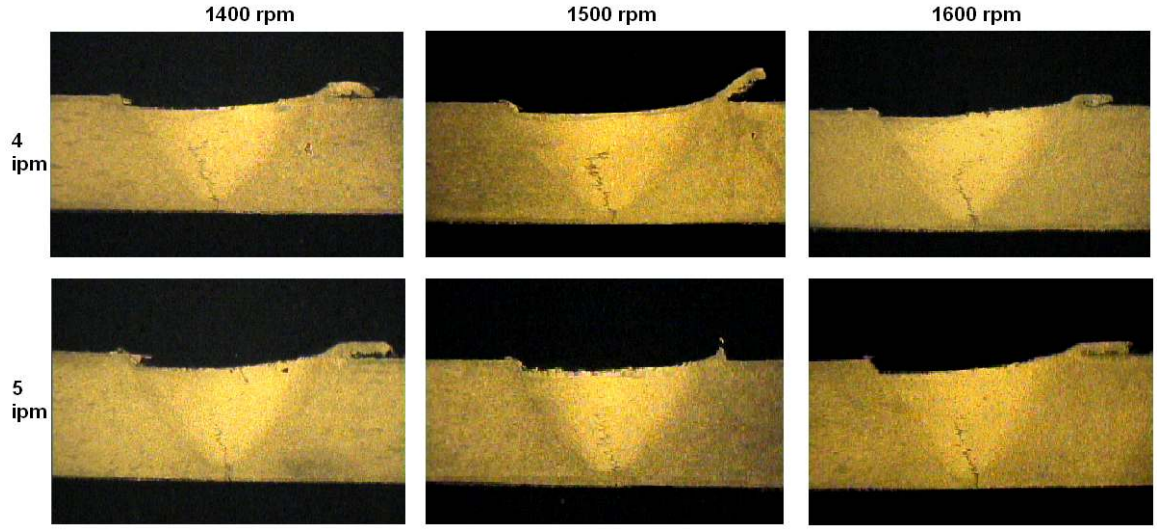

Figure 74: Run 2, 80° conical tool macrosections

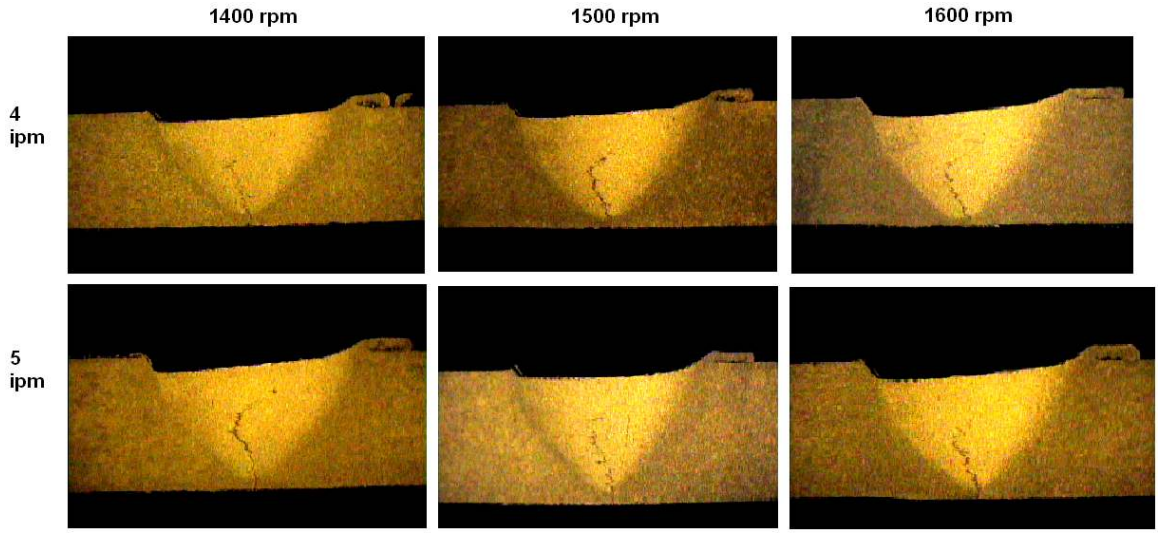

Figure 75: Run 3, 80° conical tool macrosections

Figure 76: Macrosection of the strongest conical weld (90°,1600rpm, 4ipm, Run#1). A minimal penetration ligament is crucial to weld strength. Failure in the tensile coupon occurred along the retreating (right) side weld nugget boundary.

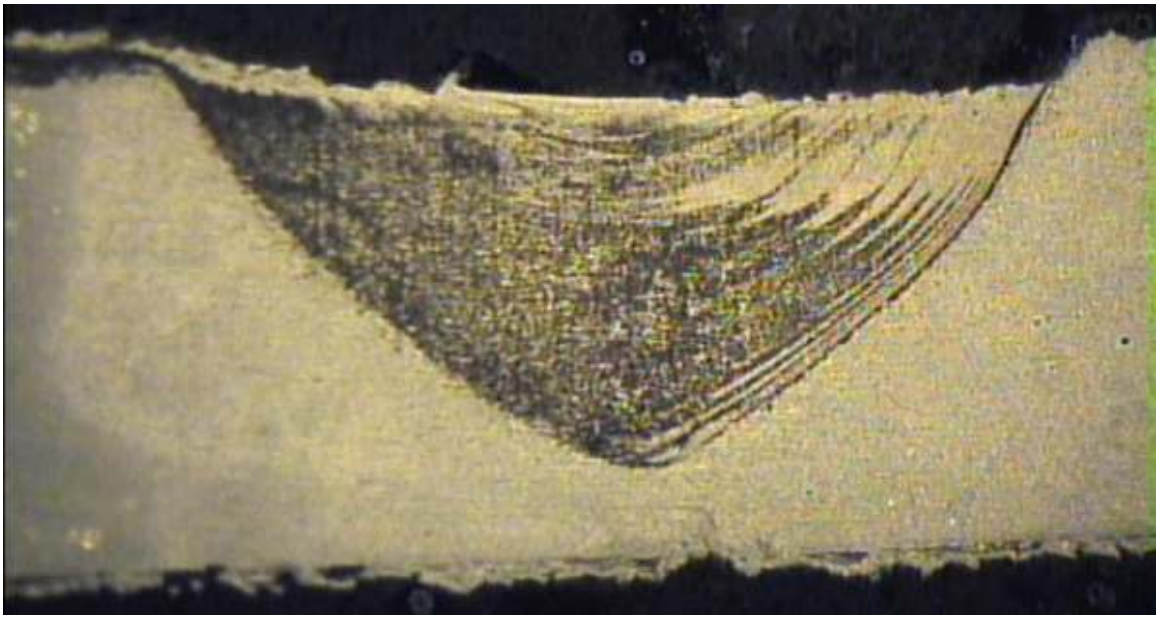

Figure 77: Macrosection of the weakest 90° conical weld(90°,1400rpm, 4ipm, Run#1). Failure occurred at the jointline and along the retreating side weld nugget boundary. A significant lack of penetration (weld root) defect can be seen in this weld indicating a slight error in the automated zeroing process for this particular weld. Three welds at each parameter set were performed to distinguish such outliers.

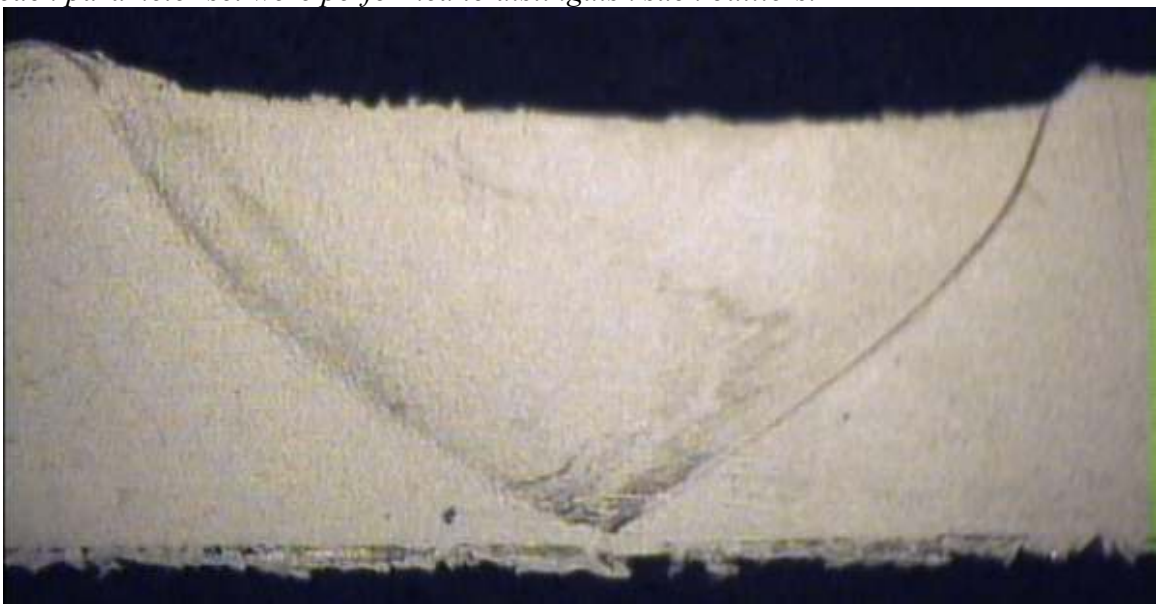

Figure 78: A particularly revealing macrosection (90°,1400rpm, 5ipm, Run#1). A jointline remnant can be seen curving through the weld nugget center. In addition, the lack of consolidation near the cone tip which is typical of a cone weld can be seen clearly here. The lack of sufficient probe surface area, heating, and pressure at the cone tip result in a lack of consolidation there.

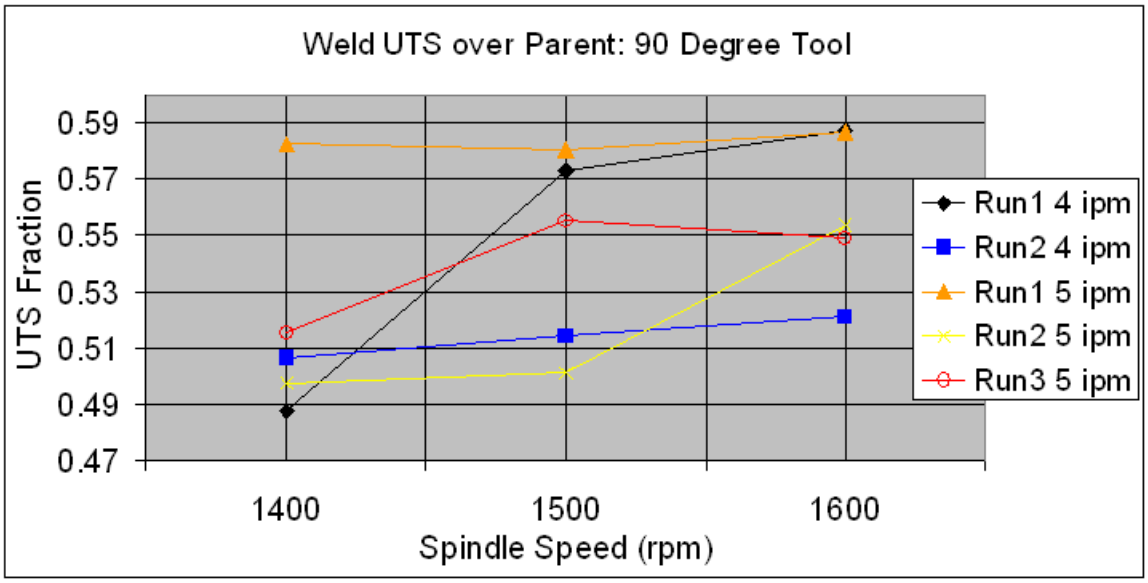

Figure 79: (90° tool) Ultimate tensile strength of weld specimen over that of the parent plotted against spindle speed in rpm. Three welds were performed at each parameter set (ipm,rpm).

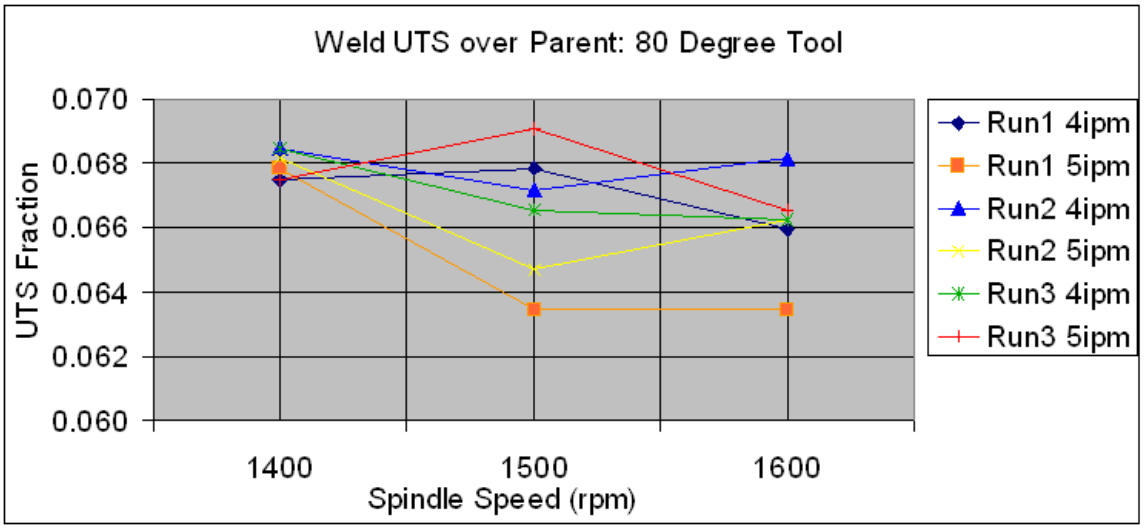

Figure 80: (80° tool) Ultimate tensile strength of weld specimen over that of the parent plotted against spindle speed in rpm. Three welds were performed at each parameter set (ipm,rpm).

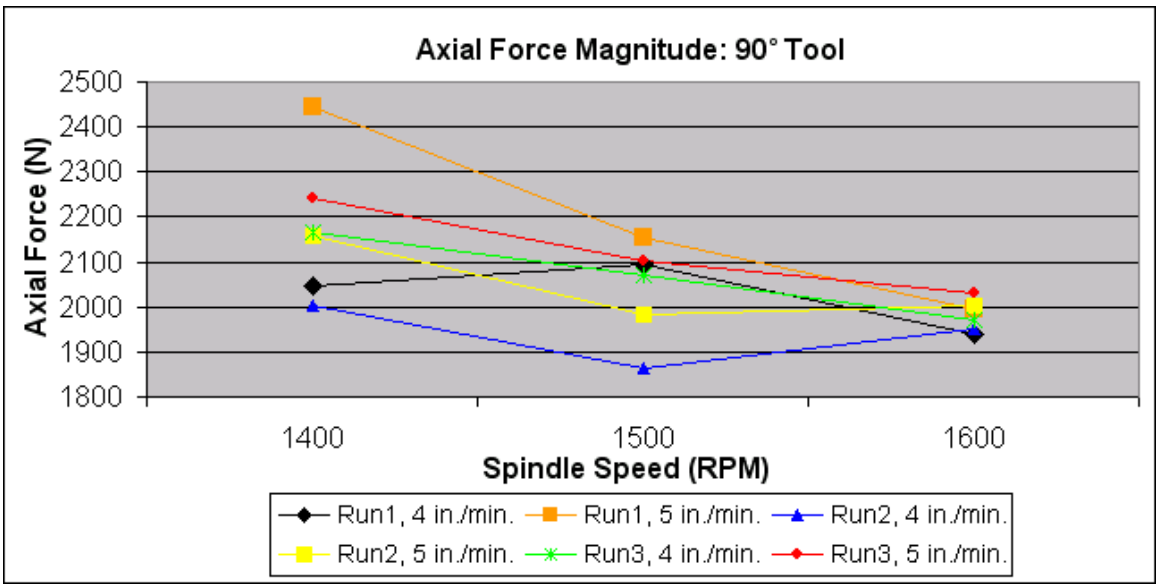

Figure 81: (90º tool) Axial force magnitude for each weld plotted against spindle speed in rpm. Three welds were performed at each parameter set (ipm, rpm). 8000 N is typical for a similar conventional weld (3/4in. dia. shoulder, ½"-20 pin). Conical welds produce significantly lower axial force.

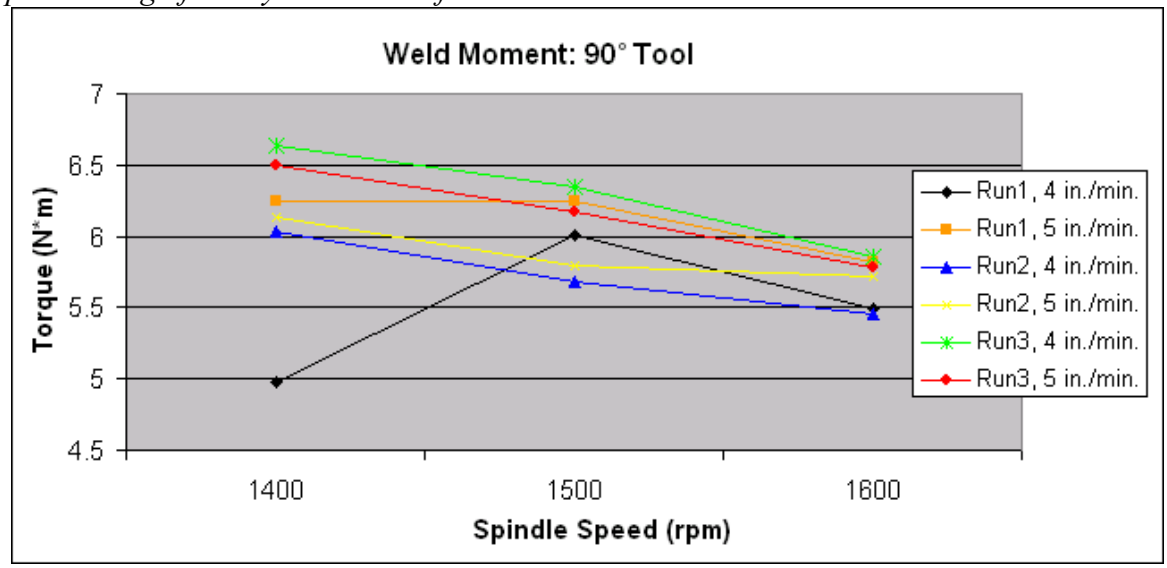

Figure 82: (90º tool) Weld moment for each weld plotted against spindle speed in rpm. Three welds were performed at each parameter set (ipm, rpm.) 18 N·m is typical for a similar conventional weld (3/4in. dia. shoulder, ½"-20 pin). Conical welds produce significantly lower weld moment.

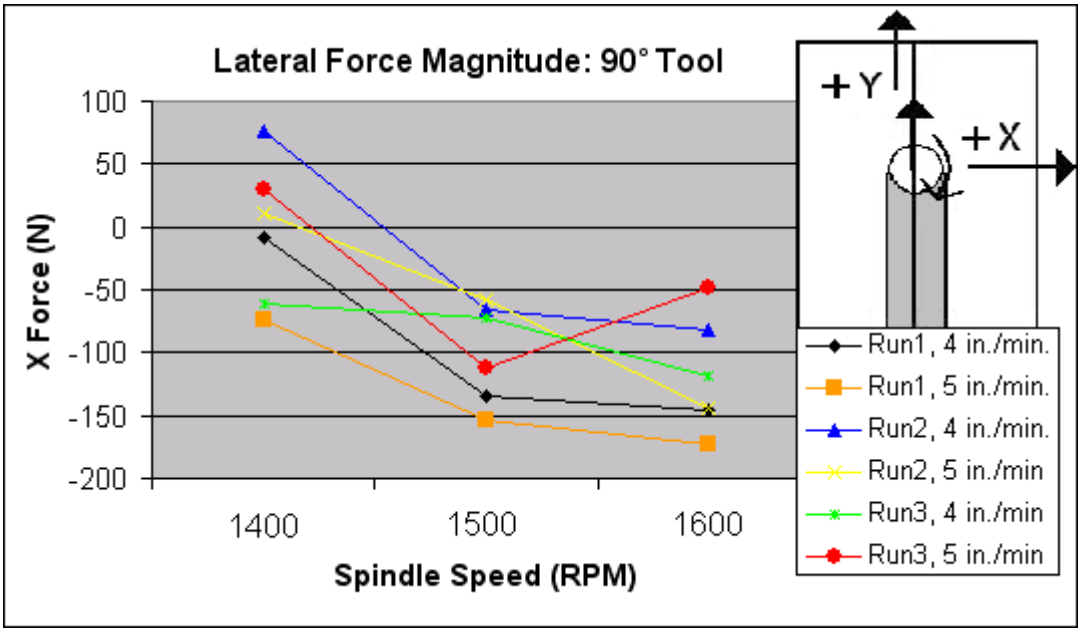

Figure 83: (90° tool) Lateral force magnitude for each weld plotted against spindle speed in rpm. Three welds were performed at each parameter set (ipm, rpm). +2500 N Y is typical for a similar conventional weld (3/4in. dia. shoulder, ½"-20 pin). Conical welds produce significantly lower lateral force(change in sign due to clockwise vs. counter-clockwise rotation).

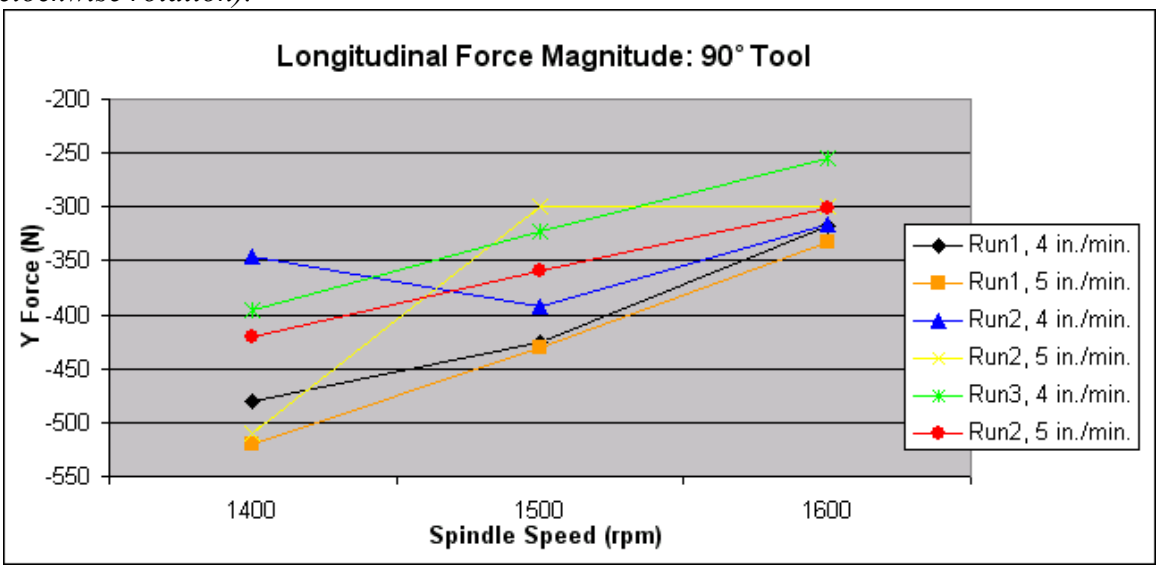

Figure 84: (90° tool) Longitudinal force magnitude for each weld plotted against spindle speed in rpm. Three welds were performed at each parameter set (ipm, rpm). +2500N X is typical for a similar conventional weld (3/4in. dia. shoulder, ½"-20 pin). Conical welds produce significantly lower longitudinal force. Sign for a particular weld is dependent to clockwise vs. counter-clockwise rotation. All conical welds in this experiment were made with clockwise rotation.

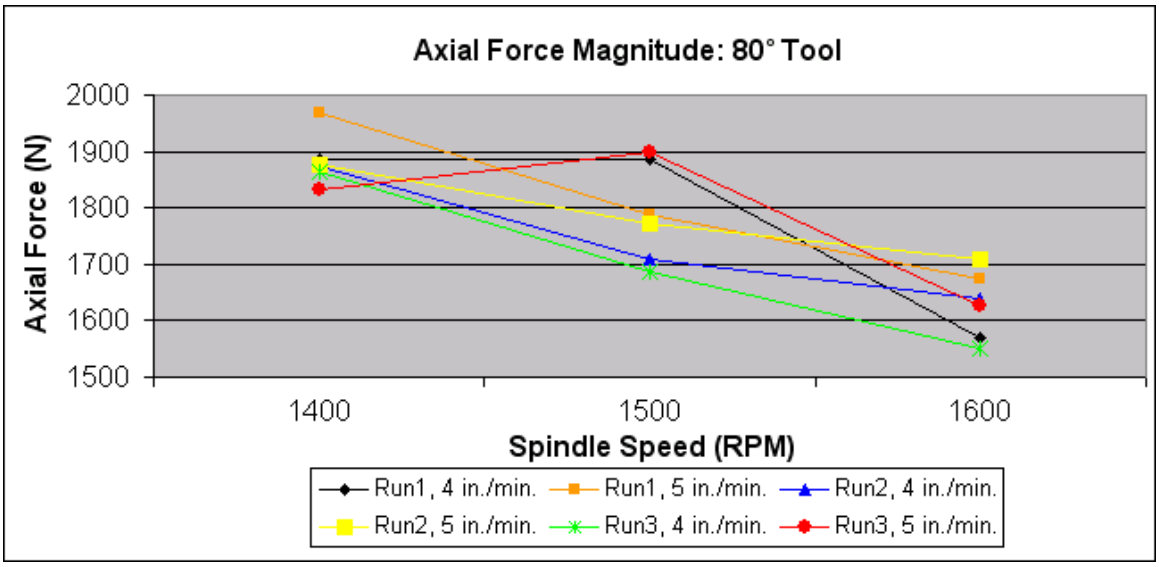

Figure 85: (80° tool) Axial force magnitude for each weld plotted against spindle speed in rpm.

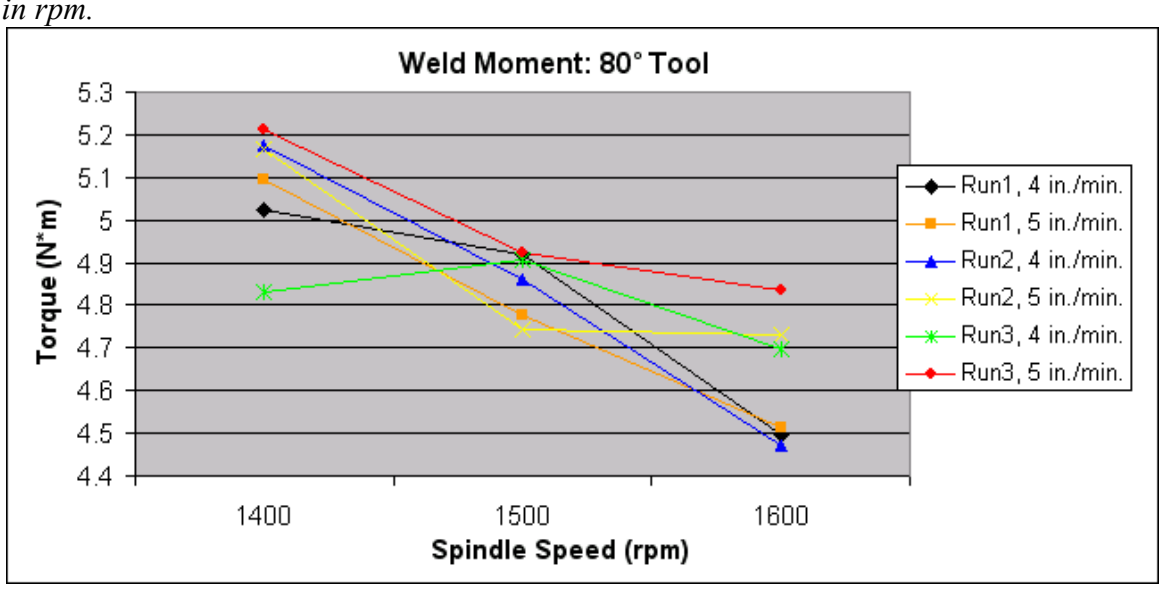

Figure 86: (80° tool) Weld moment for each weld plotted against spindle speed in rpm.

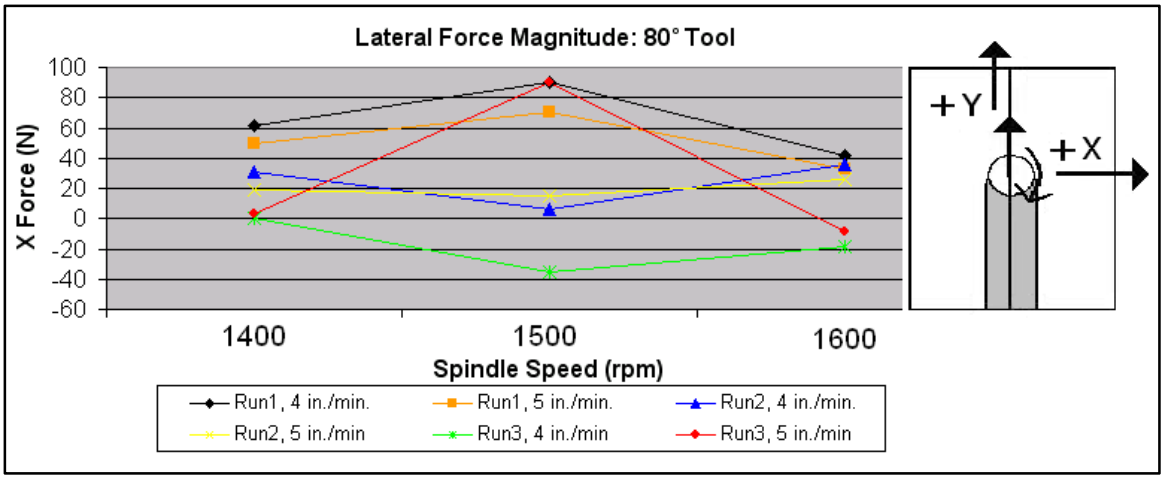

Figure 87: (80º tool) Lateral force magnitude for each weld plotted against spindle speed in rpm.

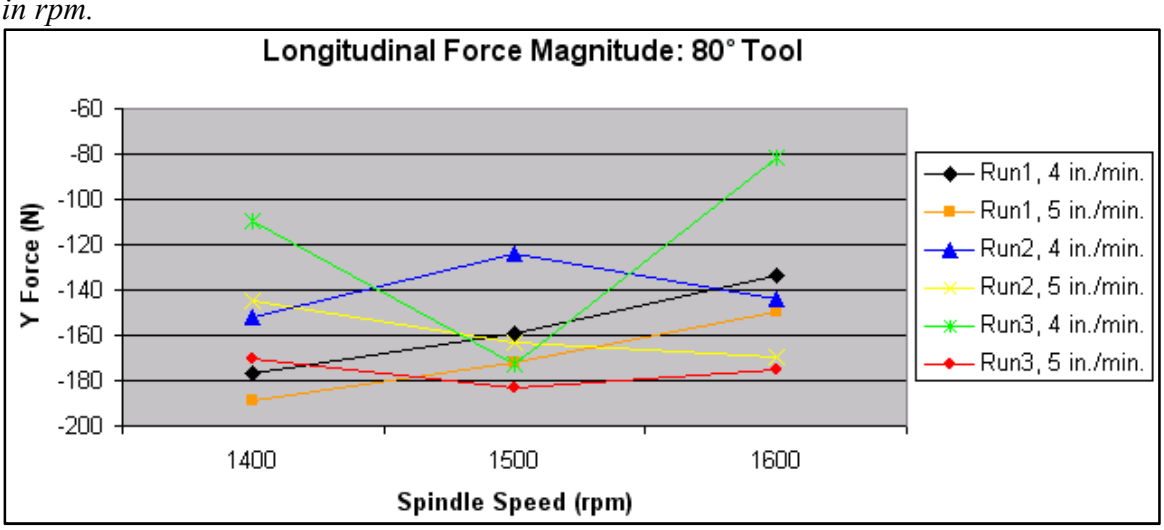

Figure 88: (80º tool) Longitudinal force magnitude for each weld plotted against spindle speed in rpm.

The thermal camera was calibrated to the emissivity of the conical tool surface. The weld temperatures listed in the charts below in Figure 89 and Figure 90 were calculated by taking the average temperature from a rectangular area on the tool surface just above the weld material surface at increments in time. Ten images at one second intervals were used from the thermal camera video and those were then averaged to produce an approximation of the temperature on the cone surface during the steady-state portion of the weld. It should be noted that the temperature continued to creep upward even during the steady state period. In addition, welds made later in the day (when the

machine, fixturing, and backing plate were warm) were noticeably warmer (as much as 20º C).

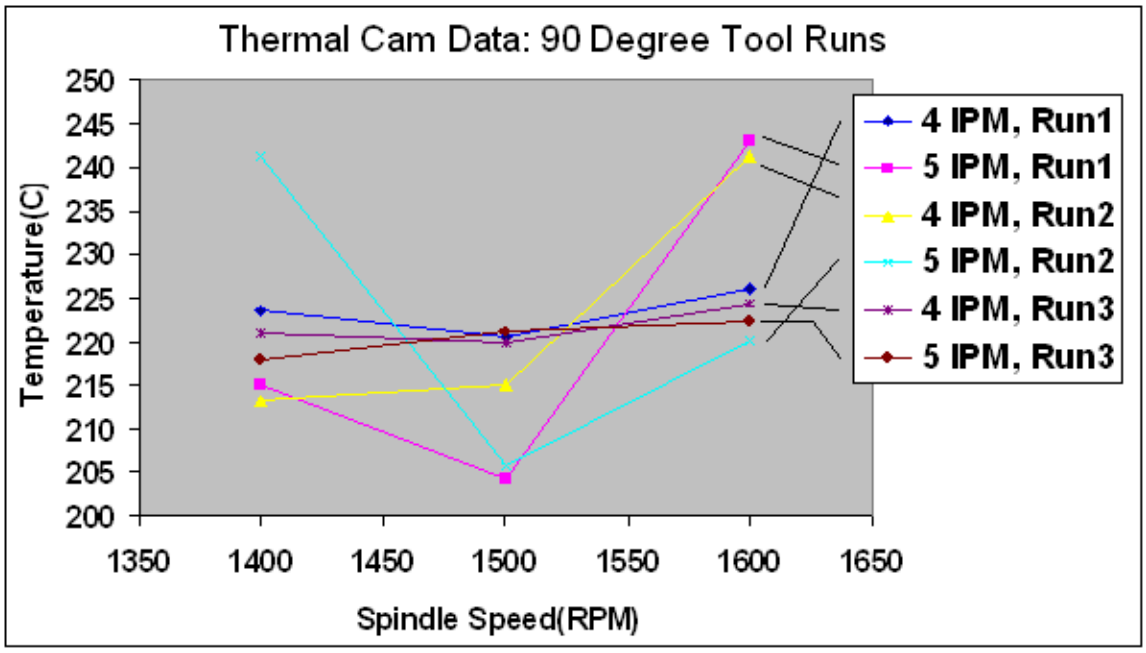

Figure 89: Thermal camera data for 90º tool runs.

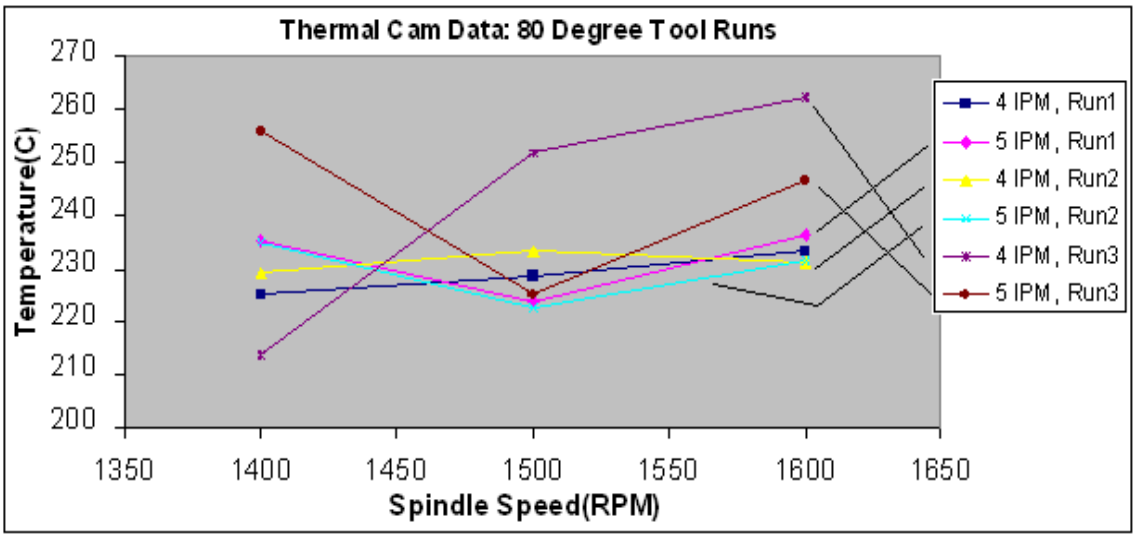

Figure 90: Thermal camera data for 80º tool runs.

CFD Model of Conical Tool FSW

The Eulerian, finite volume, CFD solver, Ansys FLUENT was used with the implicit formulation. The weld material viscosity function was set by user-defined function and defined according to the visco-plastic model of Sheppard and Wright [4] as modified from the initial formulation proposed by Sellars and Tegart [5] Flow stress is defined as an inverse hyperbolic sine function of the local strain rate magnitude and absolute temperature in this following commonly used form:

$$Z = \dot{\varepsilon} \exp(\frac{Q}{RT}) = A(\sin \alpha\sigma_e)^n$$

or equivalently,

$$\sigma_e = \frac{1}{\alpha} \sinh^{-1}\left[\left(\frac{Z}{A}\right)^{\frac{1}{n}}\right] \qquad Z = \dot{\varepsilon} \exp\left(\frac{Q}{RT}\right)$$

where α, A, n are material constants (α = 0.045 (Mpa)-1, Q = 145 kJ mol^{-1}, A = 8.8632E6 s^{-1}, n = 3.55), σe is the equivalent steady state flow stress (Mpa), R the gas constant (R = 8.314 $mol^{-1}K^{-1}$), T the absolute temperature (K), Q is the activation energy (J mol^{-1}) and Z is the Zener-Hollomon parameter. The material constants used are determined using a hot compression test. The material viscosity is defined in the following manner:

$$\mu = \frac{\sigma_e}{3\dot{\varepsilon}}$$

The visco-plastic model is valid at temperatures reasonably below the metal's solidus temperature. As the material approaches the solidus temperature significant softening occurs.

The total heat input was calculated via the weld power method [6-14]:

$$P = \omega \cdot M$$

$$Q = P \cdot \beta$$

where P is the weld power (W), Q is the heat input to the tool and weld material (W), ω is the tool rotational speed (rad/s), M is the measured torque (N·m), and β is the fraction of mechanical work dissipated as heat into the tool shank and the weld. Chao et al. [15] arrive at a β value of approximately 0.8 under similar conditions using a boundary value approach and determine that approximately 5% of this dissipated heat is dissipated via the tool shank. Those ratios are found to be reasonable in the current study. The weld

moment was found experimentally by means of a rotating cutting force dynamometer and the spindle speed setting was verified by optical interrupters. This calculated total heat input was then applied in the model at the tool-material interface via a user-defined function which varies heat input over the tool surface according to the local tangential velocity magnitude. Heat input is therefore highest near the tool shoulder edge and zero at the center of the probe tip with the total heat input equal to the weld power. Heat input to the tool shank is determined by imposing the local weld material temperature at the interface onto the corresponding local tool surface element via a user-defined function. A variable slip shear condition was set at the weld interface [16]. The tool rotational velocity was set to 70% of the experimental parameter and a pure stick condition was used. This simple boundary condition was used because the actual relationship is unknown and unwarranted complexity is not desired in the model.

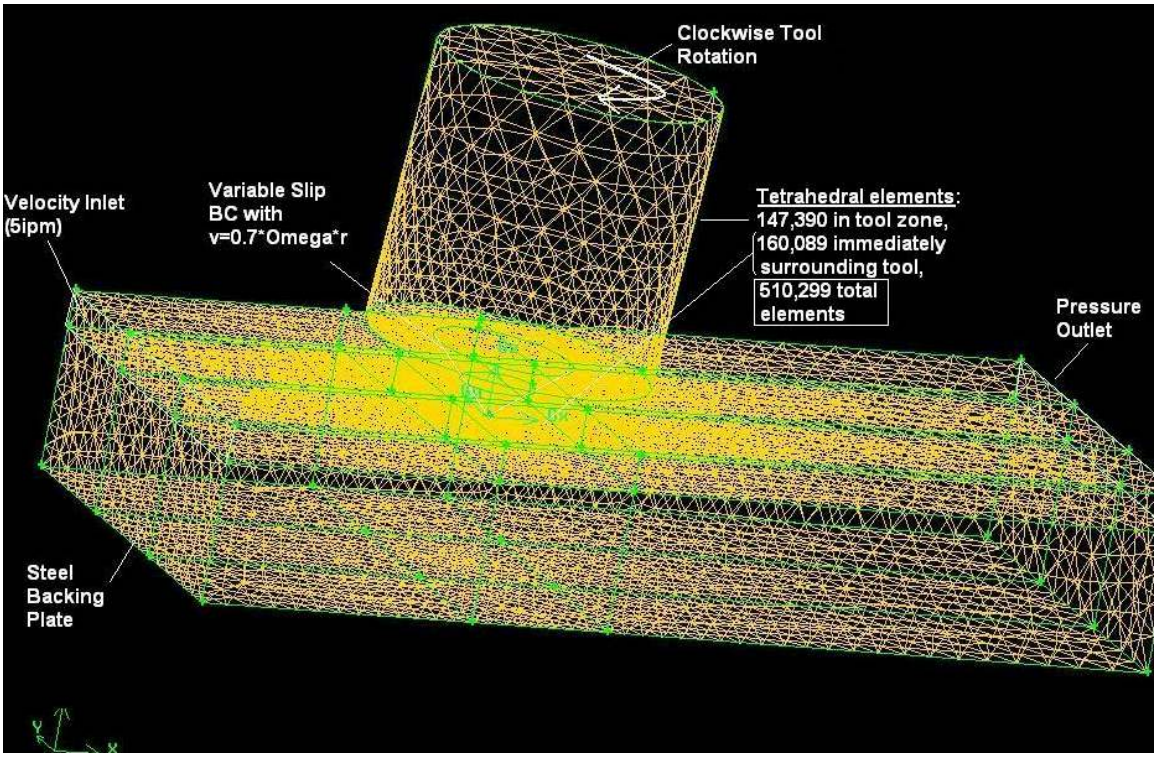

Figure 91 shows the CFD model geometry consisting of 510,299 tetrahedral elements. The tool traverse was imposed in the model by leaving the tool at the model origin and establishing a velocity inlet and pressure outlet for the aluminum plate.

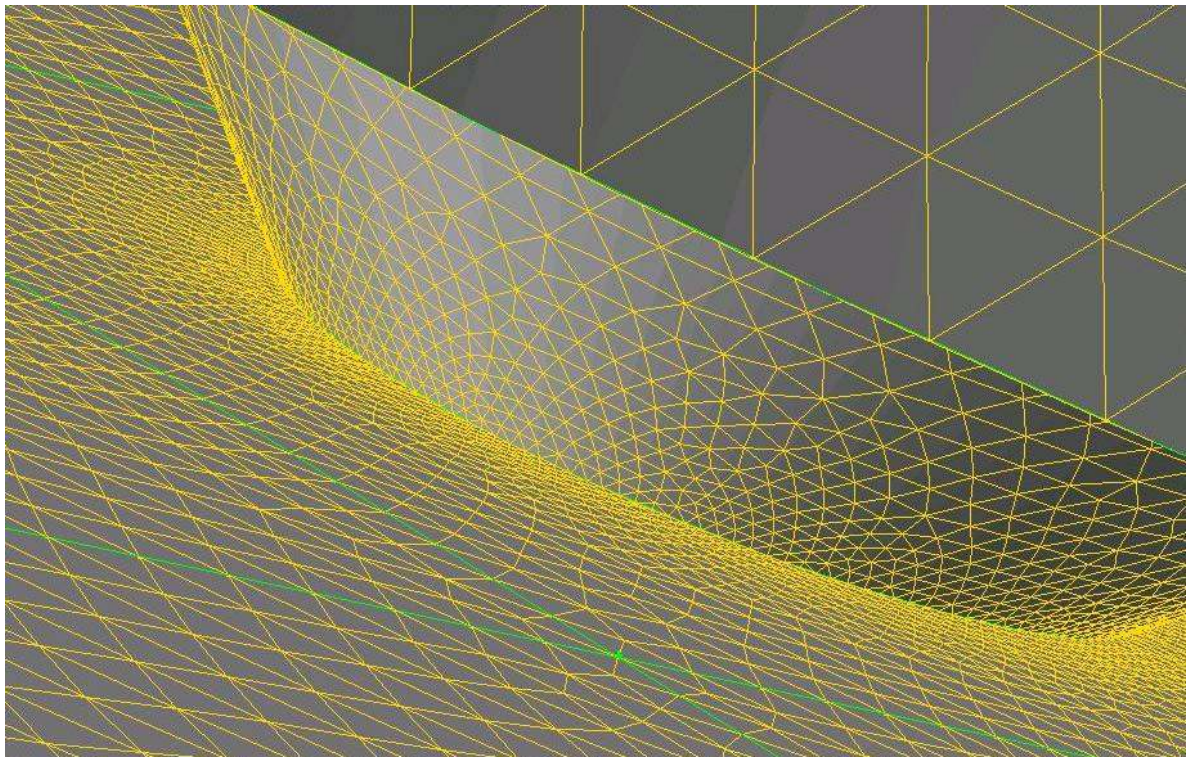

Figure 92 shows the increasing element refinement towards the weld interface.

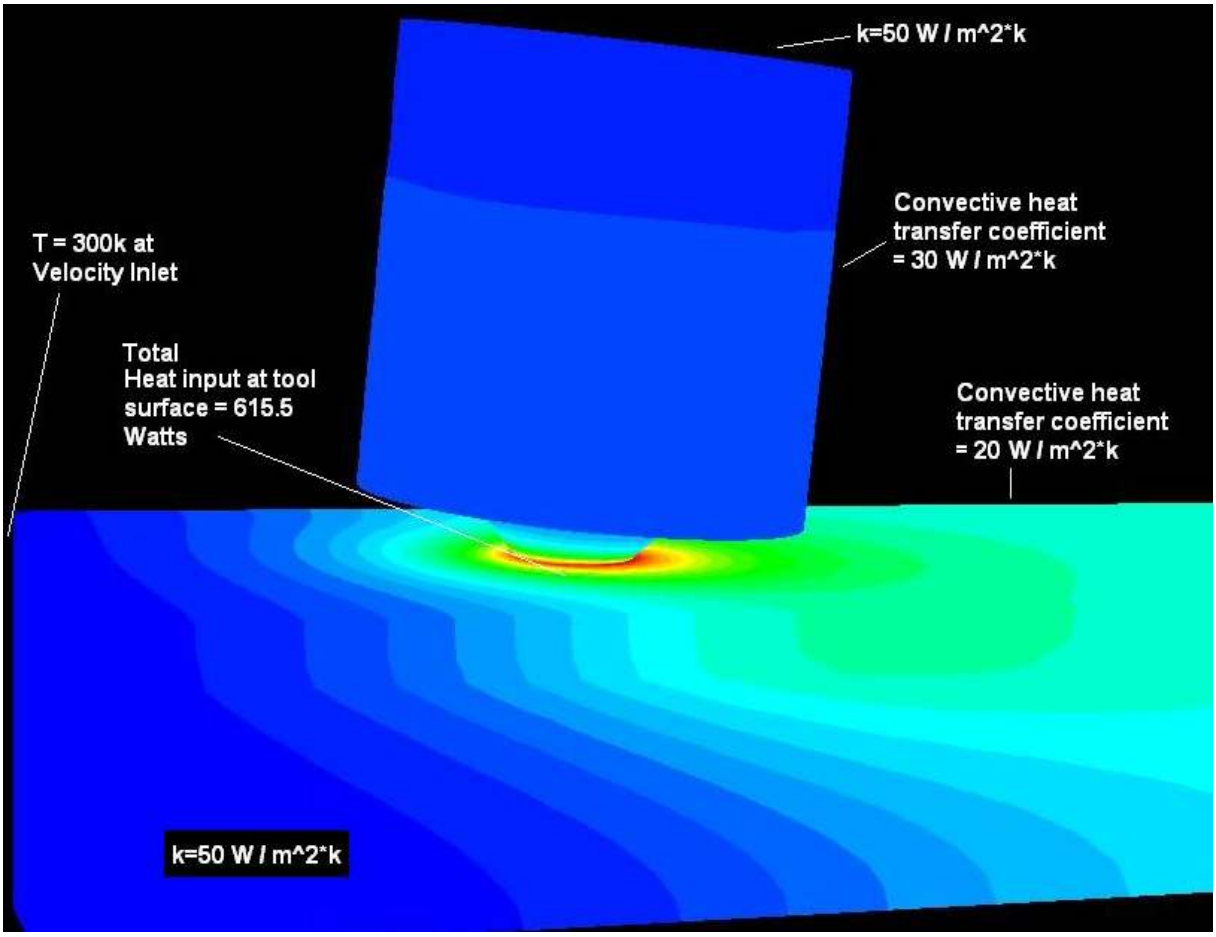

Figure 93 shows the thermal boundary conditions used in the model. The resulting temperature gradients can also be seen. Figure 94 shows the temperature gradients in the vicinity of the weld interface. Figure 95 is a lateral cross-section of the weld model showing contours of velocity magnitude in the material surrounding the tool. This type of graph outlines the thermomechanically affected zone (TMAZ). The model shows a lack of stirring at the tip of the conical probe. This agreed with experimental observations in the weld macrosections and in the manner of tensile coupon failure. Porosity, lack of consolidation, and crack-like defects can be seen in some of the macrosections, particularly those from weaker weld runs. In addition, the line of failure in tensile samples intersected the weld root in almost all cases, indicating weakness near the probe's tip as indicated by the lack of stirring seen in the CFD model.

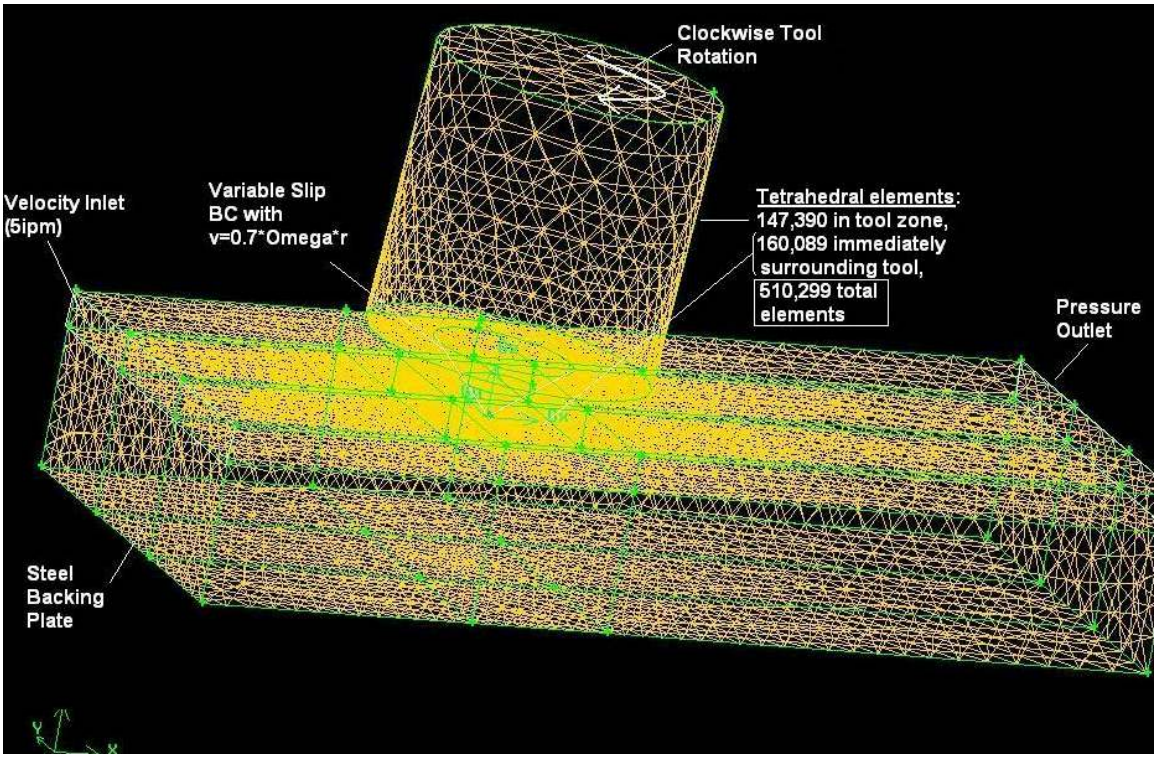

Figure 91: CFD model geometry consisting of 510,299 tetrahedral elements.

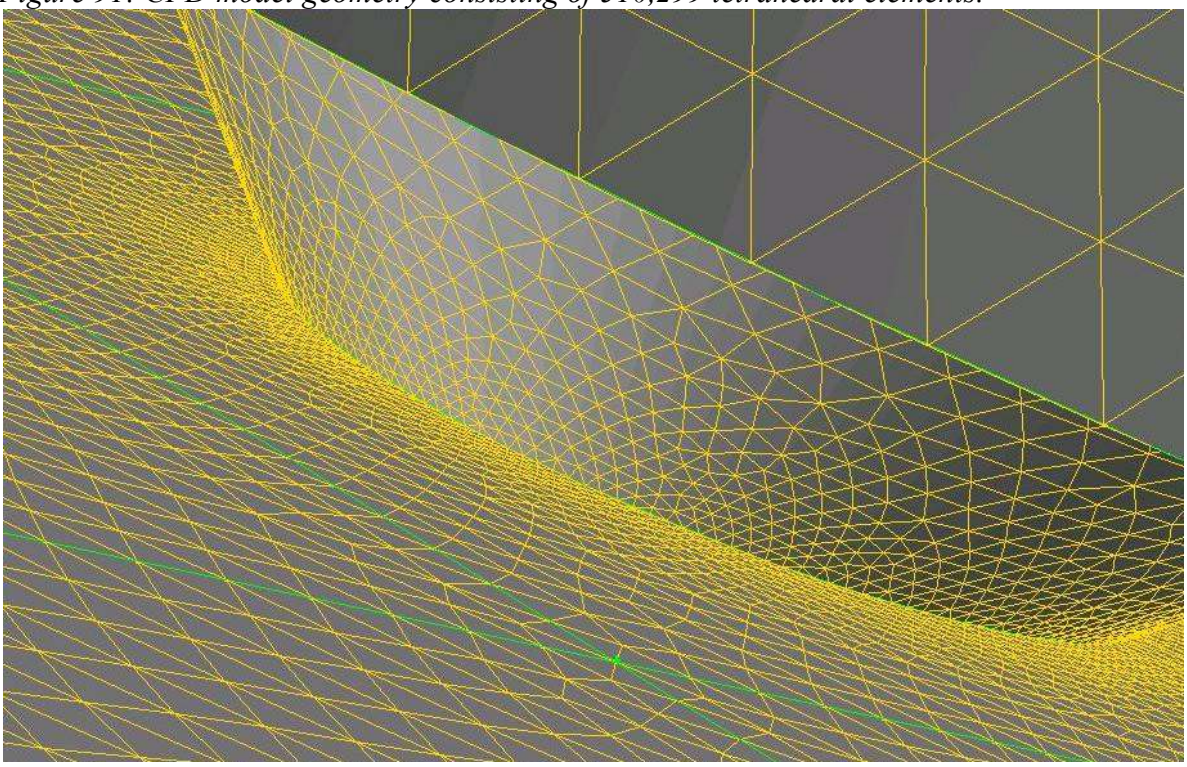

Figure 92: Increasing element refinement towards the weld interface.

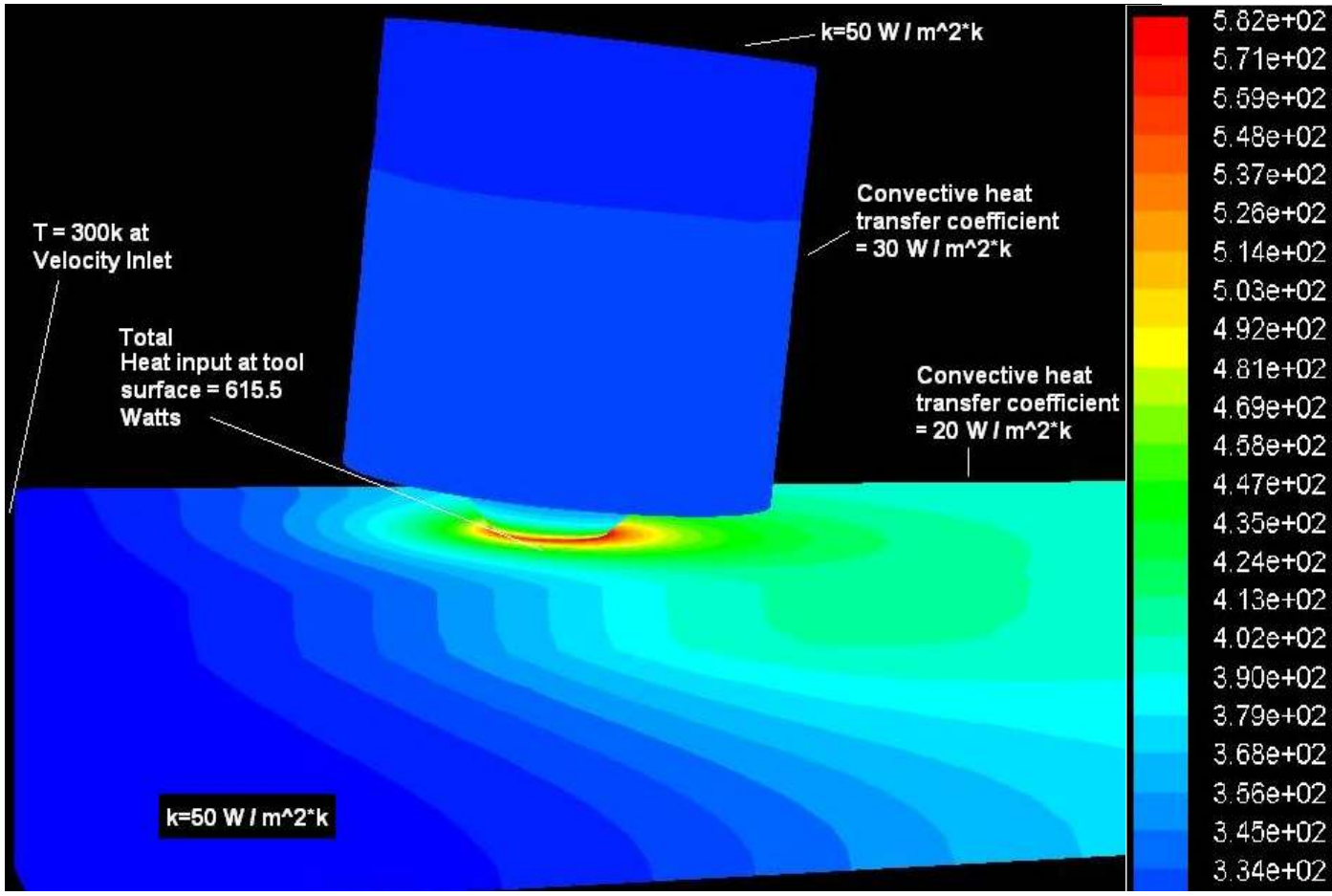

Figure 93: Thermal boundary conditions used in the model.

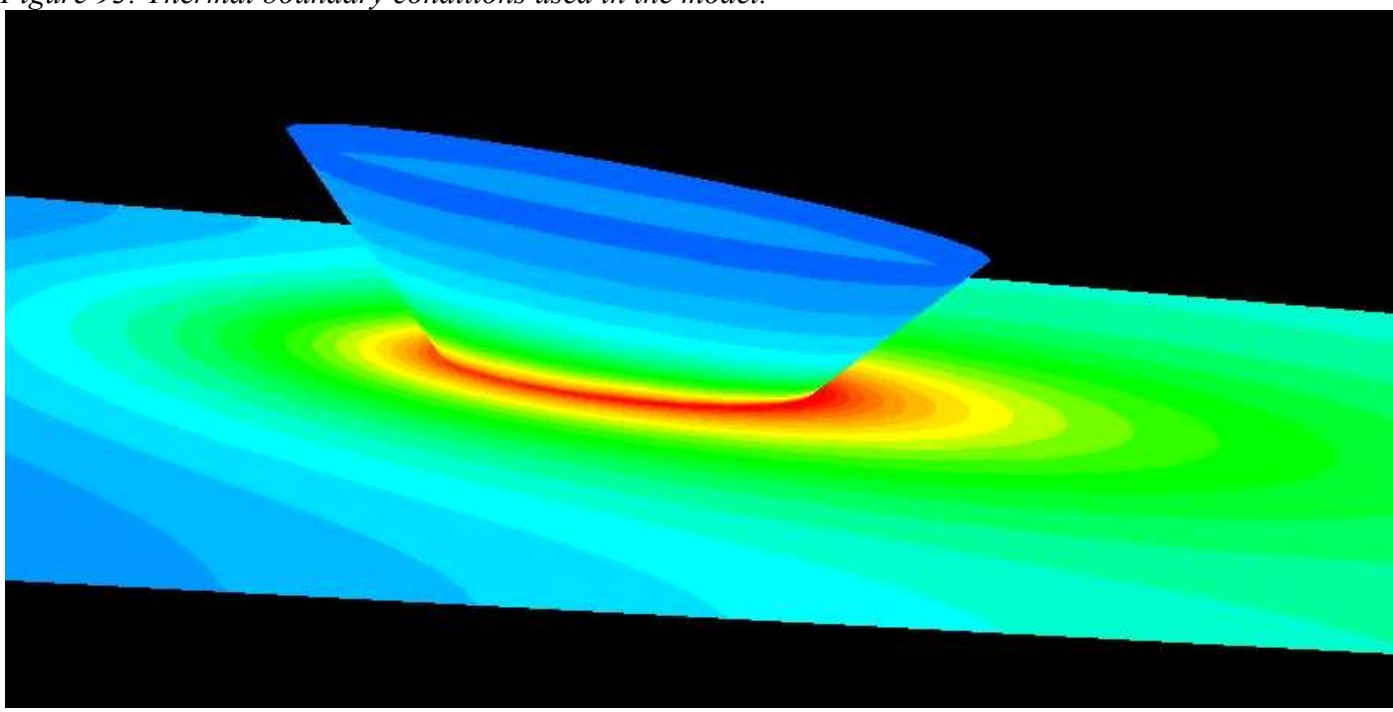

Figure 94: Temperature gradients in the vicinity of the weld interface.

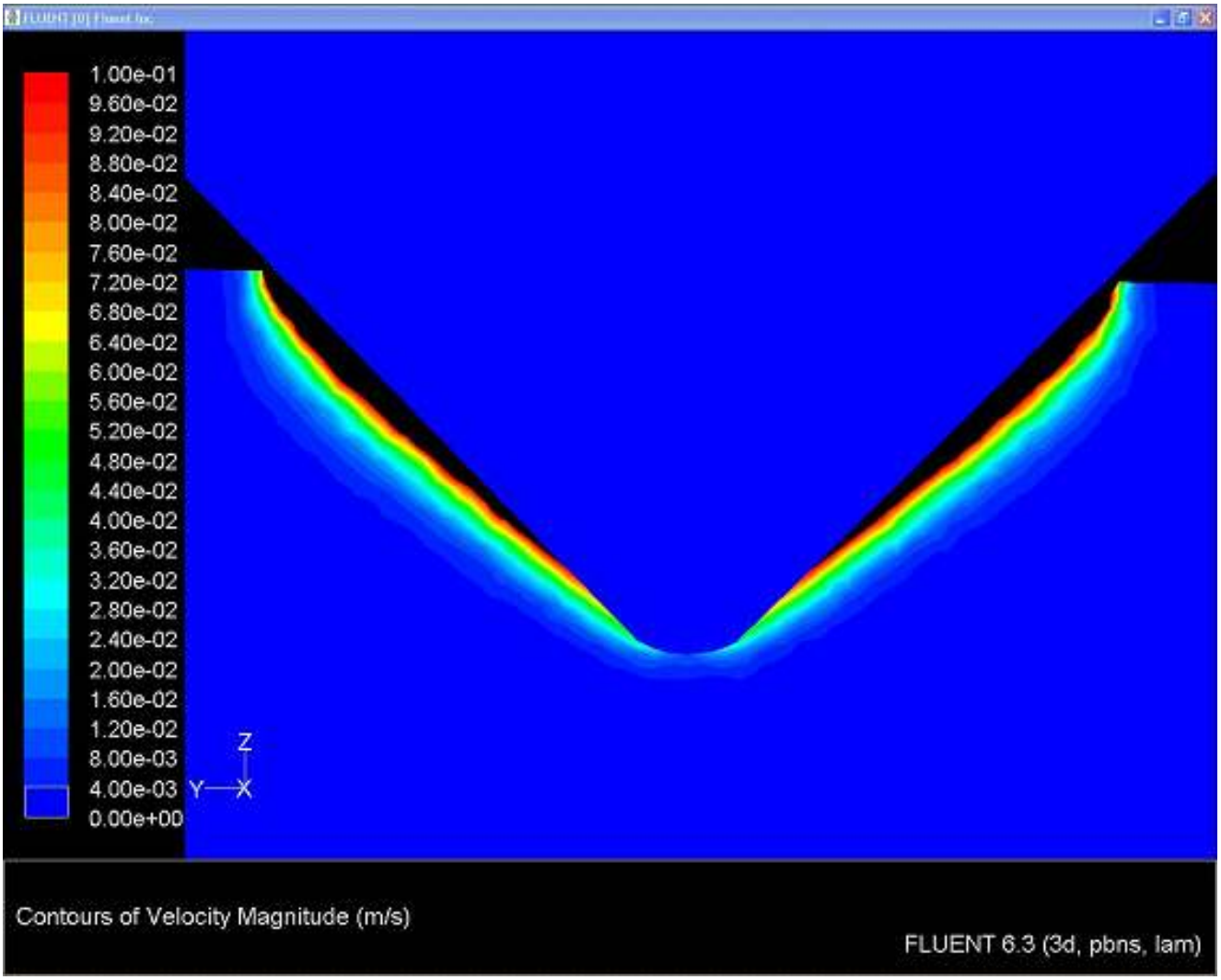

Figure 95: Lateral cross-section of the weld model showing contours of velocity magnitude in the material surrounding the tool. This outlines the so-called thermo-mechanically affected zone (TMAZ). The blackened area in the vicinity of the tool is outside the scale of this particular contour graph, which has been cropped to accentuate flow near the TMAZ boundary.

Conclusions

The conical tool reduces the process forces drastically (particularly the vertical). In this experiment the 90º tool welds retained a reasonable percentage of parent material strength (50-60%). The lack of the stabilizing influence of the shoulder results in increased tool deflection in XY plane but the difficulty can be alleviated with a large (4º here) spindle head angle. Weld line following was found to be more critical with a

conical tool because the decreasing diameter of the cone near its tip leaves little room for tool to weld line alignment errors. This sort of lateral misalignment will result in a so-called weld root defect.

The 90º tool was shown to work better than the 60º, 80º, or 120º tools. Small cone inclusive angles require higher spindle speeds and create more flash while large angles produce larger processed and heat affected zones. Failures typically occurred at the jointline (appropriate penetration ligament and jointline following are critical) and along the retreating side boundary of the weld nugget where a lack of consolidation (dark line) could sometimes be seen in macrosections.

Full probe tapered retraction proved to be difficult. Pictured below in the appendix are some preliminary attempts at this using various retraction rates, spindle speeds, and traverse rates (Figure 96). The cone tip tends to drag through the material towards the end of the retraction when probe surface area, probe tangential velocity, heat, and pressure are insufficient for proper FSW consolidation. Pin tapered retraction from a full penetration weld is likely achievable with an aggressive increase in spindle speed as the tool retracts. A shallow dimple in the material surface would however be difficult to eliminate. Application to variable depth welding and open-loop control welding are trivial tasks. From this experiment it can be concluded that a conical FSW tool could produce high quality, full penetration welds without the assistance of force control in materials which vary in thickness over their length.

Figure 96: Attempts a probe tapered retraction from 1/8" material full penetration welds at various parameters. The probe tends to 'drag' through the material near exit.

Acknowledgements

Completion of this chapter was made possible by a research license from the Edison Welding Institute (EWI) for use of a Variable Penetration Tool (VPT). This work was funded by the NASA Space Grant Consortium of Tennesse and by Vanderbilt University. The authors would like to thank Kate Lunsford and UTSI for assitance in etching and microscopy. The authors would like to thank Bob Patchin and John Fellenstein for assistance in the design and machining of tools and fixturing. In addition, the authors would like to acknowledge valuable advice and expertise provided by Jeff Bernath and Michelle Laverty of EWI.

References:

[1] Trapp, Fischer, and Bernath; Edison Welding Institute(EWI); U.S. Patent #7,234,626
[2] Bernath J, Friction Stir Welding Technology Engineering Team Leader, Edison Welding Institute(EWI), (personal communication, Nov. 10, 2008)

[3] Ding J (1996). The Hydraulic Controlled Auto-Adjustable Pin Tool for Friction Stir Welding; The U.S. Government through the National Aeronautics and Space Administration; U.S. Patent #5,893,507.
[4] Sheppard T and Wright D: Determination of flow stress: Part 1 constitutive equation for aluminum alloys at elevated temperatures; Met. Technol., 6, 215-223, June 1979.
[5] Sellars CM, Tegart WJM; Hot workability; Int. Metall. Rev., 1972, 17, 1-24
[6] Simar A, Pardoen T, de Meester B; Influence of friction stir welding parameters on the power input and temperature distribution on friction stir welding; Proc. of the 5th International Symposium on Friction Stir Welding, 2004.
[7] Simar A, Pardoen T, de Meester B; Effect of rotational material flow on temperature distribution in friction stir welds; Science and Technology of Welding and Joining, Vol.12, No.4, p324, 2007.
[8] Santiago DH, Lombera G, Santiago U; Numerical modeling of welded joints by the friction stir welding process; Materials Research, Vol.7, Num.4, p569, 2004.
[9] Pew JW, Nelson TW, Sorensen CD; Torque based weld power model for friction stir welding; Science and Technology of Welding and Joining,Vol.12, Num.4, p341, 2007.
[10] Colegrove P, Painter M, Graham D, Miller T; 3 Dimensional flow and thermal modelling of the friction stir welding process; Proc. of the 2nd International Symposium on Friction Stir Welding, 2001.
[11] Linder K, Khandahar Z, Khan J, Tang W, Reynolds AP; Rationalization of hardness distribution in alloy 7050 friction stir welds based on weld energy, weld power, and time/temperature history; Proc. of the 6th International Symposium on Friction Stir Welding, 2007.
[12] Dickerson TL, Shi Q-Y, Shercliff HR; Heat flow into friction stir welding tools; Proc. of the 4th International Symposium on Friction Stir Welding, 2003.
[13] Nunes A.C., Bernstien E.L., McClure J.C.: A rotating plug model for friction stir welding; Proc. of the 81st American Welding Society Annual Convention, Chicago, IL, 2000.
[14] St-Georges L, Dasylva-Raymond V, Kiss LI, Perron AL; Prediction of optimal parameters of friction stir welding: Proc. of the 6th International Symposium on Friction Stir Welding, 2007.
[15] Chao YJ, Qi X; Heat transfer and thermo-mechanical analysis of friction stir joining of AA6061-T6 plates; Proc. of the 1st International Symposium on Friction Stir Welding, 1999.
[16] Liechty B.C., Webb B.W., Modeling the frictional boundary conditions in friction stir welding: International Journal of Machine Tools & Manufacture, 2008, doi:10.1016/j.ijmachtools.2008.04.005
[17] D. Lammlein, P. A. Fleming, A. M. Strauss, G. E. Cook, T. Lienert, M. Bement, D. Hartman;" Shoulder-less Conical FSW Tools: An Evaluation on 1/8” Thickness Al-6061 Butt Welds," in Presentation: American Welding Society 2007, Chicago IL, 2007.

CHAPTER IV

THE FRICTION STIR WELDING OF HEMISPHERES – A TECHNIQUE FOR MANUFACTURING HOLLOW SPHERES

D.H. Lammlein, W.R. Longhurst, D.R. DeLapp, P.A. Fleming, A.M. Strauss, G.E. Cook. The Friction Stir Welding of Hemispheres - A technique for Manufacturing Hollow Spheres. *International Journal of Pressure Vessels and Piping*, Submitted August 4, 2010.

Abstract

In this work, thin walled, small radius, aluminum 6061 hemispheres are joined using friction stir welding (FSW). Hollow spheres are used extensively and in a wide range of applications, primarily as pressure vessels. FSW of spheres presents challenges associated with tooling, system eccentricity, internal support, and the method of weld termination. FSW is an improvement on fusion welding in terms of strength, reliability, and surface finish. Additionally, a welded solution is preferred for weight considerations to joining by flange, gasket, and fasteners; this is particularly true in aluminum alloys selected for their low density. Here, FSW is adapted to the joining of small diameter hemispheres using two separate approaches. The first approach assumes the use of an interior supporting anvil is acceptable and a series of full penetration welds are made using a cupped shoulder, threaded probe tool. A second approach assumes the use of internal support is unacceptable because this anvil cannot be retrieved. Here, unsupported welds are made with a shoulder-less, conical tool at partial penetration. For analysis, lateral macrosections, tensile tests, process force data, and computational fluid models (CFD) are presented.

Introduction

Friction stir welding (FSW) is a proven solid state joining technology with a growing range of application [1]. To accommodate a wider variety of engineering structures, FSW must be adapted to highly curved surfaces and surfaces with dual

curvature. These geometries are used extensively in aerospace vehicles, in nautical vessels, and in pressure vessels. In this work, friction stir welding is applied to the joining of two small diameter, thin-walled, hollow hemispheres. This geometry presents a case of practical significance with both a high degree of curvature (relative to the dimensions of the tool and work material) and dual curvature. FSW of small diameter hemispheres is not present in the literature, although a collaboration led by Lawrence Livermore National Lab has joined pairs of aluminum alloy hemispherical forgings of approximately 40" diameter by FSW [2]. In the work presented here, the radius of curvature is an order of magnitude smaller and the surface curvature is correspondingly greater.

The sphere has less surface area than that of any equivalent geometric volume. The hollow sphere can withstand both external and internal pressures (as a spherical pressure vessel) more efficiently than any other geometry, and consequently fuel tanks, gas storage vessels, pneumatic reservoirs, and submarine vessels often utilize this shape. Metal spheres are additionally used as precision bearings in mass properties test equipment and aerospace attitude control system testing equipment [3,4].

The applications of spherical pressure vessels are manifold and pervasive. They are found in industrial applications (oil refineries, petrochemical plants [5], nuclear power plants, communication satellites [6], and propane tanks), space vehicles (propellant tanks [6], oxygen tanks, and water tanks), underwater applications (submarine vehicles, flotation elements, tanks, and buoys), and military applications (UAV's, projectiles, torpedoes, ships, aircraft, and nosecones [8]). Spherical pressure vessels are commonly made of steel, titanium, aluminum, inconel, fiber reinforced polymer (e.g. carbon fiber reinforced polymer [9] or kevlar reinforced polymer), or some combination of these materials. Ceramics and glass are also used for applications subject to external compression [10].

In the case of metals, the geometry does not permit a single forged, cast, or machined piece of material and the sections must be joined together by some secondary means. In the case of steel, sections are welded together by conventional means or joined by fastener and gasket [11,12,13]. Fastener and gasket joining can be used in applications where weight and size are not a consideration, as fasteners and flanges add considerable weight and bulk to the vessel. Despite its high cost, titanium is used heavily in aerospace

applications for its high strength and low density. Titanium partial sphere sections can be made by spin forming, blow forming, or machining. The titanium pieces are then joined by Tungsten Inert Gas (TIG) welding or solid-state diffusion bonding [14]. Although aluminum has a lower yield strength than titanium, it is also used extensively in aerospace due to its low density and moderate cost.

Carbon fiber reinforced polymer vessels have a high tensile strength to weight ratio but limited impact resistance, durability, and compressive strength. Compressive strength is required in deep sea applications [15]. Additionally, the shape of a carbon fiber vessel is limited by the ability of a fiber winding machine to accommodate the chosen geometry. Some radial and axial asymmetries can be accommodated but concavities in the part cannot. The process is further limited by the necessity of an inner supporting boss for winding.

Often, a layered approach is taken in the design of pressure vessels in order to meet all design requirements [16,17]. One example is winding a kevlar reinforced polymer outer layer for tensile strength and low weight around an aluminum inner sphere for stiffness and leakage reduction. Leakage via material voids and diffusion is lowest in metal vessels or vessels with some metallic layer. Aluminum spheres are low leakage, lightweight, stiff, durable, and moderate cost vessels with applicability to external and internal compression applications. The results reported here demonstrate that Friction Stir Welding is an efficient and effective method for manufacturing spherical aluminum pressure vessels. The techniques developed here can also be applied to manufacturing steel, titanium, and other metallic spheres.

Experimental Approach

In friction stir welding, a large magnitude force is directed vertically downward through the tool, the workpiece, and into an anvil which traditionally opposes the tool axial force. The anvil is necessary in full penetration welds to support the region around the weld root and prevent material expulsion and failure on the underside of the weld. In the case of a highly curved surface with dual curvature, the interior of the workpiece is

often an inaccessible area (e.g. spherical pressure vessel) or an area where setup and fixturing is difficult (e.g. nosecone). In these cases the insertion or removal of interior support is complicated. In this work, cases with and without an anvil are tested to accommodate both applications where an anvil can be used and those situations where an anvil cannot be used. It is shown in this work that FSW of spheres can be accomplished at partial penetration without an interior supporting apparatus. This sort of weld capability can also be used in making full penetration welds with minimal interior support. The latter case would differ slightly in geometry from the case presented here, as it would be a butted and lapped weld with two butted sections welded over and joined to a separate sheet of underlying material (see Appendix, Figure 137). In airframes, this configuration is used when an outer skin is joined to an interior skin or a supporting member (e.g. rib).

Partial penetration type welds of butted joints, where some unwelded interface is left below the weld nugget, are useful in situations where the tensile loading is significantly less than the compressive loading [18-21]. The particular experimental geometry in this work; that of a two hemispherical shells joined by a partial penetration weld (50%), is useful in external compression applications (e.g. submersibles [Yano, et al.]). Research has shown that in external compression applications the effectiveness of the vessel is negligibly reduced by decreases in weld penetration [22].

The flat shoulder geometry of a traditional FSW tool is not ideal for spherical applications and in this work two alternative tool geometries are tested: one consisting of a cupped shoulder and threaded probe for supported welds, and the other consisting of only a conical probe with a snubbed, cupped nose (see Appendix, Figure 135) for unsupported welds [23-25]. For the experiment, sections of 0.20” thickness, 4.5” diameter, Al-6061-T6 pipe were machined into rings with the external surface curvature of a sphere. These samples, depicted in Figure 97, are intended to represent a sphere (or when halved, two hemispheres).

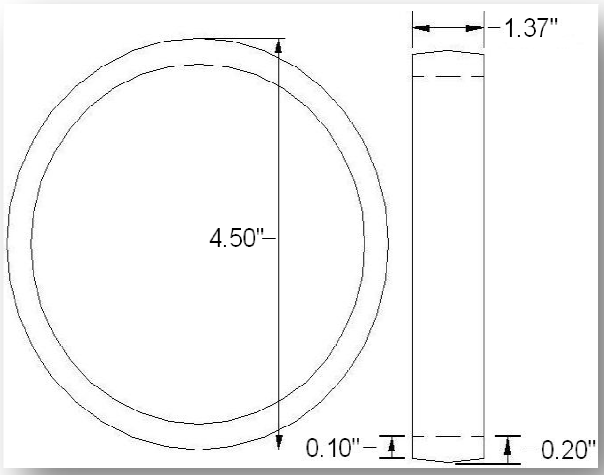

Figure 97: Experimental weld samples were machined from pipe with the external curvature of a sphere. These samples were halved and then joined in a butted configuration.

Full penetration welds of butted hemispheres were performed with an internal supporting ring-anvil. Additionally, welds at 50% penetration depth were made with a shoulder-less, conical tool and without the use of an internal supporting ring-anvil. The full penetration portion of the experiment was performed with a cupped shoulder, threaded cylindrical probe tool. The cupped shoulder was designed to mate with the spherical curvature of the sample surface. When a ring-anvil backing was used, sound welds with good surface appearance were achieved. It was found that welds made with the threaded probe tool and without a backing anvil at various penetration depths (adjusting the length of the probe accordingly) approaching 50% of the material thickness produced a bead-like protrusion defect, shown in Figure 98, in the interior of the sample in bead on plate type welds and a more serious protrusion and splitting type defect in butted hemisphere welds, shown in Figure 99 and Figure 100. During cupped shoulder (5/8” diameter), threaded probe (0.20” diameter) tool welds made with a backing ring anvil in a butt weld configuration, the material below the probe is deformed by heat and pressure, and presses against the ring anvil. In this case the ring anvil must be forcibly removed with a press.

Figure 98: Bead protrusion type defect experienced in cupped shoulder (Ø 5/8”), threaded probe (Ø 0.20”) tool, bead-on-plate type welds made without a backing ring anvil. Surface quality was more difficult to maintain. (Ø = diameter).

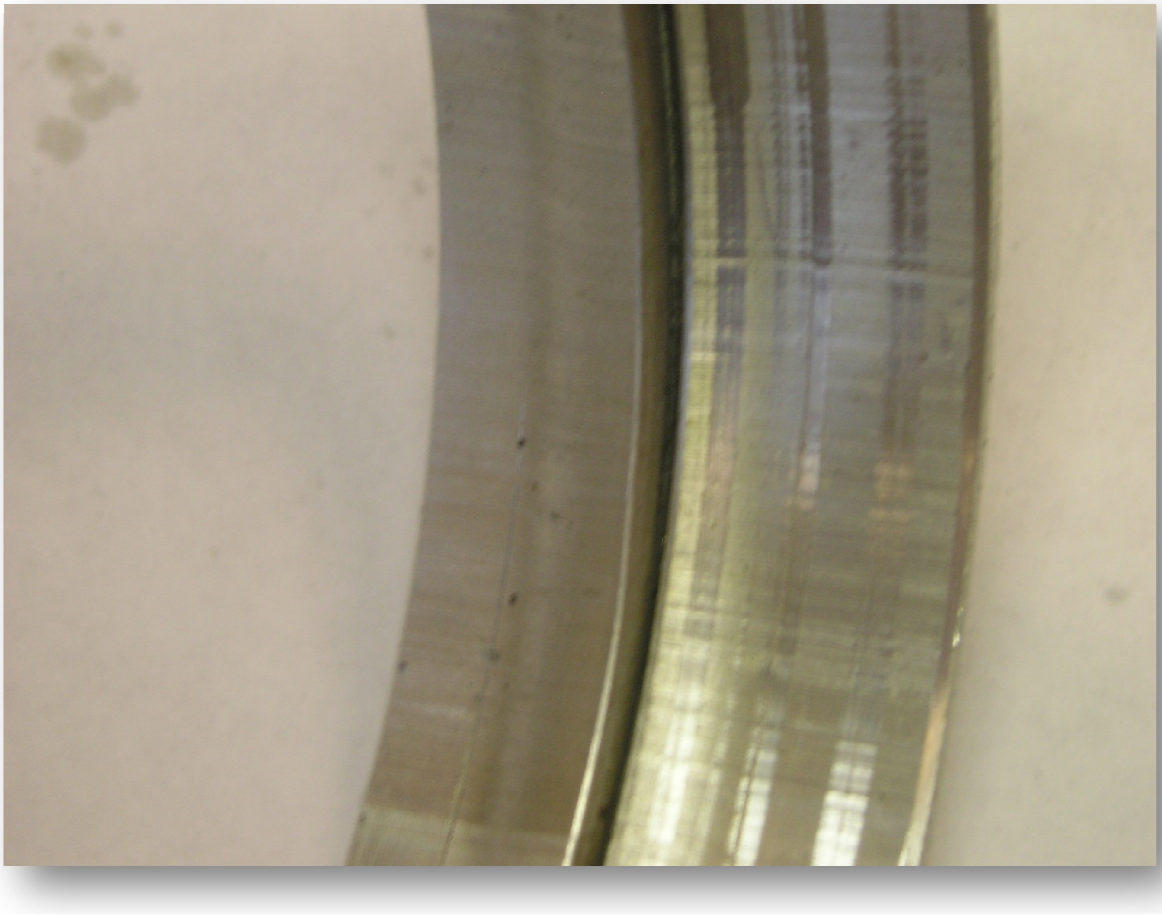

Figure 99: Split protrusion type defect experienced in cupped shoulder (Ø 5/8”), threaded probe (Ø 0.20”) welds made without a backing ring anvil at 50% material penetration in a butt weld configuration. This defect was present at all tested parameters with this weld depth and tooling. The unsupported portion of the experiment was therefore performed with a shoulder-less, conical tool. The conical tool experienced no visible deformation at the weld root at this weld depth over the parameters tested in butted configuration welds. (Ø = diameter)

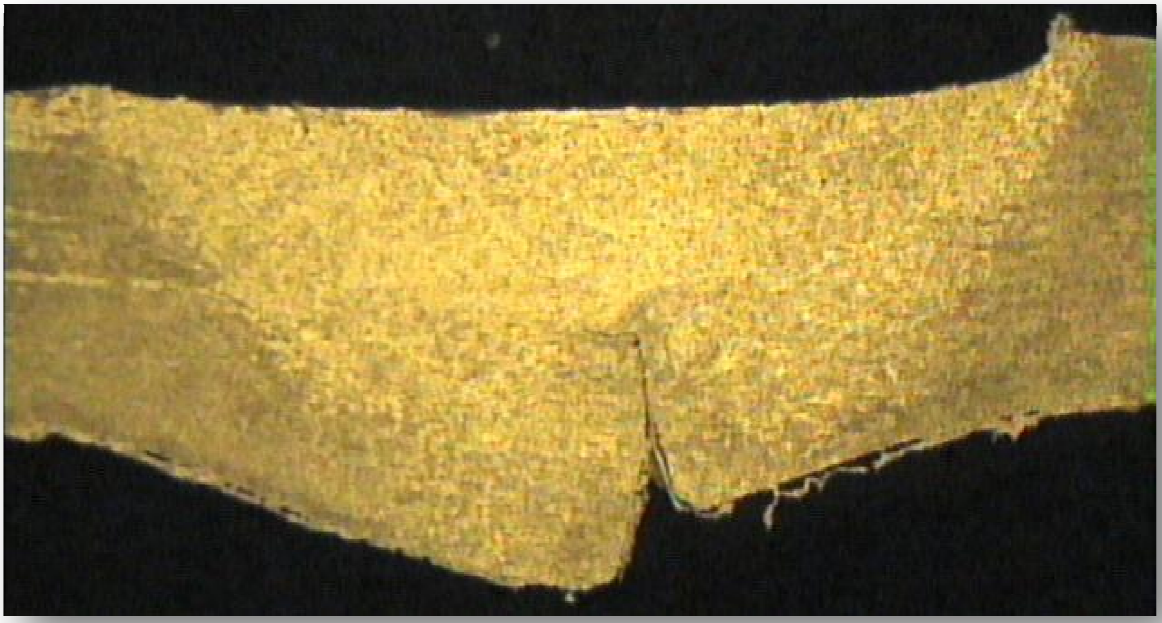

Figure 100: Macrosection view of the split protrusion type defect experienced in cupped shoulder (Ø 5/8”), threaded probe (Ø 0.20”) tool weld made without a backing ring anvil at 50% material penetration in a butt weld configuration.

It was concluded that the large, flat surface of the probe bottom contributed most significantly to this weld material distortion and an alternative probe geometry had to be selected for successful welding without an internal ring-anvil. It was found that a tool consisting of only a simple 100º conical probe (no shoulder) redirected weld forces in such a way as to eliminate the protrusion or splitting defect on the backside of the material at penetration depths approaching 60% of the material thickness in both bead on plate and butted weld configurations. Additionally, a conical tool geometry with a small diameter (0.025”) snub nose was desired for use in a taper retraction or tapered extraction type weld disengagement procedure. It was found that a 0.015” diameter hemispherical cup cut into the snub of the tool relieved influences on the weld material root to an extent which allowed a 50% (0.10”) penetration weld in a butted configuration without the assistance of an inner anvil ring. No protrusion or splitting was experienced at this depth and with this tooling within the parameter range tested. Figure 101 shows the typical appearance of a sample welded with this tool geometry. It was found that without a cupped recess in the snubbed nose of the tool that deformation occurred at the base of the joint in the weld material at some parameters. The conventional probe tool was not tested

with a cupped recess. It is however the belief of the authors that a cupped recess in the probe bottom of the conventional probe tool would allow for unsupported welding without deformation at the material base at some shallow penetration depth, possibly 15% of the material thickness.

Figure 101: Surface appearance for a butt configuration weld made with a 100º conical tool (Ø 0.025" snub-nose and Ø 0.015" cupped nose recess). No backing ring anvil was used.

Subsequently, the applicability of various tool extraction procedures was tested using the cone-snub-cup tool, initially in a bead on plate weld configuration. The goal was disengagement from the weld material without a serious defect. The procedure involved a steady state weld period at the desired weld depth followed by a gradual decrease in the tool depth via a computer controlled vertical motor. In some cases the rotation rate (analogous to traverse rate) of the weld hemispheres was decreased to some lower but constant value when the retraction procedure was triggered. Additionally, the spindle speed is increased during the tapered retraction, in some instances at multiple instants during the retraction (e.g. from 900 rpm to 2000rpm in 100rpm increments on some time interval). It was found the extraction could be performed rather cleanly and leaving essentially no indentation as shown in Figure 102.

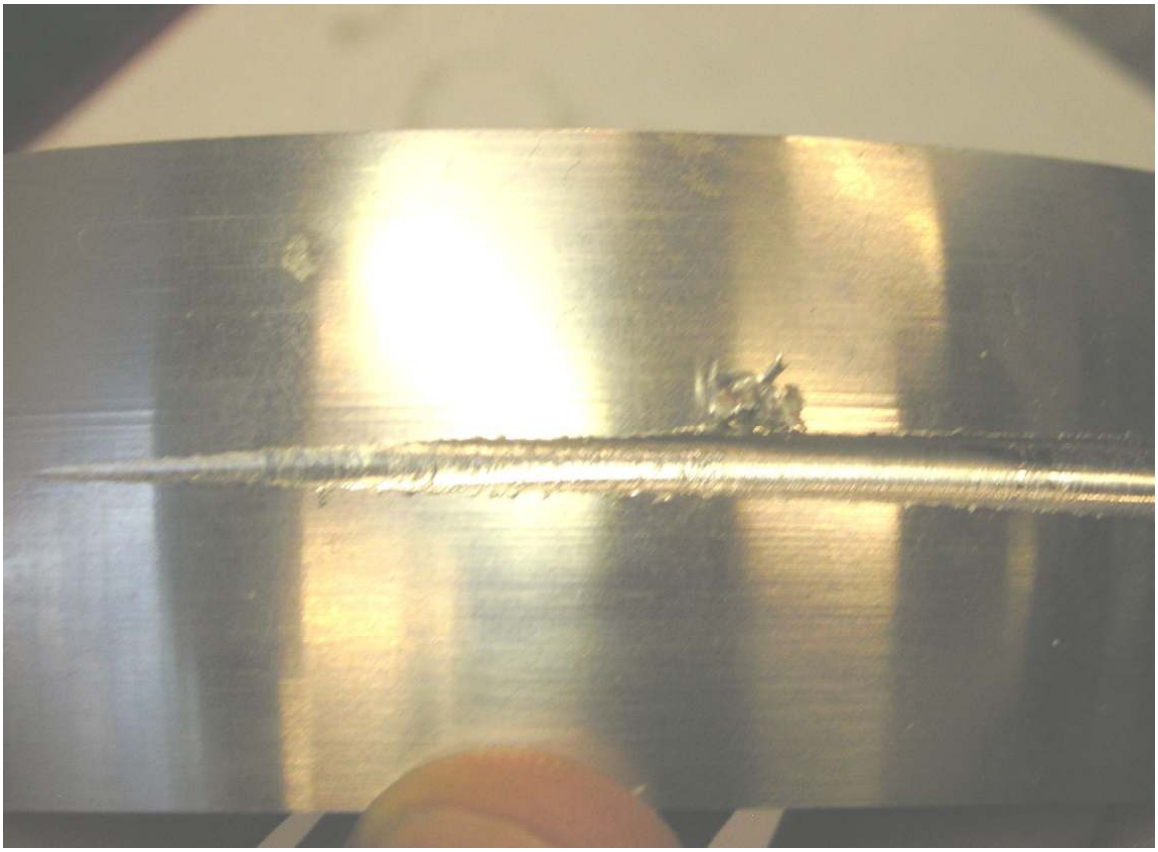

Figure 102: Tapered retraction procedure performed in a bead on plate configuration. A snubbed nose, cupped nose, 100º conical tool was used. The final segment of the retraction is essentially flush with the sphere surface (i.e. no indentation).

A tapered retraction procedure was then performed in a butted configuration after and over a full, circumferential weld. A snubbed nose, cupped nose, 100º conical tool was used. The retraction begins at the weld surface mark on the far right in Figure 103 (the mark is due to the change in rotational rate of the sphere, analogous to traverse rate). The result here is not as clean as the retractions over unwelded material. It is believed that this drawback can be overcome by performing the tapered retraction in a direction perpendicular to the original weld path, either by rotating the sphere about a new axis or by translating the sphere in a perpendicular direction. The latter is slightly different geometrically as it could be done without engaging the vertical motor because the sphere curves away in the lateral direction as well. It is the belief of the authors, however, that this type of tapered retraction (via translation of the sphere perpendicular to the weld path or equivalently translating the tool in a direction perpendicular to the weld path) should be accompanied by vertical motor action in the direction opposite to the former method

of tapered retraction (i.e. move the sphere up relative to the tool during extraction). This will allow for a more extended retraction zone and a more gradual disengagement.

Figure 103: Tapered retraction procedure performed in a butted configuration after and over a full, circumferential weld

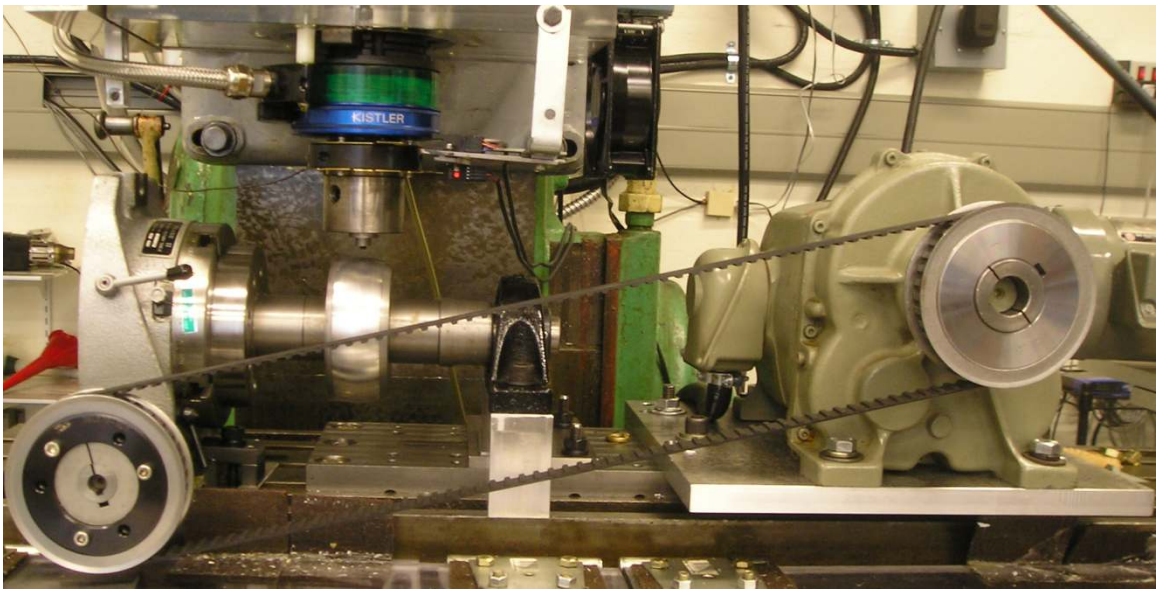

Figure 104: Experimental setup for rotary FSW of hemispherical butted sections.

Force Control and Torque Control

For full circumferential welds, the eccentricity of the experimental setup, shown in Figure 104, is approximately 0.02". This level of eccentricity results in significant and unacceptable changes in the vertical position of the sphere surface relative to the tool, and thus unacceptable variations in weld depth. An in-process, force feedback control algorithm was therefore employed for the conical tool experiments as a means of maintaining a constant penetration depth around the entire sphere. The vertical position was adjusted based on torque signals received from a rotating cutting force dynamometer oriented in series with the tool. For the conical type tools it was found that desired position was better maintained if torque, rather than force, was used as the input in the decision making algorithm. An auto-zeroing procedure is performed over the start of the weld to determine the height of the material surface here relative to the tool. The tool is then plunged to the assigned penetration depth and the weld traverse is started. After 1" of weld traverse the measured torque from the dynamometer is set as the desired torque and from this point forward this torque value is maintained by vertical adjustments of tool position using the weld machine's vertical axis motor. Figure 123 in a later section shows the weld torque increasing with penetration depth at the 1000rpm, 10ipm parameter setting. The relationship between weld depth and process forces will be discussed later. Figure 105 and Figure 106 below demonstrate the torque control process for two welds runs(1000rpm, 10.4ipm, 0.095" weld depth). In the upper frame the axial force (blue) and desired axial force (green) are shown. The desired axial force is not used in the control algorithm and is shown for comparison with the measured axial force and the torque panel below. Torque was found to be a more reliable indicator of depth. These relationships are discussed later. The middle panels in Figure 105 and Figure 106 show the measured torque (blue) and desired torque (green). It can be seen in the figures that the desired torque, set after 1" of weld traverse, is followed closely. The bottom panel of the two figures is the vertical position of the tool relative to the height of the material surface at the weld plunge site (weld start). A linear encoder is used to track movements relative to this initial calibration. In this manner the vertical adjustments made by the tool to maintain the desired torque can be seen. As torque is highly sensitive to plunge depth and a constant torque is closely maintained throughout the weld traverse, it can be concluded that tool penetration depth is closely maintained throughout the weld traverse.

The adjustments in vertical position in the bottom panel of the figures therefore shows the eccentricity of the setup or how the material surface height at the tool engagement site changes relative to its initial measurement as the weld piece is rotated. Additional details and description of the torque control method used in these experiments can be found in Longhurst et al. [26].

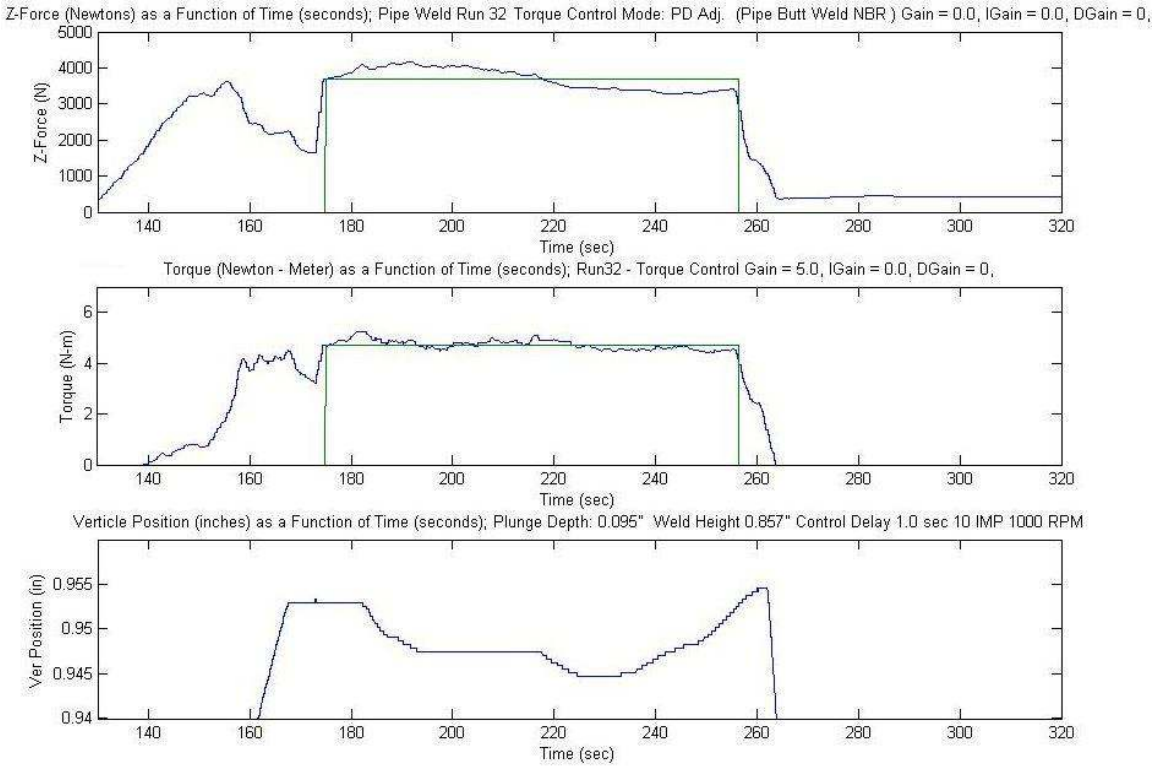

Figure 105: Dynamometer data for a butted configuration, sphere weld (1000rpm, 10.4ipm, 0.095" depth) using a 100º conical tool (snub-cup). The top frame shows measured force(blue) and desired force (green). The desired force is presented for comparison and not used in the control algorithm. The middle panel shows measured torque(blue) and desired torque (green). Toque is highly sensitive to plunge depth. The desired depth is followed closely by maintaining weld torque via vertical adjustments of tool position. The weld is a full circumferential weld and the eccentricity of the setup can be seen in the lower frame which shows the vertical position of the tool relative to its initial calibration on the material surface.

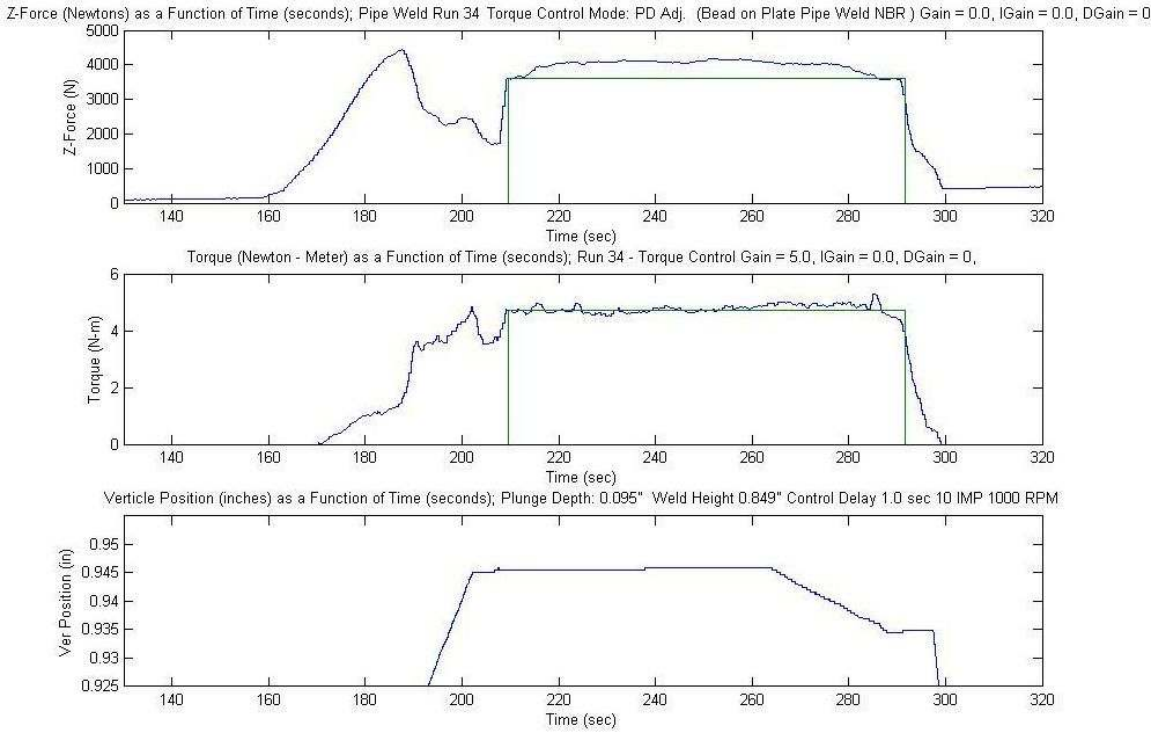

Figure 106: Dynamometer data for a butted configuration, sphere weld (1000rpm, 10.4ipm, 0.095" depth) using a 100° conical tool (snub-cup). The weld is a full circumferential weld and the eccentricity of the setup can be seen in the lower frame, which shows the vertical position of the tool relative to the machine stage. The eccentricity was generally around 0.02" but varied in its manifestation from weld to weld. The desired torque is closely maintained. From approximately 159 to 203 seconds the spinning tool is being gradually lowered (plunged) into the material at approximately 0.002" per second. From 203 to 209 seconds the vertical and rotary (traverse) motors are stopped during a brief dwell period prior rotary motor engagement. Reductions in axial force from 188 to 203 seconds are due to material softening [27].

Accounting for system eccentricity in the experimental setup for the cupped shoulder, threaded probe tool was done by mapping the eccentricity prior to the weld via a series of auto-zeroing procedures as both force and torque control proved to be inconsistent for this particular tool. The relative height of the butted hemisphere surface to the system was obtained at 60° intervals for each weld sample prior to the weld and a vertical position path was programmed into the computer for welding at the desired depth. The tool was brought from the current vertical position to the desired vertical position (moving from calibration point to calibration point around the sphere) via a linear function with parabolic blends as described in Chapter 7 of Craig [28]. In these

manners the assigned depth was maintained around the entire weld within a tolerance of several thousandths of an inch for the experimental welds presented.

Experimental weld matrix

A 6 weld matrix (7.8ipm, 10.4ipm; 800rpm, 900rpm, 1000rpm) was performed using cupped shoulder (Ø 5/8"), threaded probe (Ø 0.20"), tool at full penetration with backing ring anvil. The surface finish and lateral macrosections for this portion of the experimental welds are shown in Figure 107 and Figure 108. With a probe length of 0.178", a shoulder plunge of 0.006", and a material thickness after bisection of approximately 0.198"; the desired penetration ligament of 0.014" was reached. A more ideal penetration ligament would be something like 0.007", but with the eccentricity of the experimental setup it was feared that the probe would frequently collide with the backing anvil and the larger clearance was used in the experiments. With the knowledge gained in these experiments, a second iteration of the experiments could be performed with a smaller penetration ligament using the pre-programmed path control method described earlier or some force feedback control algorithm. Reducing the penetration ligament would strengthen the welds to some degree.

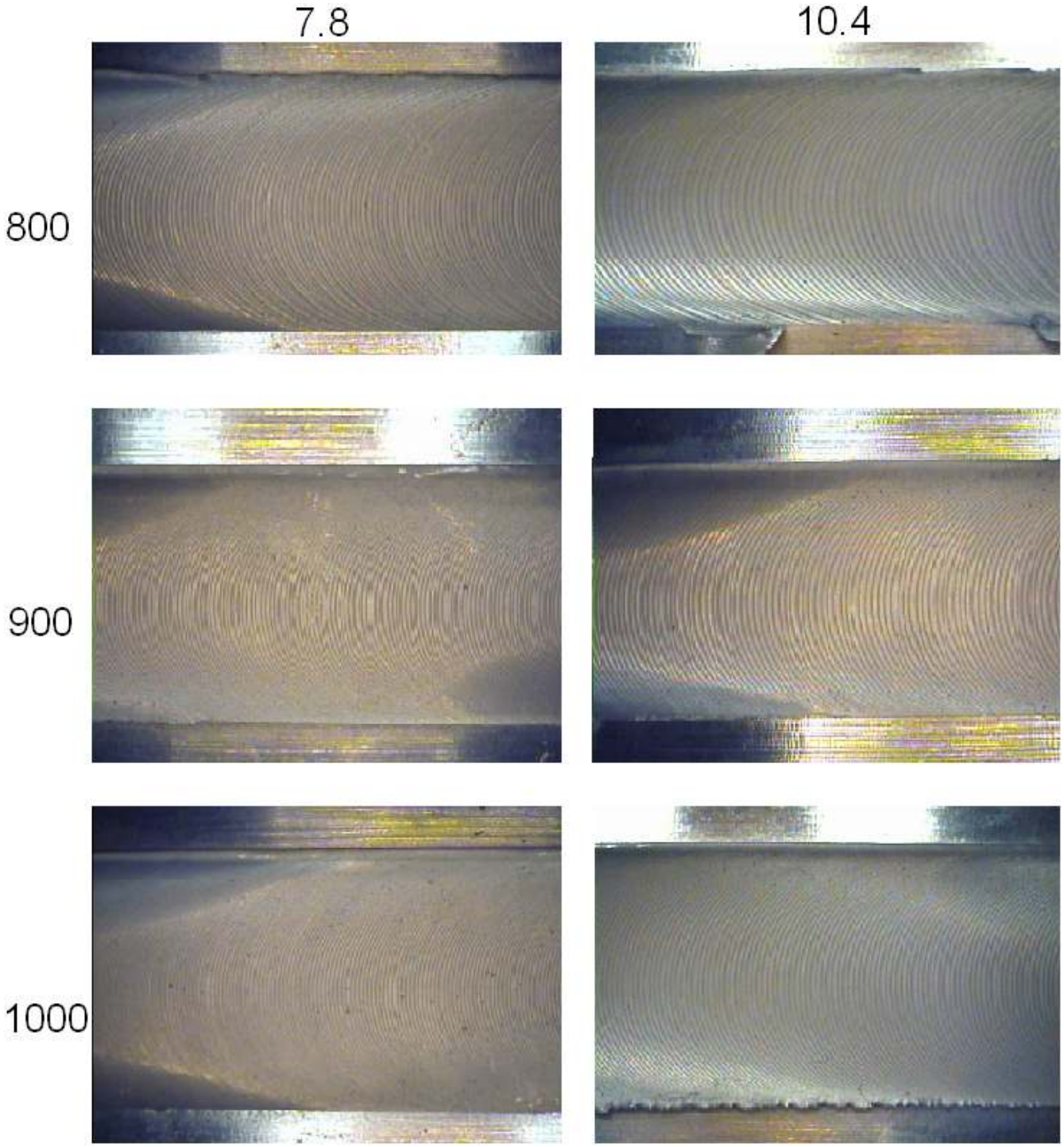

Figure 107: Surface appearance for full-penetration, supported welds made with the cupped shoulder, threaded probe tool. Samples are taken from the steady-state, steady-depth portion of each weld.

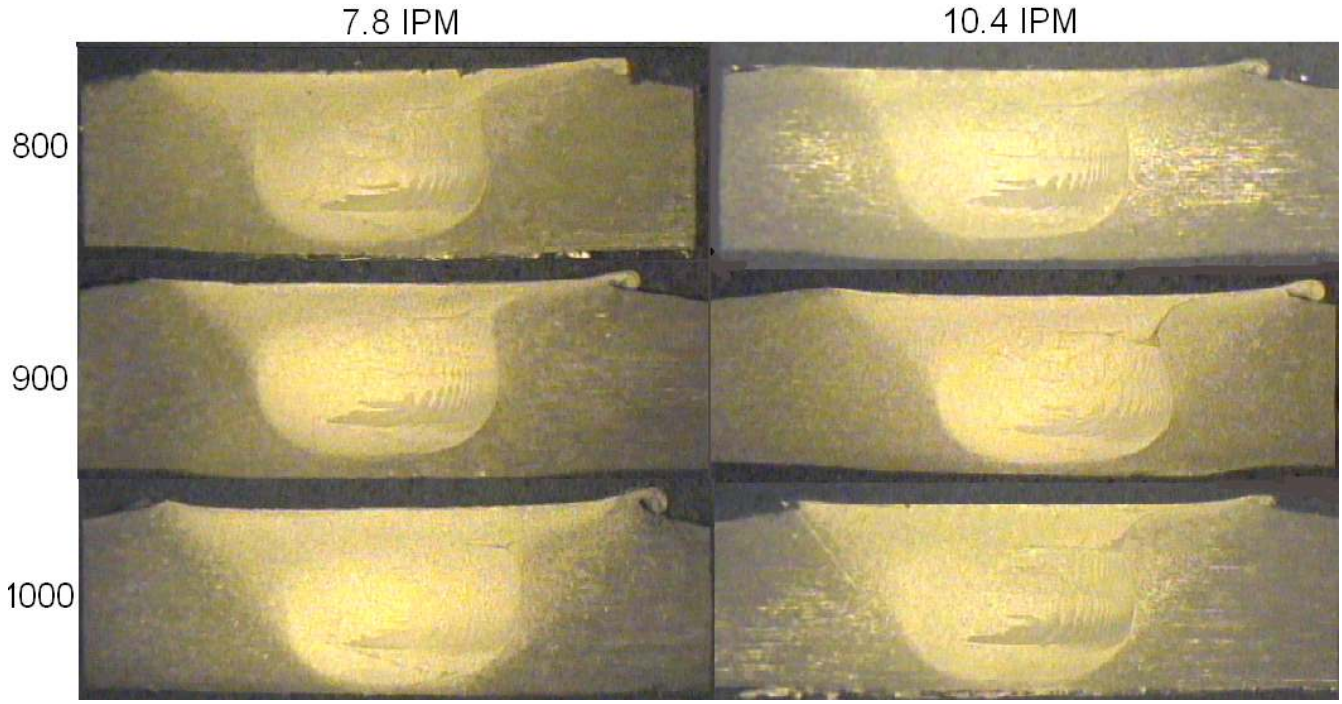

Figure 108: Lateral macrosections for full-penetration, supported welds made with the cupped shoulder, threaded probe tool. Samples are taken from the steady-state portion of each weld. Bose's reagent was used for etching.

Additionally, a matrix of 6 welds was performed at parameters identical to the full penetration experiment at 50% material penetration and without interior support to the material. A shoulder-less, 100°conical tool with a snub nose (Ø 0.025”) and hemispherical cup indentation (Ø 0.015”) was used. Welds were performed using the desired torque weld control method described above to maintain the desired depth throughout the weld process. Lateral macrosections for this portion of the experiment are shown in Figure 109.

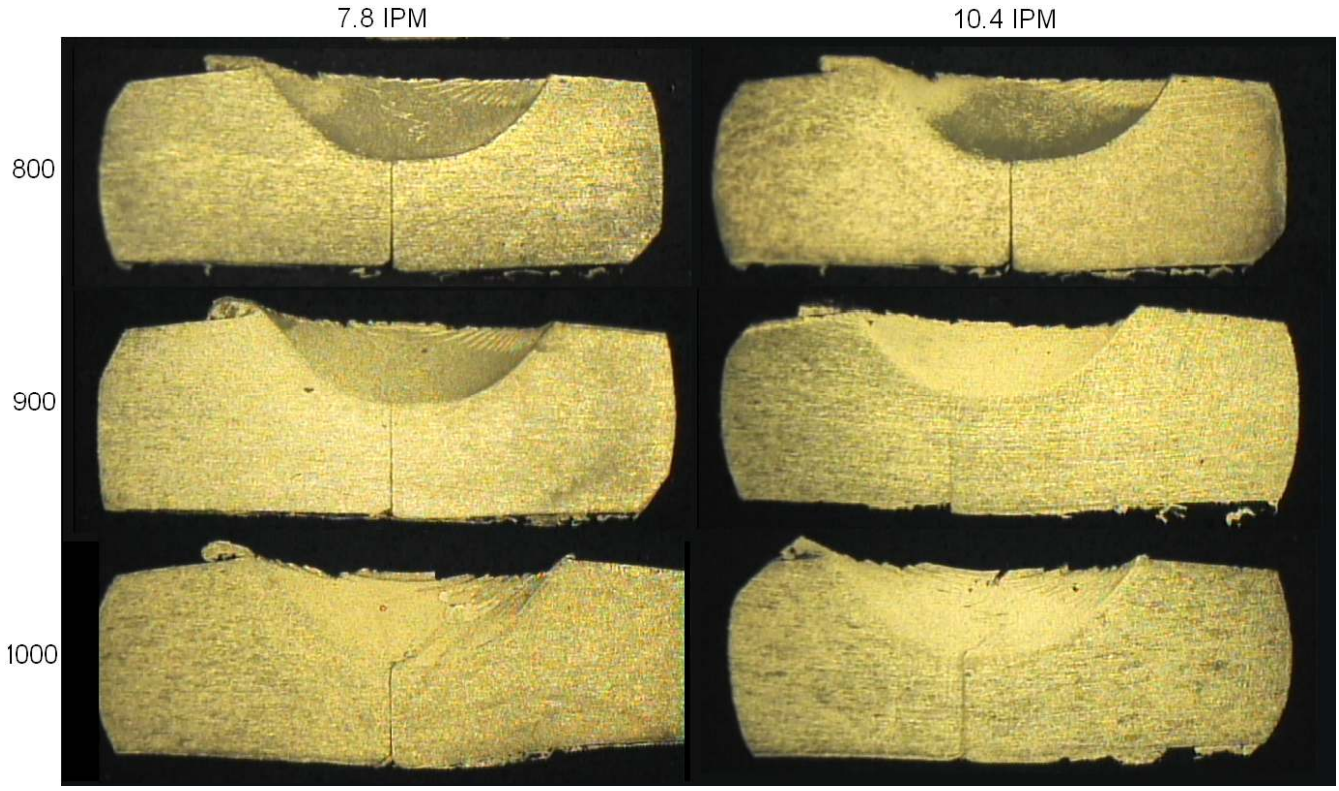

Figure 109: Lateral macrosections for partial-penetration, unsupported welds made with the conical tool. Samples are taken from the steady-state portion of each weld.

The axial force data, presented in Figure 110 and Figure 111, shows Z direction force decreasing with increasing rotational speed and an increasing with increasing traverse speed. Increased rotational speed can to soften the material (reduce viscosity) due to increased heat input (if torque remains somewhat constant) and increased shearing forces. A higher traverse rate means a colder weld and reduced axial force. It should be noted that the axial force was significantly lower for all parameters with the conical tool in unsupported welds.

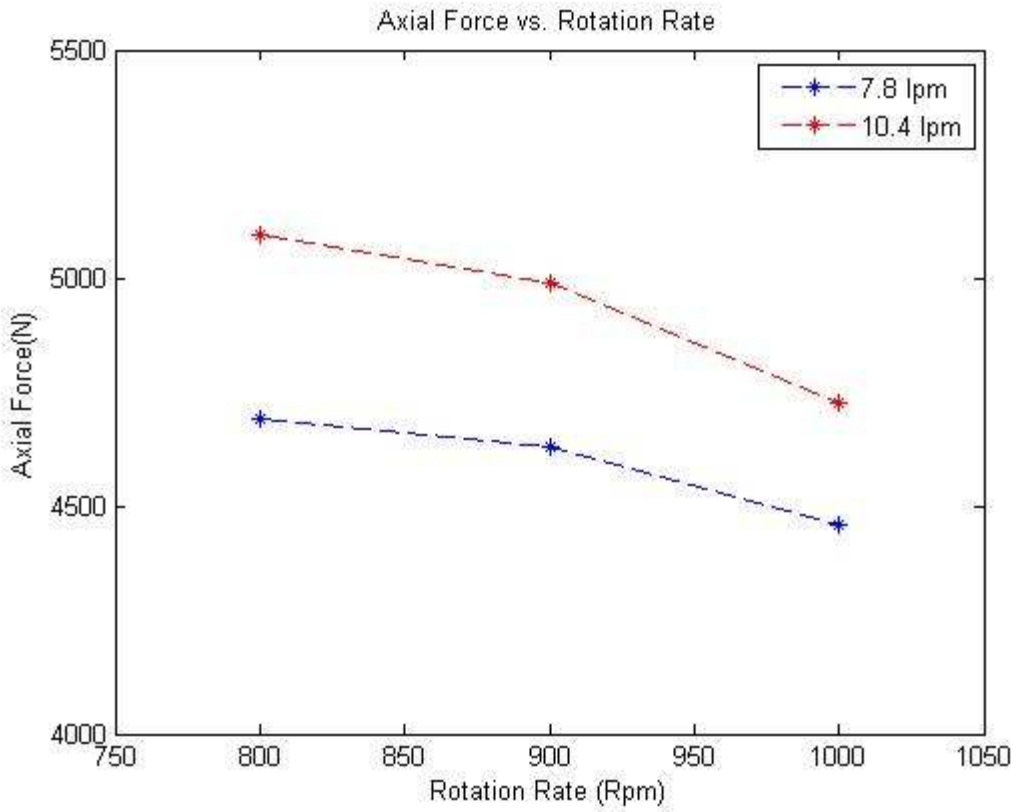

Figure 110: (Supported, cupped tool) A plot of axial (z-direction) force showing an inverse relationship with rotation rate and a direct relationship with traverse speed.

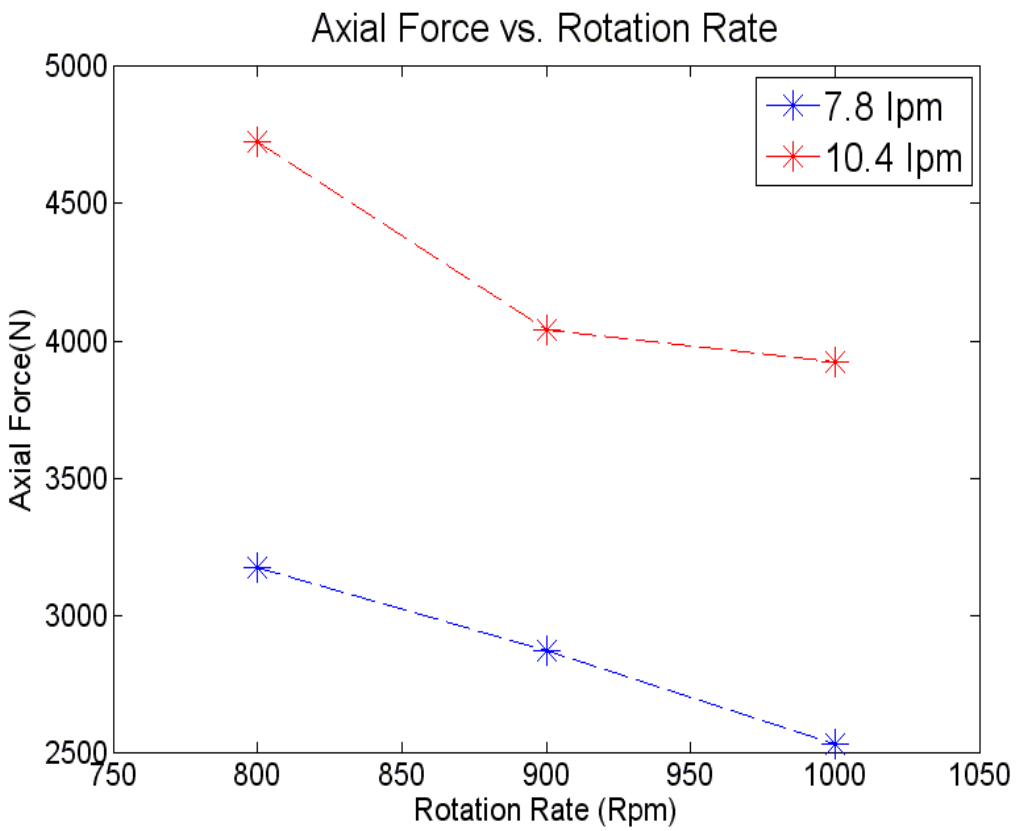

Figure 111: (Unsupported, conical tool) A plot of axial (z-direction) force showing an inverse relationship with rotation rate and a direct relationship with traverse speed.

Figure 112 and Figure 113 show the weld moment about the vertical, z-axis plotted against rotational speed for each weld. The torque input consistently increased with increasing traverse speed for the cupped tool and the opposite relationship held for the conical tool, somewhat inexplicably. The relationship between torque and rotational rate for the cupped tool and supported setup was not consistent but shows a general tendency towards reduced torque at higher rotational speeds. For the conical tool this relationship was seen more reliably. Figure 113 shows that torque reduced in all cases with increased rotational speed for the conical tool. The reduction in measured torque is due to material softening at higher rotational speeds but this is mitigated somewhat by the fact that were the tool spun in a medium of constant viscosity, higher rotational speeds would result in a larger moment on the tool.

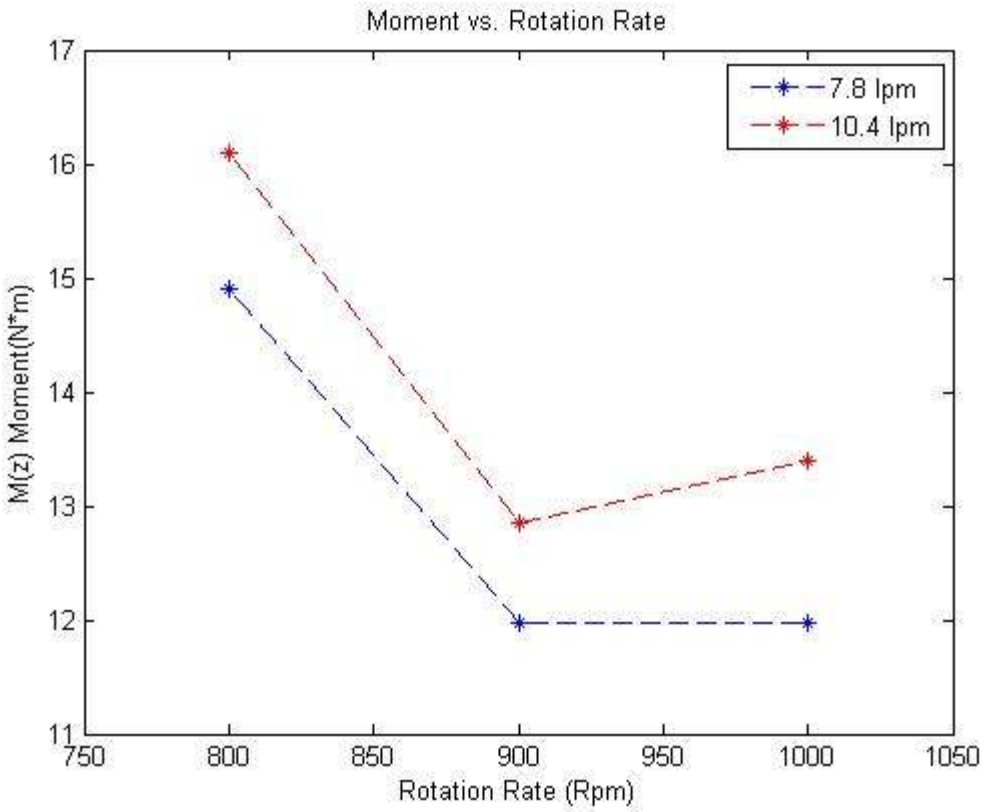

Figure 112: (Supported, cupped tool) A plot of moment (z-axis) showing an increased moment with increased traverse speed for all rotation rates. The moment was also generally reduced with increasing rotational speed.

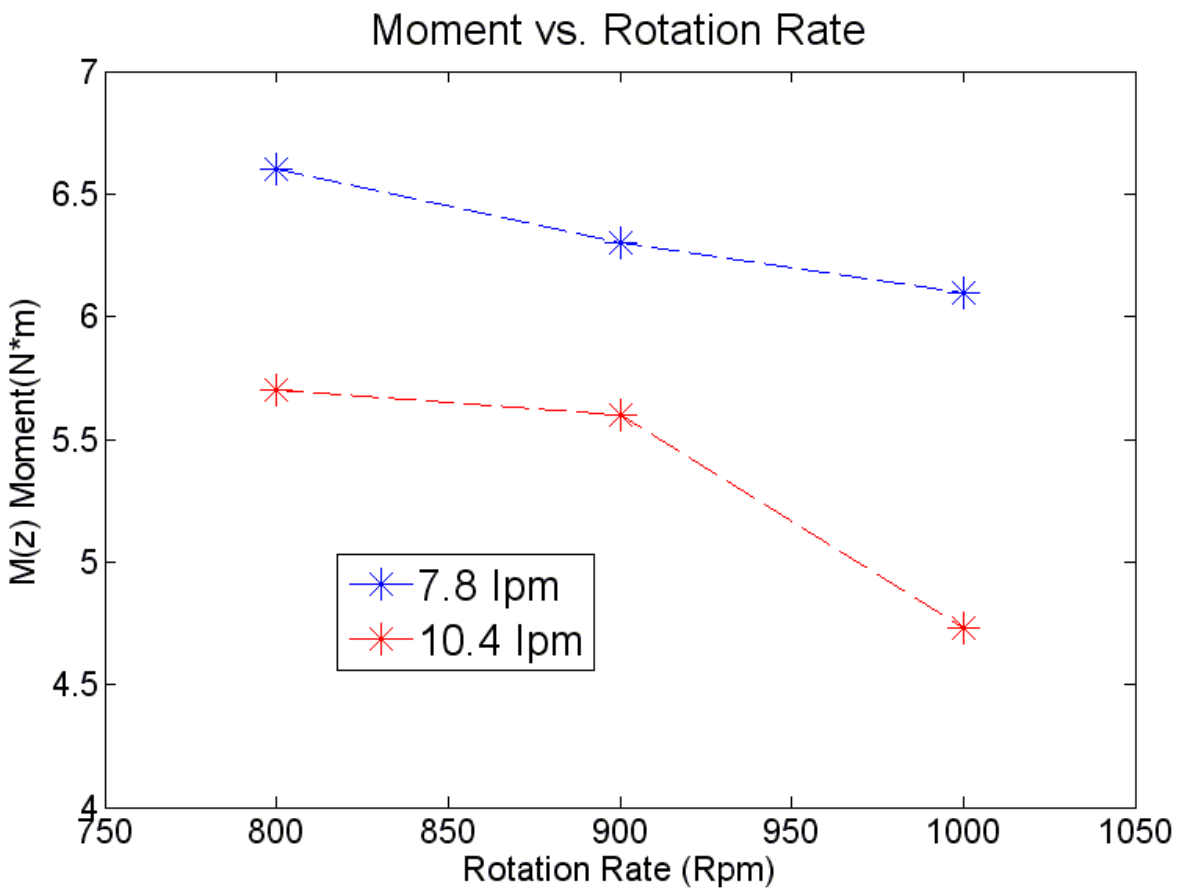

Figure 113: (Unsupported, conical tool) The moment decreased consistently with increasing rotational rate. Moment values were much lower for the partial penetration, conical tool portion of the experiment.

The xy-plane force direction and magnitude data for the cupped tool, supported setup is presented in Figure 114. It can be seen that increasing the traverse rate has the consistent and intuitive effect of pushing the tool more forcefully in the direction opposite the tool travel. Figure 115 shows the xy-plane force vectors for the conical tool, unsupported welds. In all cases for the conical tool the tool is being pushed towards the advancing side and against the direction of travel. For both the cupped and conical tools, the tool is pushed towards the advancing side in all cases. This is because the leading edge of the tool is moving towards the retreating side and it is at the tool leading edge where cooler and undisturbed metal is encountered.

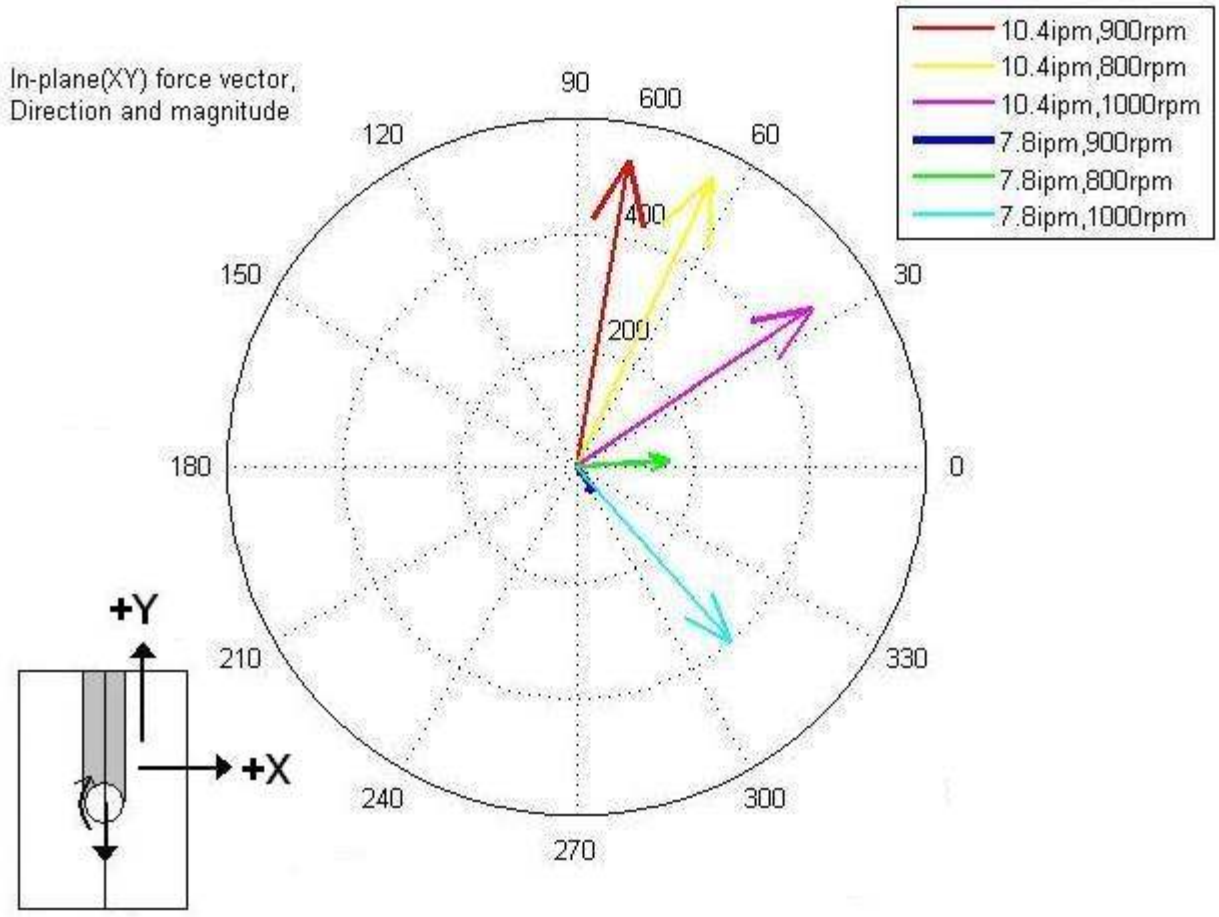

Figure 114: (Supported, cupped tool) The tool is deflected towards the advancing side at both traverse rate settings. At the higher travel speed setting the tool is deflected to the trailing side.

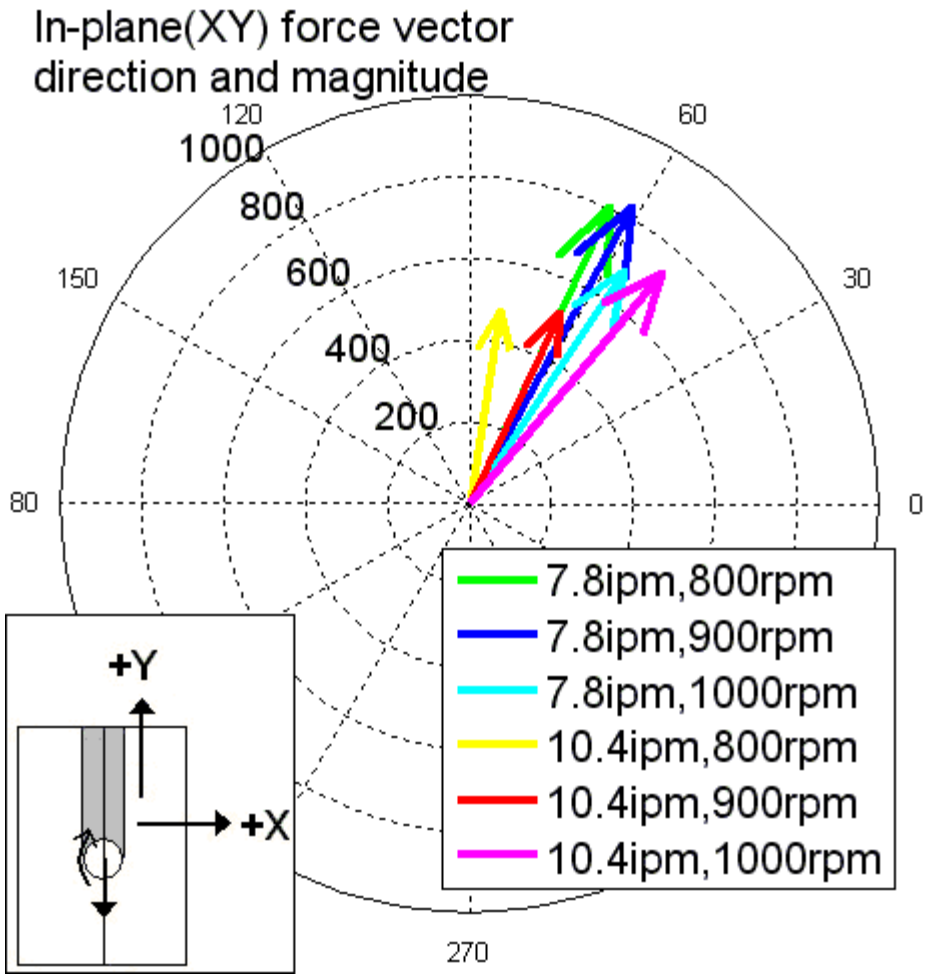

Figure 115: (Unsupported, conical tool) The tool is deflected towards the advancing, trailing quadrant.

For a valid comparison of partial and full penetration welds, both the apparent stress and the true stress of the partial penetration welds must be considered in the analysis. The true stress differs significantly from the apparent stress in the case of a partial penetration weld because the depth of the weld nugget differs significantly from the thickness of the material. Figure 116 defines the true and apparent stress of the weld samples. In the case of full penetration welds, the difference between true and apparent stress is small and is due an indentation left at the weld surface which was approximately 0.008" in depth. The apparent strength is of more practical significance because the entire thickness of the butted surfaces is available for joining and any indentation at the material surface or lack of penetration at the weld root is not desired. Tensile results are presented in Figure 117. The partial penetration, unsupported welds reached a maximum

apparent strength of 26% parent while the full penetration welds achieved a maximum of 68% parent.

The tensile testing results show that the true strength of the partial penetration welds is approximately equal to the apparent strength of the full penetration welds. The partial penetration welds are slightly reduced in strength (approximately 10%) in a proportional comparison, or true stress comparison, with the full penetration welds. This is likely due to the stress concentration factor presented by the crack-like, unwelded portion of the jointline. However, the effects of tooling cannot be ruled out.

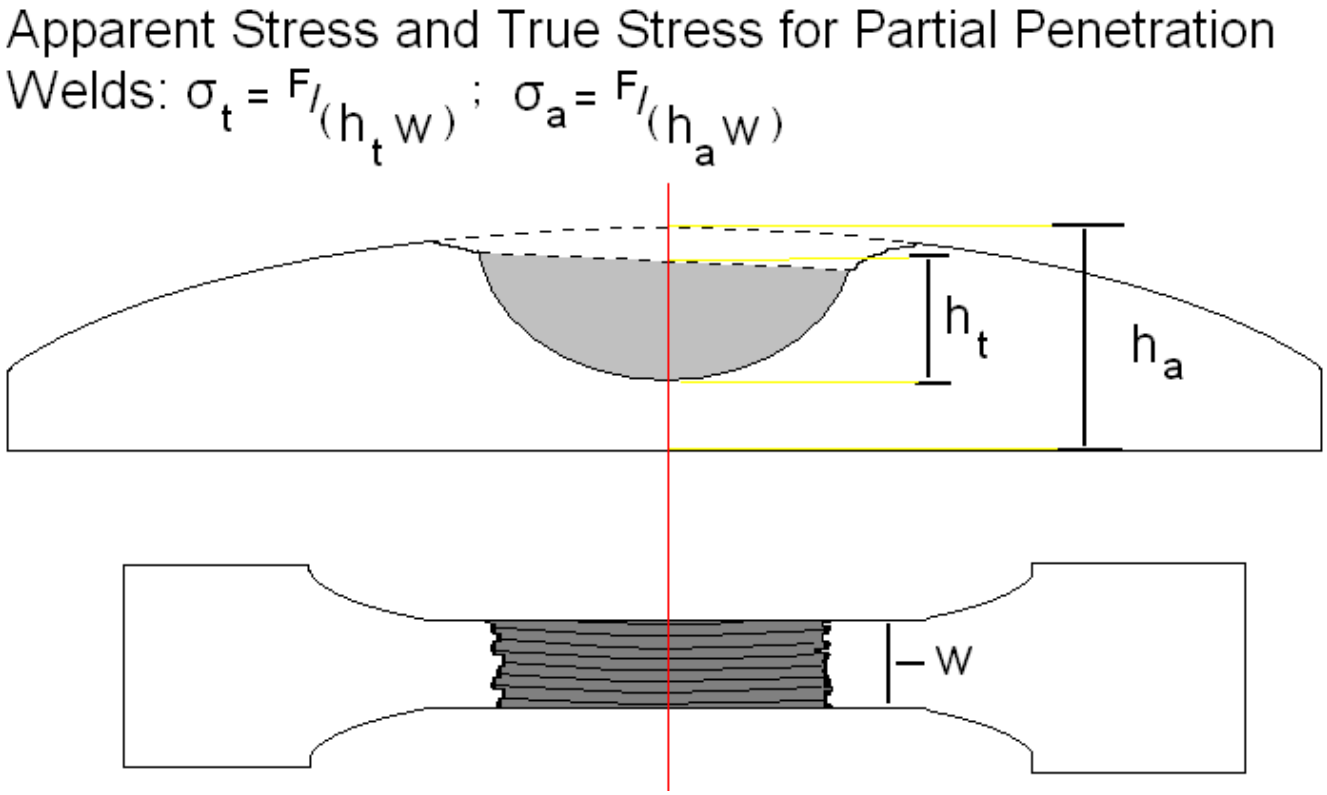

Figure 116: Explanation of true stress and apparent stress for partial penetration samples. All partial penetration welds were done in an anvil-less (unsupported) configuration.

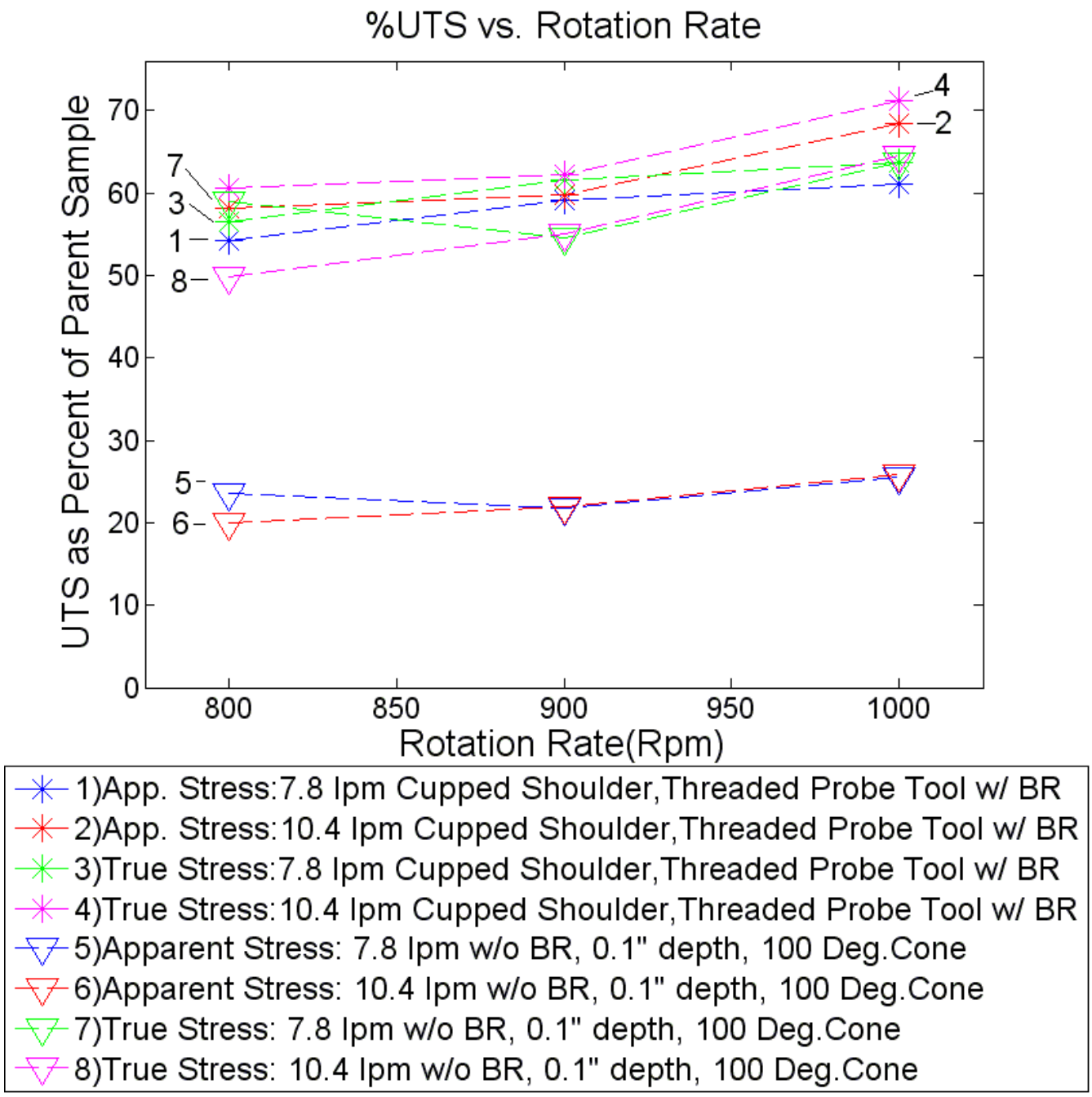

Figure 117: A comparison of apparent stress in full penetration weld tensile samples and apparent and true stress in partial penetration tensile samples. One tenth inch is 50% of the material thickness and partial penetration welds were made with the conical tool and no backing ring anvil.

For the partial penetration portion of the experiment, the experimental matrix depth was determined based on the depth at which weld root failure began to occur. Figure 119 a lateral macrosection view of an unsupported, butt configuration weld made

with a 100º conical tool (0.025” diameter snub-nose and 0.015” cupped nose recess) at 800rpm, 5.2 ipm, and a penetration depth of 0.11”. Figure 120 shows a similar weld made at 1000rpm, 10.4ipm, and a penetration depth of 0.11”. At this depth, unsupported welds made with the conical tool begin to split and protrude at the root for some of the tested weld parameters. The initiation of protrusion and splitting in the weld root at 0.110” was deemed undesirable by the authors for the some suggested applications (under external compression the strength is maintained only when the full butted jointline is undeformed). The experimental matrix was therefore performed at 0.100” where this did not occur. It should be noted however that the strength of the unsupported welds increased with depth beyond the experimental matrix depth of 0.100”. This can be seen in Figure 118 which shows the apparent tensile strength of all conical tool, partial penetration, unsupported welds performed.

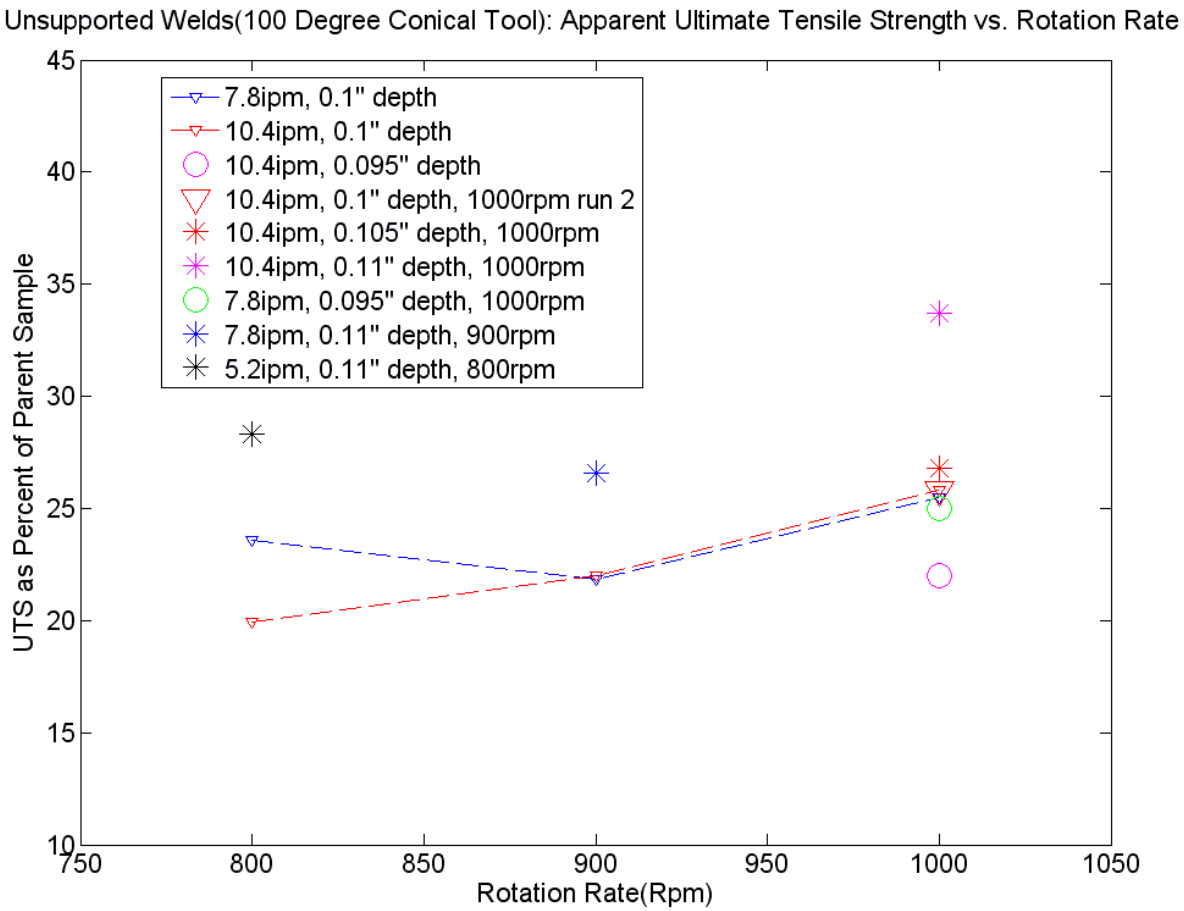

Figure 118: A comparison of apparent tensile strength in all unsupported, partial penetration experimental welds. The travel speed, penetration depth, and spindle rate setting are indicated. Note that strength continues to increase with depth beyond the matrix depth of 0.10" despite distortion at the base of the joint (see Figure 119 and Figure 120).

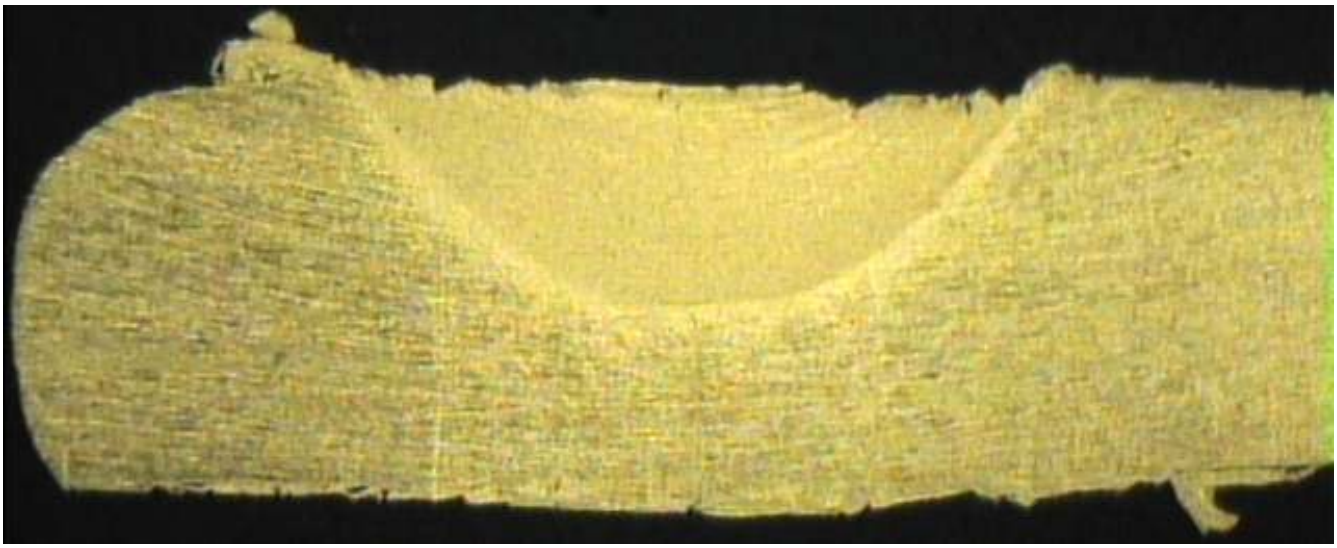

Figure 119: Macrosection view of an unsupported, butt configuration weld made with a 100º conical tool (0.025" diameter snub-nose and 0.015" cupped nose recess) at 800rpm, 5.2 ipm, and a penetration depth of 0.11".

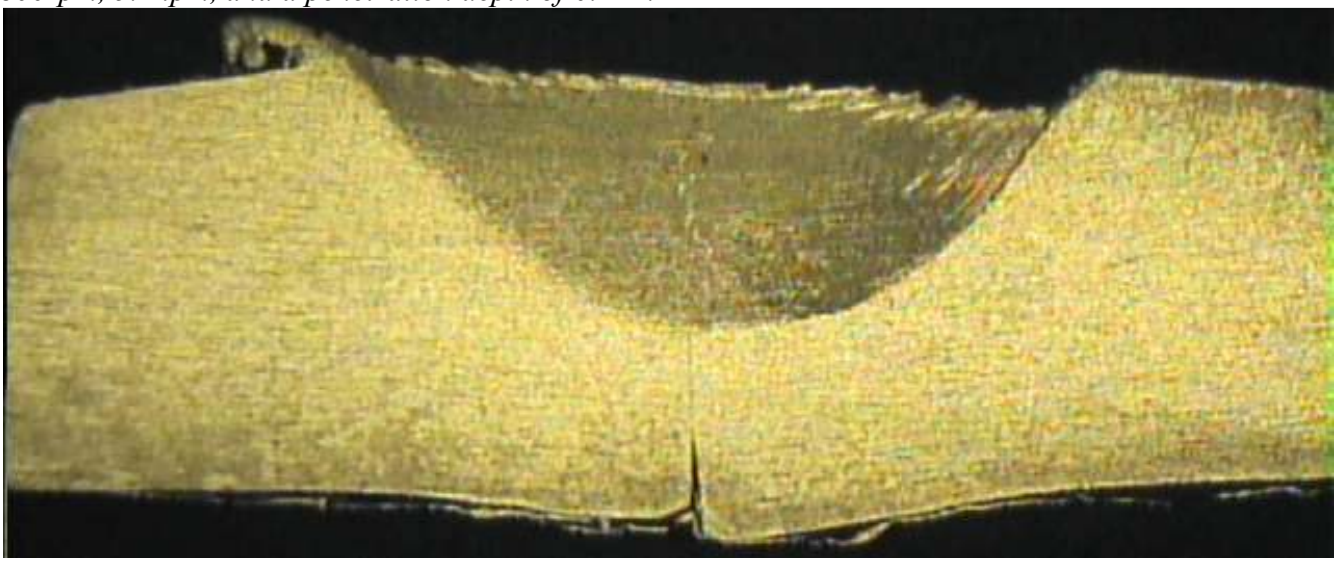

Figure 120: Macrosection view of an unsupported, butt configuration weld made with a 100º conical tool (0.025" diameter snub-nose and 0.015" cupped nose recess) at 1000rpm, 10.4ipm, and a penetration depth of 0.11". At this depth, unsupported welds made with the conical tool begin to split and protrude at the root for some of the tested weld parameters. The initiation of protrusion and splitting in the weld root at 0.110" was deemed undesirable by the authors for the suggested applications. The experimental matrix was therefore performed at 0.100" where this did not occur. It should be noted however that the strength of the unsupported welds increased with depth beyond the experimental matrix depth of 0.100".

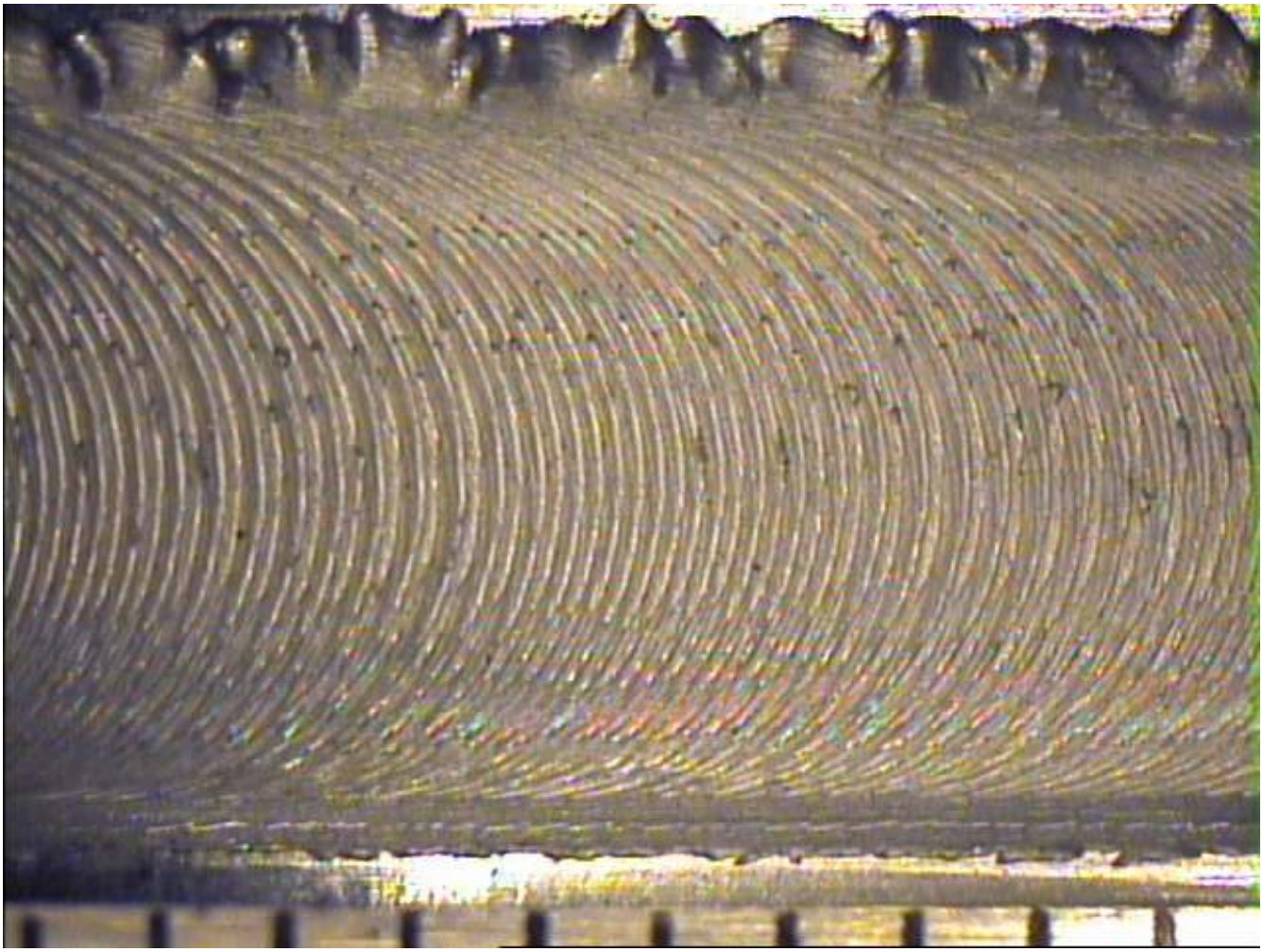

Figure 121: Surface appearance of an unsupported, butt configuration weld made with a 100° conical tool (0.025" diameter snub-nose and 0.015" cupped nose recess) at 1000rpm, 10.4ipm, and a penetration depth of 0.11" (1/16th inch demarcations).

In addition to the primary experimental matrix conical tool, unsupported, partial penetration welds were performed at four depths at the 10.8ipm and 1000rpm parameter setting to determine the effect on weld strength as well as to determine moment and axial force relationships with depth for control purposes. Figure 122 and Figure 123 show that both axial force and weld moment increase in a somewhat linear fashion with respect to weld depth at this parameter setting. Note in these charts that the relationship between depth and moment is a more reliable one and it is for this reason that a torque based feedback control algorithm was used to maintain constant depth around the circumference of the sphere. Both axial force and torque based control algorithms were tried and it was found that the torque method was more reliable for this particular setup

and tooling. Torque is highly dependent on the surface area of the weld interface (or the tool contact area) and this value increases in a reliable fashion with penetration depth for a conical tool. For this reason, torque is a reliable indicator of penetration depth and a torque based control algorithm is especially effective for reliably following the desired depth path with a conical tool.

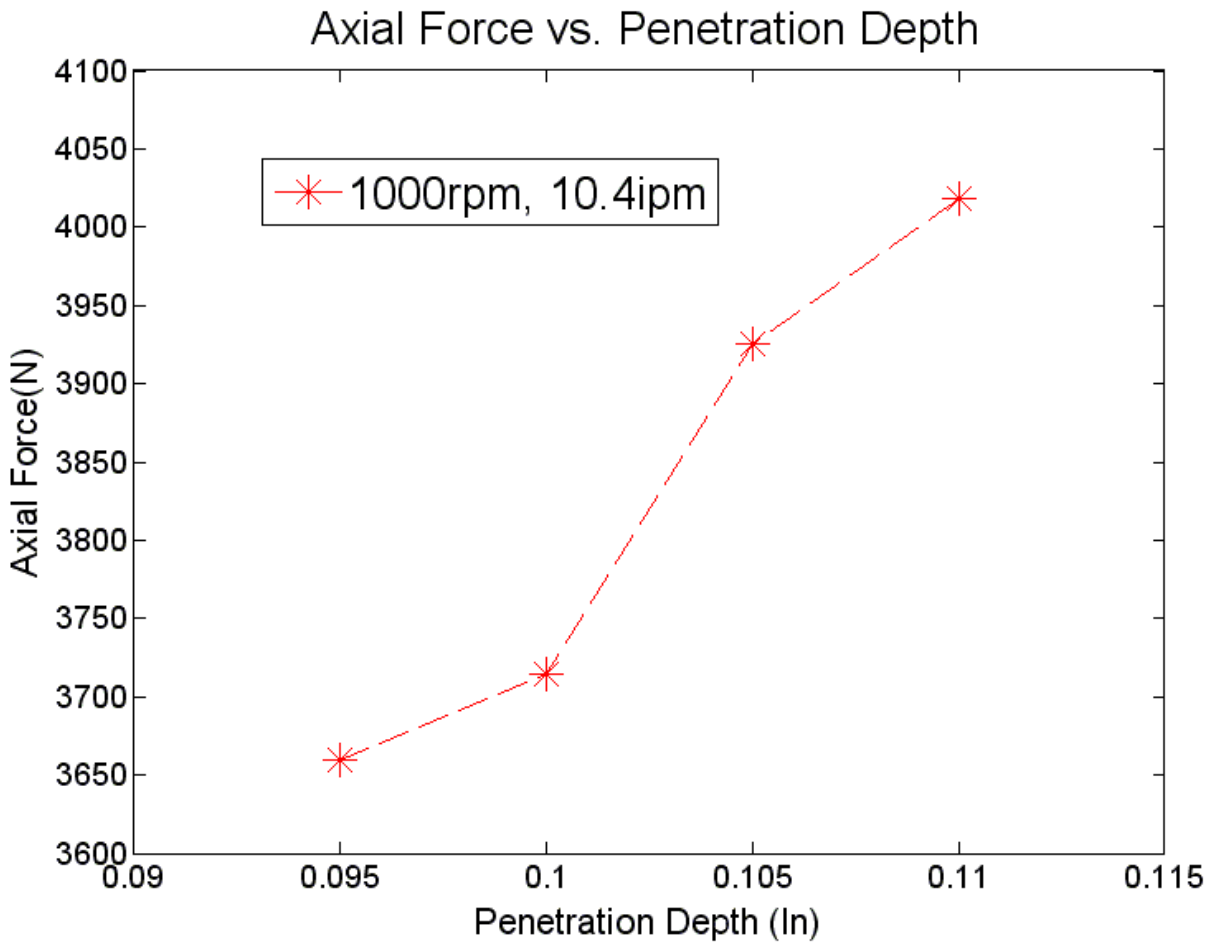

Figure 122: Conical tool, unsupported, partial penetration welds were performed at four depths at the 10.8ipm and 1000rpm parameter setting and showed a consistent increase in axial force with penetration depth.

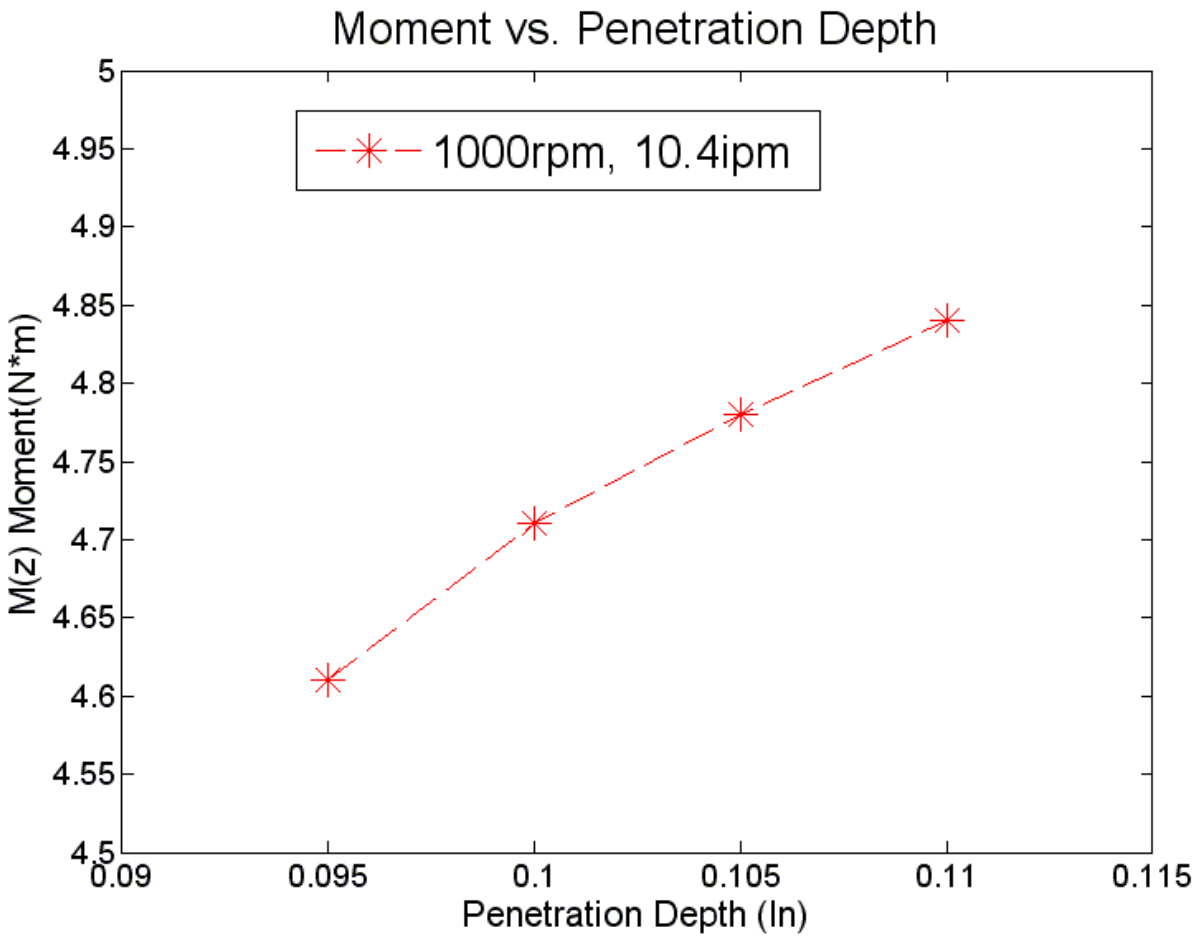

Figure 123: Weld moment was a better indicator of penetration depth for the conical tool and a torque based control method was used in the experiment to maintain penetration depth.

Fluent CFD Model

A computational fluid dynamics (CFD) model was made for the tool used in the supported experiment and the tool used in the unsupported experiment. The Eulerian, finite volume, CFD solver, Ansys FLUENT was used with the implicit formulation. The weld material viscosity function was set by user-defined function and defined according to the visco-plastic model used by Sheppard and Wright [29,30]. Fluent separates the weld interface into a surface and shadow surface. Heat energy was input at the weld interface into the material as defined by a user-defined function which applied heat

locally in proportion to the local tool velocity. Another user defined function input heat at the interface on the tool side by equating the temperature in these cells to the temperature of adjacent cells on the material side of the interface. The total heat input at the interface (both sides included) was defined by the weld power method as the product of tool radial velocity (rad/s), weld torque (N·m), and some weld efficiency factor (β). In the models presented, it was assumed that all mechanical energy from the tool was converted to heat input into the tool and weld material (β=1) [31]. A rotational velocity of 1000rpm and traverse speed of 7.8ipm were used in the presented model. The tool rotational axis remained stationary while a velocity inlet and an outflow boundary condition (BC) were used to simulate a traverse speed. Thermal BC's are defined as follows (W/(m^2·K)): surface, 10; bottom unsupported, 8; bottom supported 50; shank, 15; tool-top, 30. Figure 124 shows the geometry and mesh (584,401 tetrahedral cells) of the threaded probe tool and the weld material created in the preprocessor Gambit. The mesh was created by finely meshing the interface and establishing a mesh growth rate in the tool and material volumes. The mesh was thus finest at the interface where temperature and momentum gradients were highest and most course near the model boundaries. Figure 125 shows the threads of this geometry created in gambit.

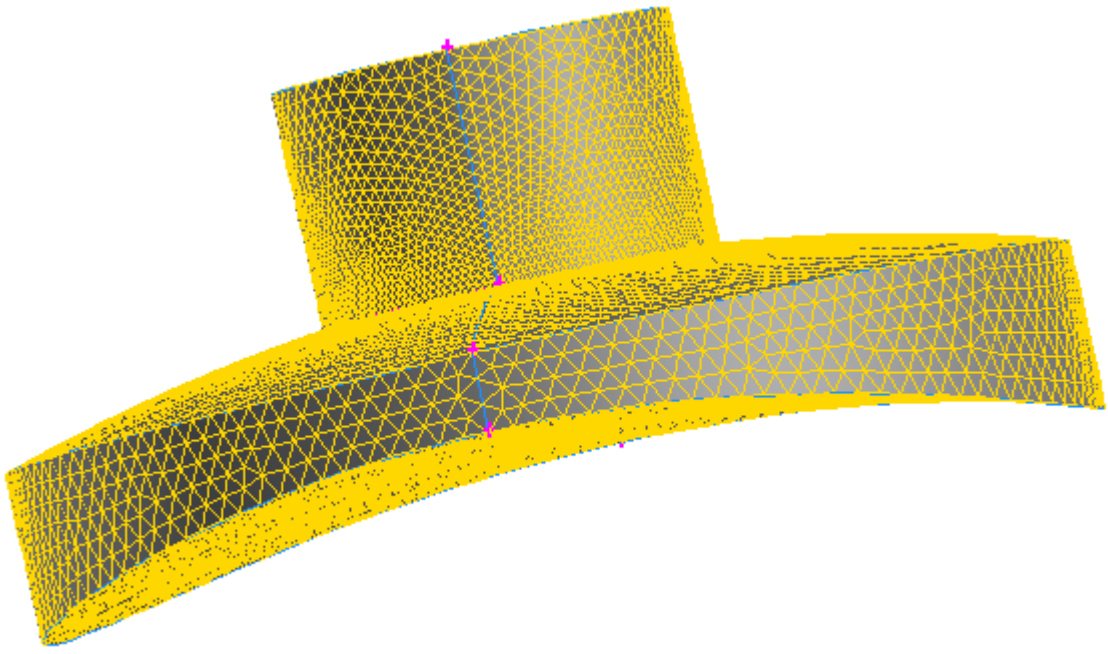

Figure 124: (threaded tool) Tetrahedral mesh created in the Fluent preprocessor Gambit.

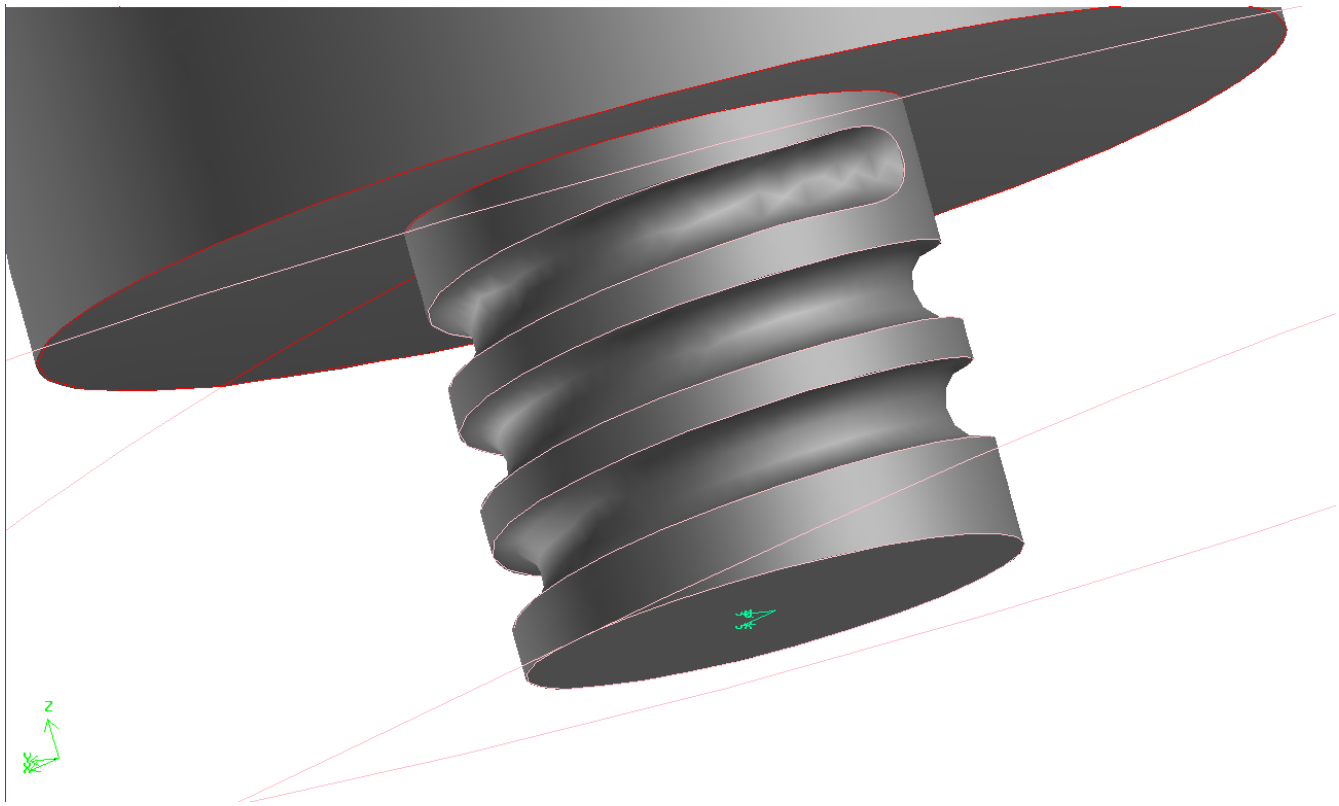

Figure 125: (threaded tool) Geometry

Figure 126 shows the resulting temperature contours around the surface of the tool for the threaded geometry. The temperature is highest on the shoulder of the tool and where the probe meets the shoulder. Figure 127 shows the temperature field over the material surface reported by the model for the threaded tool and supported geometry.

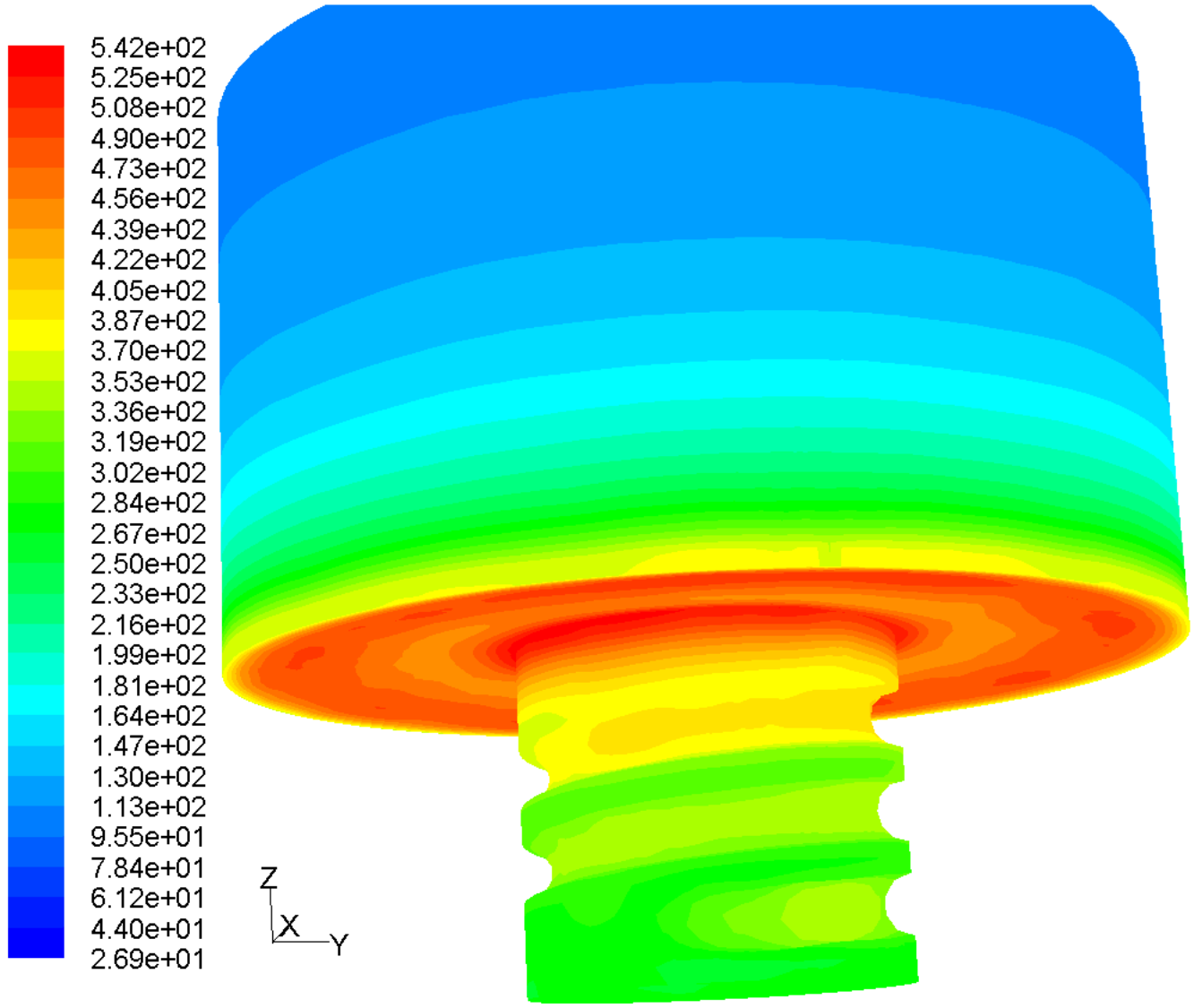

Figure 126: (threaded tool) Contours of temperature in degrees Celsius.

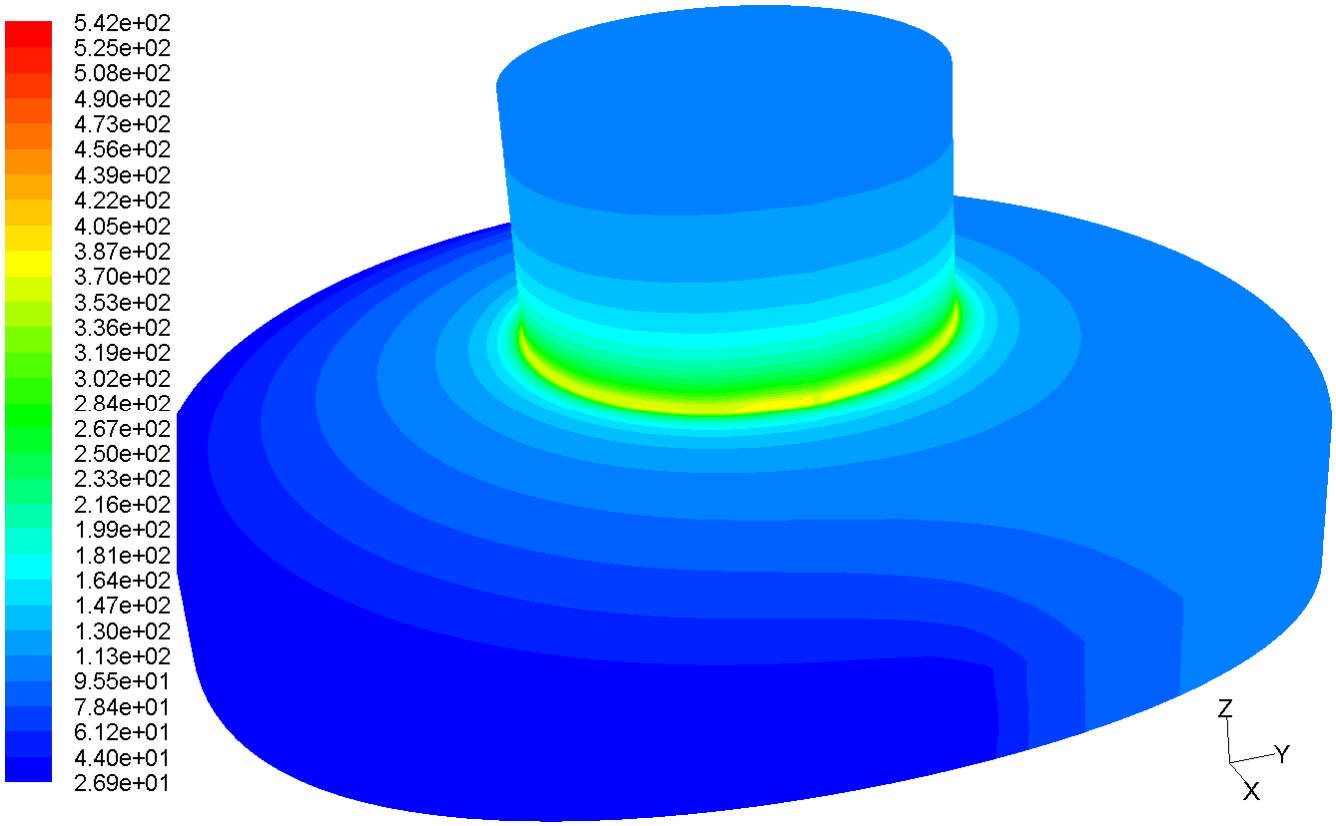

Figure 127: (threaded tool) Contours of temperature in degrees Celsius.

A similar model containing 363971 tetrahedral cells was created for the conical tool geometry and setup. The discrepancy in cell count is justified by the relative complexities of the two geometries. The complicated geometry of the threaded tool called for a finer mesh than the relatively trivial conical geometry. The thermal boundary condition on the bottom side of the material was reduced from 50 to 8 W/(m^2·K) for the unsupported geometry to reflect the absence of an internal steel anvil. The conical tool, unsupported geometry is shown in Figure 128.

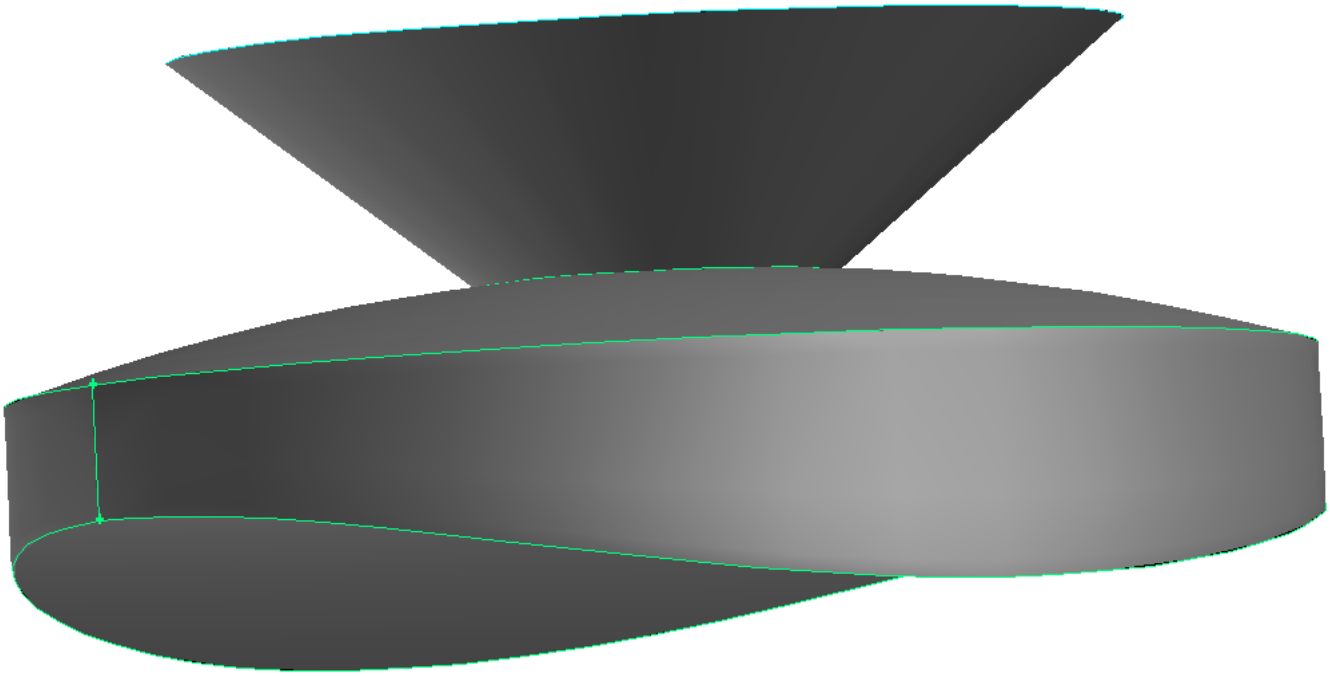

Figure 128: (conical tool) Geometry created in the Fluent preprocessor Gambit.

The CFD model contours of temperature across the lateral cross section are shown in Figure 129 and Figure 132 and can be used to predict the appearance of the heat affected zone in experimental welds. The model temperature contours which are taken at the same orientation as the experimental macrosections, shown in Figure 131 and Figure 134, can be compared to the heat affected zone visible in experimental macrosections. The macrosections show three distinct regions: the central, bright thermo-mechanically affected zone (TMAZ) containing the weld nugget; the darker, parent metal; and a transition region of intermediate appearance, the HAZ. Good agreement in the shape and size of the HAZ can be seen when lateral section temperature contours are compared with the macrosections from the experiment. Additionally, contours of velocity magnitude taken across a lateral cross section in the CFD model, shown in Figure 130 and Figure 133, can be compared to the shape and size of the TMAZ. Again, comparison with the macrosections shows good agreement.

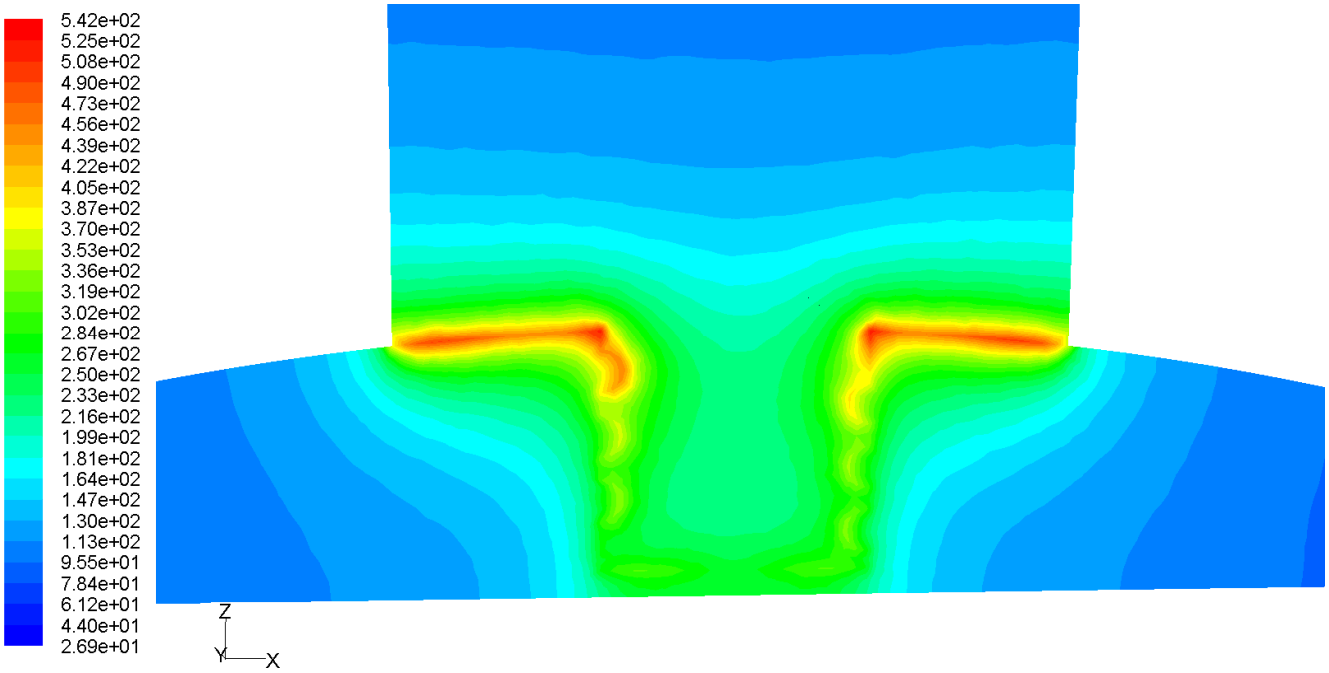

Figure 129: (threaded tool) Lateral contours of temperature (C) showing the heat affected zone (HAZ).

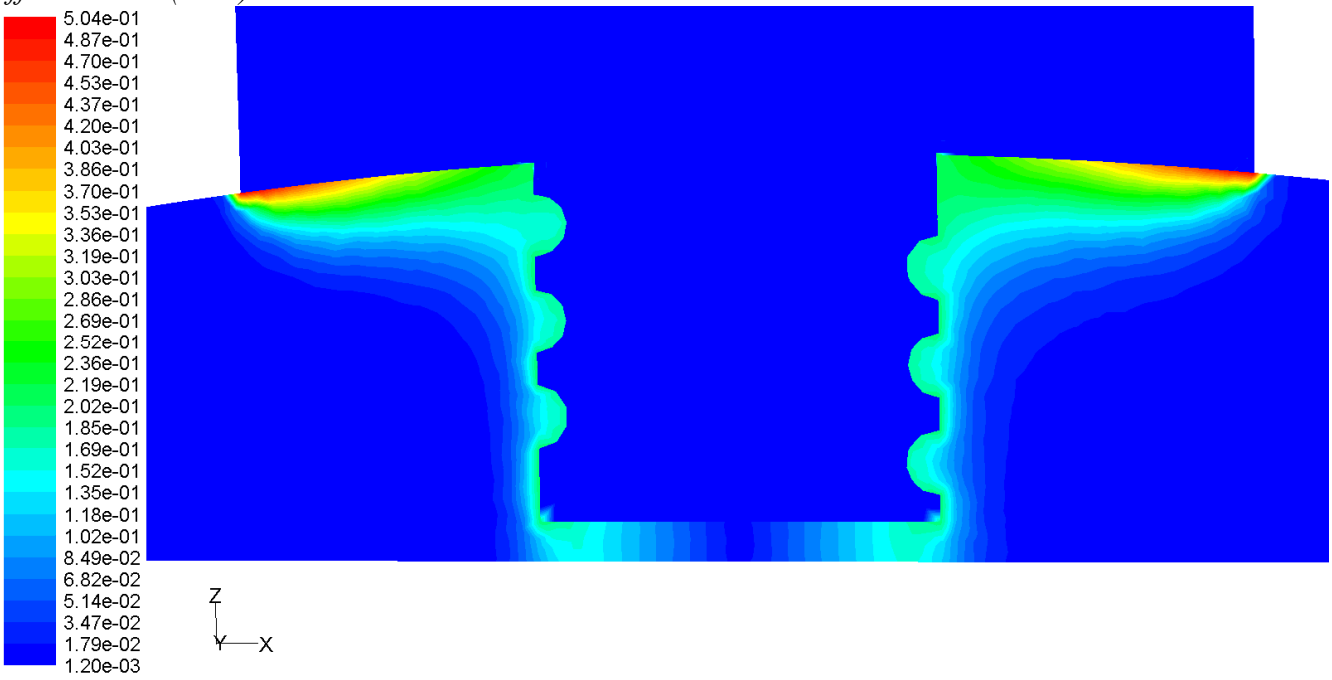

Figure 130: (threaded tool) Lateral contours of velocity magnitude (m/s) showing the thermo-mechanical affected zone (TMAZ).

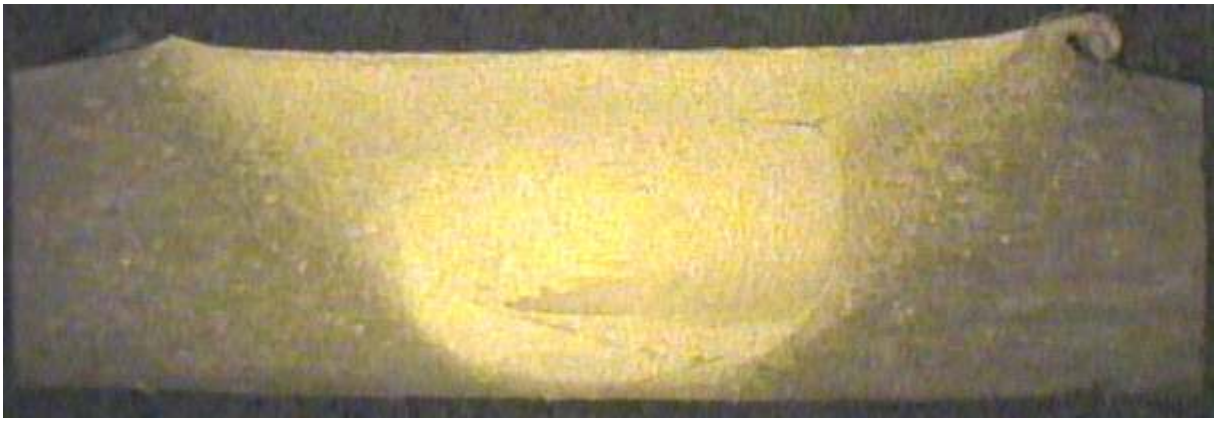

Figure 131: (threaded tool) Lateral macrosection corresponding (1000rpm, 7.8ipm) to the CFD simulated weld showing the TMAZ(bright), parent metal(dark), and transitional HAZ (intermediate). The HAZ region can be compared to isotherms in Figure 129 and the TMAZ or stirred zone can be compared to the velocity magnitude contour in Figure 130.

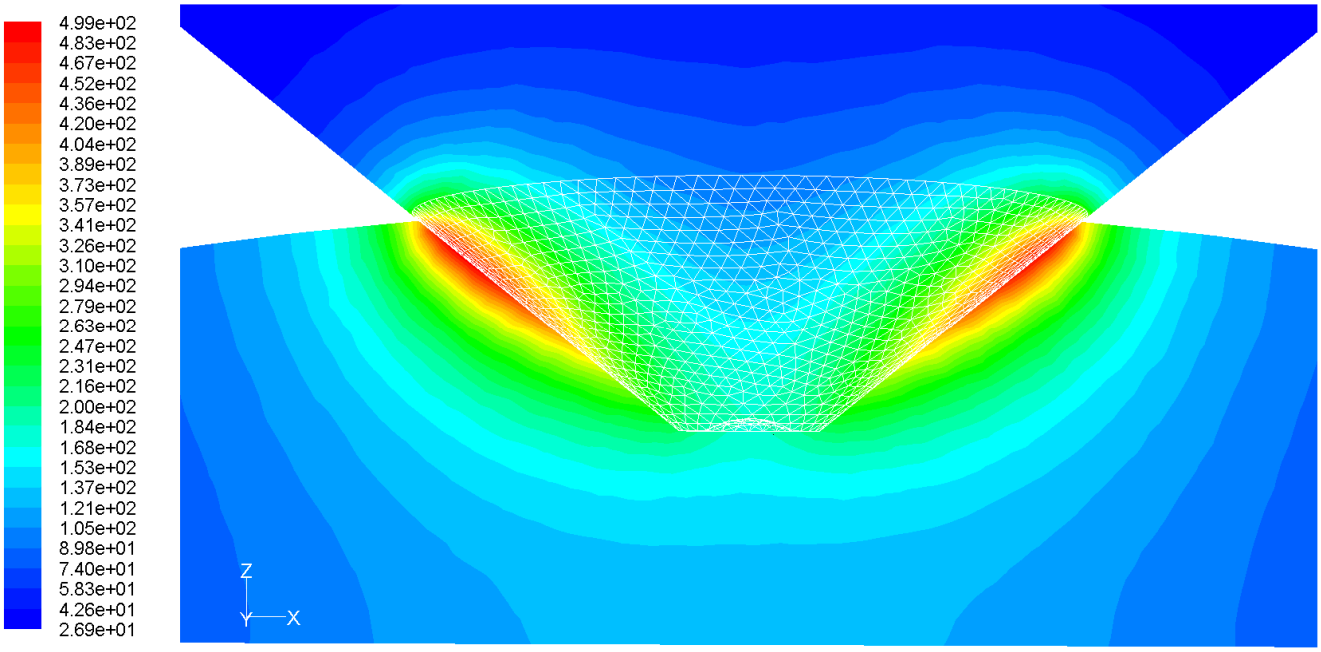

Figure 132: (conical tool) Lateral contours of temperature (C) showing the heat affected zone (HAZ).

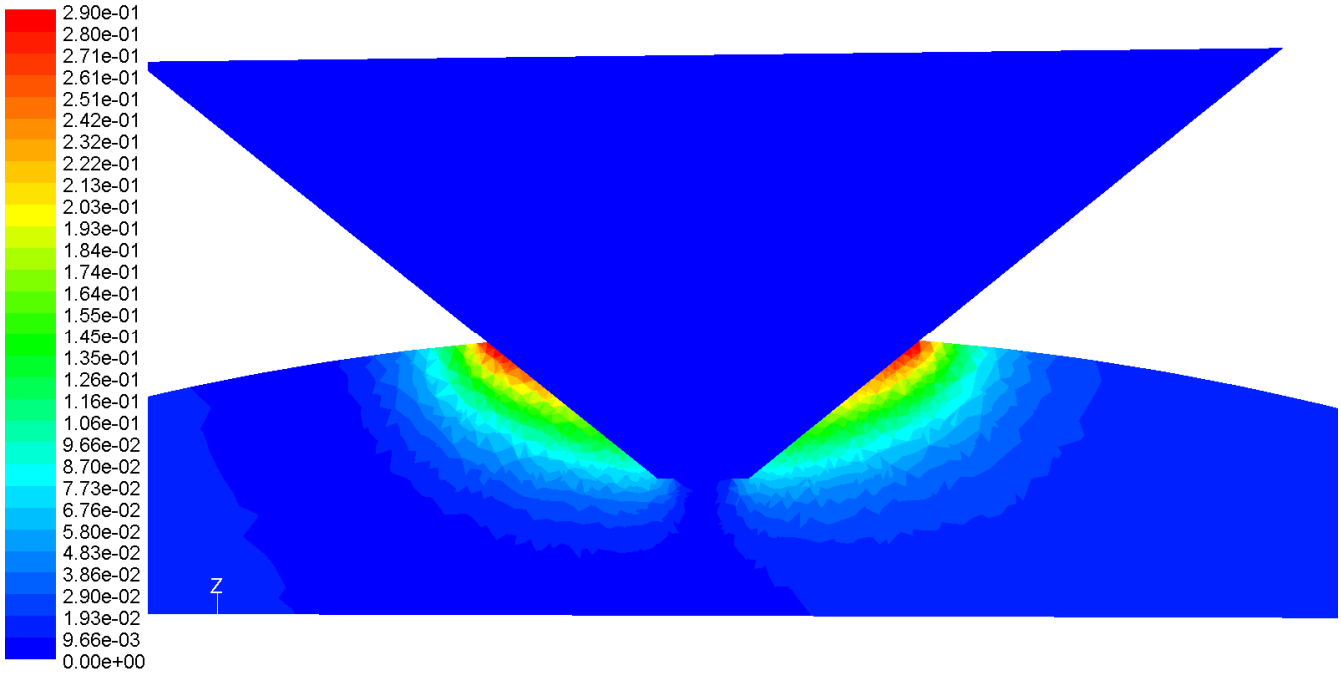

Figure 133: (conical tool) Lateral contours of velocity magnitude (m/s) showing the thermo-mechanical affected zone (TMAZ).

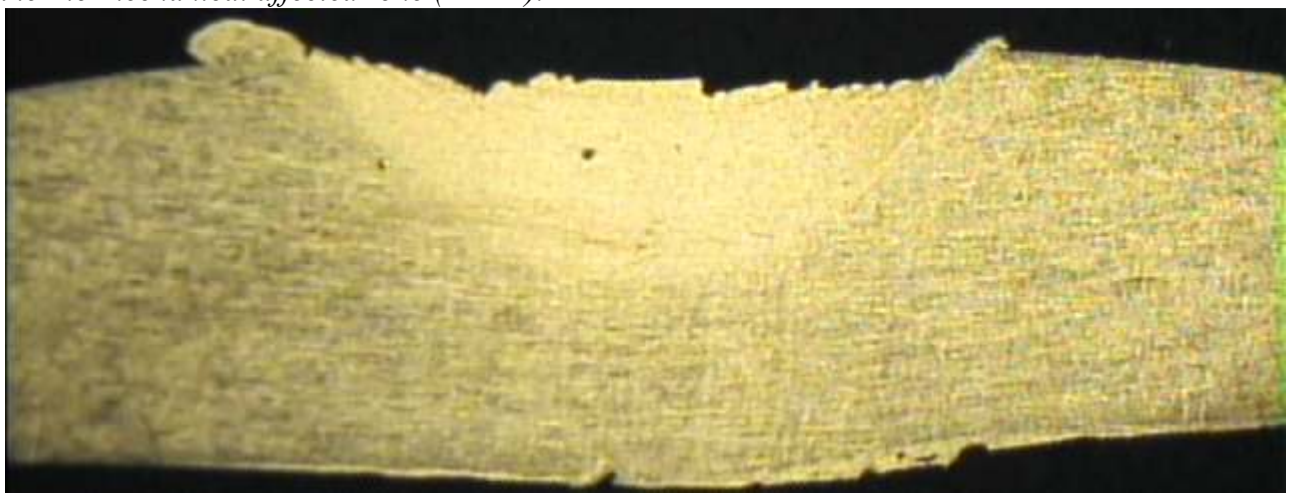

Figure 134: (conical tool) Lateral macrosection corresponding (1000rpm, 7.8ipm) to the CFD simulated weld showing the TMAZ(bright), parent metal(dark), and transitional HAZ (intermediate). Figure 132 and Figure 133 show the HAZ and TMAZ respectively forming transposed bowl shaped regions around the weld tool in the experimental model and this shape is verified in the macrosection.

Conclusions

The results presented here show that aluminum alloy hemispheres can be reliably joined by FSW. Additionally, the control techniques used in this experiment show that system eccentricities can be accounted for via multiple methods. The relative height of the material surface can be taken at various points around the circumference of the sphere and a preplanned path can be taken by the tool to maintain the appropriate penetration depth. The unique geometry of the conical tool can be used advantageously in torque based feedback control of weld penetration depth, as measured weld toque proved to be a strong and reliable indicator of weld depth. Additionally, it was shown that for cases where the interior of the vessel is inaccessible and internal support is not possible, partial penetration welds of similar proportional strength can be achieved without compromising the material interior surface. A lack of material distortion at the joint base is required for external compression applications.

The conical tool produced, 50% penetration welds in an unsupported configuration which ranged from 20-26% parent material strength in a practical comparison using their apparent stress. The cupped shoulder tool produced full penetration welds with interior support which ranged from 54-68% of the parent material strength comparing apparent stress. The maximum strength could be improved by testing a wider range of parameters, as welds made with both setups were stronger at higher travel and rotational settings. Additionally, a penetration ligament of 0.014" was used in the full-penetration portion of the experiment. A more aggressive penetration ligament (i.e. one closer to 0.006") would likely increase weld strength by eliminating any joint remnant at the weld root. Partial penetration welds continued to increase in strength with depth outside the matrix depth of 0.10", however with the introduction of some distortion at the weld root. In this experiment it was assumed that this distortion was unacceptable and the experiment was done at a depth where no distortion occurred. Future work could explore the depth to which this relationship continues to hold should a suitable application be identified.

Additionally, modifications to the tooling used in the experiment would likely result in strength increases as only a single tool geometry was considered for each case. A more complicated probe geometry and scrolled shoulder design could improve test strengths for the supported welds. Adjustments to the inclusive angle of the conical tool

and the addition of features (e.g. spiraled groove) to its surface would likely improve strengths in the unsupported welds. It should also be considered that in the supported setup the joint material could be welded to the anvil with a sufficiently long probe if removal of the interior anvil was considered unnecessary. The anvil could be composed of an identical or dissimilar alloy. The resulting joint would then be of high extrinsic strength.

Appendix

Figure 135: Tools used in the experiments (from left: 90° conical tool; cupped shoulder (5/8" diameter), threaded probe (0.20" diameter) tool; snubbed nose, cupped nose, 100° conical tool; snubbed nose, 100° conical tool; 100° conical tool; 140° spiral-cut, conical tool(Edison Welding Institute test design)).

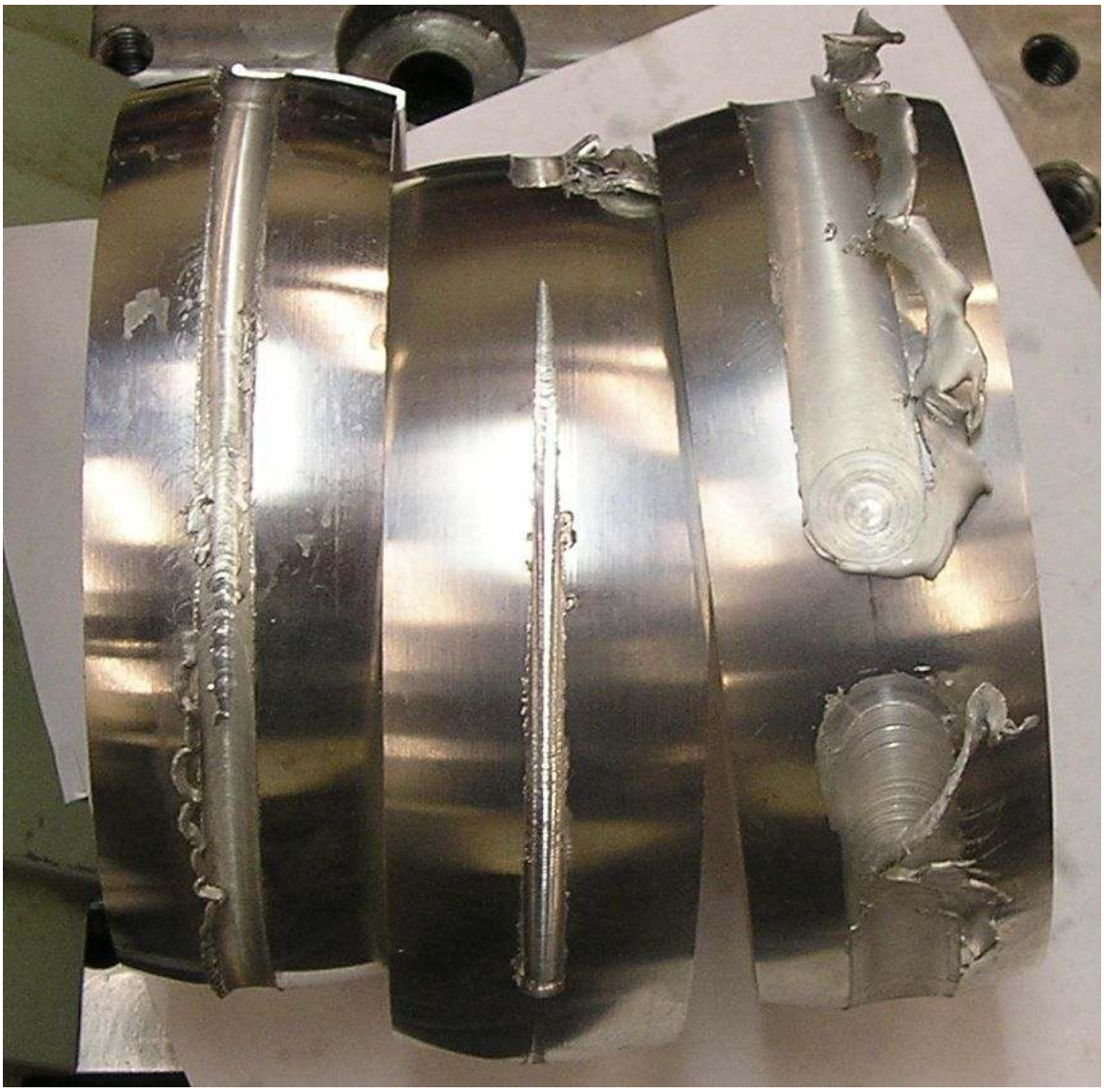

Figure 136:(from left: Tapered retraction over welded material (100º snub-cup); bead on plate tapered retraction (100º snub-cup); 0.09" depth weld made with a 140º spiral-cut, conical tool).

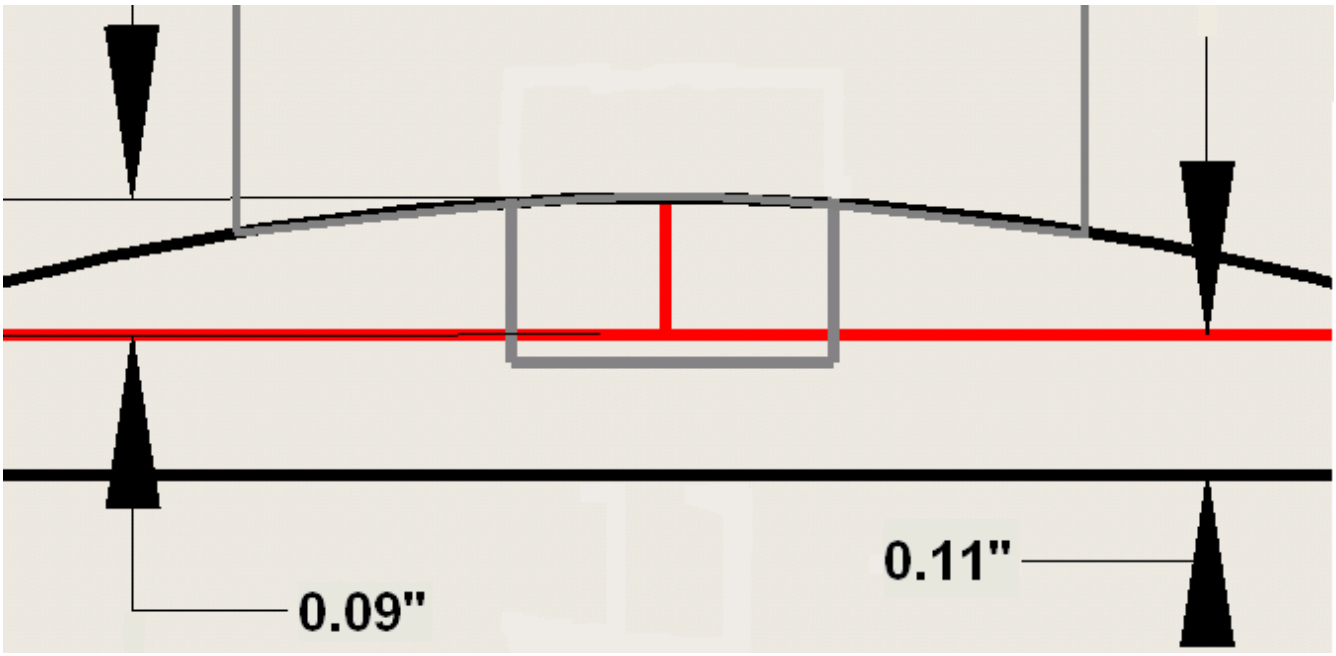

Figure 137: Anvil-less butt/lap type weld joining 3 material sections and not performed in the experiments presented in this work. The joint and materials could alternatively be configured with the lateral interface following the curvature of the top surface. Unsupported welds of this kind with a traditional FSW tool create a bead type defect on the underside. A shoulder-less, conical tool was used in unsupported welds in the experiment.

References:

[1] Friction-stir butt welding; GB Patent No. 9125978.8, International patent application No. PCT/GB92/02203; W M Thomas, E D Nicholas, J C Needham, M G Murch, P Temple-Smith, C J Dawes; 1991
[2] Bobbin-Tool Friction-Stir Welding of Thick-Walled Aluminum Alloy Pressure Vessels; E N Dalder, J W Pastrnak, J Engel, R S Forrest, E Kokko, K Mc Ternan, D Waldron; Welding Journal (AWS), April 2008, 40-44
[3] Website: Space Electronics LLC, http://www.space-electronics.com/Products/air_bearings.php
[4] Personal comunication with Dan Otlowski Space Electronics LLC
[5] Stress and strain analysis of the spherical pressure vessel: analytical and numerical approach: J Sertić, D Kozak; Int Conf on Adv Tech for Developing Countries, Jun 28-30, 2006 Rijeka, Croatia
[6] Spin dynamics of the LAGEOS satellite in support of a measurement of the earth's Gravitomagnetism; S Habib, D E Holz; Phys. Rev. D 50, 6068 - 6079 (1994)
[7] Website: Armadillo Aerospace, http://www.armadilloaerospace.com/n.x/Armadillo/Home/News?news_id=330 http://www.armadilloaerospace.com/n.x/armadillo/home/news?news_id=309

[8] Metallurgical analysis of ablated aluminum alloy hemispheres; G J Fischer, R Maciag ; Internal Report, Polytechnic Inst of Brooklyn NY, Jul 1962
[9] Numerical analysis of the nonlinear deformation of a spherical pressure vessel made of laminated glass-plastic; Y M Grigorenko, A T Vasilenko, N N Kryukov, and T V Krizhanovskaya; Prikladnaya Mekhanika, Vol. 23, No ii, pp. 27-32, November, 1987
[10] Experimental study of shape imperfections and the load-carrying capacity of hemispherical glass shells; P F Zolotarev; Problemy Prochnosti, No. I0, pp. 91-95, October, 1981
[11] Cryoformed stainless steel pressure vessels for space applications; A Faure, L Gourgeon; Proc Eur Conf on Spacecraft Struc, Mat and Mech Testing, Braunschweig Germany, 4-6 Nov 1998
[12] Estimating the carrying capacity of spherical vessels from dynamic loading data; I V Belinskii, E I Zharkov, N A Zvonarev; Fizika Goreniya i Vzryva, Vol. 28, No. 5, pp. 117-119, Sep-Oct, 1992
[13] Elastic analysis for thick cylinders and spherical pressure vessels made of functionally graded materials; Y.Z. Chen, X.Y. Lin; Comp Mat Sci, 44 (2008) 581–587
[14] A study on failure characteristic of spherical pressure vessel; H S Lee, J H Yoon, J S Park, Y M Yi; Journal of Mat Processing Tech 164–165 (2005) 882–888
[15] Study on spherical pressure vessel of ceramics for deep-sea buoyancy module applications; Y Yano, S Takagawa; Japan Agency for Marine-Earth Science and Technology (JAMSTEC); Oceans 2004 MTS, 1554- 1559 Vol.3
[16] Design and development of an aluminum lined composite overwrapped spherical pressure vessel; R Veys, A Cederberg, D B Tiller; Brunswick Corporation, Defense Division, Lincoln Nb, Internal Report AIAA-89-2642, 1989
[17] Design and development of a carbon overwrapped aluminum lined spherical pressurant tank; D B Tiller, C F Murray, R B Veys; Brunswick Corporation, Defense Division, Lincoln Nb, Internal Report, 1990
[18] Behavior and ultimate tensile strength of partial penetration groove welds; D P Gagnon, D J Kennedy, 1987
[19] Evaluation and tensile strength of partial penetration butt welded joints by ultrasonic testing; H Matsuura, A Kaji; Jpn Soc Mech Eng , Vol 66, No 647, A, 1419-1424, 2000
[20] The Effect of Mismatch on the Collapse Strength of Machined Hemispherical Shells; M G Costello; Naval Ship Research and Development Center, Washington DC, Internal Report Ad0874760, 1970
[21] A new, highly efficient deep water ROV buoyancy system; E M Patton, T S Rennick; Offshore Technology Conference, 3 May-6 May 1999, Houston Tx
[22] Partial-penetration welded connections for aluminum compression members; J H Jennison, R S Gill; Naval Ordinance Test Station, China Lake Ca, Internal Report AD0602361, 1964
[23] Method of friction stir welding and retractable shoulderless variable penetration friction stir welding tool; US Patent #7,234,626; T Trapp, J Fischer, J Bernath; Edison Welding Institute (EWI), 2007
[24] Retractable shoulderless variable penetration friction stir welding tool; US Patent #7,404,510; T Trapp, J Fischer, J Bernath; Edison Welding Institute (EWI), 2007

[25] The application of shoulderless conical tools in friction stir welding: An experimental and theoretical study; D H Lammlein, D R DeLapp; Mat. And Design, Volume 30, Issue 10, 4012-4022, Dec 2009
[26] Torque control of friction stir welding for manufacturing and automation; W R Longhurst, A M Strauss, G E Cook, P A Fleming; International Journal of Advanced Manufacturing Technology; .Submitted June 17, 2009 and under review.
[27] Experimental investigation of the influence of the FSW plunge processing parameters on the maximum generated force and torque; S Zimmer, L Langlois, J Laye, R Bigot; Int J Adv Manuf Technol, July 2009
[28] Introduction to Robotics: Mechanics and Control (3rd Edition); J J Craig
[29] Determination of flow stress: Part 1 constitutive equation for aluminum alloys at elevated temperatures.; T Sheppard, D Wright; Met Technol 1979, Jun 6, 215–23
[30] Hot workability; C M Sellars, W J M Tegar; Int Metall Rev 1972; 17:1–24
[31] Torque based weld power model for friction stir welding J W Pew, T W Nelson, C D Sorensen; Sci Technol Weld Join 2007;12(4):341

CHAPTER V

FRICTION STIR WELDING OF SMALL DIAMETER PIPE: AN EXPERIMENTAL AND NUMERICAL PROOF OF CONCEPT FOR AUTOMATION AND MANUFACTURING

D.H. Lammlein, B. T. Gibson, D. R. DeLapp, C. Cox, A. M. Strauss, G. E. Cook. Friction Stir Welding of Small Diameter Pipe: An Experimental and Numerical Proof of Concept for Automation and Manufacturing. *Proceedings of the Institution of Mechanical Engineers, Part B: Journal of Engineering Manufacture*, Submitted July 15, 2010.

Abstract

Friction stir welding (FSW) is a powerful joining process which is limited by its range of application and processing rate. Here the range of application is extended to small diameter butted pipe sections and high processing rates are applied for increased productivity in manufacturing. Full penetration friction stir welds are performed on butted sections of aluminum alloy 6061-T6 pipe. These pipe sections are relatively small in diameter, 4.2 inches, and relatively thin walled, 0.2 inches. The small radius of curvature distinguishes this weld configuration geometrically from a butted plate configuration and presents unique challenges. This work confronts these challenges using experimental and numerical methods. A FSW process method producing acceptable pipe joints is demonstrated.

Introduction

Friction stir welding (FSW) is an effective and consistent materials joining technology which produces high strength and high integrity joints, particularly in aluminum alloys (Thomas, 1991). FSW is also attractive because it is a solid-state process, with temperatures not exceeding the melting point of the work material. Its use is limited primarily by the combined expense of the FSW machine itself and the lack of an operating knowledge base. However, superb joint quality and low continuing

operating costs for the machine mean this initial expense can often be justified, particularly in vehicular applications (aerospace, automotive, and rail). FSW has been demonstrated on standard geometries like butted, lapped, and t-oriented joints. Its implementation on small diameter pipes could extend its use to the petroleum, petrochemical, and natural gas industries where high weld volume would justify the upfront costs of FSW.

Additionally, FSW at a high rate of travel would increase output for manufacturing and further reduce the energy expended per unit length of weld. High traverse rates are tested in this work with good results. By increasing the rate of travel, the time spent by the work at elevated temperatures is reduced and the total heat input into the pipe sections is reduced. Excessive heat is undesirable, as it causes detrimental changes in the material properties of the parent material.

Fusion welds are performed commonly on small diameter aluminum pipe (Kou & Le) (Na & Lee). The high heat input and temperatures present in fusion welding are the primary drawback to this approach, particularly in small diameter pipes. Groove type, gas shielded arc welding is the most common fusion welding method performed on aluminum alloy pipes. The primary drawback of this method is the high temperatures and heat input result in a softening of the surrounding base metal. In these welds the heat affected zone (HAZ) controls the as-welded tensile strength of the joint in most cases (Newell, Sperko, Mannings, Anderson, & Connell). This problem is exacerbated in small diameter pipes and the reduced heat and solid-state nature of FSW makes it an attractive alternative in this application.

In this work, full penetration friction stir welds are performed on butted sections of aluminum alloy 6061-T6 pipe. These pipe sections are relatively small in diameter, 4.2 inches, and relatively thin walled, 0.2 inches. The small radius of curvature distinguishes this weld configuration geometrically from a butted plate configuration and presents unique challenges. These challenges necessitate the use of specialized techniques and specialized equipment. Friction stir welded joints of this type are not presented in academic literature, although FSW of large diameter steel pipe sections is being done at a research level.

Collaboration between Advanced Metal Products Inc., Oak Ridge National Lab, and Megastir Technologies has produced an orbital welding apparatus for joining X65 steel (Feng, Steel, Packer, & David) (Defalco & Steel, 2009) (Packer & Matsunaga, 2004). The test device is designed to produce full penetration welds on 12" diameter, 0.25" wall thickness pipe. This device revolves the tool about the stationary pipe and uses a hydraulic internal support fixture. Additionally, ExxonMobil has conducted research on FSW of linepipe steels (Fairchild, Kumar, Ford, & Nissley, 2009).

Experimental Setup

In the present experiment, an experimental apparatus was designed, shown in Figure 138 and Figure 139, which rotates the pipe sections beneath a stationary tool axis. The apparatus is mounted to a FSW machine and belt driven by a computer controlled motor. The experimental apparatus has also been used by the authors to join small diameter, butted Al-6061 hemispheres (Lammlein, Longhurst, Delapp, Flemming, Strauss, & Cook, 2010). The internal support fixture, or mandrel, used in the present experiment serves an identical purpose to that used with the AMP/ORNL/Megastir orbital apparatus, but is of a different, manually actuated design.

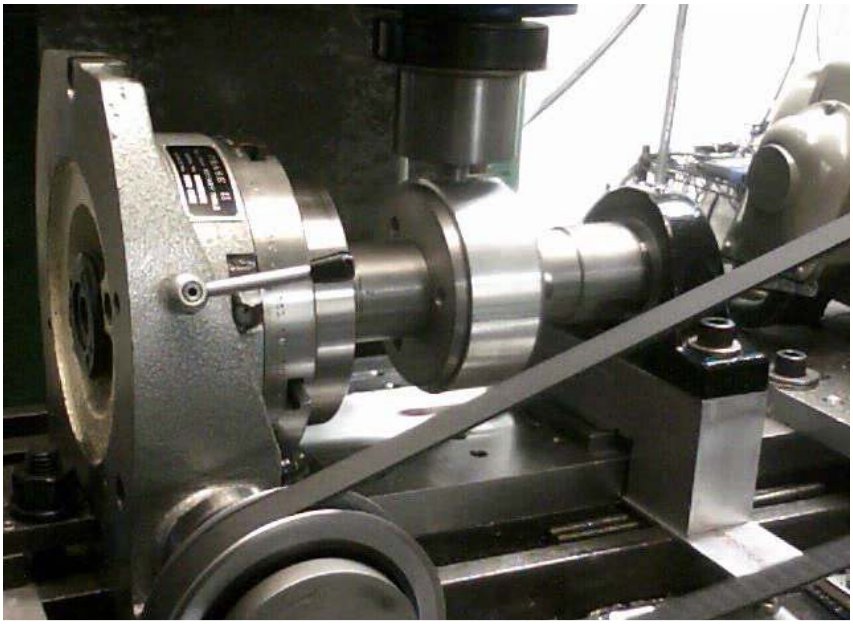

Figure 138: The rotary welding apparatus used in this experiment is mounted to a standard FSW machine and rotates butted pipe sections below a stationary tool axis.

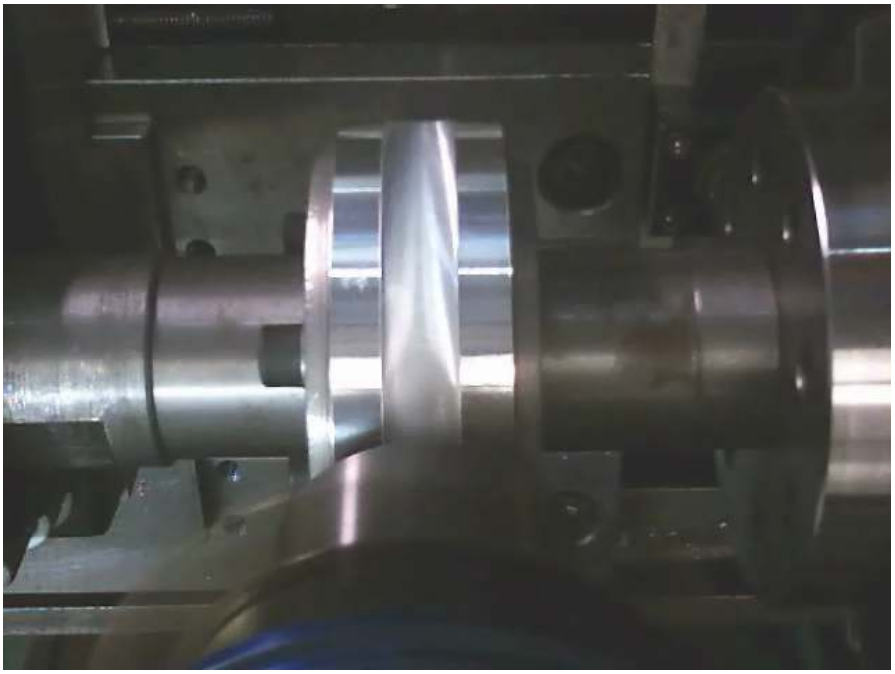

Figure 139: A still image taken from video made during an experimental weld (top view).

The cylindrical work geometry presents a number of challenges that must be addressed. In addition to the obvious issue of tool geometry, the issues of secondary heating at the end of the weld, variation in the height of the work surface due to system

eccentricity, the method of interior support, and the method of tool disengagement must be addressed. In this work, the significance of these issues are determined based on experimental and numerical results, and solutions are presented with applications to manufacturing.

It is apparent that the contact condition between a traditional, flat shoulder tool and small diameter cylindrical work differs significantly from that of butted plate welding. Figure 140 shows the experimental tool and cylindrical work. The flat, circular shoulder cannot be sit flush with the work surface and, at a reasonable plunge depth, the shoulder must hang over the front of the cylinder, over the back of the cylinder, or both depending on the tool's offset from the work axis of rotation. This creates potential problems for the shoulder in its material containment role. It must be demonstrated experimentally that this issue is not significant in pipe welding if a traditional shoulder is to be used. In this work, the tool is offset 6.0mm forward of the work to create the plowing effect common in FSW. This effect means the trailing edge of the shoulder is the portion deepest in the work. This plowing effect is achieved on flat work by tilting the tool and creating a so called angle of attack. The method presented in this work results in a similar contact condition and acceptable results.

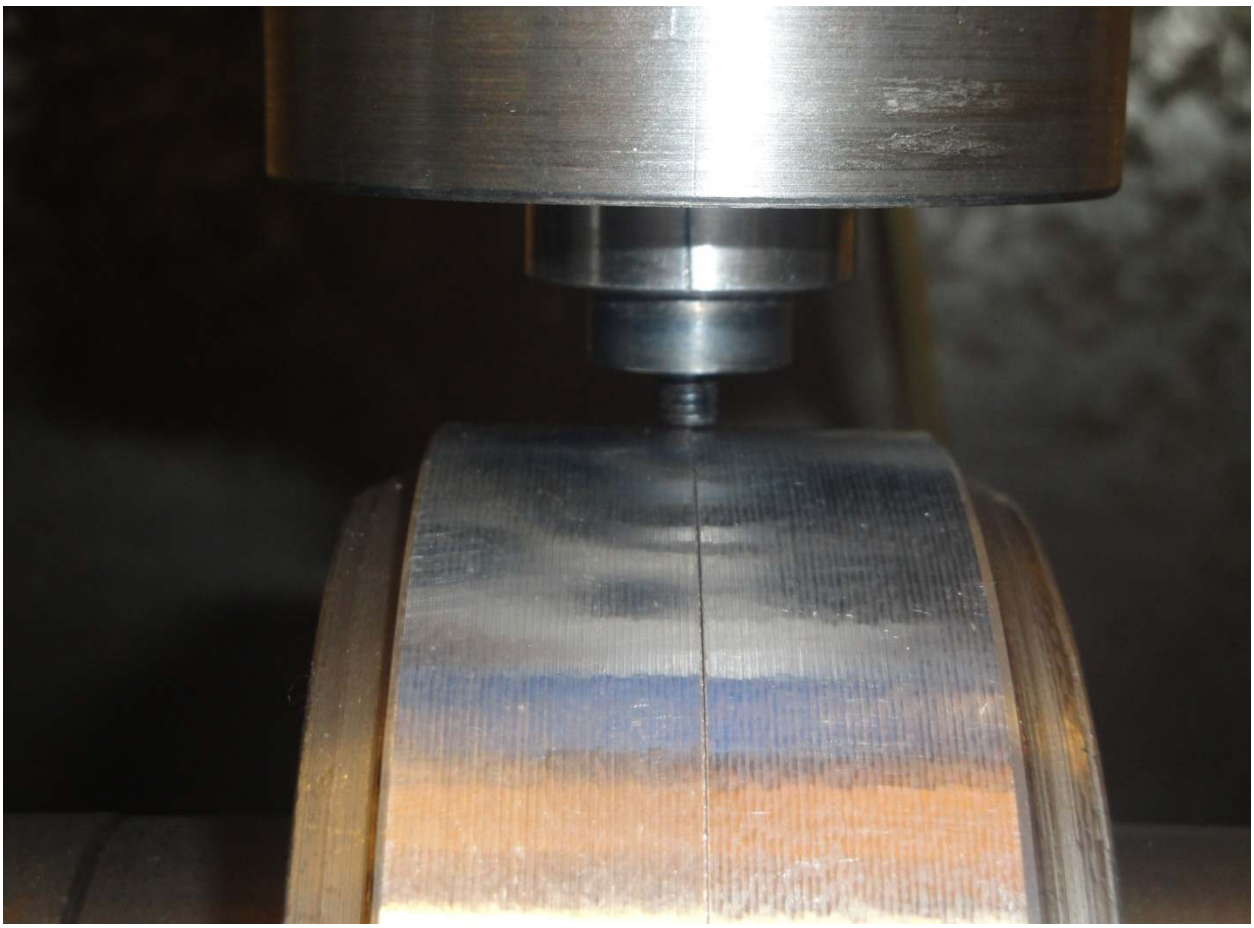

Figure 140: A closeup view of a tool used in the experiment and the butted weld specimens used in the experiment. The pipe sections are shown mounted in the welding apparatus. The experiment is started from this position. The tool probe was position was calibrated, or zeroed, against the surface of the work. The tool rotation is started and the probe is plunged into the material until the desired contact is achieved with the shoulder on the cylindrical surface of the work.

The circular nature of the weld path in a butted pipe configuration results in a secondary heating at the end of the weld. To complete a full, circumferential weld, the tool must cross over the weld initiation site which remains warm for a small diameter pipe. This additional heat affects the steady state portion of the weld and the weld termination. The highly coupled nature of the thermal and mechanical phenomena in FSW means this thermal effect can affect the weld mechanical properties. In this work, welds are observed by thermal camera and the effect of secondary heating is seen in the thermal data and the CFD model contours. The shank temperature is observed to increase throughout the weld. A similar problem is observed by Kou et al. in autogenous

gas tungsten arc welding of small diameter Al-6061 pipe (Kou & Le). The authors conclude that computer model and experiment show a uniform fusion zone girth during seam welding and a continually increasing fusion zone girth under the same conditions in circumferential welds on small diameter pipe. The authors propose a preprogrammed reduction in weld power during the weld to reduce fusion zone growth during the process. Lee et al. used a state-space optimization method of process parameters to successfully maintain weld pool geometry around the circumference of small diameter Al-6061 pipe (Na & Lee). Weld pool geometry was maintained but it was noted that the 450°C isotherm continued to expand.

In a butted pipe configuration, the cylindrical work must be rotated about its axis and this presents three issues which complicate the ability to maintain a constant contact condition between the work and shoulder. Eccentricity in the rotation of the pipe combined with eccentricity in the circumference of the pipe sections and variations in pipe thickness result in varying height of the work surface at the tool contact location. If this variation is significant, it can be accounted for by mapping the system eccentricity prior to welding by touching the tool to the work surface at various locations around the circumference. A mapped height path can then be followed during welding. Additionally, process force feedback control can be used to compensate for system eccentricity by adjusting vertical tool position or weld parameters based on axial force, torque, or both (Longhurst, Strauss, Cook, Cox, Hendricks, & Gibson, Investigation of force controlled friction stir welding for manufacturing and automation, 2010) (Longhurst, Strauss, & Cook, Identification of the key enablers for force control of friction stir welding) (Longhurst, Strauss, & Cook, Enabling Automation of Friction Stir Welding: The Modulation of Weld Seam Input Energy by Traverse Speed Force Control, 2009) (Longhurst, Strauss, Cook, & Fleming, Torque control of friction stir welding for manufacturing and automation, April 28, 2010).

In this work an expandable inner mandrel is used to support and locate the pipe sections during welding. A photo of this setup is shown in Figure 141. Screws force an interior plug with an outer diameter taper into the ring anvil which has an inner diameter taper. A gap cut in the ring anvil allows the ring (or c-shape) to expand against the interior of the pipe sections. An expandable mandrel, as opposed to a press fit or

interference fit mandrel, allows for insertion and removal of the mandrel without damage to the interior of the pipe. Additionally, this mandrel type can be adjusted to exert the desired degree of support to the interior of the pipe. It was found that a tight inner mandrel both prevented the expulsion or distortion of work material at the root of the weld and more significantly, forced the pipe sections into a more uniformly circular shape. When the pipe sections are forced against one another by the clamping system and inner mandrel is expanded, the inner circumferences of the two pipe sections are forced to mate and the outer circumferences are mated within the tolerance of the pipe wall thickness. This is important because pipe sections will not be perfectly cylindrical and allowing a greater error tolerance reduces costs and setup time. The precise nature of this clamping methodology readies the pipe sections for the friction stir welding process.

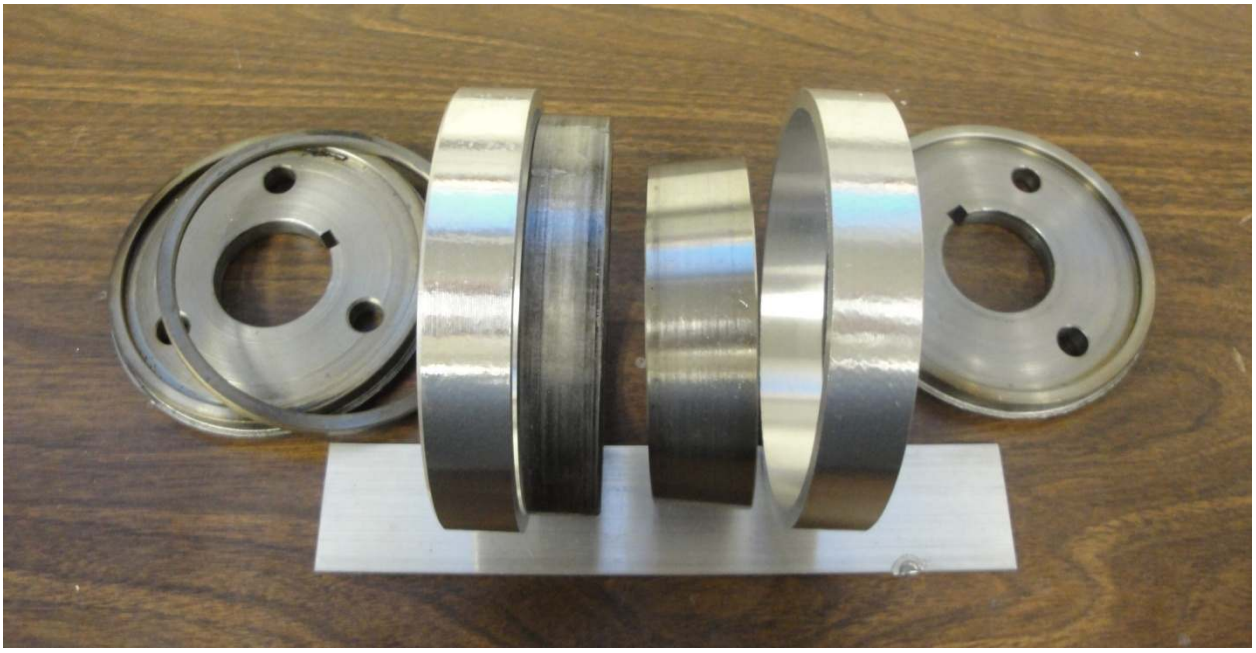

Figure 141: The expandable mandrel consists of slotted end caps which mate with the keyed axle of the rotary apparatus, a ring anvil with an expansion gap and inner taper, a spacer for centering the anvil, an expansion plug with an outer taper, and bolts (not pictured) to expand the mandrel by pulling the plug towards an end cap and into the taper of the anvil.

Weld Tests

Full penetration welds of 4.2” (107mm) diameter, 0.2” (5.1mm) thickness butted aluminum alloy (6061-T6) pipe sections were made with two 5/8” (15.9mm) diameter scrolled shoulder, 0.18” length, threaded probe tools of differing probe diameter. Parameters for a 3/16” (4.8mm) probe diameter tool were determined based on the superficial appearance, lateral macrosection appearance, and tensile strength of preliminary test welds. Adjustments to all aspects of the setup were then made with emphasis on improving tensile strength. A matrix of welds were then performed with the 3/16” (4.8mm) probe diameter tool. Process forces were recorded along with the tool shank temperature using a thermal camera. Tensile tests and macrosections were then performed. Based on these results, a second matrix of welds was performed with a 0.236” (6.0mm) diameter tool. A CFD Fluent model was creating for each geometry to compliment the experimental results and establish a numerical basis for estimating axial force (Lammlein, DeLapp, Fleming, Strauss, & Cook, 2009) (Atharifar, Lin, & Kovacevic, Studying Tunnel-like Defect in Friction Stir Welding Process Using Computational Fluid Dynamics, 2007).

Weld Results and Disscusion

The tensile strengths of the experimental welds are presented in Figure 142. The ultimate tensile strength (UTS) is plotted as a percentage of the parent UTS. Because of the large number of tested parameters, each data point represents the strength of a single tested tensile coupon. The parent strength (314.6MPa) was determined by averaging five samples. Generally, the results show an increase in weld strength with increasing traverse rate and rotation rate. This trend holds for all welds with the exception of several at the fastest parameter settings, where increasing speed results in weaker welds. The strength appears to be largely independent of which probe diameter was used. In addition to reduced strength, weld appearance was inconsistent and of reduced quality for the 1400rpm by 13.1ipm and 1600 by 17.0ipm cases. The reduced weld appearance quality experienced at these high traverse rate settings limited the range of tested

parameters. Specially designed clamps were used to hold the pipe section tensile coupons. The tensile test setup is shown in Figure 143.

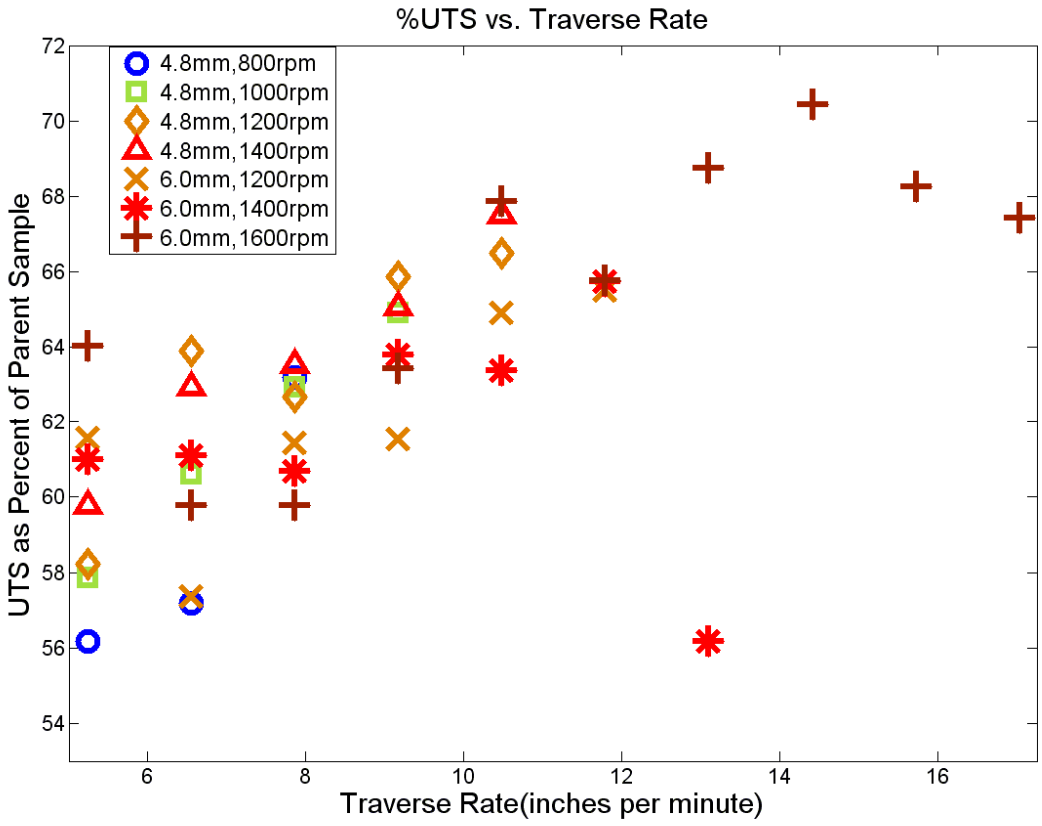

Figure 142: Ultimate tensile strength (UTS) as a percentage of the parent material UTS vs. Traverse Rate for full-penetration butted pipe welds made with 5/8" diameter, scrolled shoulder and 0.18" length, threaded probe tools. Data is shown for both the 3/16"(4.8mm) diameter probe tool and the 0.236"(6mm) diameter probe tool used in the experiment. Weld tensile strength is observed to increase with increasing process rates with the exception of the extreme cases.

Figure 143: The curvature of the pipe tensile coupons required the use of specialized clamps. The tensile jaws pictured above were designed to grip tensile coupons cut from welds of butted pipe and butted hemisphere sections. Each jaw uses six bolts to grip each coupon. Bolt tips are spiked, snubbed, or flat depending on the geometry gripped and the location contacted on the coupon.

The axial force was recorded for welds done with the 6mm diameter probe tool via strain gauges mounted to the cast-iron spindle head of the welding machine. An FEA model of the spindle head was used to determine strain gauge locations which maximized the influence of axial force and minimized the influence of in-plane (x & y direction) forces on the strain gauge array output. The strain gauge setup was calibrated using a load cell and it was determined that output mapped directly to axial force with negligible cross-influence from in-plane forces. Figure 144 plots the average axial force during the steady state portion of the weld against traverse rate, for welds made with the scrolled shoulder and 6mm dia. threaded probe tool. The plot clearly shows axial force increasing with traverse rate and a strong correlation between the two. Additionally, forces are more

often reduced with increasing rotation rate, however, this association is very loose over the parameter range tested. The highest average axial force occurred at a parameter setting of 1600rpm and 17.0ipm. This parameter setting should be considered as on the edge, or outside of, the parameter window which defines acceptable welds as ideal surface appearance was not be maintained throughout the weld, particularly in the initial portion of the weld where the weld temperature was the lowest. The abrupt jump in axial force at this setting indicates both a lack of plastization and that additional heating is needed to prevent a breakdown of the FSW process.

Computational fluid models (CFD) have been used with some success to predict the expected axial force encountered during the FSW process based on work material, tool and work geometry, and process parameters (Atharifar, Lin, & Kovacevic, Numerical and Experimental Investigations on the Loads Carried by the Tool During Friction Stir Welding, 2009). Figure 145 shows corresponding axial force values obtained from the Fluent CFD models presented later. The numerical results provide a reasonable estimate of the axial force values seen during the experiment.

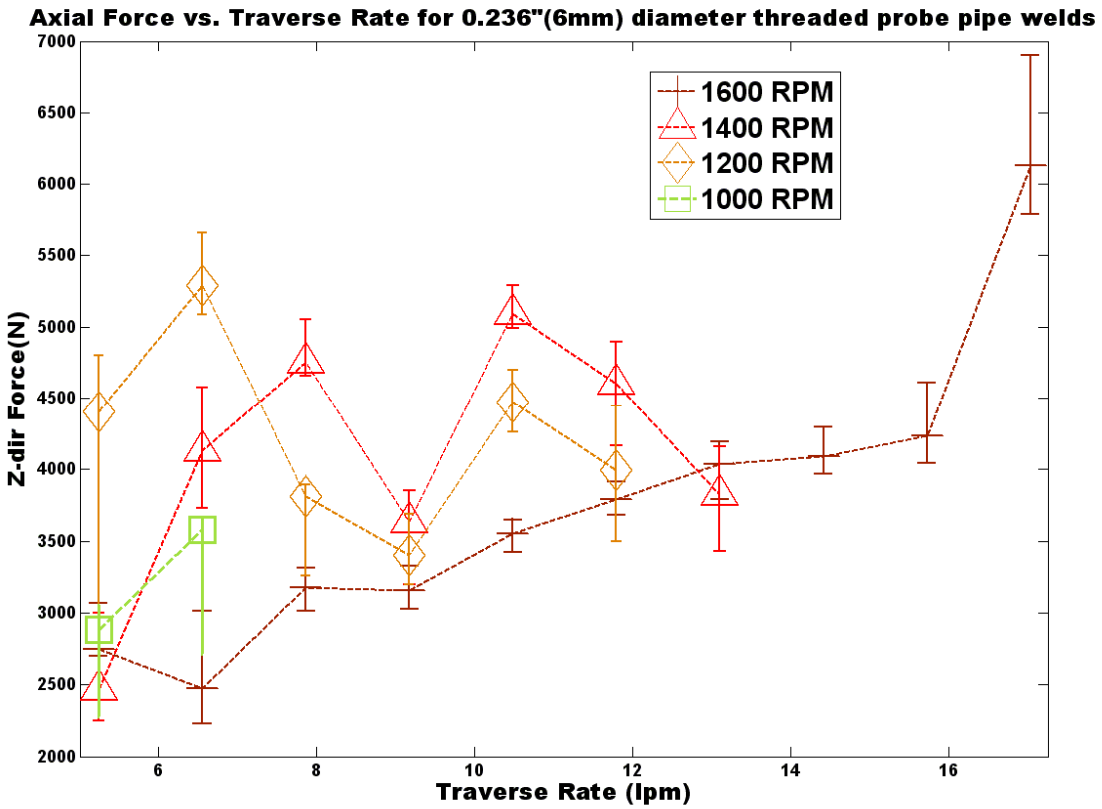

Figure 144: Experimental axial forces plotted with traverse rate for butted pipe welds made with a 5/8" diameter scrolled shoulder and 6mm diameter threaded probe tool.

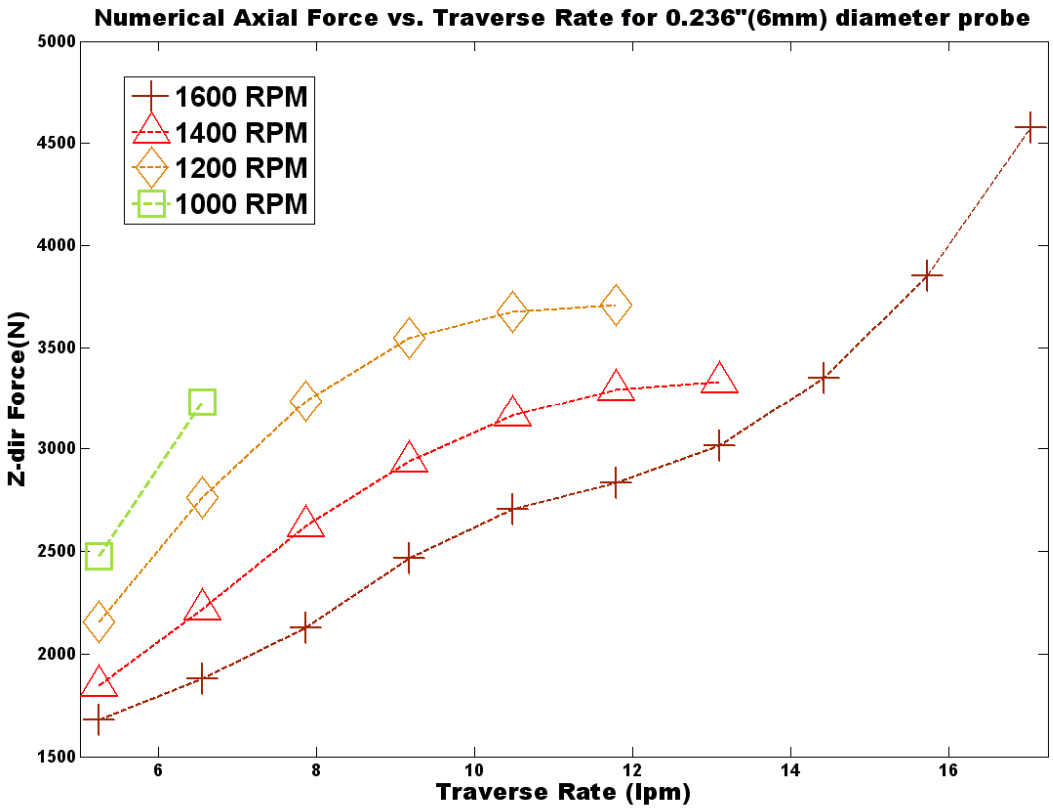

Figure 145: CFD model axial forces plotted with traverse rate for butted pipe welds made with a 5/8" diameter scrolled shoulder and 6mm diameter threaded probe tool.

Efforts were made to ensure that following proper depth and seating of the tool shoulder at the weld initiation site, forces would subsequently fluctuate within an acceptable range during the weld traverse. Figure 146 and Figure 147 show the axial force history of selected experimental welds. Keeping force fluctuations within an acceptable range was done by means of several techniques.

The parent pipe sections were machined from their received condition on their inner diameter and outer diameter. After this preprocessing, the wall thickness varied from the approximate thickness of 0.19" by a maximum of 0.005". This tolerance limit was maintained on each pipe section, and between each pipe section, ensuring near uniform thickness around the circumference of each section and well matched wall thicknesses between pipe sections.

The use of the expanding mandrel, described earlier, forced pipe sections into a more perfect circular shape and aligned the inner diameter of the pipe sections.

Together, a fine wall thickness tolerance and a tightly adjusted expanding inner mandrel served to align the joint in the geometric configuration most favorable to joining by FSW. With the use of force control and an expanding mandrel it would be possible to allow a greater wall thickness tolerance and the preprocessing step could be eliminated from the welding procedure (Longhurst, Dissertation: Force control in friction stir welding, 2009).

The shoulder of both of the tools used in the experiment used a scroll to force material inward from the edge of the shoulder during welding as the tool rotates. The scrolled shoulder is shown in Figure 148. This feature increased the tolerance of the tool to tool-work contact variations. Figure 149 and Figure 150 show the superficial appearance of the welds. Preliminary welds performed with an unfeatured shoulder tool showed consistent poor surface quality, producing either surface void defects or flash (material expulsion). It proved to be very difficult to produce superficially acceptable welds without a tool with shoulder features.

Finally, the tool was offset 6mm ahead of the geometric center of the work along the traverse direction. This created a plowing effect which reduced tolerance to vertical positioning error. This offset was arrived via experimental trial. It was found that positioning the tool directly over the high point of the pipe (i.e. no offset) resulted in buffeting and an unstable weld condition. Taking these steps meant the experiment could be performed without force control despite the difficulties of system eccentricity and secondary heating present in small diameter pipe FSW.

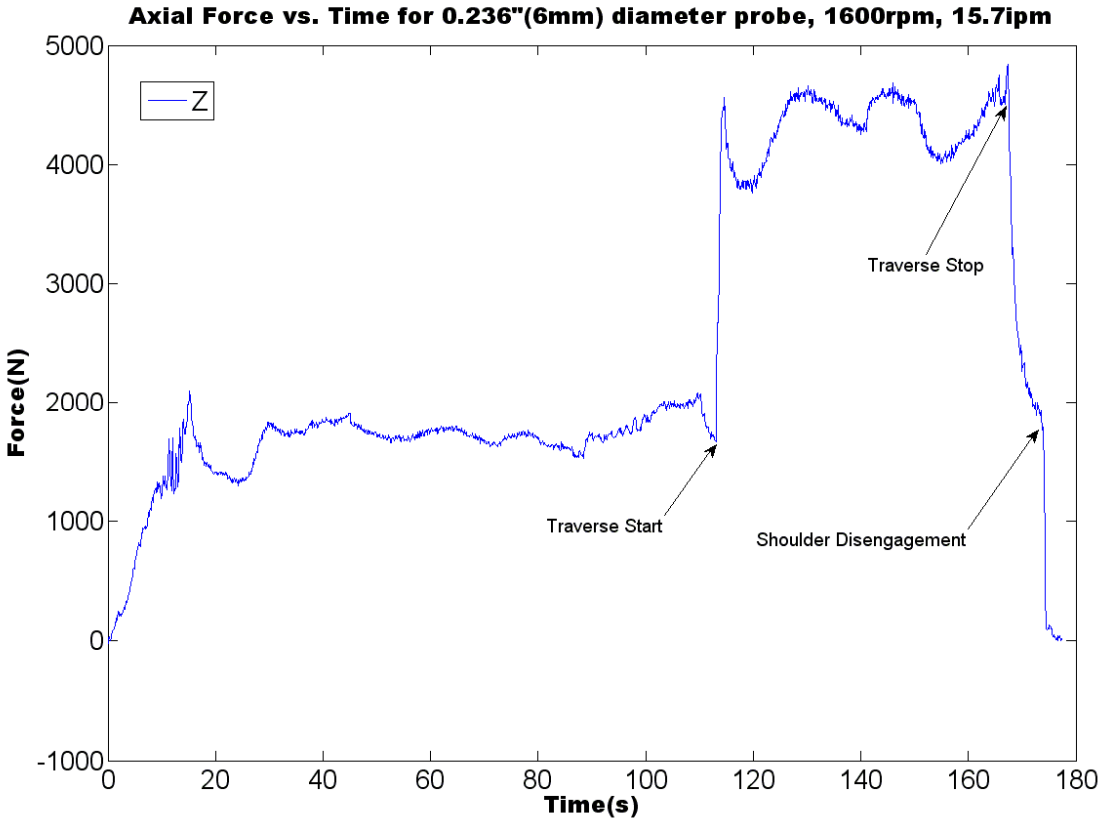

Figure 146: Axial force history recorded via a calibrated strain gauge array mounted to the spindle head for a weld performed with a 0.236"(6mm) diameter, threaded probe tool at 1600rpm and 15.7ipm. Recent equipment failure eliminated the force feedback control ability of the experimental FSW machine. Efforts were taken to ensure forces fluctuated within an acceptable range during the welding process.

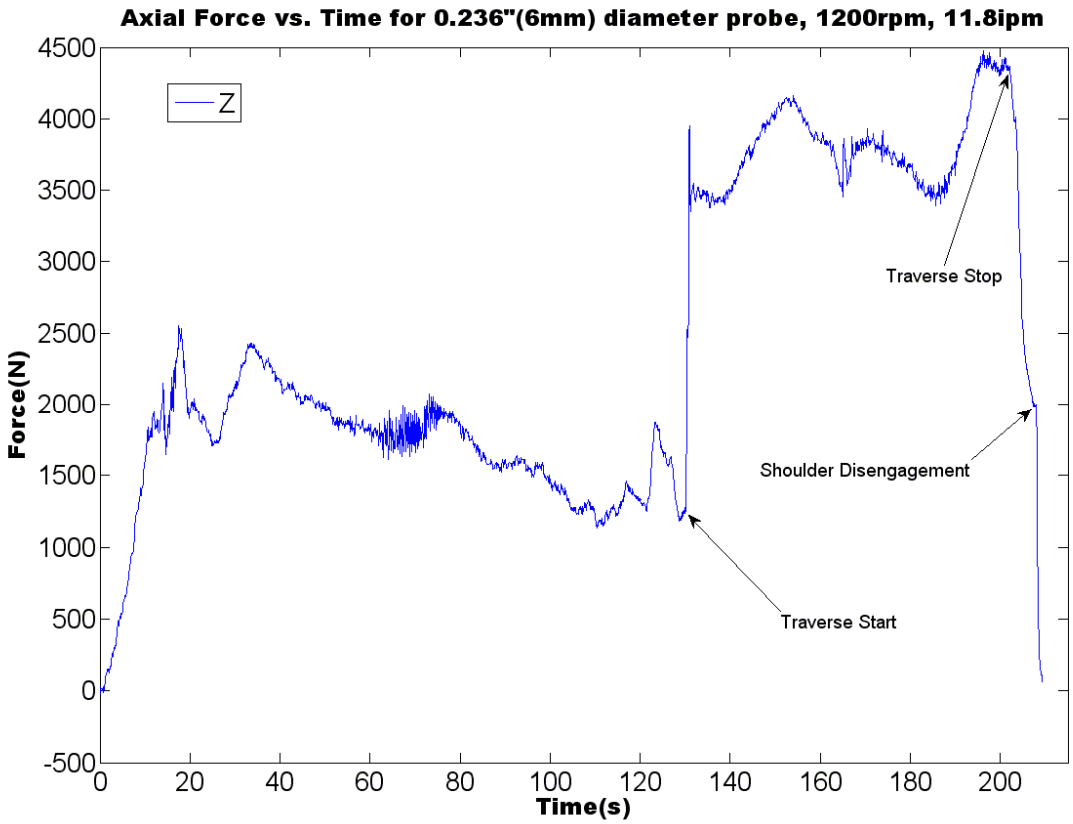

Figure 147: Axial force history for a weld performed with a 0.236"(6mm) diameter, threaded probe tool at 1600rpm and 15.7ipm. Force control was not used and axial values fluctuated within a range which did not affect weld appearance. To achieve this tolerance to weld contact pressure, a featured shoulder (scrolled) was used.

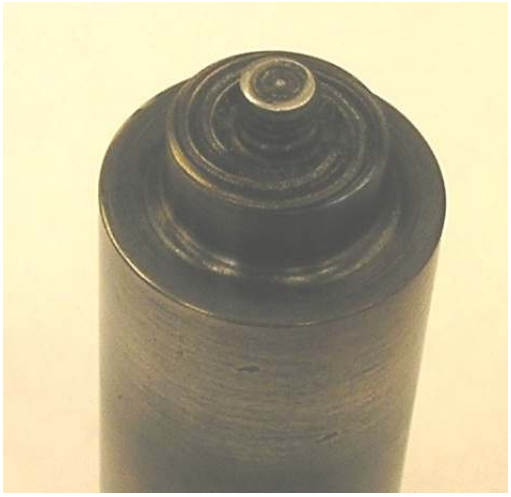

Figure 148: The 5/8" (15.9mm) diameter scrolled shoulder, 3/16" (4.8mm) probe diameter tool used in this experiment. The scrolled shoulder feature increased tolerance to variation in contact condition and improved weld appearance.

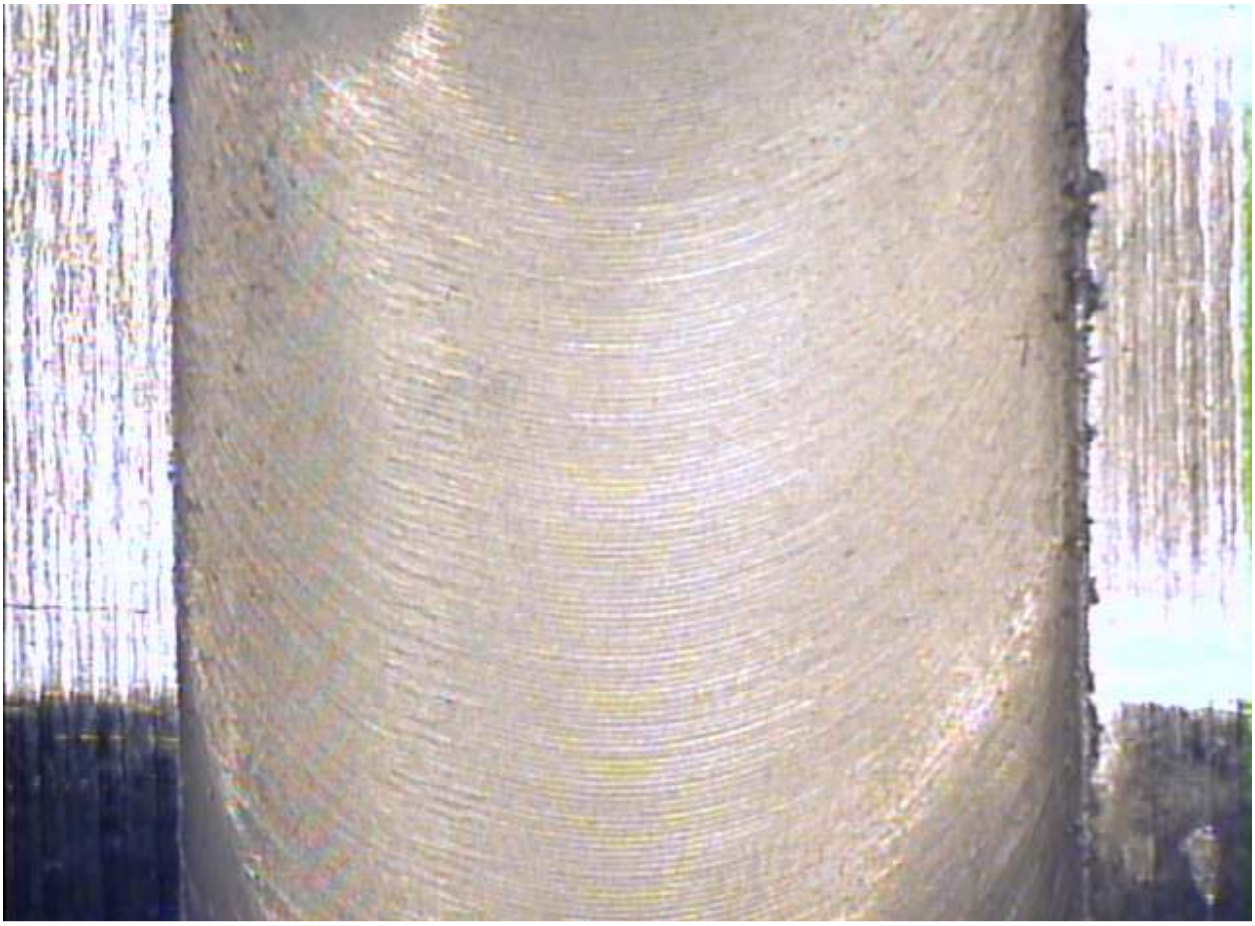

Figure 149: The superficial appearance of a typical welded pipe specimen (close)

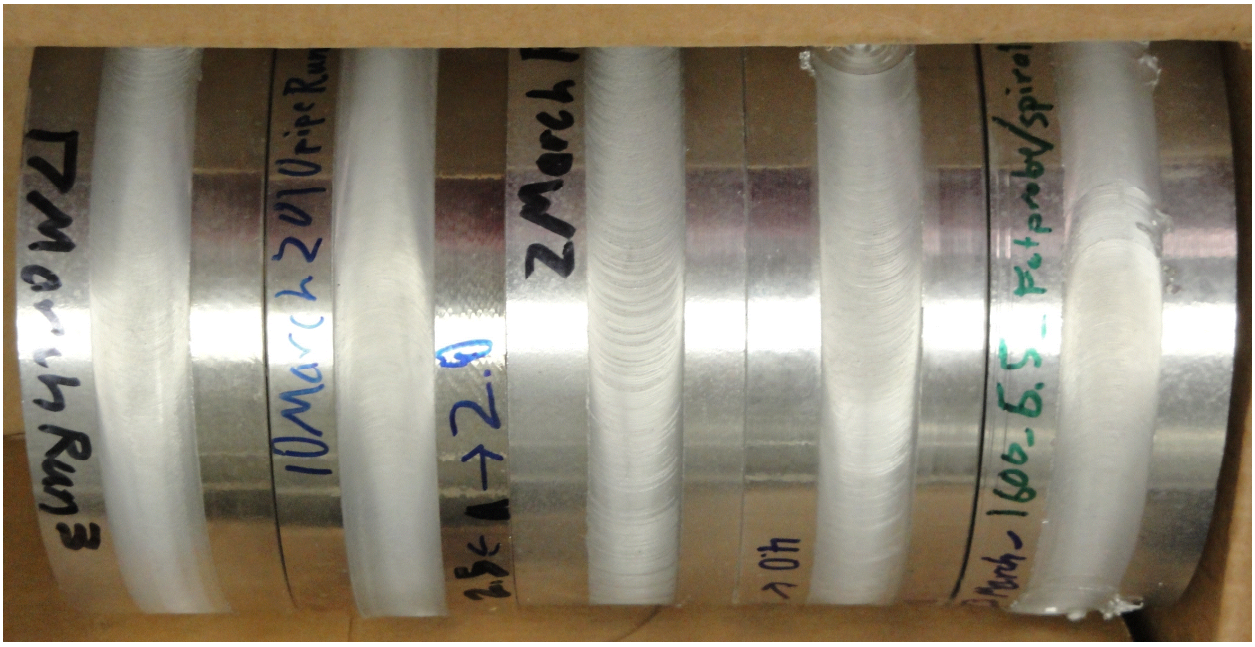

Figure 150: The superficial appearance of several pipes welded in the experiment.

The weld macrosections show complete penetration of the weld nugget through the work. Figure 151 shows the appearance of lateral-cross sections of welds made at low rates using the 3/16" dia. probe (narrow probe) tool. Frames were taken looking down the weld with the retreating side on the left. Weld samples were first mounted, then sanded over silicon carbide discs at various grits finishing with P1500, polished using 0.5μ alumina suspension, and finally etched by 1 minute bath in Keller's reagent. Figure 152 shows lateral views of remaining welds made using the narrow probe tool. Increasing the width of the probe predictably increases the width of the weld nugget. Figure 153, Figure 154, Figure 155, and Figure 156 show the lateral macrosection appearance of welds made using the 6mm dia. probe (wide probe) tool at 5.2 to 17ipm, and at 1200 to 1600rpm.

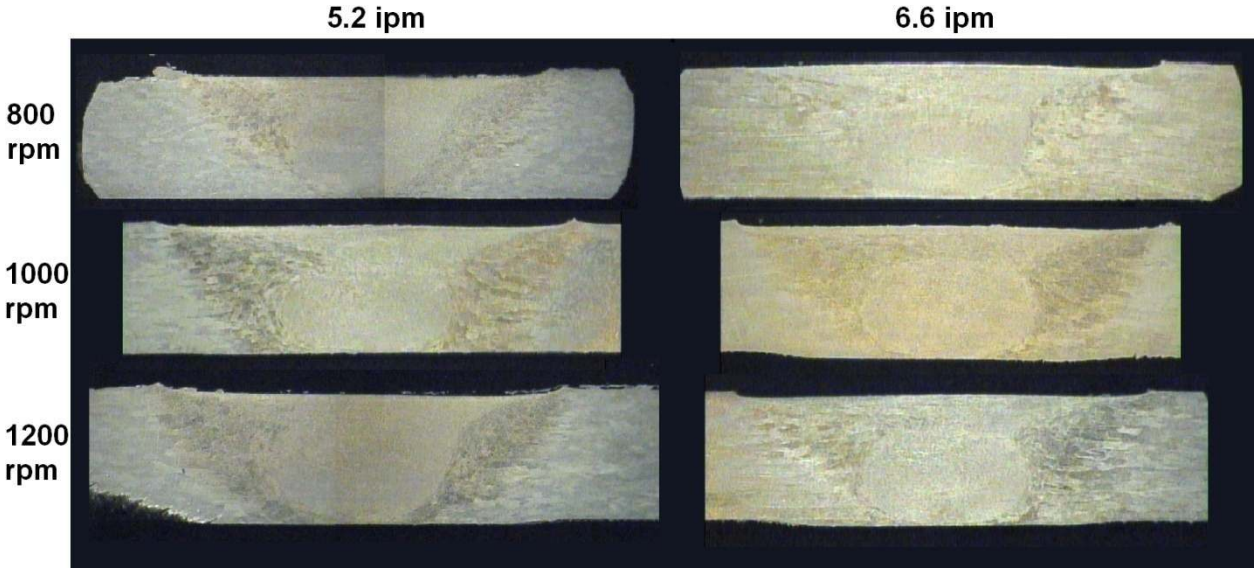

Figure 151: Lateral macrosection view of welds made at 5.2 and 6.6ipm using a 5/8" dia. scrolled shoulder, 3/16" dia. threaded probe tool. Two of the weld images presented above were made by composition of two photos due to an equipment issue.

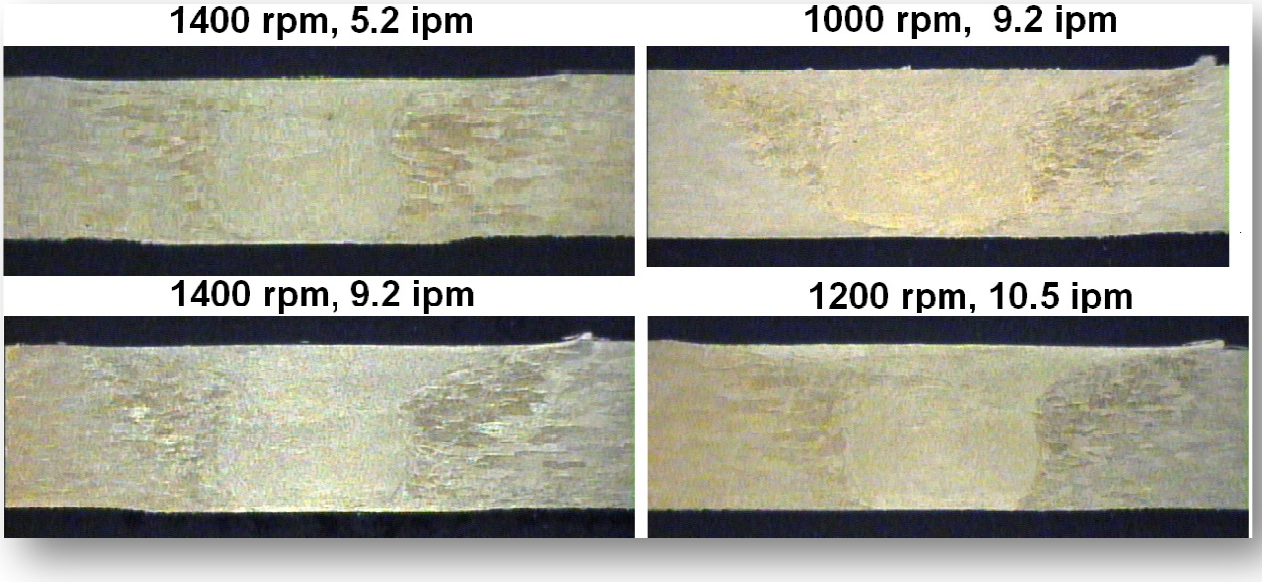

Figure 152: Macrosections of selected welds made with the narrow probe tool.

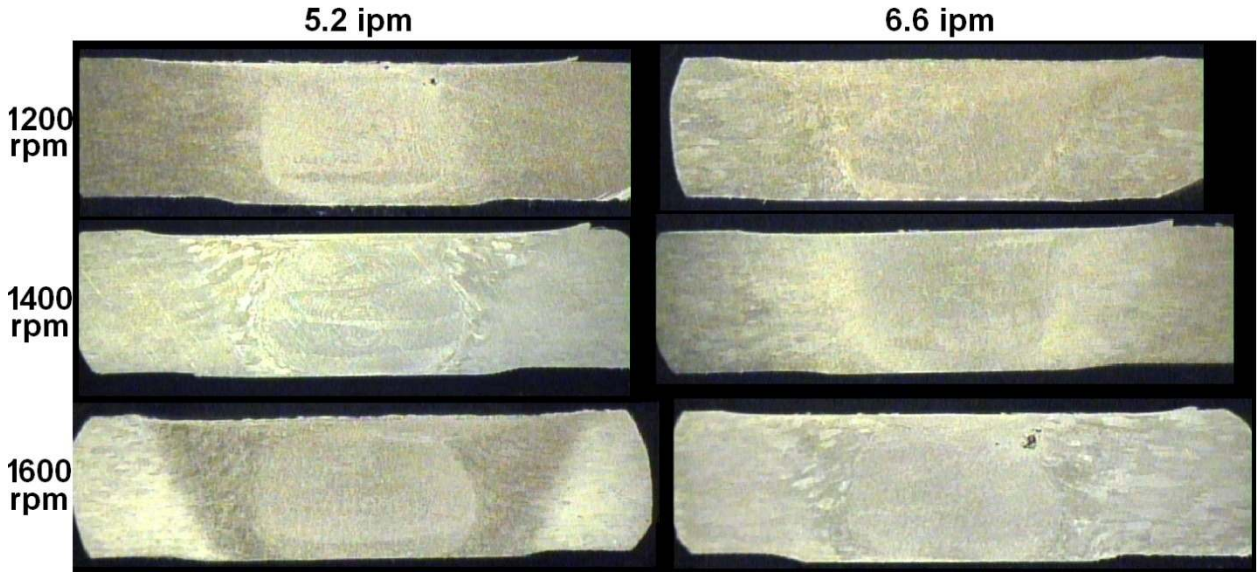

Figure 153: Lateral macrosection view of welds made at 5.2 and 6.6ipm using a 5/8" dia. scrolled shoulder, 0.236"(6mm) diameter threaded probe tool.

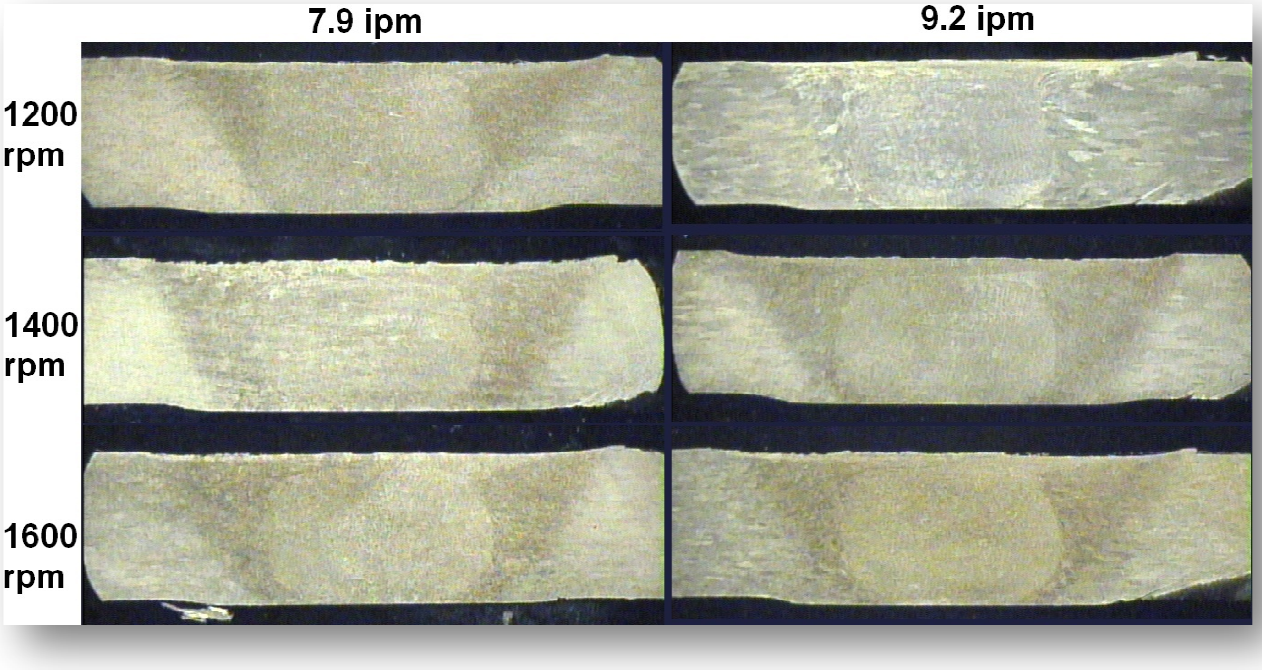

Figure 154: Macrosections of welds made at 7.9 and 9.2ipm with the wide probe tool.

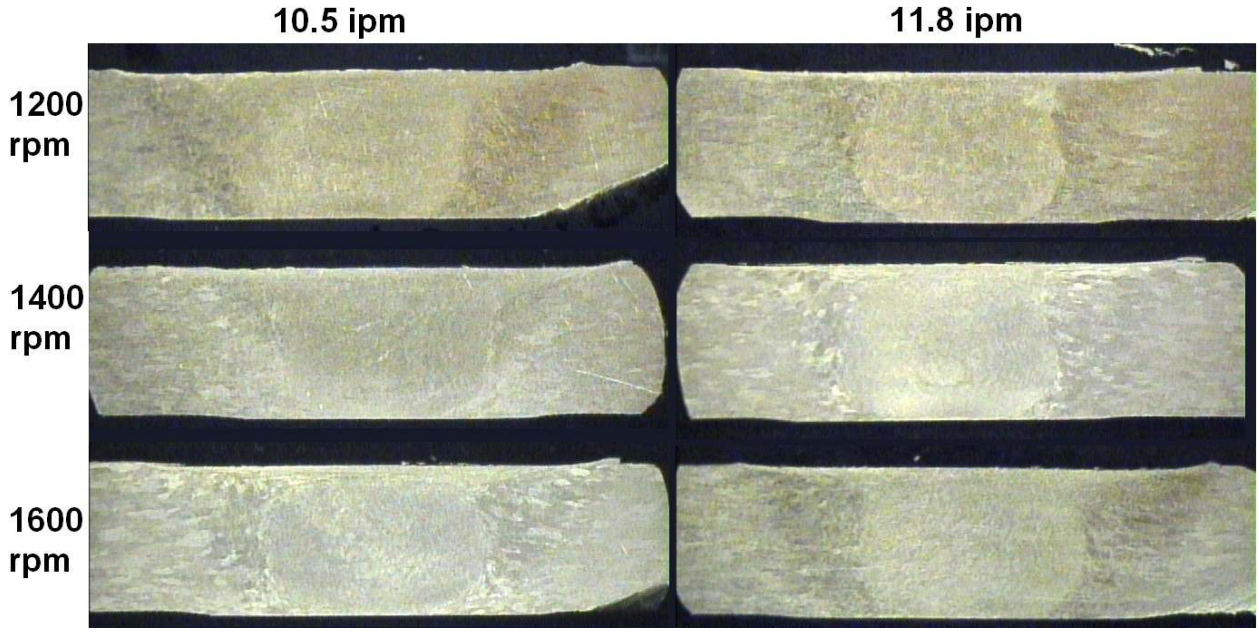

Figure 155: Macrosections of welds made at 10.5 and 11.8ipm with the wide probe tool.

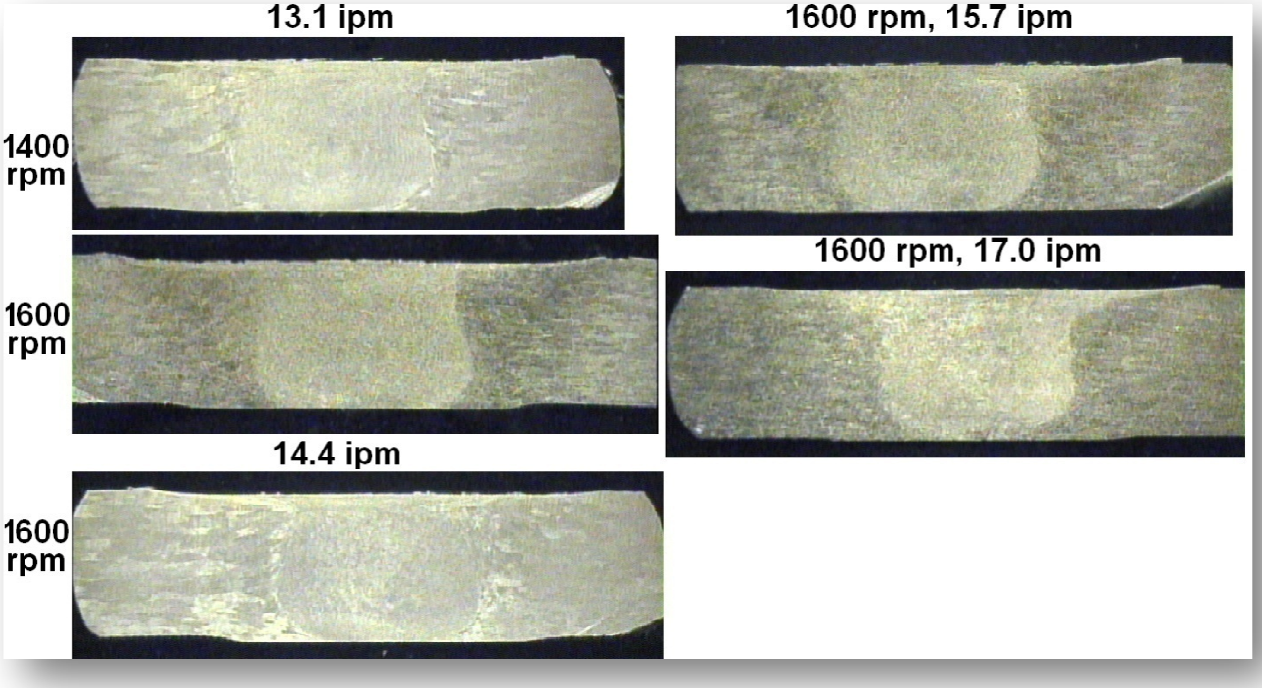

Figure 156: Macrosections of selected welds made with the wide probe tool.

A FLIR thermal camera was used to make thermal videos of the full weld cycle. The camera was calibrated to the emissivity of the tool shank. Figure 157 shows a thermal image from thermal video taken during the experiment showing the region of interest on the tool shank. The curved outer surface of the aluminum pipe sections were too reflective to give reliable emissivity calibration, thus the tool shank was used. Figure 158 shows the average tool shank temperature over the steady state portion of welds made using the narrow probe tool and Figure 159 shows the corresponding data for welds made with the wide probe tool. The charts show shank temperature decreasing predictably with increasing traverse rate. Higher rotation rates generally resulted in higher temperatures but this relationship was not as consistent in the data. The charts show the wide probe welds to be slightly hotter than the narrow probe welds. The experimental shank temperature agrees closely with the CFD model results at the modeled parameter (1000rpm, 5.2ipm) for both geometry cases.

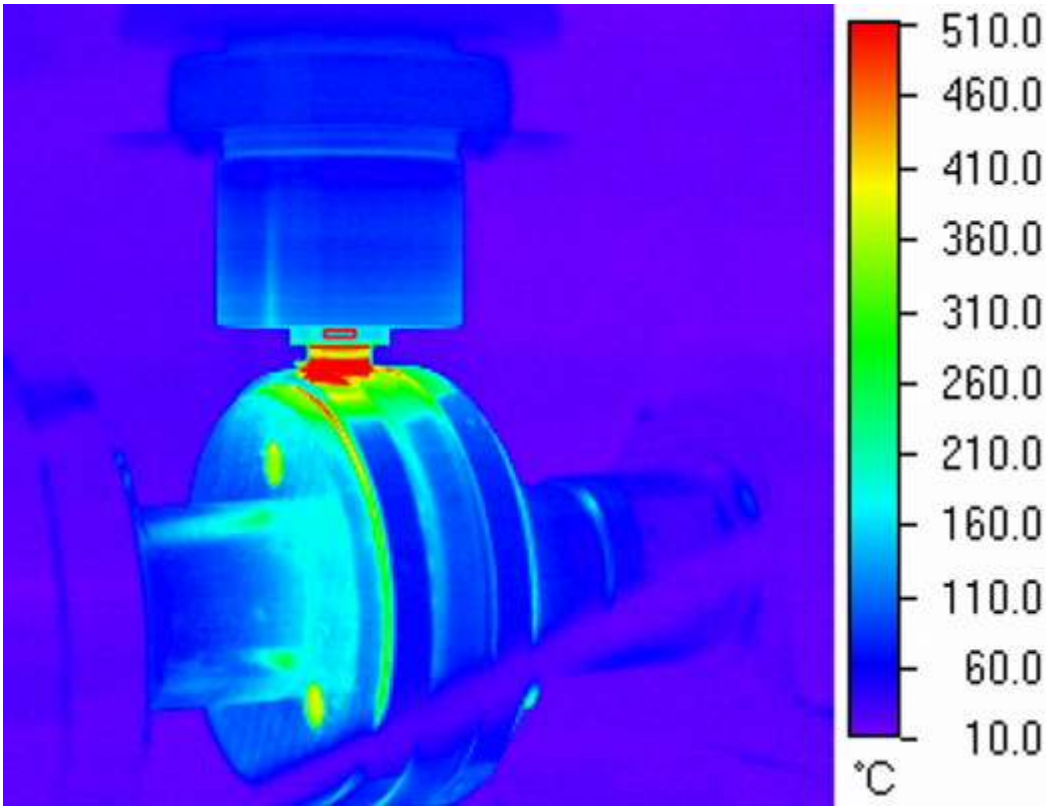

Figure 157: A thermal camera image from thermal video taken during the experiment showing the region of interest on the tool shank. The emissivity of the tool shank was determined by observing the shank with the camera at several temperatures when the temperature of the shank was known.

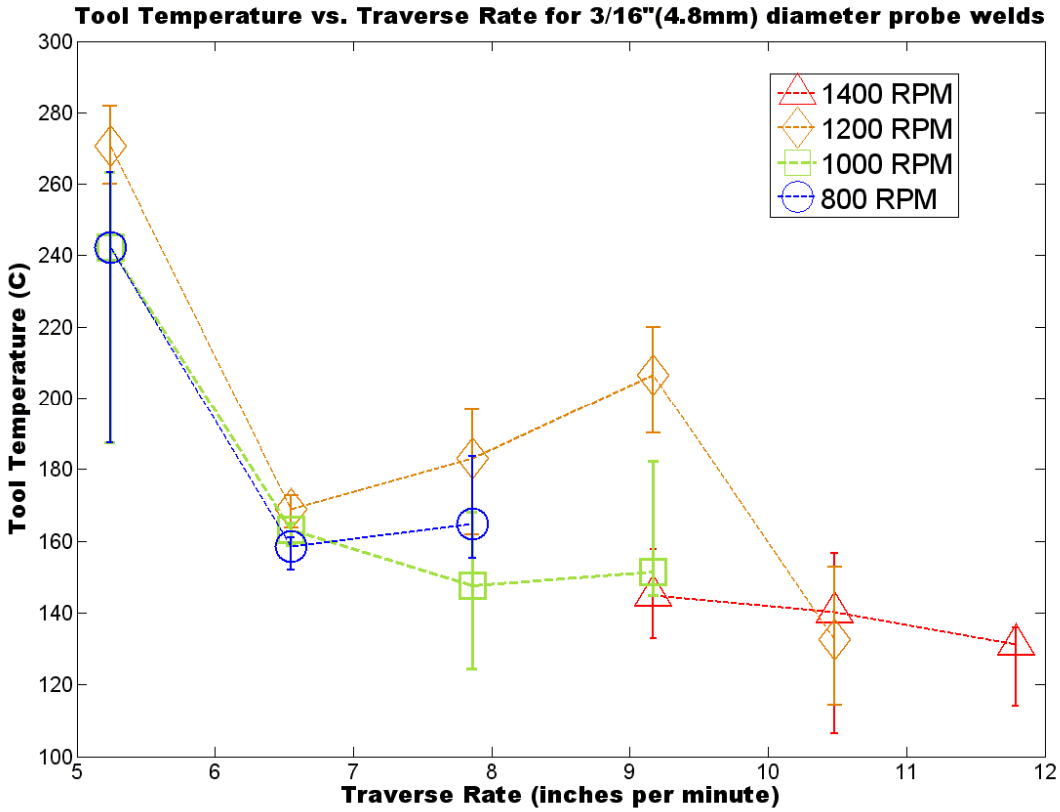

Figure 158: Average tool shank temperature obtained via thermal camera over the steady state portion of welds made using the narrow probe tool.

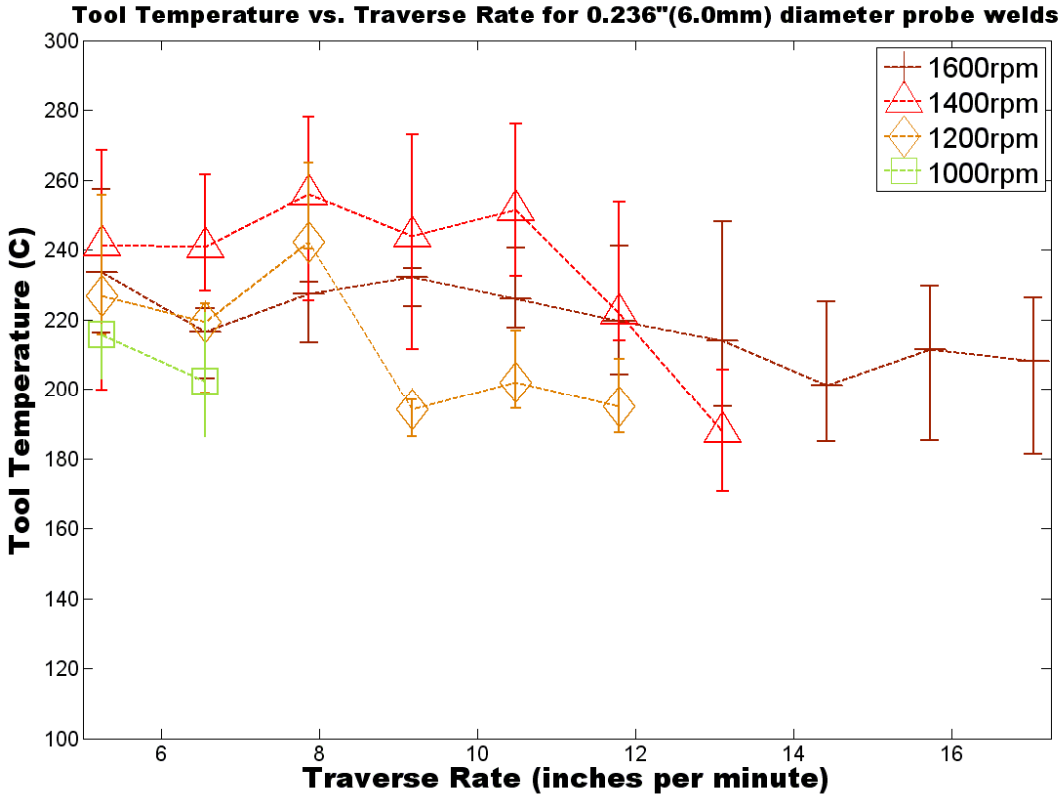

Figure 159: Average tool shank temperature obtained via thermal camera over the steady state portion of welds made using the wide probe tool.

Figure 160 shows the typical temperature history of the tool shank surface during welding. Temperature on the tool shank surface increases gradually as the probe is plunged into the material and then more rapidly as the shoulder contact condition is established. When the shoulder is at the desired position and the traverse is triggered, the temperature increases less rapidly. The issue of secondary heating can be seen during the weld proper in the presented temperature charts. The tool must pass over the weld initiation site, which has been previously subjected to the weld thermal environment, to complete a full circumferential weld. A steady state temperature is never reached and temperature increases throughout the weld cycle. In the presented experiment, this climb in temperature did not adversely affect weld quality. However, the temperature increase over the circumference of the weld is significant in small diameter pipes and could affect weld quality under other conditions. During welding of butted plates a similar problem can be encountered when the tool nears the end of the plate and the edge of the plate

presents a barrier for heat conduction. This situation near the end of a weld on butted plates is less severe, yet still presents a problem under certain conditions that must be addressed.

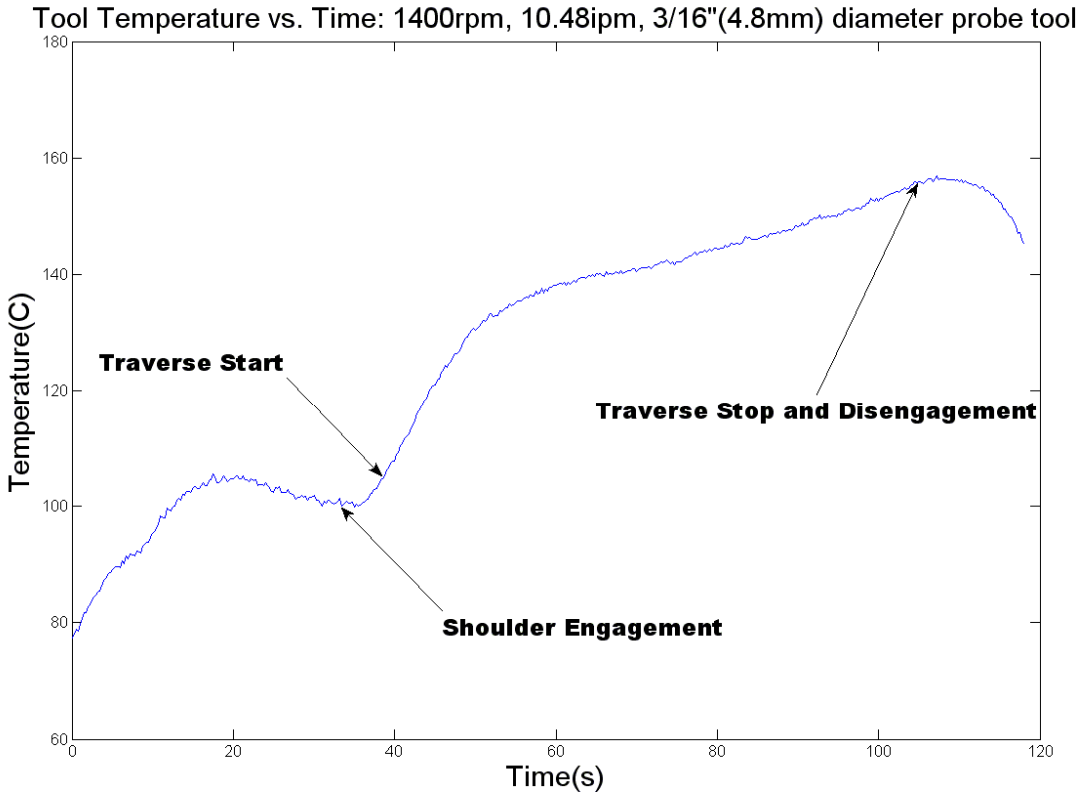

Figure 160: A chart showing the tool shank thermal history over the course of a selected weld from the experiment. This data was typical of weld thermal data taken during the experiment in that temperature continued to rise throughout the weld.

Modeling

A numerical model was created for both tool geometries using Ansys Fluent software. Fluent is an Eulerian, finite volume, computational fluid dynamics (CFD) program. The mesh geometries for each tool were created in the preprocessing program, Ansys Gambit. The narrow probe geometry contained 221,887 tetrahedral cells and 465,690 triangular faces, and the wide probe geometry contained 224,689 cells and

471,146 faces. The meshes are fine at the interface. A growth rate was established from the interface, creating tool and material volumes which are increasingly coarse with distance from the interface. The mesh is finest in the work near the interface because temperature and velocity gradients are highest in the vicinity of the tool. Figure 161 shows the mesh refinement and geometry. Figure 162 shows the mesh over the tool geometry, created in gambit. The meshes for both cases were then exported and loaded in Fluent.

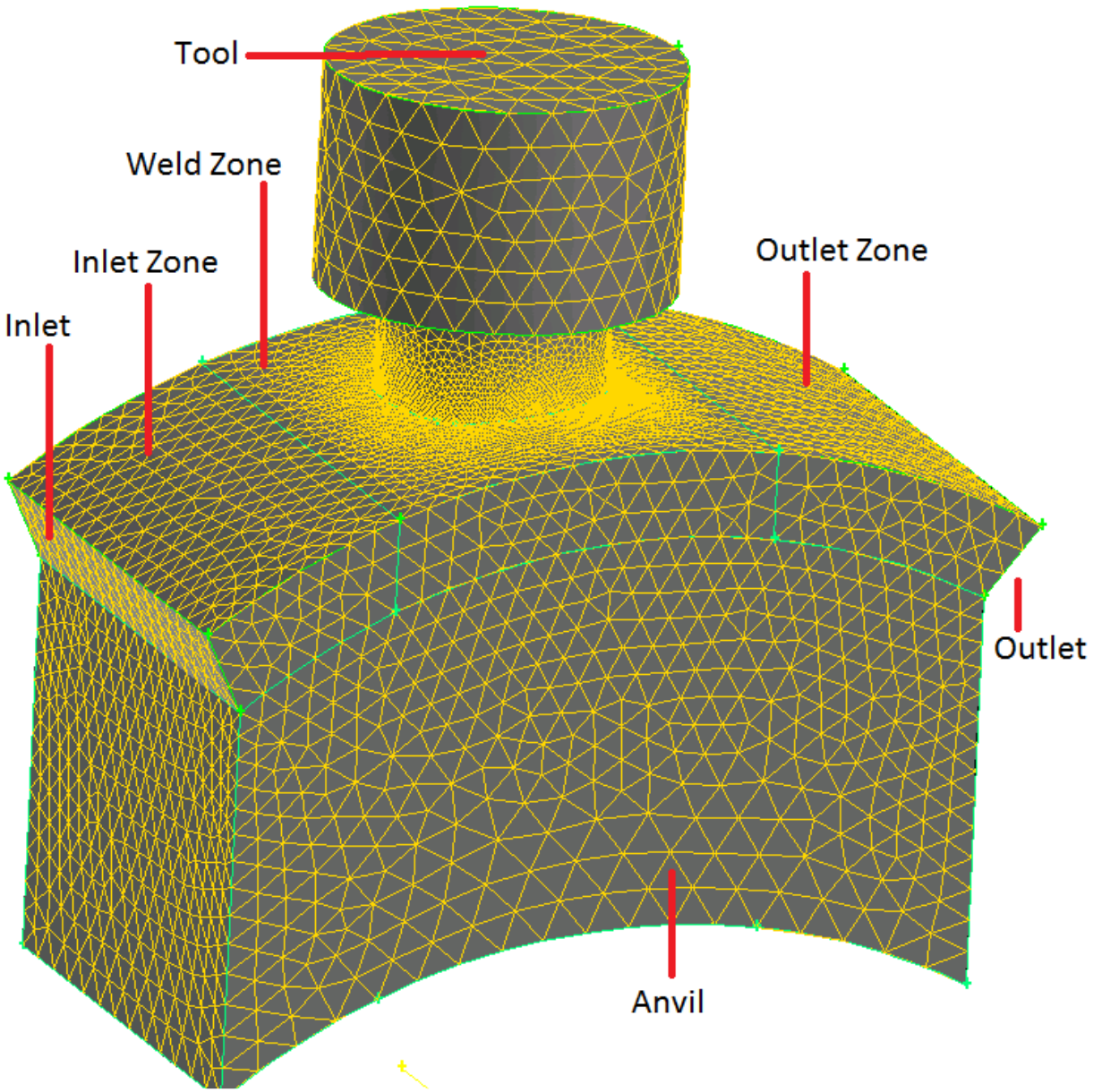

Figure 161: Computer model geometry created in the Gambit preprocessor showing the inlet, outlet, and model zones.

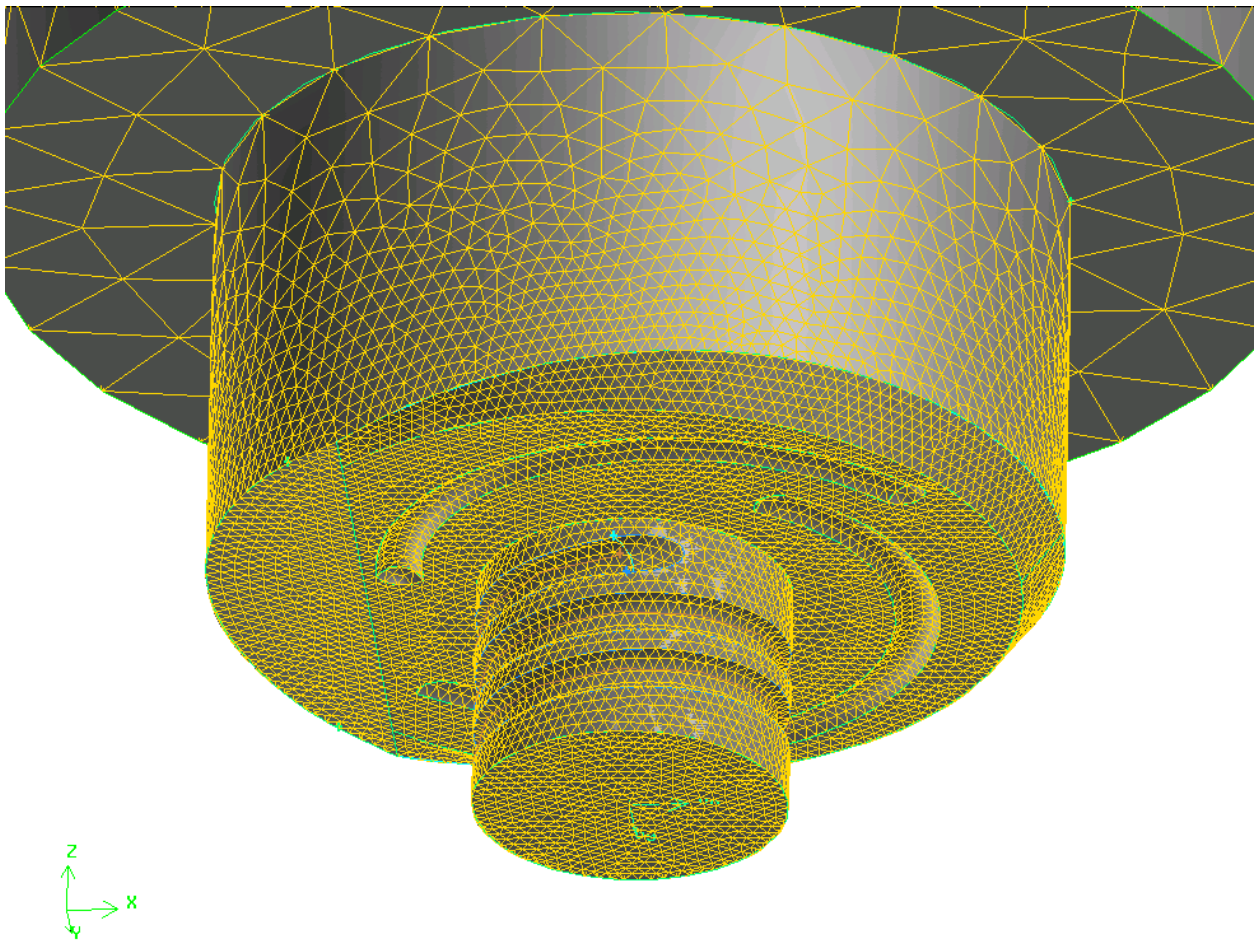

Figure 162: A closeup view of mesh refinement on the tool face. The featured shoulder and threaded probe can be seen. The mesh was finest at the interface.

The implicit formulation was used in Fluent with the laminar viscosity setting. The Presto pressure solver for highly rotating flows was selected due to the relatively high rotation rate with respect to traverse rate. The weld material viscosity function was set by user-defined function and defined using the Carreau viscosity model:

$$\mu = \mu_\infty + (\mu_0 - \mu_\infty)\left[1 + \left\{\dot{\gamma}\lambda \exp\left({}^{T_0}/_{T}\right)\right\}^2\right]^{{}^{(n-1)}/_2}$$

where μ_∞ is the infinite shear viscosity, μ_0 is the zero shear viscosity, $\dot{\gamma}$ is the local shear strain-rate, λ is the time constant, T_0 is the reference temperature, T is the local temperature, and n is the power law index. In the weld zone (see Figure 161), Carreau

constants derived from analytical experiments in Al-6061-T6 were taken (μ_∞=0, μ_0=1e8m^2/s, λ=10, n=1, T_0=300K) (Tello, Gerlich, & Mendez). For the inlet and outlet zones, a reduced μ_0 of 100m^2/s was used to aid in solution convergence as flow was not critical in these regions. The total heat input at the interface was determined using the Schmidt heat generation equation.

Schmidt's analytical equation for heat generation approximates the heat generated by the tool based on a sliding contact condition at the interface (Schmidt, Hattel, & Wert, 2004):

$$Q=\tau_{contact}\omega Ad \quad \text{where} \quad \tau_{contact}=\mu P$$

Where Q is heat generated by area, A, whose centroid is distance, D, from the axis of rotation; and $\tau_{contact}$ is the contact shear stress, μ is the frictional coefficient, P is the contact pressure, ω is the radial velocity of the tool. For a simple tool with a cylindrical probe the equation becomes:

$$Q_{total}=\frac{2}{3}\pi\tau_{contact}\omega(R^3+3r^2h)$$

where R is the radius of the shoulder, r is the radius of the probe, and h is the height of the probe. For the present case the equation must be slightly modified to account for the portion of the shoulder not in contact with the work. This portion of the shoulder is a circular section on the shoulder defined by an inclusive angle of approximately 100º. The area of this non-contact, circular section is calculated by:

$$A_{nc}=\left(\frac{1}{2}\right)R^2[\theta-\sin(\theta)]=\left(\frac{1}{2}\right)\left(\frac{5}{16}"\right)^2[1.745rad-\sin(1.745rad)]=0.037in^2$$
$$=2.40e-5\ m^2$$

where R is the shoulder radius in inches, and θ is the inclusive angle which defines the circular section (100º), in radians. The centroid of this non-contact area is located a distance, D_{nc}, from the tool axis of rotation:

$$D_{nc} = \frac{4Rsin\left(\theta/2\right)^3}{[3\{\theta - sin(\theta)\}]} = \frac{4\left(\frac{5}{16}"\right)\left(\frac{1.745rad}{2}\right)^3}{[3\{1.745rad - \sin(1.745rad)\}]} = 0.246" = 0.0063m$$

where R is the shoulder radius, in inches, and theta is the angle which defines the circular section, in radians. The contact pressure, P, can be calculated by dividing the axial force by the horizontal tool area:

$$P = \frac{F_{axial}}{A_{horz}} = \frac{F_{axial}}{\pi R^2 - A_{nc}}$$

Using the experimental axial force for the 1000rpm, 5.2ipm parameter, the setting contact pressure, P, can be calculated for the width probe and narrow probe tools. Axial force readings were not taken during the narrow probe welds so the value obtained for the wide probe will be used for both cases. The calculated contact pressure for both experimental tools at the 1000rpm, 5.2ipm setting is:

$$P_{1000,5.2} = \frac{F_{axial}}{\pi R^2 - A_{nc}} = \frac{2880.5N}{\pi(.0079m)^2 - (2.40e-5\ m^2)} = 1.66e-7\ Pa$$

For the experimental contact condition the general Schmidt equation becomes:

$$Q_{tool} = \mu P\omega\left[\frac{2}{3}\pi(R^3+3r^2h) - A_{nc}D_{nc}\right]$$

For the 1000rpm, 5.2ipm setting and the narrow probe tool using a frictional coefficient of 0.5 the heat generated by the narrow probe tool, Q_n, is:

$$Q_n = (0.7)(1.66e-7)(104.72)\left[\frac{2}{3}\pi((.0079)^3\text{-}3(.0024)^2.0046) - (2.4e-5).0063\right]$$

=1,287 Watts

where 0.7 is the friction coefficient, 1.66e-7Pa is the contact pressure, 1000rpm(104.72rad/s) is the tool rotation rate, 5/16”(0.0079m) is shoulder radius, 3/32”(0.0024m) is the probe radius, 0.18”(0.0046m) is the probe height, 0.037in^2 (2.4e-

$5m^2$) is the non-contact area, and 0.246"(0.0063m) is the non-contact centroid distance. For the wide probe tool this equation gives:

$$Q_w = (0.7)(1.66e-7)(104.72)\left[\frac{2}{3}\pi((.0079)^3\text{-}3(.003)^2.0046) - (2.4\text{e}-5).0063\right]$$

=1,403 Watts

where only the radius of the wide probe tool, 0.118" (0.003m), is substituted from the previous calculation. The slightly increased surface area of the probe and the slightly higher relative velocity of the probe wall result in higher heat input for the fat probed tool at identical parameters.

Although torque values for this experiment were not obtained, a secondary estimate of weld thermal input can be obtained via the weld power method by using a torque value taken from a similar experiment under similar conditions. A value of 10.56 N·m is taken from an experiment performed on butted spheres of identical (0.2") thickness using the same rotary welding apparatus. The tool shoulder from this case was of the same 5/8" diameter but was cupped in geometry to mate with the spherical work. Like the present case this value was taken over a 1000rpm weld, however, the lowest traverse rate recorded during the analog spherical experiment at the 1000rpm rotation rate was 7.8ipm, so an extrapolated value is taken. The probe was 3/16" diameter and threaded and therefore will be compared with the 3/16" diameter probe calculation. Using the weld power method (Pew, Nelson, & Sorensen, 2007):

$$Q_{n,weldpower} = \Omega\omega = (10.56\,N\cdot m)\left(104.7\frac{rad}{s}\right) = 1106\,Watts \cong 1287\,Watts$$

An upper limit weld power can be calculated using an upper limit weld torque obtained by applying the measured axial load at the very edge of the tool shoulder. For the wide probe modeled case this yields:

$$Q_{w,upperweldpower} = FR\omega = 2880.5N(.0079m)\left(104.7\frac{rad}{s}\right) = 2394 \text{ Watts}$$

For the presented models, the Q_n and Q_w heat rate or power values are used for the narrow probe and wide probe models respectively. Heat was distributed across the weld interface and input into the work material as defined by a user-defined function which

applied heat locally in proportion to the local tool velocity. This results in highest energy input at the edge of the shoulder where the local tool velocity is highest. A second user defined function was used to impose the temperature on the work side of the interface onto the adjacent interface cells on the tool side of the interface. This formulation resulted in 5.1% of the total weld power entering the tool in the narrow probe case and 6.6% entering the tool in the wide probe case. The total heat input into cells on both sides of the interface was equal to the values obtained by the Schmidt formula. A rotational velocity of 1000rpm and traverse speed of 5.2ipm were used in the presented models of the narrow probe and wide probe geometries. Additionally, cases were run for the wide probe geometry at all parameters used experimentally in order to provide a numerical estimation of axial force for comparison with experiment.

In Fluent, the tool rotational axis is maintained stationary while velocity inlet type boundary conditions are used at the inlet and outlet boundaries to establish material flow past the tool, as when traversing. The outlet boundary condition (BC) can be defined as a velocity inlet with negative magnitude because the flow far from the tool in the work is known to be the traverse rate. A pressure outlet or outflow boundary condition at the outlet would not take advantage of this knowledge and would instead force fluent to arrive at some flow profile. Thermal BC's are defined as 10 $W/(m^2 \cdot K)$ for exposed surfaces and 150 $W/(m^2 \cdot K)$ for intimate metal to metal contact. The rotating and exposed surface of the tool was defined as 50 $W/(m^2 \cdot K)$. Additionally, a wall emissivity of 0.2 was applied to exposed aluminum surfaces and 0.5 to exposed steel surfaces.

The FSW environment presents an extreme fluid case for Fluent software. Temperature and velocity gradients are steep in the vicinity of the tool and the tool rotational velocity is high with respect to the traverse speed. Iterating the models starting with the full zero shear viscosity and tool rotational velocity results in divergence errors. In CFD software it is best practice that best guess initial conditions be provided to simplify arrival at a solution. The models presented were initialized using the full experimental traverse speed. From this point, it was found that a solution was best reached in the presented models by successive increases in tool rotational velocity and zero shear viscosity from a small fraction of their desired values to, eventually, their

desired values. Using this method, each solution has a good guess solution from which to converge on a subsequent solution using the updated parameters.

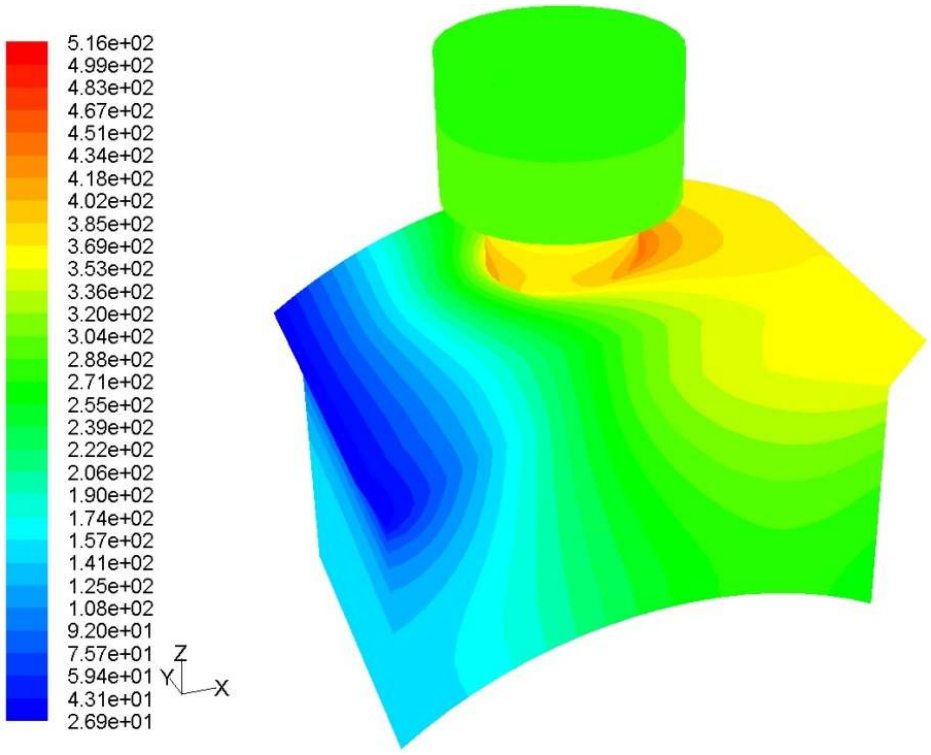

Figure 163: Modeled temperature contour (C) for the narrow 4.8mm(3/16") diameter probe tool case (Iso view).

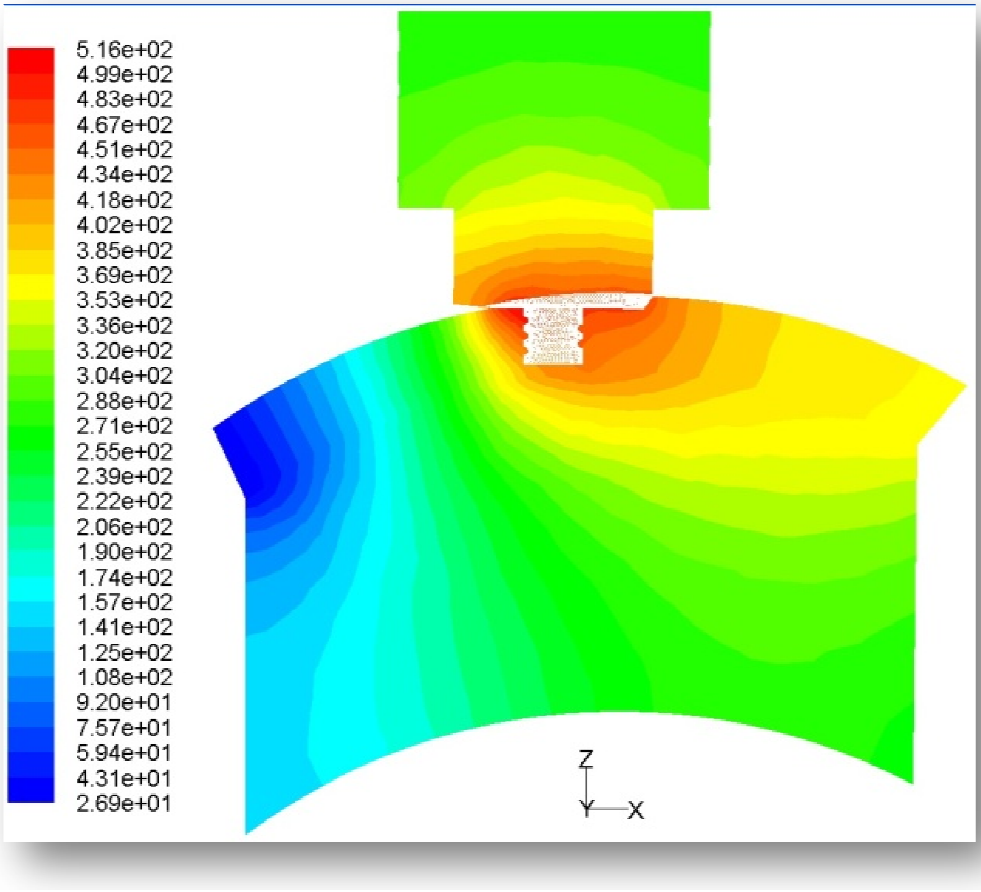

Figure 164: Modeled temperature contour (C) for the narrow probe tool case (longitudinal view).

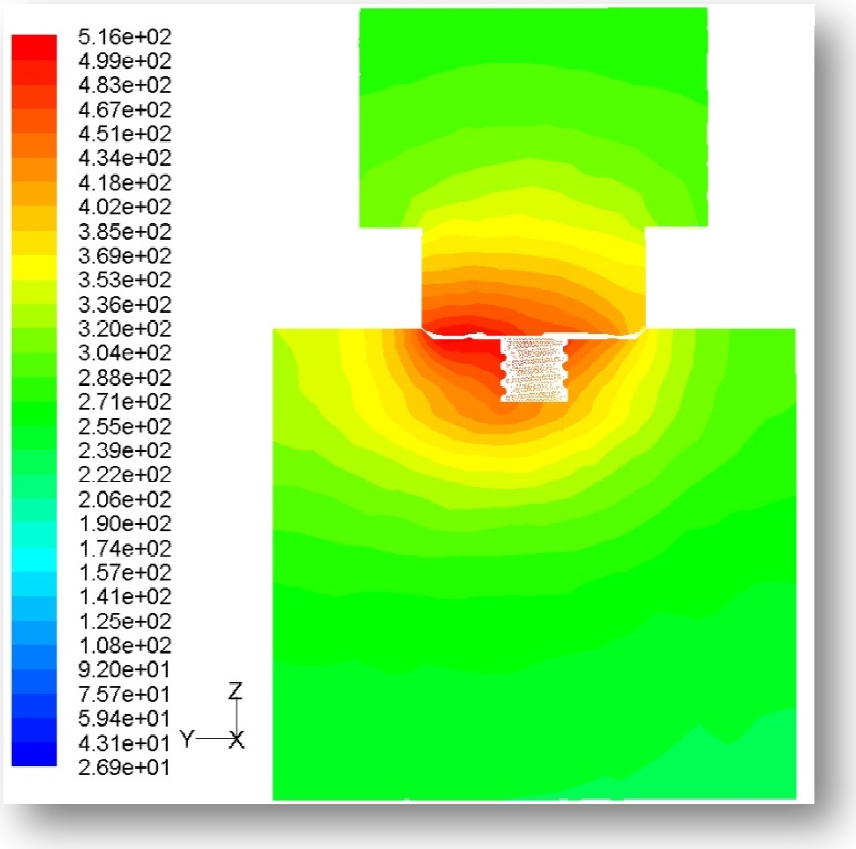

Figure 165: Modeled temperature contour (C) for the narrow probe tool case (front lateral view looking from the inlet).

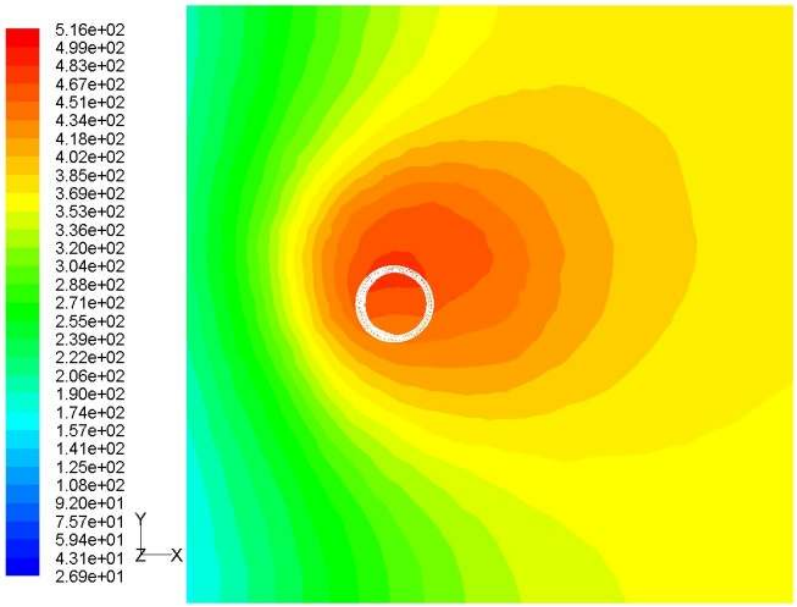

Figure 166: Modeled temperature contour (C) for the narrow probe tool case (top view of a slice taken at the middle of the probe).

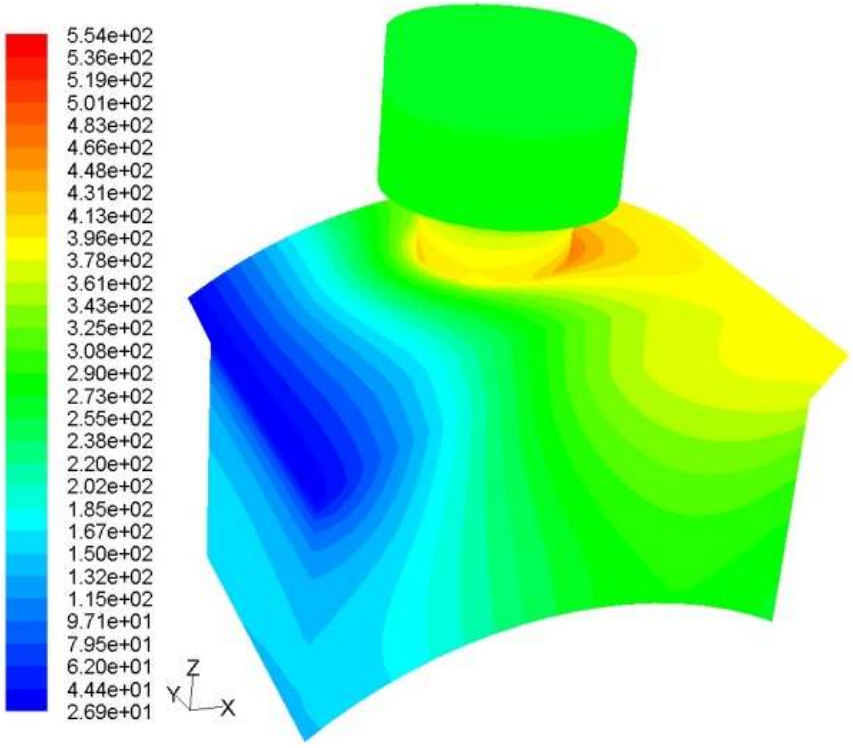

Figure 167: Modeled temperature contour (C) for the wide 0.236”(6mm) diameter probe tool case (Iso view).

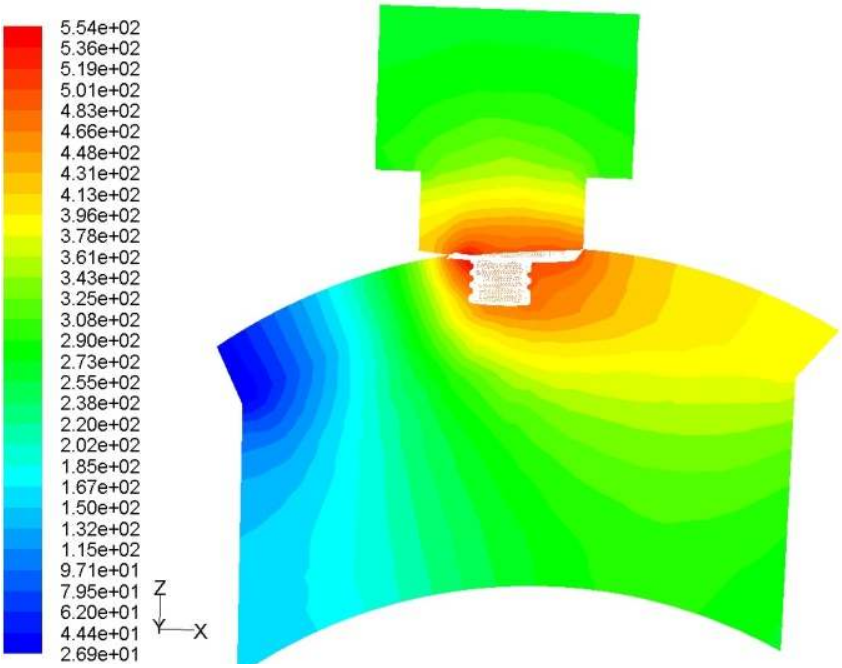

Figure 168: Modeled temperature contour (C) for the wide probe tool case (longitudinal view).

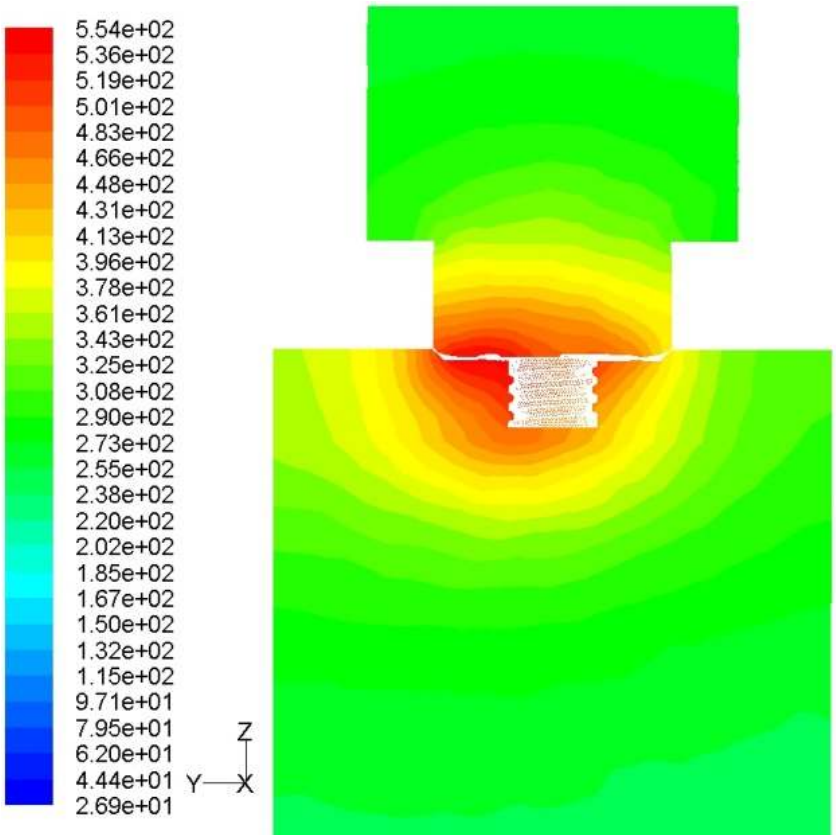

Figure 169: Modeled temperature contour (C) for the wide probe tool case (front lateral view looking from the inlet).

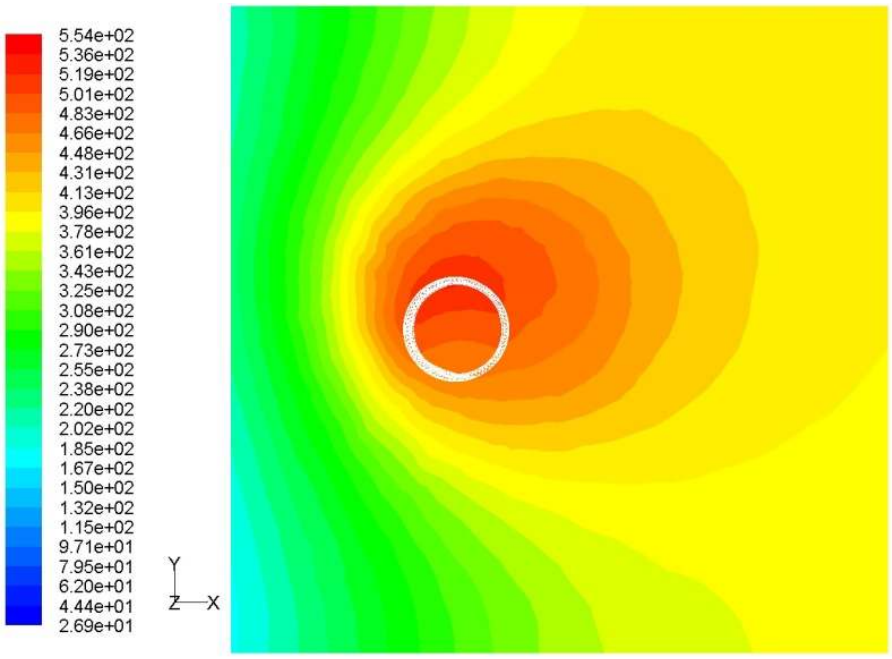

Figure 170: Modeled temperature contour (C) for the wide probe tool case (top view of a slice taken at the middle of the probe).

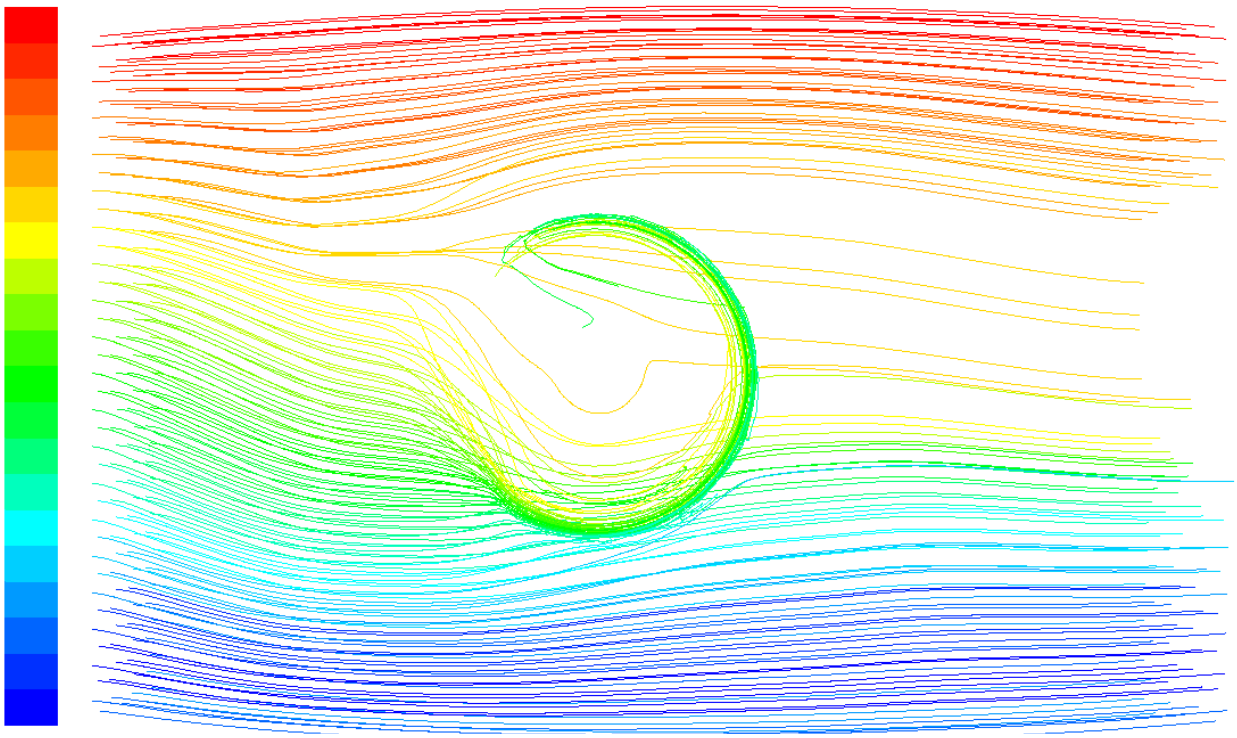

Figure 171: Model pathlines for the narrow probe tool case (looking from the top, advancing side is red).

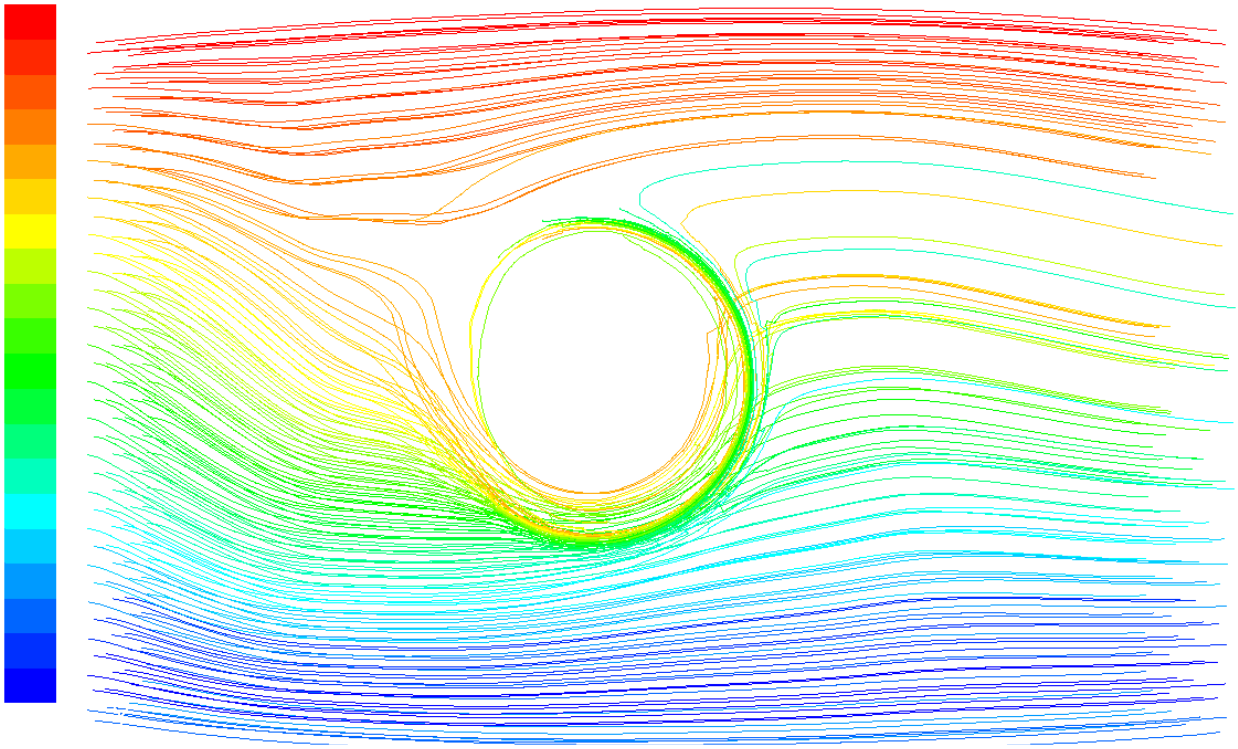

Figure 172: Model pathlines for the wide probe tool case (looking from the top, advancing side is red).

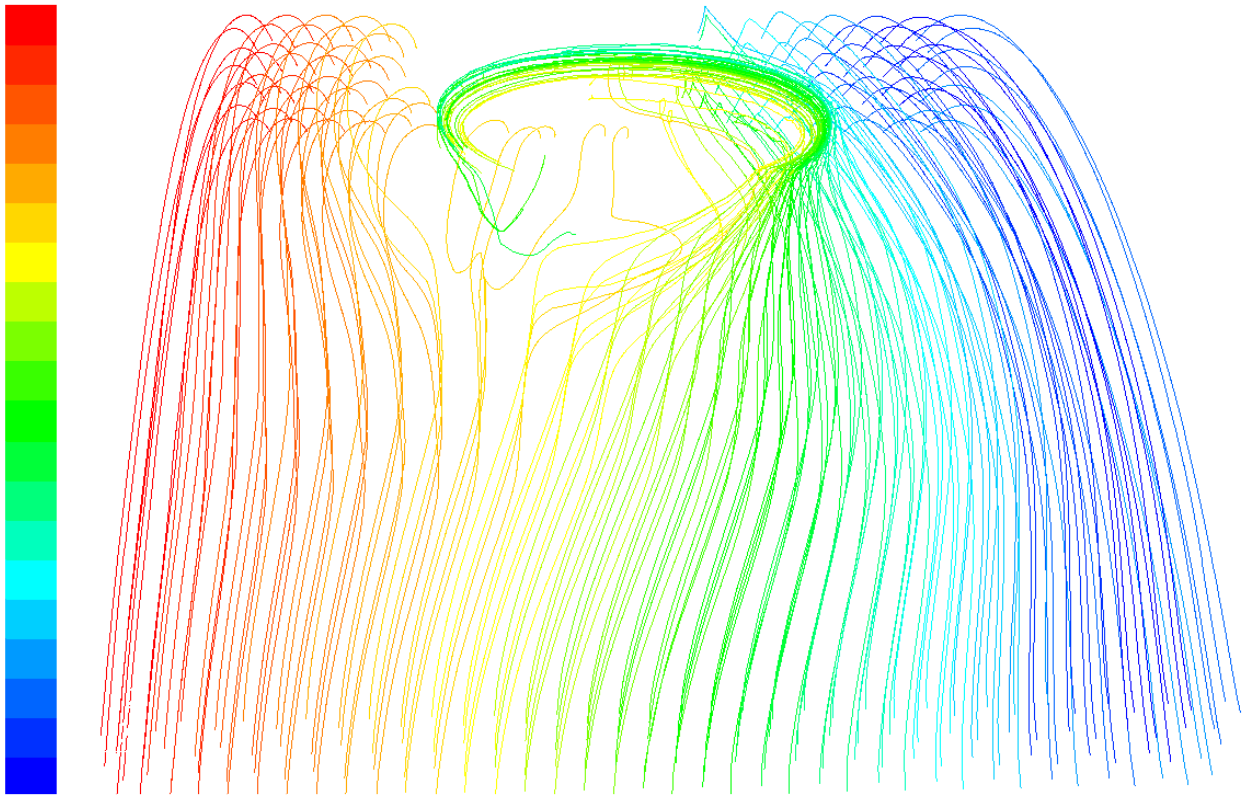

Figure 173: Model pathlines for the narrow probe tool case (looking from the inlet, advancing side is red).

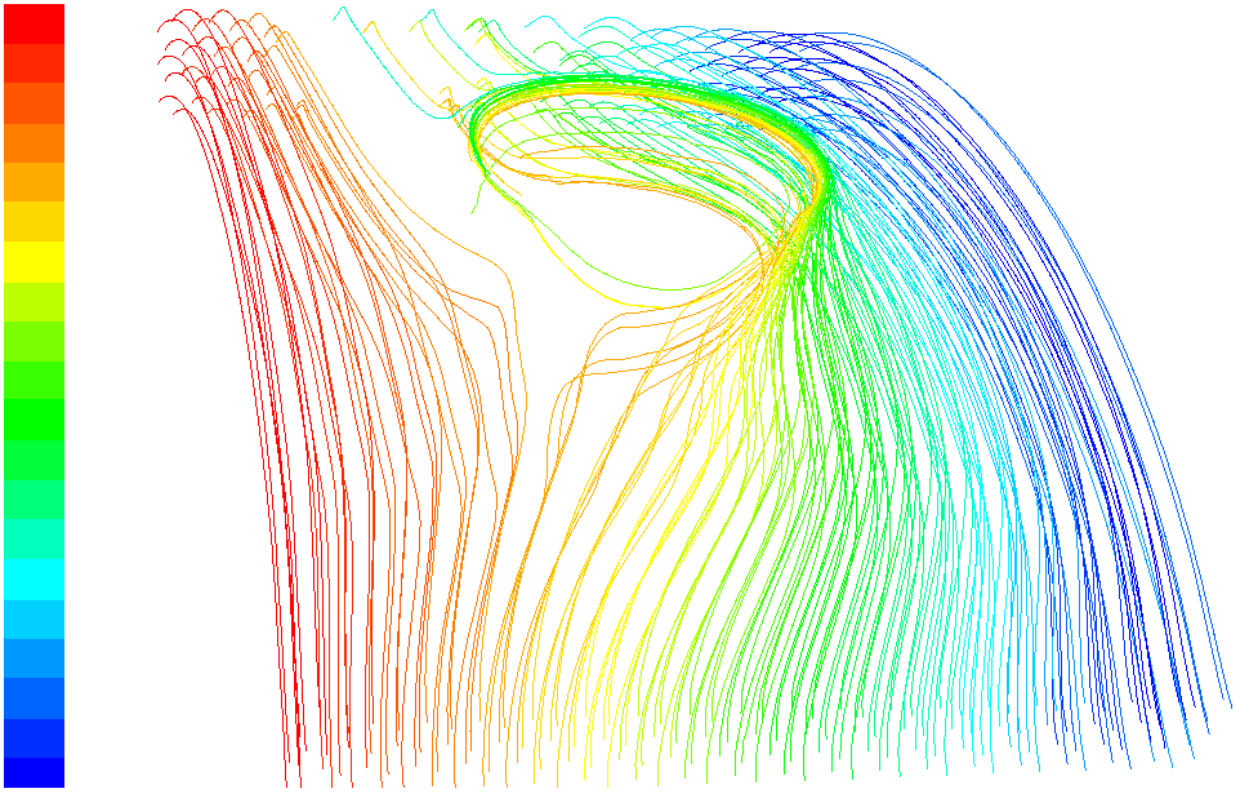

Figure 174: Model pathlines for the wide probe tool case (looking from the inlet, advancing side is red).

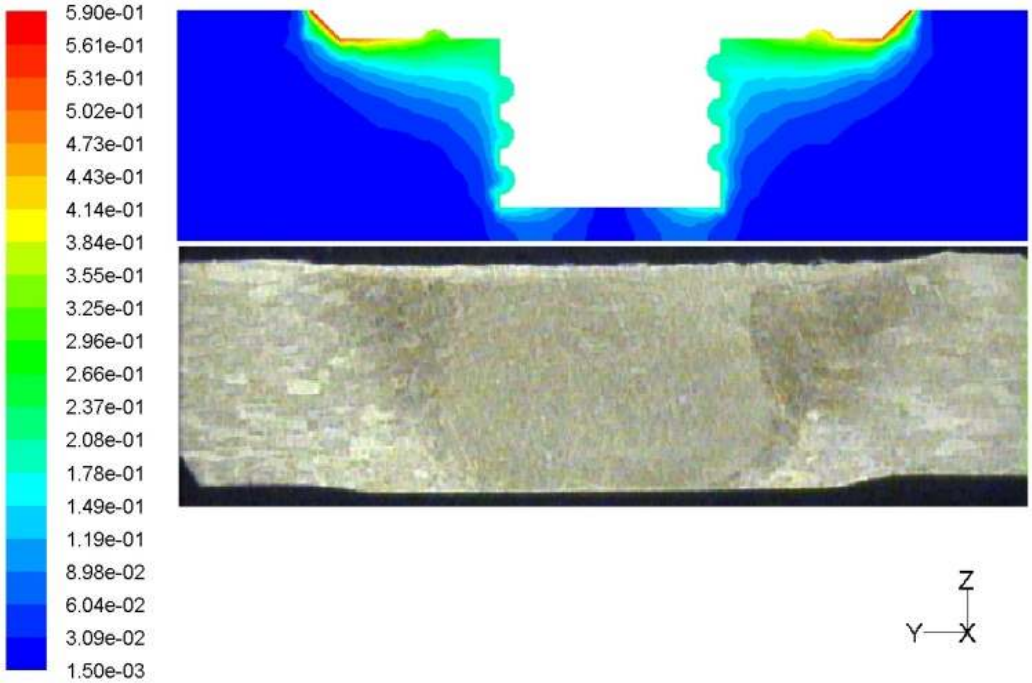

Figure 175: Lateral contour of velocity magnitude (m/s) compared with experimental lateral macrosection for the wide (6mm diameter) probe case. The stirred zone (light,

center), thermomechanically affected zone (TMAZ)(dark), and parent material (lightest) can be seen in the macrosection. The model shows significant material stirring in the stirred zone, minimal material stirring in the TMAZ, and no material stirring in the parent material.

Conclusions

Fusion welding experiments performed on this material and geometry demonstrated that process parameter adjustment was required around the circumference of the weld to maintain acceptable weld quality throughout. Heat input had to be reduced continually to avoid significant and undesirable expansion of the weldpool. It was shown in this study that the reduced welding temperature of the FSW interface minimized this problem and acceptable welds could be produced over a range of parameters. Although a steady rise in temperature was observed, it was not sufficient to require any reduction in weld power during the weld. Additionally, it was shown that a traditional FSW tool geometry could be used on a small diameter pipe provided that a scrolled shoulder was used and the tool was offset some distance from the center of the cylindrical work in the direction of traverse as described earlier.

Ideally a force feedback control system would be used to account for variation in the thickness of the pipe sections and rotational eccentricities in the setup. However it was demonstrated in this experiment that FSW of small diameter pipe can be performed without the luxury of force feedback control, provided that pipe sections were preprocessed to reduce wall thickness variation and an expanding inner mandrel was used. The expanding inner mandrel served to align the inner diameters of the pipe section and force the sections into a more uniform circular shape.

Welds presented in the experiment were of high tensile strength and sound internal and superficial appearance. This experiment demonstrated that FSW can be performed on this geometry at a wide range of parameters using at various traditional tool geometries. Additionally, it was shown that a high welding rate can be achieved. In this experiment, the highest tensile strength was achieved at travel speed of 15.7 inches per minute and travel speeds up to 17 inches per minute were tested with good results. At the

later speed setting, the tool welds the full circumference of the 4.2" diameter pipe sections in less than 50 seconds. The ability to weld at high traverse speeds increases the output of a FSW machine and increases the likelihood that the costs of the machine can be justified in a specific manufacturing setting.

It was also shown that the FSW process is well understood and simple CFD models can be used to reliably predict the thermal conditions and material flow during FSW of a given geometry. It was also shown that CFD can give a reasonable prediction of the axial forces that should be expected under various FSW conditions. The large startup costs associated with FSW make the predictive capabilities and understanding provided by a CFD model more valuable.

Appendix

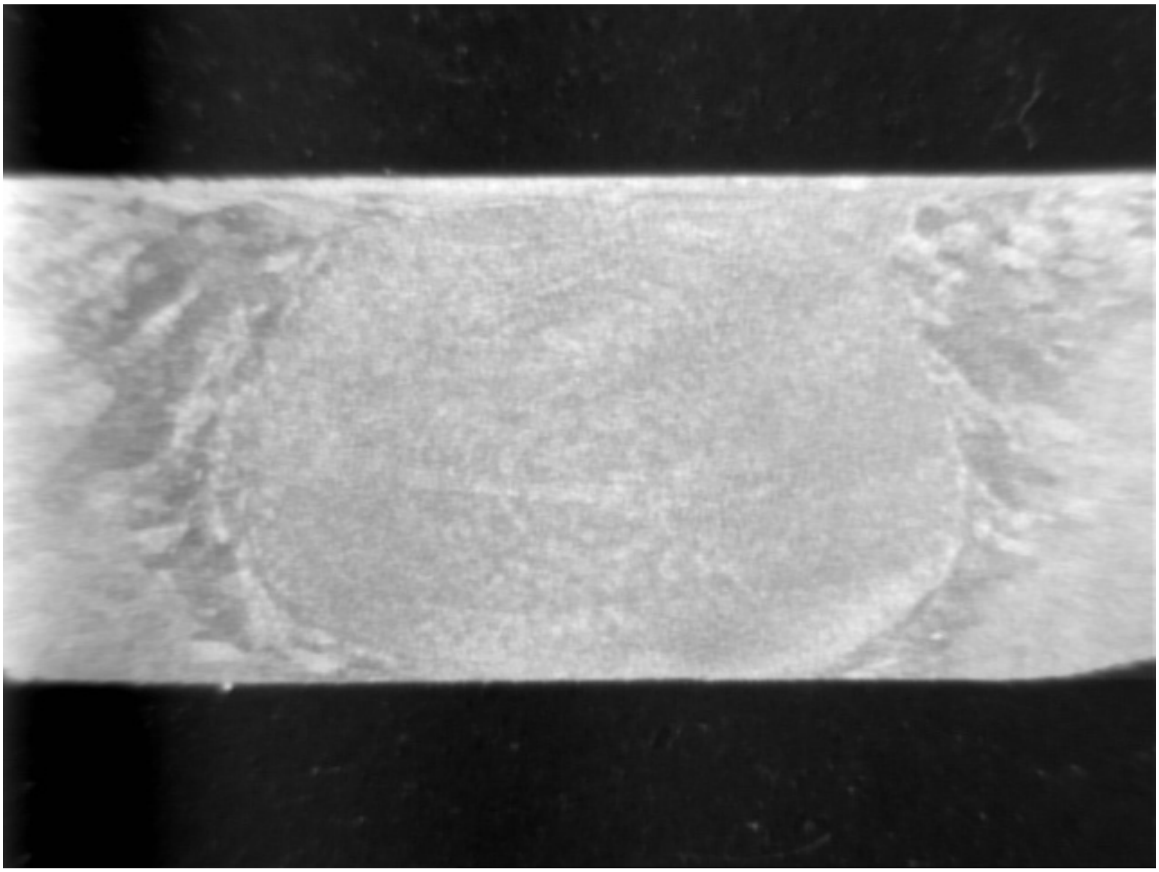

Figure 176: Zoom view of a macro taken from a full penetration butted pipe weld (1400rpm, 5.2ipm). The experimental tools had a 5/8" diameter, scrolled shoulder and 0.18" length, threaded probe. The wide (0.236" diameter) probe tool created this weld.

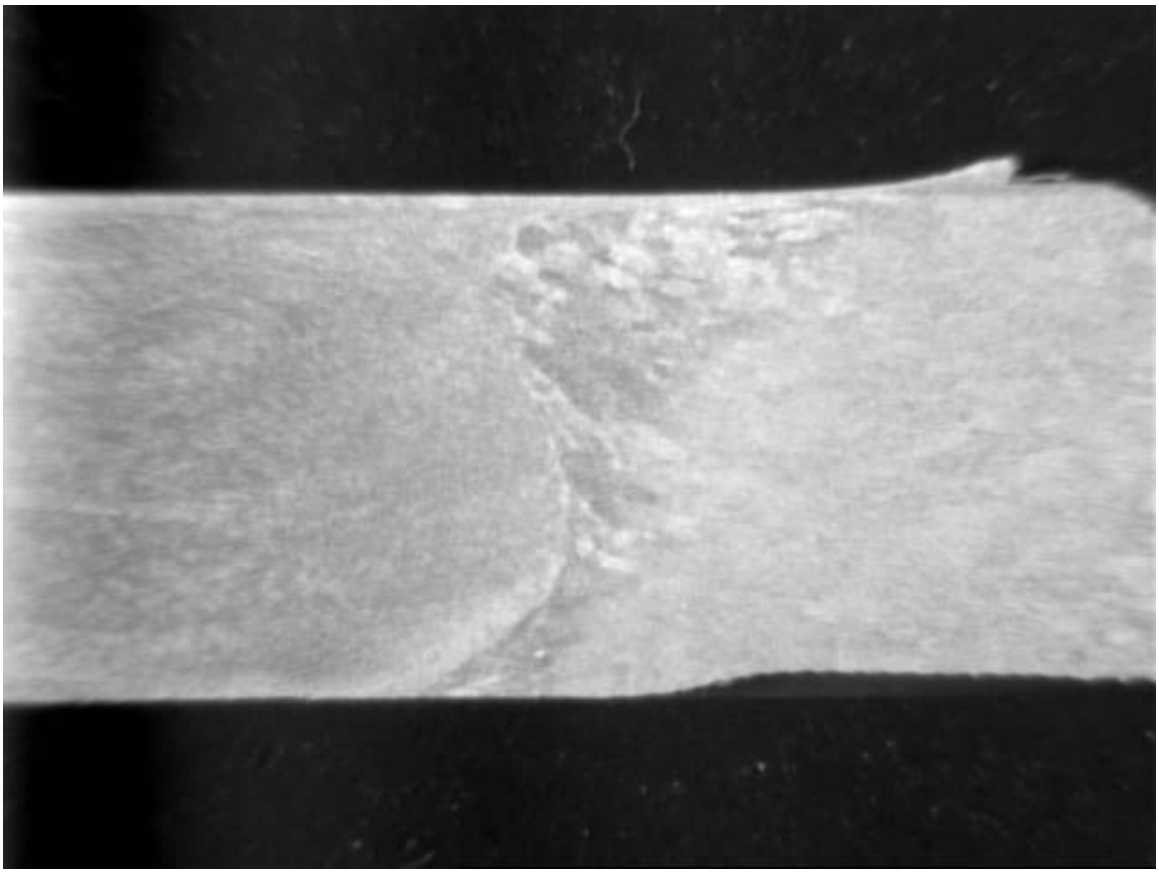

Figure 177: Zoom view of a macro taken from a wide probe weld (1400rpm, 5.2ipm). The advancing side of the weld is shown.

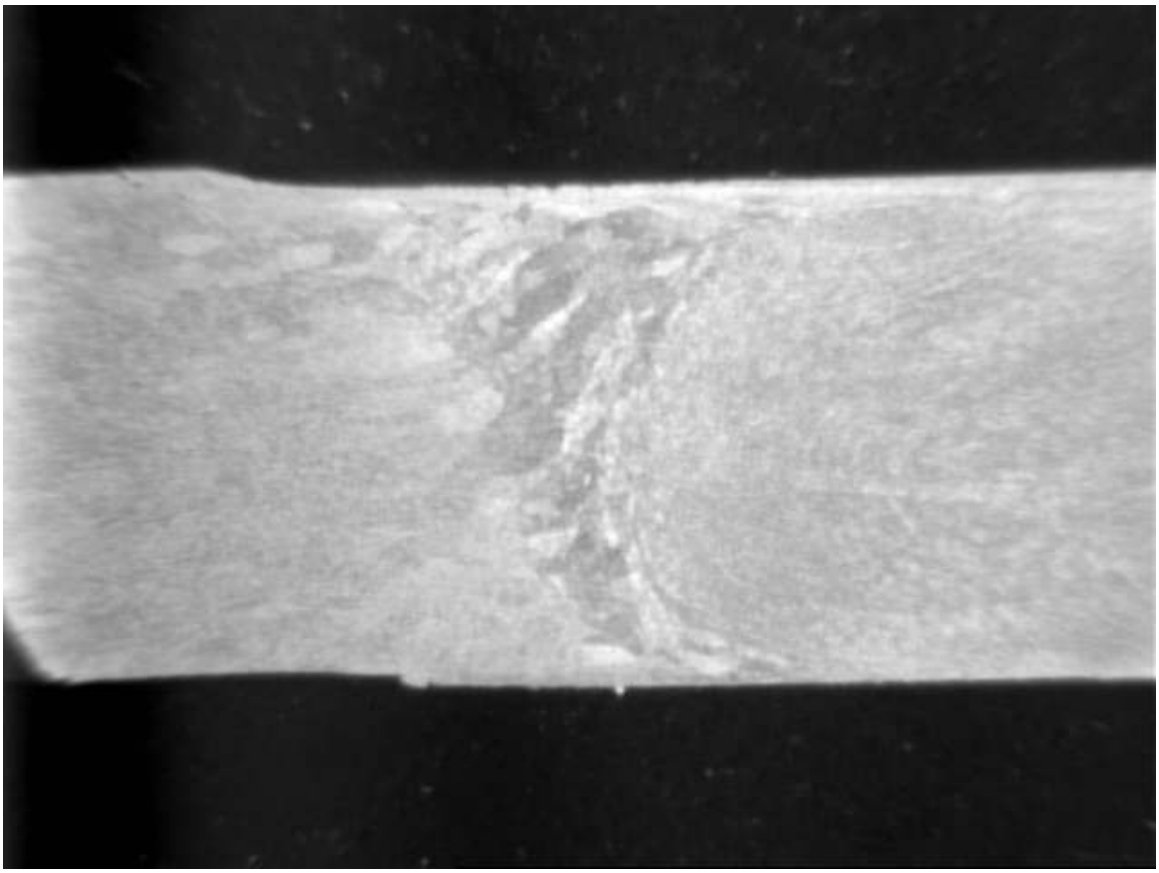

Figure 178: Zoom view of a macro taken from a wide probe weld (1400rpm, 5.2ipm). The retreating side of the weld is shown.

Figure 179: The superficial appearance of some of the pipes welded in the experiment and some additional pipe welding runs not presented in the experiment. The center and bottom sample is a tungsten inert gas, TIG, weld made for comparison with filler type 5356.

Figure 180: The superficial appearance of some of the pipes welded in the experiment and some additional pipe welding runs not presented in the experiment. The top and center sample is a TIG weld.

Figure 181: The superficial appearance of some of the pipes welded in the experiment and some additional pipe welding runs not presented in the experiment. Left and bottom is a TIG weld sample.

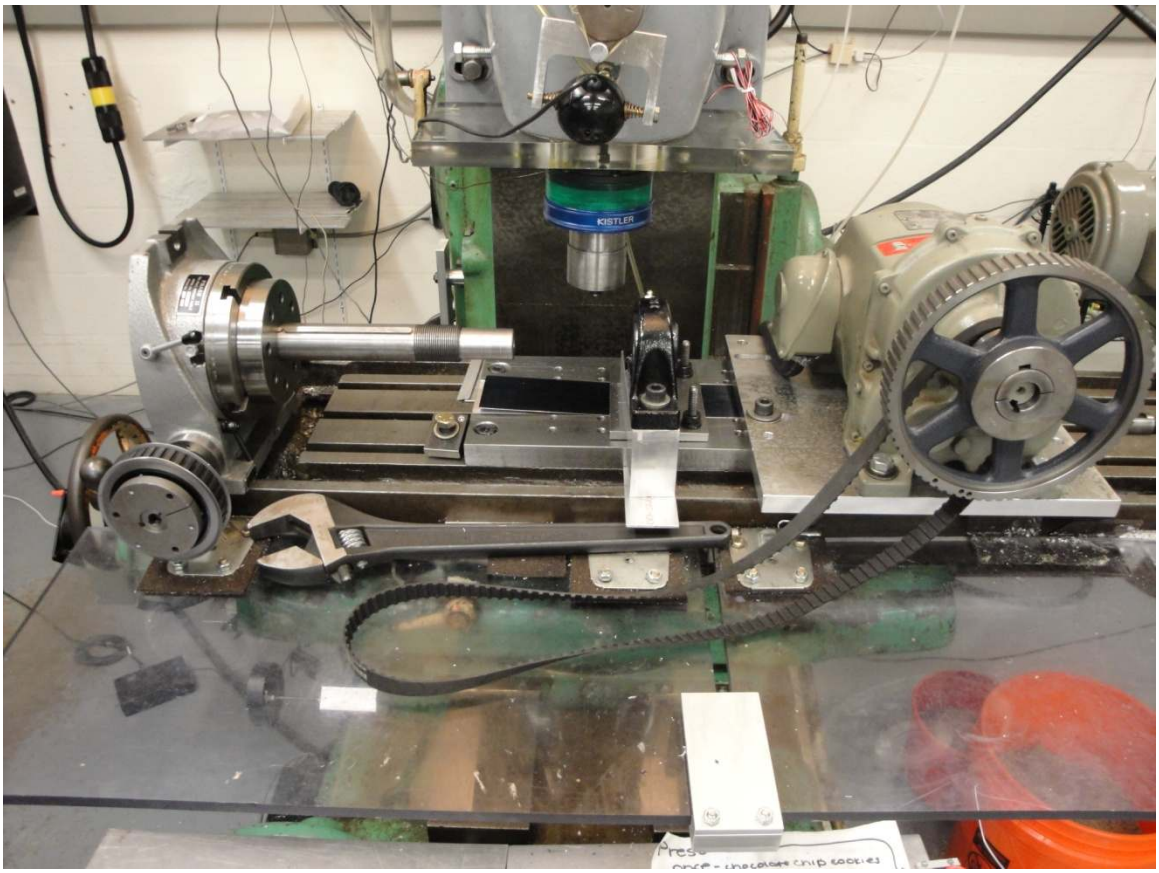

Figure 182: The rotary welding apparatus (grey, left), rotary bearing (black, center), and rotary motor (beige, right).

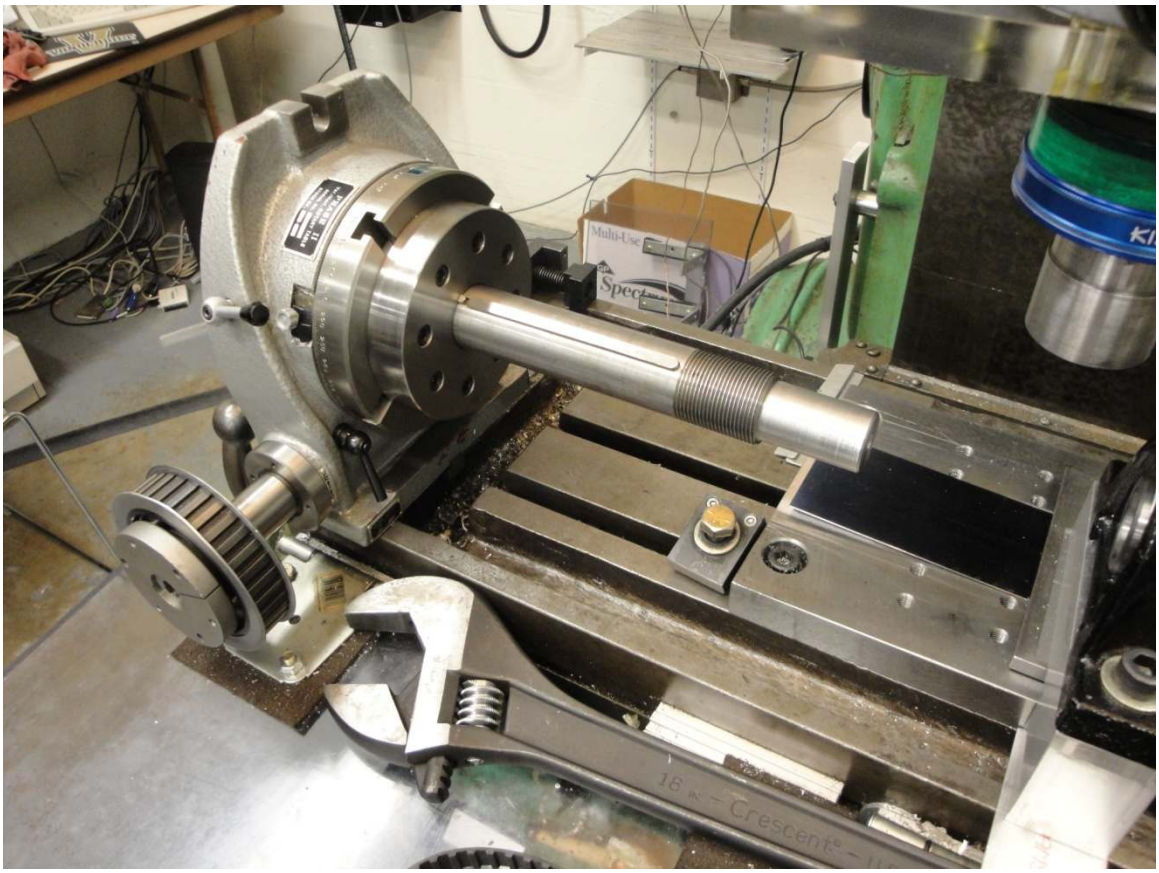

Figure 183: Rotary welding apparatus with keyed shaft.

Figure 184: Left is a pipe sample used for tensile coupons of the parent material and geometry. Right are pipe sections joined in the experiment.

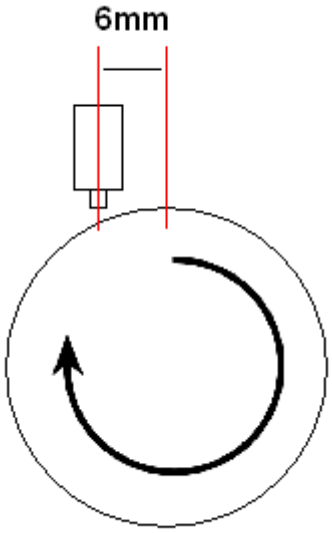

Figure 185: A diagram illustrating the tool offest with respect to the highest point of the rotating pipe sections. The offset is parallel to the weld seam and results in the desired contact condition. This offset configuration reduced vibration and improved weld quality in comparison to the case without offset.

References:

Atharifar, H., Lin, D. C., & Kovacevic, R. (2009). Numerical and Experimental Investigations on the Loads Carried by the Tool During Friction Stir Welding. *Journal of Materials Engineering and Performance* .

Atharifar, H., Lin, D. C., & Kovacevic, R. (2007). Studying Tunnel-like Defect in Friction Stir Welding Process Using Computational Fluid Dynamics. *Materials Science and Technology* , 375-391.

Defalco, J., & Steel, R. (2009, May). Friction stir process now welds steel pipe. *The Welding Journal* , pp. 44-48.

Fairchild, D., Kumar, A., Ford, S., & Nissley, N. (2009). Research Concerning the Friction Stir Welding of Linepipe Steels. *Trends in Welding Research* , 371-380.

Feng, Z., Steel, R., Packer, S., & David, S. *Friction Stir Welding of API Grade X65 Steel Pipes.* OAK RIDGE NATIONAL LABORATORY, U. S. DEPARTMENT OF ENERGY.

Kou, S., & Le, Y. *Heat Flow during the Autogenous GTA Welding of Pipes.* METALLURGICAL TRANSACTIONS A; VOLUME 15A, JUNE 1984, p1171.

Lammlein, D. H., DeLapp, D. R., Fleming, P. A., Strauss, A. M., & Cook, G. E. (2009). The application of shoulderless conical tools in friction stir welding: An experimental and theoretical study. *Materials and Design 30* , 4012–4022.

Lammlein, D. H., Longhurst, W. H., Delapp, D. R., Flemming, P. A., Strauss, A. M., & Cook, G. E. (2010). The Friction Stir Welding of Hemispheres – A technique for Manufacturing Hollow Spheres. *Journal of Advanced Manufacturing* .

Longhurst, W. R. (2009). *Dissertation: Force control in friction stir welding.* Vanderbilt University.

Longhurst, W. R., Strauss, A. M., & Cook, G. E. (2009). Enabling Automation of Friction Stir Welding: The Modulation of Weld Seam Input Energy by Traverse Speed Force Control. *American Society of Mechanical Engineers Journal of Dynamic Systems Measurement and Control* .

Longhurst, W. R., Strauss, A. M., & Cook, G. E. (n.d.). Identification of the key enablers for force control of friction stir welding. *American Society of Mechanical Engineers Journal of Manufacturing Science and Engineering* , 2009.

Longhurst, W. R., Strauss, A. M., Cook, G. E., & Fleming, P. A. (April 28, 2010). Torque control of friction stir welding for manufacturing and automation. *International Journal of Advanced Manufacturing Technology* .

Longhurst, W. R., Strauss, A. M., Cook, G. E., Cox, C. D., Hendricks, C. E., & Gibson, B. T. (2010). Investigation of force controlled friction stir welding for manufacturing and automation. *Proceedings of the Institution of Mechanical Engineers, Part B, Journal of Engineering Manufacturing., Volume 224* .

Na, S. J., & Lee, H. J. *A study on parameter optimization in the circumferential GTA welding of aluminium pipes using a semi-analytical.* Journal of Materials Processing Technology; 57, 1996, 95- 102.

Newell, W. F., Sperko, W. J., Mannings, D. C., Anderson, T., & Connell, D. *D10 COMMITTEE ON PIPE AND TUBE WELDING.* p32: American Welding Society.

Packer, S. M., & Matsunaga, M. (2004). Friction Stir Welding Equipment and Method for Joining X65 Pipe. *Proceedings of the 14th Intl. Offshore and Polar Eng. Conf.* Toulon, France.

Pew, J. W., Nelson, T. W., & Sorensen, C. D. (2007). Torque based weld power model for friction stir welding. *Sci Technol Weld Join 12(4)* , 341.

Schmidt, H., Hattel, J., & Wert, J. (2004). An analytical model for the heat generation in friction stir welding. *Modelling Simul. Mater. Sci. Eng. 12* , 143–157.

Tello, K. E., Gerlich, A. P., & Mendez, P. F. *Constants for hot deformation constitutive.* Science and Technology of Welding and Joining; 2010, VOL 15, NO 3.

Thomas, W. M. (1991). *Friction stir butt welding.* International Patent Application No PCT/GB92/02203.

CONCLUSION AND FUTURE WORK

Conclusion

The research presented is expected to expand the range of application of the FSW process. The use of force feedback control of weld seam alignment permits the use of FSW in an automated, manufacturing setting on blind type t-joints. Experimental and computational data demonstrated that the vertical member of the t-joint can be followed based on process force feedback. This will allow a FSW machine tool to follow ribs under large metal sheets without tedious alignment and tool path determination. In the case of serpentine ribs, this research will permit the application of FSW to a geometry which was previously not feasible.

In this work, the FSW was shown for the first time to be capable of welding small diameter butted hemisphere type joints. It was shown that a cupped shoulder tool in conjunction with internal support can be used to effectively join two hemispheres at a high percentage of the parent material strength. Additionally, it was shown that for cases where internal support is not permissible that a conical type tool can be used to obtain welds exceeding 50% penetration. In a practical measure of strength where these partial penetration welds are compared to the strength of the full thickness of the parent material, these unsupported welds achieved strengths exceeding 25%. These strengths were achieved using the limited weld parameter permutations attempted experimentally and can likely be increased. A partial penetration weld of butted hemispheres without the use of an internal support has applications to external compression vessels. Additionally, the use of a conical tool in FSW at partial penetration without anvil support applies to other situations where the underside of the work is inaccessible and the use of an underside support device is unfeasible.

The joining of butted hemispheres with full weld penetration was demonstrated successfully with weld strengths exceeding 70% over the limited parameter range tested.

In demonstrating the effectiveness of FSW on small diameter hemispheres, this experiment has shown that FSW is applicable to highly curved surfaces and surfaces with curvature in two degrees of freedom like a sphere. The demonstration of FSW on this particularly difficult geometry extends the range of FSW application. This has applications to things like aerospace structures and pressure vessels.

Although the small diameter butted hemisphere joint presents a FSW case with many intrinsic difficulties, in one way it is possibly less difficult than it could be. The sphere is curved equally in two degrees of freedom allowing it to mate ideally with a cupped tool even as the cupped tool is rotated about the long axis of the tool as in welding. This is not the case with a pipe where there is no tool shoulder geometry which maintains this ideal tool to work mate when the tool is rotated. The pipe therefore presents another important FSW situation with inherent difficulties.

In this work it was demonstrated that small diameter pipe sections can be joined effectively with a simple FSW tool. The scrolled shoulder and threaded probe tool was used to make full penetration welds on 4.2" diameter and wall 0.2" thickness pipes. The welds were exceptional superficially and achieved tensile strengths in excess of 70% of the parent material over the limited parameter range tested. The work done here extends the use of FSW to small diameter pipe with a wide range of application such as in the petroleum industry.

Finally, it was shown that the FSW is well understood in that equations governing the process are refined to the extent that they can reliably produce what is seen experimentally. CFD models utilizing process governing equations of limited complexity can be used to reliably model and predict the relevant aspects of the FSW process. This was demonstrated over a wide variety of FSW work geometries including t-joints, butted plates, butted hemispheres, and butted pipes. Additionally, a variety of tool geometries were tested including conically shaped FSW tools, tools with scrolled shoulders, and tools with threaded probes. It was demonstrated that the thermal contours of the tool and work can be reliably produced in CFD. It was also demonstrated the flow field in the work around the FSW tool can be reliably shown in CFD models. The FSW process forces were also predicted using CFD with a reasonable degree of accuracy. These process equations and CFD models are valuable because the experimental evaluation of a

new FSW process environment is resource intensive. CFD models provide a quick and effective means of evaluating an FSW process situation prior to making an actual weld.

Future Work

The cylindrical and spherical weld geometries presented required a circular weld path. The circular weld path resulted in a secondary heating effect which was exacerbated by the small radius of the work and correspondingly reduced conduction lengths within the work. The sum of these effects resulted in a significant increase in temperature throughout each experimental weld. This steady increase in temperature during the weld cycle is undesirable as the properties of the welded material will vary according to temperature around the circumference of the weld. It is desirable to reach a welding temperature at some point early in the weld and maintain this temperature throughout the weld. This can be achieved by either a reduction in the rotational velocity of the tool, an increase in the traverse rate of the tool, or by the implementation of a heat dissipation system.

A reduction in tool rotational velocity or an increase in traverse rate will generally result in a reduction in the power input at the weld seam and the rate of heat dissipation into the tool and work. If a particular FSW process and environment is well characterized, then a predetermined reduction in weld power can be programmed into the weld cycle. This solution is simple and effective but requires prior knowledge of how the FSW process environment will behave thermally.

A thermal (or temperature) based feedback control system could alternatively be implemented which adjusts weld parameters in real time in response to a measured temperature exceeding the desired value. This sort of system would require an instrument which provides real time temperature data to the weld controller. One example of this would be a thermal camera calibrated to the emissivity of the tool shank. The thermal camera computer could then send live temperature data from the region of interest on the tool shank to the weld controller. Another example would be a thermocouple in the tool or in the work.

When the measured temperature exceeded the desired temperature the weld controller would adjust the tool rotational velocity or traverse rate based to reduce heat input. Alternatively the weld controller could trigger a heat dissipation system when the measured temperature exceeded the desired temperature. This heat dissipation system could be a heat exchanger in the tool or work. It has also been suggested that a jet of compressed air could be focused on the work behind the traveling tool during rotary welding to eliminate the secondary heating effect.

A temperature based feedback control system for controlling thermal conditions in conjunction with an axial force or torque based feedback control system for controlling axial force would be effective methods of controlling weld quality in FSW. The temperature based controller would likely adjust tool rotational velocity to control the weld temperature while the force based controller adjusted tool vertical position to control axial force and the downward pressure excreted by the tool. The FSW is sensitive to axial force and the temperature in the vicinity of the tool. Although FSW can be done without feedback control, control systems reduce the necessary preparation time, increase the tolerance error, and increase the reliability of the system. In a manufacturing environment where a robust and flexible process is required, these feedback control systems are likely necessary.